

**A statistical study of
magnetospheric plasma mass
loading using the Cluster
spacecraft**

Jasmine Kaur Sandhu

Radio and Space Plasma Physics Group

Department of Physics and Astronomy

University of Leicester

A thesis submitted for the degree of

Doctor of Philosophy

June 2016

A statistical study of magnetospheric plasma mass loading using the Cluster spacecraft

Jasmine Kaur Sandhu

Abstract

Using Cluster data, from the WHISPER and CODIF instruments, for the interval spanning 2001 – 2012, empirical models describing the electron density, average ion mass, and plasma mass density distribution along closed geomagnetic field lines are determined. The models represent the region spanning $5.9 \leq L < 9.5$, with dependences on L shell and MLT (Magnetic Local Time) included.

An average mass density model, describing spatial variations for typical quiet time conditions, was produced by independently modelling field-aligned variations in the electron density and average ion mass, and combining these to infer the corresponding model for mass density. The resulting average models illustrates some key features of the electron density and average ion mass spatial distributions.

Dependences of the electron density, average ion mass, and total plasma mass density on the ring current intensity were also examined. Using a similar approach as for the average models, the field-aligned distributions were quantified, including variations with Dst index, providing information on how the spatial distributions vary due to storm-related processes. A key result obtained is the observed general decrease in mass density, accompanied by an increase in average ion mass, during disturbed conditions.

An application of the mass density models in improving estimates of field line eigenfrequencies is explored, using the time-of-flight technique. The analysis highlights the contribution of mass density variations in determining the frequency of standing Alfvén waves on closed geomagnetic field lines, as well as the magnetic field variations. The results provide information on the spatial distribution of field line eigenfrequencies, as well as dependences on geomagnetic activity. Furthermore, the validity of the improved time-of-flight calculations are illustrated through a comparison to a statistical analysis of ground magnetometer FLR (Field Line Resonance) observations.

Declarations

Sections of this thesis have been previously published, or submitted for publication in the following:

J. K. Sandhu, T. K. Yeoman, R. C. Fear, and I. Dandouras. A statistical study of magnetospheric ion composition along the geomagnetic field using the Cluster spacecraft for L values between 5.9 and 9.5. *Journal of Geophysical Research (Space Physics)*, 2016. doi: 10.1002/2015JA022261.

To my family

Acknowledgements

I wish to thank many people for their support throughout my PhD. Firstly, I thank my supervisor, Tim Yeoman. I am grateful for all the guidance, patience, advice, and productive conversations. I also thank my second supervisor, Mark Lester, for the insightful comments and suggestions. Working within the Radio and Space Plasma Physics group at Leicester was invaluable to my research. It is a motivated, friendly, and productive environment, and I wish to thank both past and present Head of RSPP (Stan Cowley and Mark Lester) for the opportunity to carry out my PhD in the group.

I owe thanks to the STFC for funding this research, and also to the people and institutes for providing the data used in my studies. In particular, I am grateful to the Cluster Active Archive, who have highlighted the importance of data access in science to me. In addition, I thank all those who worked, and continue to work, on the Cluster mission, who remind me of the importance of not giving up.

I have thoroughly enjoyed being part of the RSPP group. It is a sociable, cake-fuelled, crossword-obsessed group, and I thank my friends within RSPP for their support as well as distractions throughout my PhD. I am grateful to my office mates, past and present, for putting up with my high-maintenance tendencies and finding new ways to procrastinate.

Most importantly, I wish to thank my family for their support and understanding, and to whom I owe all that I have achieved.

Contents

List of Figures	v
List of Tables	xx
1 Introduction	1
1.1 Single particle motion	2
1.1.1 Gyromotion	2
1.1.2 Bounce motion	3
1.1.3 Gradient drift	5
1.1.4 Curvature drift	6
1.1.5 $\mathbf{E} \times \mathbf{B}$ drift	7
1.2 MHD	9
1.2.1 Maxwell's equations	11
1.2.2 Ohm's law	12
1.2.3 Magnetic pressure and tension	12
1.2.4 Diffusion and the frozen-in-flux theorem	13
1.3 Earth's magnetosphere	16
1.3.1 Corotational flows	17
1.3.2 Solar wind-magnetosphere coupling	19
1.3.2.1 Chapman-Ferraro currents	20
1.3.2.2 Dungey cycle and convective flows	21
1.3.3 Magnetospheric configuration	26
1.3.3.1 Cusp	26
1.3.3.2 Tail lobes	27

1.3.3.3	Plasma sheet	28
1.3.3.4	Plasmasphere and plasmatrough	28
1.3.4	Current systems	30
1.3.5	Plasma source and loss processes	31
1.4	Magnetospheric dynamics	33
1.4.1	Steady magnetospheric convection events and substorms	33
1.4.2	Geomagnetic storms	35
1.4.2.1	Initial phase	36
1.4.2.2	Main phase	37
1.4.2.3	Recovery phase	38
1.5	ULF waves and FLRs	39
1.5.1	Standing Alfvén wave formation	41
1.5.2	Wave energy sources	42
2	Literature Review	44
2.1	Statistical studies of magnetospheric mass density	44
2.2	Dependences on geomagnetic activity	46
2.3	FLR observations	47
3	Instrumentation and Data	52
3.1	Method	52
3.2	Cluster	53
3.3	WHISPER	54
3.4	CIS	55
3.4.1	CODIF	56
3.4.2	RPA mode	56
3.4.3	HIA	57
3.5	PEACE	57
3.6	Ground magnetometer data	58
4	Data Reduction	59
4.1	Binning data	59
4.2	Field line tracing	59
4.2.1	Identifying the L value position	59

4.3	Removal of observations on open field lines	60
4.4	CODIF radiation belt contamination	63
4.5	Method verification	65
4.5.1	WHISPER usage	66
4.5.2	CODIF usage	70
4.6	Reduced datasets	75
4.6.1	Electron density	75
4.6.2	Average ion mass	76
5	Average Density Model	78
5.1	Field-aligned distribution of electron density	78
5.1.1	Power law model	80
5.1.2	Gaussian model	83
5.2	Field-aligned distribution of average ion mass	87
5.3	Mass density model	89
5.4	Discussion	90
5.4.1	Electron density	90
5.4.2	Average ion mass	98
5.4.3	Mass Density	102
6	Geomagnetic Variations	107
6.1	Binning data for Dst index	107
6.2	Field-aligned distribution of electron density	109
6.3	Field-aligned distribution of average ion mass	112
6.3.1	Cusp enhancement	116
6.4	Mass density model with Dst index dependence	117
6.5	Dependences on Kp index	118
6.5.1	Field-aligned distribution of electron density	119
6.5.2	Field-aligned distribution of average ion mass	123
6.5.3	Mass density model with Kp index dependence	123
6.6	Discussion	124
6.6.1	Electron Density	124
6.6.2	Average Ion Mass	130

6.6.2.1 Cusp enhancement	133
6.6.3 Mass Density	134
6.6.4 Comparison to parametrisation with Kp index	138
7 Applications	143
7.1 Time-of-flight method	143
7.1.1 Wild et al. [2005] study	145
7.2 Results	146
7.2.1 Average mass density model	147
7.2.2 Dependence on geomagnetic activity	149
7.3 Discussion	155
7.3.1 Average mass density model	155
7.3.1.1 Contribution of equatorial enhancement	157
7.3.2 Dependence on geomagnetic activity	159
7.4 A comparison to ground magnetometer observations	161
7.4.1 Automated FLR identification	161
7.4.2 Statistical analysis of ground magnetometer observations	166
8 Conclusions and Future Work	172
References	175

List of Figures

1.1	Diagram illustrating three important forms of single particle motion in electromagnetic fields: gyromotion, bounce motion, and drift motion [Kivelson, 1995a].	3
1.2	Diagram illustrating the bounce motion of a particle moving in a converging magnetic field, where the dashed horizontal line indicates the mirror point of the particle.	5
1.3	A schematic illustrating the drift of a positively and negatively charged particle due to a gradient in the magnetic field strength perpendicular to the magnetic field direction. The opposing drift directions of the ion and electron imply a current, \mathbf{j}	6
1.4	Diagram showing the centrifugal force exerted on a negatively particle moving along a curved field line [Baumjohann and Treumann, 1996]. Curvature drift occurs in the direction out of the page.	7
1.5	Particle drifts in a constant magnetic and constant electric field. The magnetic field is directed out of the plane, and the electric field is directed perpendicular to the magnetic field.	8
1.6	Schematic illustrating the diffusion of magnetic field lines [Baumjohann and Treumann, 1996].	14
1.7	Diagram showing a surface of plasma, S , moving with bulk velocity \mathbf{u} , permeated by a magnetic field, \mathbf{B} , at times t_1 and t_2 . The surface represents a cross-section of a magnetic flux tube. (Figure adapted from Kivelson [1995a])	15
1.8	Density profiles for the ionised (solid) and neutral (dashed) species, indicating the composition in Earth's ionosphere under daytime conditions [Johnson, 1969; Luhmann, 1995].	17

1.9 Schematic showing the relative directions of the magnetic field, \mathbf{B} , velocity, \mathbf{v} , and electric field, \mathbf{E} , for corotational flows of magnetospheric plasma and magnetic flux tubes. The diagram corresponds to the magnetic equatorial plane of the magnetosphere, with the Sun positioned to the left. 18

1.10 Illustration of the open magnetosphere model in the noon-midnight merid-
ian plane (adapted from Hughes [1995]). The bow shock and magnetopause
boundaries are indicated by dashed grey lines, the bulk plasma flow directions
(blue), current flow directions (green), and electric field directions (red) are
also shown. Low latitude reconnection takes place at the sub-solar point of
the magnetopause under a southward directed IMF, \mathbf{B}_{IMF} , and reconnection
also occurs in the tail region. Reconnection sites are represented by purple
stars. 20

1.11 Diagram illustrating the motion of solar wind ions and electrons at the magne-
topause boundary, corresponding to an intersection of the magnetopause nose
in the equatorial plane (adapted from Baumjohann and Treumann [1996]).
Ions and electrons exhibit gyromotion, with gyroradii r_{gi} and r_{ge} , respectively,
as they encounter the geomagnetic field, \mathbf{B} . The resulting direction of the
Chapman-Ferraro current, \mathbf{j} , is indicated. 22

1.12 Reconnection process occurring between anti-parallel magnetic field lines, for
the example of reconnection with southward IMF at the magnetopause, where
each panel corresponds to a time step in the process. The IMF, \mathbf{B}_{IMF} , and
magnetospheric dipole, \mathbf{B} , field lines are shown in the noon-midnight merid-
ian. The solar wind plasma and magnetospheric plasma are separated by
the magnetopause (grey region), where duskward Chapman-Ferraro currents,
 \mathbf{j} , (green vectors) are present. The blue vectors indicate the plasma flow
vectors. Panel (a) illustrates the diffusion of field lines towards the magne-
topause. Panel (b) describes the formation of a reconnection x-line, where a
reconnection region is represented by a purple star. Panel (c) shows plasma
outflow of newly reconnected magnetic field lines. 24

1.13 Schematic showing the relative directions of the magnetic field, \mathbf{B} , veloc-
ity, \mathbf{v} , and electric field, \mathbf{E} , for convectional flows of magnetospheric plasma
and closed magnetic flux tubes. The diagram corresponds to the magnetic
equatorial plane of the magnetosphere, with the Sun positioned to the left. . . 25

1.14	Diagram of the key plasma regions of the Earth’s magnetosphere in the noon-midnight meridian plane (adapted from Wolf [1995]).	26
1.15	Diagram illustrating the combination of corotational flows (Figure 1.9) and convective flows (Figure 1.13) for the magnetic equatorial plane of the Earth’s magnetosphere (adapted from Kavanagh et al. [1968] and Chappell [1972]). The directions of the flow vectors, \mathbf{v} , and magnetic field, \mathbf{B} , are shown. The magnetopause boundary is represented by the dashed black line, and the stagnation flow line, or plasmopause, is represented by the thick dashed grey line. The region within the plasmopause, the plasmasphere, is shaded light grey.	29
1.16	Schematic illustrating the geomagnetic configuration in the noon-midnight meridian plane for the 3 phases of the substorm process: growth phase (upper), expansion phase (middle), and recovery phase (lower) [Baumjohann and Treumann, 1996]. The radial location of the NENL and DNL reconnection x-lines in the magnetotail are indicated.	34
1.17	A SYM-H trace for a typical geomagnetic storm, with the initial phase, main phase, and recovery phase indicated [Hutchinson et al., 2011]. The horizontal dotted line represents the quiet time SYM-H value.	37
1.18	Friedrichs diagrams showing the (a) phase velocity and (b) group velocity for the Alfvén wave mode and the fast wave mode.	39
1.19	Schematics of (a) fundamental ($n = 1$) and (b) second harmonic ($n = 2$) FLR oscillations of a closed dipolar geomagnetic field line [Kivelson, 1995b]. The upper diagrams illustrate the field line displacements, with the dashed magnetic field lines representing displacements from the unperturbed solid magnetic field lines. The lower plots show the variation in the electric field perturbation, E , and magnetic field perturbation, b , along the magnetic field line.	41
2.1	Resonant pulsation period (s) as a function of field line L value, from Samson and Rostoker [1972]. The solid lines show linear fits to data, separated into 1730 - 0730 MLT and 0730 - 1730 MLT sectors, and the dot-dash lines show the 95% confidence intervals. Previous observations of FLR periods are also indicated.	49

LIST OF FIGURES

2.2	Average pulsation period (s) as a function of MLT and UT, observed by the STARE radars. Plot is taken from Poulter et al. [1984].	49
2.3	Contour map showing average frequency values (mHz) in the Earth's magnetic equatorial plane, from Takahashi et al. [2002].	50
2.4	Intensity plot showing the average frequencies (mHz) of toroidal waves, in the Pc4 and Pc5 bands, plotted in the Earth's magnetic equatorial plane. Figure is taken from Liu et al. [2009].	51
2.5	Frequency (mHz) as a function of L values, where each profile corresponds to a different Kp index bin, for data obtained in the 0400 - 0800 MLT sector. Figure is taken from Takahashi et al. [2002].	51
3.1	Cluster trajectory showing the spacecraft configuration for orbit 588 in each of the GSE (Geocentric Solar Ecliptic) coordinate planes. The four spacecraft positions are indicated at 15 minute intervals, where a scaling factor of 100 is used for the spacecraft separations. A key indicating the colour coding for the Cluster spacecraft is included. For reference, the average model position of the magnetopause and bow shock is shown by the blue solid and blue dashed lines, respectively.	53
3.2	Ground magnetometer station locations in AACGM latitude and longitude coordinates, for the IMAGE magnetometer array. Stations are labelled by the station identification codes, and stations that are not utilised in the study have been excluded.	58
4.1	T96 magnetic field line configurations in the X-Z GSM plane, with the dotted line indicating the magnetic dipole axis. The vectors representing the maximum radial distance along the field line (blue line), the field line midpoint (red line), and the minimum in magnetic latitude along the field line (green line) are shown, with the grey shaded region covering $\pm 10^\circ$ magnetic latitude of the field line midpoint.	60

4.2 HIA/CIS ion energy flux data measured by C1 on 5 September 2002 (case study of Clausen et al., 2009). First panel: ion energy flux spectrogram. Second panel: DEF (Differential Energy Flux) profile for 0.7 keV ion energies, with the red line corresponding to field lines close to the magnetopause that have been identified as open. Third and fourth panels: DEF profiles corresponding to ion energies of 0.02 keV and 0.7 keV, respectively, where the red line indicates where the values exceed a threshold (indicated by horizontal dashed lines). Fifth panel: L values of the spacecraft position. 62

4.3 CODIF/CIS ion energy flux data measured by C1 on 4 July 2001. The first, second, and third panels show the energy flux spectrograms for the H^+ , He^+ , and O^+ ion species, respectively. The fourth panel shows the ratio of count rates of each time-energy bin for the O^+ and H^+ ion species (ratio of third and first panels). The fifth panel shows the hourly Dst index (nT) for the time interval, and the sixth panel shows the L values of the spacecraft position. The vertical dashed lines indicate the visually identified upper L values of observed contamination for the inbound and outbound spacecraft passes, where the labels below the panel indicate the corresponding L values. 64

4.4 Histogram showing the percentage of cases where contaminated CODIF measurements, due to energetic radiation belt particles, were observed as a function of L shell. This is based on a representative sample of 38 passes through the radiation belt region. The vertical dashed line at $L = 5.9$ indicates the lower L shell boundary of CODIF data used in this study. 65

4.5 Polar plots showing distributions in L -MLT space, where values are binned for field line L value (using a bin width of 0.5) and MLT (using a bin width of 1 hour). The plots show the average of values within each bin. Panel (a) shows the fraction of the total spacecraft passes where WHISPER data is available. Panel (b) shows the distribution of total electron density, n_e , (cm^{-3}), as measured by WHISPER. 67

4.6 WHISPER (green), PEACE (blue), and EFW (red) observations obtained by C1 during the perigee pass of orbit 745. Panel (a) and panel (b) show electron density, n_e , (cm^{-3}) timeseries for the WHISPER and PEACE instruments, respectively. Panel (c) shows the spacecraft potential, $V_S - V_P$, (V) timeseries. Panel (d) and panel (e) show the spacecraft L value and Dst index (nT) variation, respectively. For the observations of each instrument, the data are binned for L value, using a binsize of 0.2, and averaged (panel (f)). The solid profiles correspond to electron density, and the dotted profile corresponds to spacecraft potential. Electron density measurements for the EFW instrument were inferred from spacecraft potential measurements using relations from Lybekk et al. [2012]. 69

4.7 Plots showing correlations of CODIF measurements in the RPA (corresponding to 0.7 - 25 eV/charge energy range) and MAG (0.025 - 40 keV/charge energy range) modes, and WHISPER total electron density measurements. All data are binned for L value (represented by the colour of the points), with a binsize of 0.1, and the horizontal and vertical bars on each point correspond to the statistical standard error of the data in the L value bin. The dashed lines on each panel indicates $y = x$. Panels (a,b,c): correlation of H^+ , O^+ , and He^+ ion densities, n_{H^+} , n_{O^+} , and n_{He^+} , (cm^{-3}) respectively, measured by CODIF in the RPA and MAG modes. Panel (d): correlation of the total ion density, n_i , (cm^{-3}) measured by CODIF in the RPA and MAG modes. Panel (e): correlation of the total ion density, n_i , (cm^{-3}) measured by the CODIF in the MAG mode with the total electron density, n_e , (cm^{-3}) measured by WHISPER. Panel (f): correlation of average ion mass, m_{av} , (amu) values calculated from CODIF measurements in the RPA and MAG modes. . . 71

4.8	CODIF ion observations during the perigee pass of orbit 356, for C1 (blue) and C4 (red). Panel (a) and panel (b) show the total ion density, n_i , and H^+ energy, E , spectrogram, respectively, observed by C1, where the CODIF instrument was operating in MAG mode. Panel (c) and panel (d) show the ion density and energy spectrogram, respectively, observed by C4, where the CODIF instrument was operating in RPA mode. Panel (e) shows the L values corresponding to the spacecraft positions. Panel (f) shows the ion density variation with L , corresponding to the observations shown in panel (a) and panel (c) binned for L value.	74
4.9	Spatial distribution of (a) average electron density (cm^{-3}) and (b) the number of measurements obtained by WHISPER in the X-Z plane (SM coordinate system).	75
4.10	Spatial distribution of (a) average ion mass (amu) and (b) the number of measurements obtained by CODIF in the X-Z plane (SM coordinate system).	76
5.1	Electron density, n_e , (cm^{-3}) plotted as a function of normalised radius, R_{norm} , for $8.5 \leq L < 9.5$ at 3 hour MLT intervals, where the colour of each point indicates the number of WHISPER measurements, n , averaged in each bin. The upper and lower quartiles of the distribution of points averaged in each bin is shown by the grey line, intersected by a short horizontal line at the median value. The vertical dashed line indicates the boundary between the power law and Gaussian dependences. The blue line represents the best fitting power law dependence, where the dashed blue line is the extrapolated dependence. The green line represents the best fitting Gaussian function.	82

5.2	Spatial distribution in the X-Z SM plane using the field-aligned models for (a,b) electron density and (c) average ion mass, defined by equation 5.2 and equation 5.3, respectively. These models are combined to determine the corresponding distribution for (d,e) the plasma mass density. The distributions using both the extrapolated power law form (upper row) and Gaussian function (lower row) for the low latitude electron density dependence are shown for comparison. Note that the scales have been adjusted relative to the data plots (Figure 4.9 and Figure 4.10) to focus on the most relevant regions. The T96 magnetic field model used in this case corresponds to spring equinox, with a solar wind dynamic pressure of 2nPa.	85
5.3	The spatial distribution of (a,b) electron density, (c) average ion mass and (d,e) mass density in the T96 magnetic equatorial plane, in the same format as Figure 5.2.	86
5.4	Average ion mass, m_{av} , (amu) plotted as a function of normalised radius, R_{norm} , for $6.5 \leq L < 7.5$ at 3 hour MLT intervals, where the colour of each point indicates the number of CODIF measurements, n , averaged in each bin. The upper and lower quartiles of the distribution of points averaged in each bin is shown by the grey line, intersected by a short horizontal line at the median value. The blue line represents the best fitting power law dependence.	88
5.5	Contour plots showing the variation of the electron density and average ion mass model parameters (as defined in equations 5.2 and 5.3, respectively) with L value and MLT.	92

5.6 Data corresponding to $8.5 \leq L < 9.5$ and 06 ± 1.5 MLT. The first and third panels show the averaged WHISPER observations of electron density, n_e , plotted as a function of normalised radius, R_{norm} , using the same format as Figure 5.1. The first panel corresponds to averaged values over the full WHISPER dataset, reproduced for convenience from Figure 5.1. The third panel shows the field-aligned profile for data obtained before October 2004, represented by the plus symbols, and data obtained following October 2004, represented by the cross symbols. The second panel shows the average electron DNF (Differential Number Flux), $\text{cm}^{-2} \text{s}^{-1} \text{ster}^{-1} \text{keV}^{-1}$, observed by the PEACE instrument onboard the C1 spacecraft, in an energy - pitch angle spectrogram. The radial and angular position of a given bin corresponds to the energy and pitch angle, respectively. 95

5.7 Panels showing the mass density, ρ , ($\text{amu} \cdot \text{cm}^{-3}$), electron density, n_e , (cm^{-3}) as defined by equation 5.2, and average ion mass, m_{av} (amu) as defined by equation 5.3, plotted as a function of normalised radius, R_{norm} . The left (right) panels show profiles for $L = 6$ ($L = 9$) and the upper (lower) panels show profiles for 1200 MLT (0000 MLT). The vertical dashed lines on each panel indicates the boundary between the power law and Gaussian dependences, corresponding to the electron density model. 103

6.1 Histograms showing the distribution of the number of data points with Dst index (nT) for (a) electron density data from WHISPER and (b) average ion mass data from CODIF. The differing colours of the bars indicate the division of the datasets into 6 bins for Dst index. 109

6.2 Electron density, n_e , (cm^{-3}) plotted as a function of normalised radius, R_{norm} , for $5.5 \leq L < 6.5$ and 0900 MLT. The panels display data for each Dst index (nT) bin (as defined in Figure 6.1). The vertical dashed line indicates the boundary between the power law and Gaussian dependences, and the overplotted coloured lines represent the best fitting functions to the overall dataset. 111

6.3 Spatial distribution in the X-Z SM plane using the field-aligned models for (a-d) electron density and (e-h) average ion mass, defined by equation 6.1 and equation 6.2, respectively. The models are combined to infer the corresponding total mass density distributions (i-l). Each vertical panel shows the distribution for a different value of the Dst index (nT). The T96 magnetic field model used corresponds to spring equinox, with a solar wind dynamic pressure of 2 nPa. The expected locations of the magnetopause under these conditions are included as the blue solid lines for reference. 113

6.4 Same format as Figure 6.3, for the spatial distribution in the T96 magnetic equatorial plane. 114

6.5 Average ion mass, m_{av} , (amu) plotted as a function of normalised radius, R_{norm} , for $6.5 \leq L < 7.5$ and 0900 MLT. The panels display data for each Dst index (nT) bin (as defined in Figure 6.1). The overplotted coloured lines represent the best fitting functions to the overall dataset. 115

6.6 Each panel shows the spatial distribution of average ion mass (amu) for a different MLT sector using the field-aligned model (equation 6.2) for Dst = 0 nT. The central diagram indicates the MLT sectors of the surrounding panels. The x axes correspond to the radial distance in the magnetic equatorial plane, R (R_E), and the z axes correspond to the Z SM coordinate (R_E). The unfilled quarter circles represent the Earth. 117

6.7 Same format as Figure 6.6, but for Dst = -100 nT 118

6.8 Histograms showing the distribution of the number of data points with Kp index for (a) electron density data from WHISPER and (b) average ion mass data from CODIF. The differing colours of the bars indicate the division of the datasets into 4 bins for Kp index. 120

6.9 Spatial distribution in the X-Z SM plane using the field-aligned models for (a-d) electron density and (e-h) average ion mass, defined by equation 6.3 and equation 6.4, respectively. The models are combined to infer the corresponding total mass density distributions (i-l). Each vertical panel shows the distribution for a different value of the Dst index (nT). The T96 magnetic field model used corresponds to spring equinox, with a solar wind dynamic pressure of 2 nPa. The expected locations of the magnetopause under these conditions are included as the blue solid lines. 121

6.10 Same format as Figure 6.9, for the spatial distribution in the T96 magnetic equatorial plane. 122

6.11 Panels showing the mass density (amu.cm^{-3}) as a function of the normalised radius, R_{norm} . The mass density values are calculated by combining the electron density (equation 6.1) and average ion mass (equation 6.2) field-aligned models using equation 3.1. Each panel shows the field line distribution at a different value of the Dst index (nT), as indicated by the linestyle. The left (right) panels show profiles for $L = 6$ ($L = 9$), and the vertical panels show profiles for multiple MLT values. The vertical dashed lines on each panel indicate the boundary separating the power law and Gaussian form field-aligned dependence for the electron density model. 136

7.1 Field line oscillation frequency calculated using the time-of-flight approximation, where a dipole magnetic field model and a radial power law mass density model were employed. The left panel shows the frequencies mapped to the field lines' position in the magnetic equatorial plane. The right panel shows the frequencies mapped to the AACGM latitude and MLT of the field line footprints in the northern hemisphere. 144

7.2 Same format as Figure 7.1, where the time-of-flight calculated frequencies correspond to the use of the T96 magnetic field model and a radial power law mass density model. 146

7.3 Same format as Figure 7.1, where the time-of-flight calculated frequencies correspond to the use of the T96 magnetic field model and the empirical average mass density model (a combination of the electron density model defined by equation 5.2 and the average ion mass model defined by equation 5.3, as discussed in Chapter 5). The frequencies using both the extrapolated power law form (upper row) and Gaussian function (lower row) for the low latitude electron density dependence are shown for comparison. 148

7.4 Field line oscillation frequency as a function of AACGM latitude, calculated using the time-of-flight approximation with the T96 magnetic field model and various mass density models (as indicated by the profile colours). The grey lines correspond to a radial power law mass density model, and the green and blue lines correspond to the empirical mass density model (a combination of the electron density model defined by equation 5.2 and the average ion mass model defined by equation 5.3, as discussed in Chapter 5). The blue lines show calculated frequencies using the extrapolated power law form for the low latitude electron density dependence, based on hypothetical spacecraft observations of electron density off-equator (solid) and in the equatorial plane (dashed). The green solid lines show calculated frequencies using the Gaussian function for the low latitude electron density dependence. Each panel corresponds to field lines at different MLTs, as indicated. 149

7.5 Field line oscillation frequency as a function of MLT, calculated using the time-of-flight approximation with the T96 magnetic field model and various mass density models (as indicated by the profile colours). The same colour coding is used as in Figure 7.4. Each panel corresponds to field lines at different AACGM latitude, as indicated. 150

7.6 Same format as Figure 7.1, where the time-of-flight calculated frequencies correspond to the use of the T96 magnetic field model and the empirical Dst-dependent mass density model (a combination of the electron density model defined by equation 6.1 and the average ion mass model defined by equation 6.2, as discussed in Chapter 6). Each row corresponds to frequencies calculated for different values of the Dst index. 152

7.7 Same format as Figure 7.4, where frequencies are calculated using the time-of-flight approximation with the T96 magnetic field model and various mass density models (as indicated by the profile colours). The grey profiles correspond to the empirical average mass density model (a combination of the electron density model defined by equation 5.2 and the average ion mass model defined by equation 5.3, as discussed in Chapter 5). The red, green, blue, and purple profiles correspond to the use of various Dst index values with the empirical Dst-dependent mass density model (a combination of the electron density model defined by equation 6.1 and the average ion mass model defined by equation 6.2, as discussed in Chapter 6). The legend above the panels indicates the colour coding of the profiles using the empirical Dst-dependent mass density model. 153

7.8 Same format as Figure 7.5, where frequencies are calculated using the time-of-flight approximation with the T96 magnetic field model and various mass density models (as indicated by the profile colours). The same colour coding is used as in Figure 7.7. 154

7.9 Schematic plots considering a resonant field line oscillation at frequency ω_N and a separate resonant field line oscillation at frequency ω_S [Waters et al., 1991]. The amplitude response (top panel) and crossphase difference (bottom panel) as a function of frequency, ω , are shown. 162

7.10 Magnetic field data for 10 November 2006, illustrating the automated FLR identification method. Panel (a) and panel (b) show B_x data (nT) from Abisko (ABK) and Tromsø (TRO), respectively, bandpass filtered between 100 s to 1000 s. Panel (c) and panel (d) show the power ($\text{nT}^2 \text{ Hz}^{-1}$) spectrum and crossphase (deg) spectrum, computed from the ABK and TRO data. Panel (e) and panel (f) show the corresponding power and crossphase spectra, where hourly averages have been taken for each frequency bin. Frequency bins corresponding to a hourly power value below the hourly median power are plotted as black. Panel (g) shows the t statistic spectrum, defined as the mean crossphase divided by the crossphase standard deviation. Values where $t \leq 1$ are plotted as black. Panel (h) shows frequency (mHz) values corresponding to the peak hourly crossphase, for each hour interval. Frequencies that meet the $t > 1$ criterion are validated and plotted as black, otherwise frequencies are not valid and plotted as grey. The green dashed line shows frequencies calculated under the time-of-flight approximation, assuming the T96 magnetic field model, and the empirical average mass density model presented in Chapter 5. 165

7.11 Panel (a) shows the station AACGM latitudes (degrees) (grey points) and midpoint AACGM latitude (red points) for the station pairs used in the IMAGE data analysis, with station identification codes labelled on the left of the panel. Panel (b) shows time-of-flight calculated frequencies (mHz) employing the empirical average mass density model and the T96 magnetic field model at spring equinox. The average frequency (mHz) and number of detections using the automated FLR identification method are shown in panel (c) and panel (d), respectively, where values have been binned for MLT (hours). Following the same format as panel (a), each row corresponds to a station pairing, where the midpoint AACGM latitude was used for the time-of-flight calculations. 167

7.12 Field line oscillation frequency (mHz) as a function of AACGM latitude (degrees), where each panel corresponds to field lines at different MLT (hours) values, as labelled. Time-of-flight calculated frequencies are shown by the green profiles and the grey profiles. The T96 magnetic field model is used, and the green profile corresponds to use of the empirical mass density model, whereas the grey profile corresponds to use of a simple radial power law mass density model. The average frequencies identified in the ground magnetometer dataset are shown by the purple points, where each point corresponds to a different station pairing, and are plotted at the midpoint latitude between stations. The error bars on the purple points indicate the upper and lower quartile values. 169

7.13 Field line oscillation frequency (mHz) as a function of MLT (hours), where each panel corresponds to a different station pair used in the ground magnetometer data analysis, as labelled. The purple profiles correspond to the average frequency observed for the station pair, with upper and lower quartile values indicated by the error bars. Using the midpoint AACGM latitude of the station pair, frequencies are calculated using the time-of-flight approximation, as shown by the green profiles and the grey profiles, assuming the T96 magnetic field model. The green profiles correspond to the use of the empirical mass density model, and the grey profiles correspond to the use of a simple radial power law mass density model. 170

List of Tables

3.1	Summary of CIS instrument status for all spacecraft (adapted from Dandouras et al. [2014]).	57
-----	---	----

Chapter 1

Introduction

Variations in magnetospheric plasma mass density provide information on the morphology of the magnetosphere and the different dynamical processes occurring. For example, the magnetospheric mass density plays a crucial role in determining the propagation of wave modes implicated in radiation belt energisation and decay [Meredith et al., 2003; O’Brien et al., 2003]. In addition, the magnetospheric mass density is a significant factor in influencing dayside reconnection rates [Borovsky and Denton, 2006], and therefore has implications for the coupling of the solar wind to the magnetosphere. This thesis has determined an empirical model of how the mass density is distributed in the closed magnetosphere, as well as considering variations in the distribution with geomagnetic activity. An important application for models of the magnetospheric mass density is in determining the frequencies of magnetospheric ultra-low frequency (ULF) waves, and hence the response time of the magnetosphere to perturbations. The use of the mass density models to estimate ULF wave frequencies is explored in this thesis. This first chapter presents an overview of the plasma physics theory and the key features of Earth’s magnetosphere. Chapter 2 provides a literature review of previous studies, and Chapter 3 contains details on the relevant instrumentation used in the study. Chapter 4 presents the data reduction and verification techniques applied to the datasets used. Chapter 5 determines an empirical model for the total plasma mass density, and Chapter 6 considers dependences on geomagnetic activity. Chapter 7 illustrates the use of the mass density models to estimate standing Alfvén wave frequencies for closed geomagnetic field lines, and compares the estimations to ground magnetometer data. Finally, the thesis is summarised and future areas of research discussed in

Chapter 8.

The near Earth space plasma environment can be approximated as a collisionless, quasi-neutral, ionised gas, where the motion of the charged particles is dominated by electromagnetic forces. This chapter reviews the motion and characteristics of plasma permeated by electromagnetic fields, and considers the structure and behaviour of plasmas in the context of Earth's magnetosphere. The dynamics and structure of the magnetosphere is discussed, specifically focusing on the substorm, geomagnetic storm, and field line resonance processes.

1.1 Single particle motion

The equation of motion for a particle of charge q , with mass m , in an electromagnetic field is

$$m \frac{d\mathbf{v}}{dt} = q (\mathbf{E} + \mathbf{v} \times \mathbf{B}) \quad (1.1)$$

where $d\mathbf{v}/dt$ is the rate of change of the velocity, \mathbf{v} , of the particle, \mathbf{E} is the electric field, and \mathbf{B} is the magnetic field. Note that other forces, such as the gravitational force, are not included in the equation of motion, as they are insignificantly small in comparison to the electromagnetic forces. From the equation of motion (equation 1.1), charged particles in electric and magnetic fields have 3 specific types of motion: gyromotion, bounce motion, and drift motion. These motions will now be introduced, and for further details and derivations, Kivelson [1995a] and Baumjohann and Treumann [1996] are recommended.

1.1.1 Gyromotion

Initially, an absence of electric fields will be assumed, considering only the effects of magnetic fields on particle motions, until subsection 1.1.5. The magnetic field force on the particle acts in the direction perpendicular to both \mathbf{v} and \mathbf{B} , as shown by equation 1.1. This is a centripetal force, such that the particle moves in circles around a magnetic field line at a speed, v_{\perp} , equal to the component of \mathbf{v} perpendicular to \mathbf{B} . The direction of this force is charge dependent, such that oppositely charged particles rotate in the opposite sense. The component of the particle's velocity parallel to the magnetic field, v_{\parallel} , remains constant under a constant magnetic field, as the magnetic field force only acts perpendicular to \mathbf{v} . Therefore, it can be seen that the overall motion of a particle is to gyrate along magnetic field lines, termed gyromotion, as illustrated in Figure 1.1.

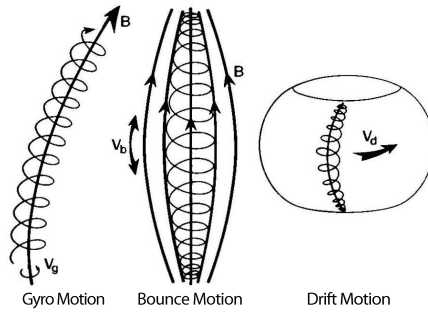


Figure 1.1: Diagram illustrating three important forms of single particle motion in electromagnetic fields: gyromotion, bounce motion, and drift motion [Kivelson, 1995a].

Furthermore, by solving the equation of motion for a particle in a constant magnetic field (equation 1.1 with $\mathbf{E} = 0$), it can be shown that a particle gyrates around a magnetic field line with an angular frequency equal to the gyrofrequency

$$\Omega = \frac{qB}{m} \quad (1.2)$$

Equation 1.2 shows that particles will gyrate at a higher frequency in stronger magnetic fields, and also lighter particles will have a higher gyrofrequency. The radius of the circle the particle follows around the magnetic field line, referred to as the gyroradius, r_g , is determined by the perpendicular velocity component and the gyrofrequency of the motion, and is defined by:

$$r_g = \frac{v_{\perp}}{\Omega} = \frac{mv_{\perp}}{qB} \quad (1.3)$$

It is clearly shown by equation 1.3 that stronger magnetic fields and less massive particles result in smaller gyroradii. For the space plasma environment of Earth, 1 keV electrons typically have a gyrofrequency of the order of 10^4 rad s^{-1} , and a gyroradius of a few km. Correspondingly, 1 keV protons have a gyrofrequency of the order of 10^1 rad s^{-1} , and a gyroradius of the order of 10^1 km.

1.1.2 Bounce motion

As well as gyromotion, particles exhibit further features when introduced to spatially varying magnetic fields, in a region absent of any electric fields. By considering the equation of motion (equation 1.1) in a spatially varying magnetic field, it can be found that the total

velocity of a particle remains constant. This is shown by taking the scalar product of equation 1.1 with the particle velocity, \mathbf{v} :

$$m\mathbf{v} \cdot \frac{d\mathbf{v}}{dt} = q\mathbf{v} \cdot (\mathbf{v} \times \mathbf{B})$$

the right side is equal to zero, as \mathbf{v} is perpendicular to $\mathbf{v} \times \mathbf{B}$

$$m \frac{d}{dt} \left(\frac{1}{2} \mathbf{v} \cdot \mathbf{v} \right) = 0$$

$$\frac{d}{dt} \left(\frac{1}{2} m v^2 \right) = 0 \tag{1.4}$$

Equation 1.4 shows that the kinetic energy, and therefore the total speed of the particle ($v = \sqrt{v_{\perp}^2 + v_{\parallel}^2}$), is constant over the path of the particle. This is because the magnetic field force acts perpendicular to \mathbf{v} , implying that no work is done on the particle.

Bounce motion of a particle occurs in regions where the magnetic field strength varies along the \mathbf{B} direction, resulting in a converging field. This situation is illustrated in Figure 1.1. This process can be understood by considering an electron moving in a flux tube of converging magnetic field, referring to Figure 1.2. The particle will move in a helical motion along the flux tube, due to the particle having perpendicular and parallel components of its speed, v_{\perp} and v_{\parallel} respectively. As indicated by equation 1.1, the magnetic field force acting on the electron is directed in the $\mathbf{v} \times \mathbf{B}$ direction, which is perpendicular to \mathbf{B} . However, unlike the simple case of gyromotion for a uniform magnetic field, Figure 1.2 shows that this magnetic field force has a component acting in the v_{\parallel} direction, away from the direction of increasing magnetic field strength. Therefore, the magnetic field force will act to decrease the parallel velocity of the particle, v_{\parallel} , and the conservation of speed (equation 1.4) implies a corresponding increase in the perpendicular velocity, v_{\perp} . As the electron travels in a converging magnetic field, v_{\parallel} decreases and v_{\perp} increases until the point where $v_{\parallel} = 0$. This is termed the magnetic mirror point, where the particle gyrates around the magnetic field line with no parallel motion. At the magnetic mirror point the magnetic force, which is acting in the direction away from increasing magnetic field strength, causes the particle to move away from the mirror point. The particle moves in the direction of decreasing magnetic field strength, with v_{\parallel} increasing and correspondingly v_{\perp} decreasing. This is the bounce motion of the particle.

The bounce motion can be further understood through the pitch angle of the particle.

The pitch angle, α , is defined as the angle between \mathbf{v} and \mathbf{B} , or equivalently

$$\tan \alpha = \frac{v_{\perp}}{v_{\parallel}} \quad (1.5)$$

As a particle moves in a region of converging magnetic field strength, the perpendicular velocity, and thus the pitch angle, α , increases. Equation 1.5 shows that at the magnetic mirror point, where the parallel velocity is zero, α is equal to 90° .

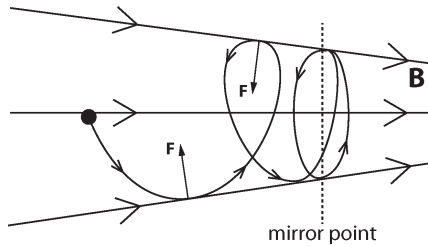


Figure 1.2: Diagram illustrating the bounce motion of a particle moving in a converging magnetic field, where the dashed horizontal line indicates the mirror point of the particle.

As well as the total speed of the particle being conserved (equation 1.4), it can also be shown that the parameter $\sin^2 \alpha/B$, referred to as the first adiabatic invariant, is constant along the path of a given particle. Therefore, if the pitch angle, α , in a region of magnetic field strength, B , is known, then the magnetic field strength at which the particle will mirror at is

$$B_m = \frac{B}{\sin^2 \alpha} \quad (1.6)$$

Therefore, all particles with the same pitch angle at a given magnetic field strength, irrespective of charge or mass, will mirror at the point for a converging magnetic field. It is also noted that equation 1.6 indicates that particles with a smaller pitch angle, α , will mirror in regions of increased magnetic field strength.

1.1.3 Gradient drift

It has been shown that gradients in the magnetic field strength parallel to \mathbf{B} results in the bounce motion of particles (section 1.1.2). Gradients perpendicular to \mathbf{B} will now be presented. Figure 1.3 illustrates the motion of particles moving in a magnetic field, with a gradient in the magnetic field perpendicular to \mathbf{B} . As particles gyrate, they will experience

regions of differing magnetic field strength. In regions of high magnetic field strength the particle gyroradius is decreased, and in regions of low magnetic field strength the particle gyroradius is increased, referring to equation 1.3. As a consequence of the varying gyroradii, the guiding centre is shifted in the direction perpendicular to both \mathbf{B} and $\nabla\mathbf{B}$, corresponding to a drift (illustrated by Figure 1.3). The resulting drifts in the particles motion is referred to as gradient drift, and the velocity of the gradient drift, $\mathbf{v}_{\nabla B}$, is

$$\mathbf{v}_{\nabla B} = \frac{1}{2}mv_{\perp}^2 \frac{\mathbf{B} \times \nabla\mathbf{B}}{qB^3} \quad (1.7)$$

It is shown by equation 1.7 that the gradient drift velocity, $\mathbf{v}_{\nabla B}$, increases with the kinetic energy of the particle, $\frac{1}{2}mv_{\perp}^2$, which is due to the increased particle gyroradius (see equation 1.3). Particles with an increased gyroradius will experience more of the gradient of the field, as they cover a larger region with each gyration, so the drift will be increased. Another key feature of the gradient drift is the charge dependency. Equation 1.7 implies that particles of opposing sign will drift in opposite directions, which is due to the opposite sense of gyration as illustrated in Figure 1.3. Therefore, this drift results in the flow of electric currents.

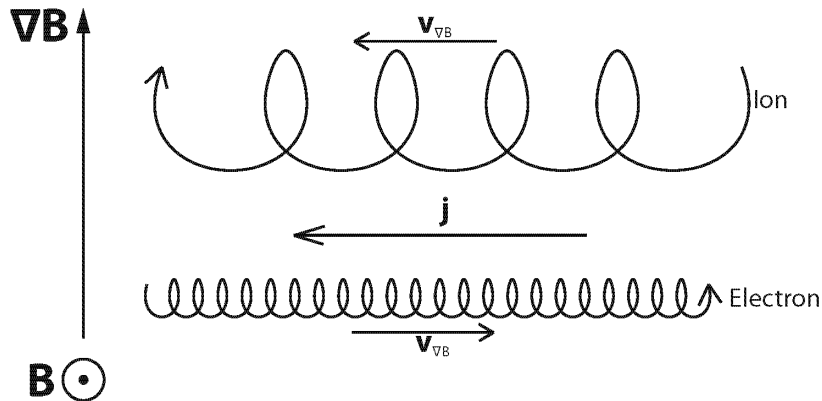


Figure 1.3: A schematic illustrating the drift of a positively and negatively charged particle due to a gradient in the magnetic field strength perpendicular to the magnetic field direction. The opposing drift directions of the ion and electron imply a current, \mathbf{j} .

1.1.4 Curvature drift

Particle drifts are also associated with the curvature of magnetic field lines. Particles with velocity components parallel and perpendicular to the magnetic field direction, v_{\parallel} and v_{\perp} ,

respectively, will gyrate around magnetic field lines while moving along them. If the field lines are curved, the particle will experience a centrifugal force directed away from the centre of the field line curvature, as depicted in Figure 1.4. As with the gradient drift, this force will act to increase the centripetal force, responsible for the gyromotion, on part of the orbit, resulting in an increased gyroradius. On the other part of the orbit, the force acts to decrease the centripetal force, and the gyroradius is decreased. The variation in gyroradii over several orbits causes a drift in the guiding centre of the particles in a direction perpendicular to \mathbf{B} and the field line's local radius of curvature, \mathbf{R}_c . It can be shown that the drift velocity due to field line curvature is

$$\mathbf{v}_c = \frac{mv_{\parallel}^2}{q} \frac{\mathbf{R}_c \times \mathbf{B}}{R_c^2 B^2} \quad (1.8)$$

This drift is also charge-dependent, implying a flow of current in the $\mathbf{R}_c \times \mathbf{B}$ direction.

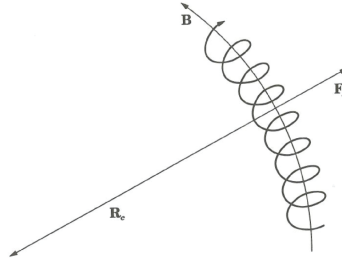


Figure 1.4: Diagram showing the centrifugal force exerted on a negatively particle moving along a curved field line [Baumjohann and Treumann, 1996]. Curvature drift occurs in the direction out of the page.

1.1.5 $\mathbf{E} \times \mathbf{B}$ drift

So far the motion of particles have been constrained to regions with no electric field present. For space plasmas electric fields are an important contribution to the motion of the charged particles, and the effects of an electric field being present, as well as a magnetic field, are now presented.

Considering a charged particle in a constant magnetic field and constant electric field, the equation of motion (equation 1.1) shows that the electric field force acts in the direction of the electric field, \mathbf{E} . Consequently, it can often be assumed for space plasmas, that the component of the electric field parallel to \mathbf{B} vanishes. This is due to the electric field force

acting to produce a charge separation, which acts to cancel out the parallel component of the electric field.

However, the component of the electric field perpendicular to \mathbf{B} plays an important role in determining the path of a charged particle. Figure 1.5 illustrates the motion of both a positively and negatively charged particle in an electromagnetic field. The electric and magnetic fields are assumed to be constant, and the electric field is perpendicular to the magnetic field (as it has been established that any parallel components can be considered to be zero). The magnetic field force causes particles to gyrate, in opposite directions for the positive and negatively charged particles. The inclusion of an electric field results in an additional force acting on the particles. On part of the orbit, the electric field force acts to decrease the magnetic centrifugal force acting on the particle, resulting in an increased gyroradius. On the other part of the orbit, the electric field acts in the opposite direction, increasing the centrifugal force and decreasing the gyroradius of the motion. The varying gyroradii corresponds to a drift in the direction perpendicular to both \mathbf{B} and \mathbf{E} (illustrated by Figure 1.5). This is termed $\mathbf{E} \times \mathbf{B}$ drift, and it can be shown that the particle drift velocity, \mathbf{v}_E , over several particle gyrations is

$$\mathbf{v}_E = \frac{\mathbf{E} \times \mathbf{B}}{B^2} \quad (1.9)$$

Equation 1.9 indicates that the drift velocity is independent of a particle's charge, so ions and electrons in the plasma move in the same direction, and the $\mathbf{E} \times \mathbf{B}$ drift does not introduce any currents.

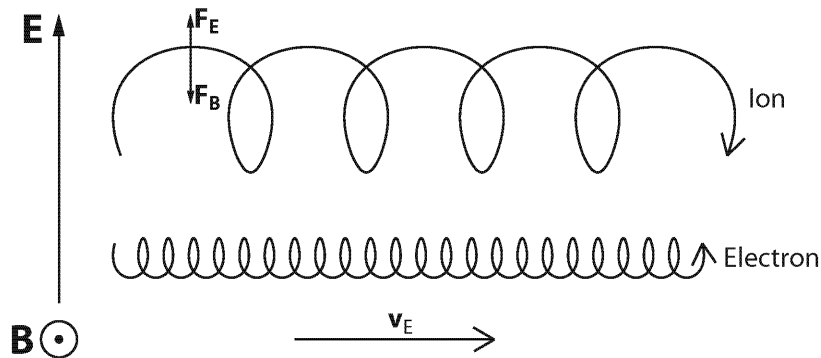


Figure 1.5: Particle drifts in a constant magnetic and constant electric field. The magnetic field is directed out of the plane, and the electric field is directed perpendicular to the magnetic field.

1.2 MHD

The previous section discussed the motions of individual particles. An alternative approach is to consider the bulk motion of the ions and electrons, averaged over the gyromotions, and treat the plasma as a conducting fluid. This approach is referred to as magnetohydrodynamics (MHD), as the forces associated with electromagnetism are included as a contribution to the dynamics of the fluid.

It is assumed that the plasma consists of two species, ions and electrons (the subscripts i and e will be used here to refer to each of these species respectively), and that no sources or losses of the plasma are present. The motion of each species, s , is governed by the fundamental conservation laws. The mass conservation law for species s is

$$\frac{\partial \rho_s}{\partial t} + \nabla \cdot (\rho_s \mathbf{v}_s) = 0 \quad (1.10)$$

where $\rho_s = n_s m_s$ is the mass density (equal to the product of the number density, n_s , and the particle mass, m_s) and \mathbf{v}_s is the bulk flow velocity. The conservation of momentum is defined as

$$\rho_s \frac{d\mathbf{v}_s}{dt} = \rho_s \mathbf{g} - \nabla P_s + n_s q_s \mathbf{E} + n_s q_s \mathbf{v}_s \times \mathbf{B} \quad (1.11)$$

where contributions from gravitational, pressure, and electromagnetic forces are considered. In equation 1.11, \mathbf{g} is the acceleration due to gravity, P is the gas pressure tensor, and q_s is the particle charge. Note that it is assumed here that the ions are protons, such that $q_i = e$.

In a one-fluid MHD approximation, the plasma is considered as a conducting fluid, neglecting the difference between species, with electromagnetic fields and currents embedded in the fluid. Considering a quasi-neutral plasma consisting of both singly-charged ions and electrons, the fluid number density, n , fluid mass, m , and fluid velocity, \mathbf{v} , are

$$n = n_e = n_i \quad (1.12)$$

$$m = m_i + m_e = m_i \quad (1.13)$$

$$\mathbf{v} = \frac{m_i n_i \mathbf{v}_i + m_e n_e \mathbf{v}_e}{m_i n_i + m_e n_e} = \mathbf{v}_i \quad (1.14)$$

where it is reasonably assumed that the electron mass is negligible compared to the ion mass ($m_i \gg m_e$). The expression for the fluid velocity (equation 1.14) indicates that the electron velocity, \mathbf{v}_e , can be discarded for the one-fluid MHD approach. This is because the fluid velocity is defined as the centre of mass velocity, and as the ion mass is considerably larger

than the electron mass, it is the dominant species. By summing the mass conservation laws for the ion and electron species (equation 1.10), the continuity equation for the total plasma is obtained

$$\frac{\partial \rho}{\partial t} + \nabla \cdot \rho \mathbf{v} = 0 \quad \text{Continuity equation} \quad (1.15)$$

where $\rho = nm$ is the fluid mass density.

When considering the momentum conservation of a one-fluid plasma, momentum transfer between species through frictional collisions must be accounted for. Through the inclusion of this additional force in equation 1.11, the momentum conservation laws for the ions and electrons become

$$\rho_i \frac{d\mathbf{v}_i}{dt} = \rho_i \mathbf{g} - \nabla P_i + n_i e \mathbf{E} + n_i e \mathbf{v}_i \times \mathbf{B} - \mathbf{F}_{ei} \quad (1.16)$$

$$\rho_e \frac{d\mathbf{v}_e}{dt} = \rho_e \mathbf{g} - \nabla P_e - n_e e \mathbf{E} - n_e e \mathbf{v}_e \times \mathbf{B} + \mathbf{F}_{ei} \quad (1.17)$$

where \mathbf{F}_{ei} , representing the frictional coupling force on electrons is

$$\mathbf{F}_{ei} = n\nu_{ei}m_e(\mathbf{v}_i - \mathbf{v}_e) \quad (1.18)$$

This frictional force acts in the equal and opposite direction for ions, and ν_{ei} is the collision frequency. The momentum conservation equations for the ion and electron species (equation 1.16 and equation 1.17) are summed to give

$$\rho \frac{d\mathbf{v}}{dt} = -\nabla P + \mathbf{j} \times \mathbf{B} \quad \text{Equation of motion} \quad (1.19)$$

providing the equation of motion for the total plasma. In equation 1.19, P is the total pressure tensor, and the current density in the plasma is defined as

$$\mathbf{j} = ne(\mathbf{v}_i - \mathbf{v}_e) \quad (1.20)$$

Note that the gravitational contribution has been discarded in the momentum conservation equation, as gravitational effects can usually be considered negligible compared to electromagnetic effects for space plasmas. Equation 1.15 and equation 1.19 determine the key properties of the total plasma in the one-fluid approximation.

1.2.1 Maxwell's equations

The plasma is permeated by electromagnetic fields which play an important role in the properties of the plasma. These electric and magnetic fields, \mathbf{E} and \mathbf{B} respectively, are defined by a set of equations called Maxwell's equations, and are presented below in equation 1.21. These equations describe the relation between electromagnetic fields and the particles in a plasma.

$$\nabla \cdot \mathbf{E} = \frac{\rho_q}{\varepsilon_0} \qquad \text{Gauss' law for electricity} \qquad (1.21a)$$

$$\nabla \cdot \mathbf{B} = 0 \qquad \text{Gauss' law for magnetism} \qquad (1.21b)$$

$$\nabla \times \mathbf{E} = -\frac{\partial \mathbf{B}}{\partial t} \qquad \text{Faraday's law} \qquad (1.21c)$$

$$\nabla \times \mathbf{B} = \mu_0 \mathbf{j} + \varepsilon_0 \mu_0 \frac{\partial \mathbf{E}}{\partial t} \qquad \text{Ampère-Maxwell law} \qquad (1.21d)$$

The first two of Maxwell's equations (equation 1.21a and equation 1.21b) define the sources of the electromagnetic fields. Equation 1.21a shows that the source of the electric field is the total charge density, ρ_q . For the magnetic field, equation 1.21b demonstrates there are no sources of the magnetic field, implying that all magnetic field lines must be closed. Therefore, for an integral over a closed surface, there is no net flux crossing the surface.

The remaining Maxwell's equations (equation 1.21c and equation 1.21d) describe the coupling of the electric and magnetic fields due to the electromagnetic fields varying in time and space. Equation 1.21c defines the spatial variations of the electric field as a consequence of temporal variations in the magnetic field. Equation 1.21d refers to the spatial variations in the magnetic field, and consists of two terms representing currents in the plasma. The first term, $\mu_0 \mathbf{j}$, where \mathbf{j} is the conduction current, describes a magnetic field circling the current flow. The second term represents the displacement current, $\mu_0 \partial \mathbf{E} / \partial t$, where a temporally varying electric field results in the presence of a magnetic field circling the electric field. It can be shown that for low frequency phenomena (slow variations and large spatial scales

compared to the natural frequencies of the plasma and the Debye length), the displacement current term in equation 1.21d can be neglected to give $\nabla \times \mathbf{B} = \mu_0 \mathbf{j}$. This is referred to as Ampère's law.

1.2.2 Ohm's law

Key features of the plasma can be described by Ohm's law, which arises through manipulation of the continuity equation (equation 1.15) and the equation of motion (equation 1.19) in the MHD framework, assuming the plasma consists of ion and electron populations. Generalised Ohm's law, for a one-fluid MHD approximation, is given by

$$\mathbf{E} = -\mathbf{v} \times \mathbf{B} + \frac{\mathbf{j}}{\sigma} + \frac{1}{ne} \mathbf{j} \times \mathbf{B} - \frac{1}{ne} \nabla P_e - \frac{me}{ne^2} \frac{d\mathbf{j}}{dt} \quad \text{Generalised Ohm's law} \quad (1.22)$$

and describes variations in the current density with the electromagnetic fields. In equation 1.22, σ is the electrical conductivity.

For space plasmas, some of the terms in the generalised Ohm's law (equation 1.22) can be neglected, as their contributions are negligible. The last three terms on the right hand side of the generalised Ohm's law can often be neglected, reducing equation 1.22 to

$$\frac{\mathbf{j}}{\sigma} = \mathbf{E} + \mathbf{v} \times \mathbf{B} \quad \text{Ohm's law} \quad (1.23)$$

describing the current flowing through a plasma in terms of the electromagnetic fields.

1.2.3 Magnetic pressure and tension

The generalised Ohm's law (equation 1.22) includes the Hall term ($\mathbf{j} \times \mathbf{B}$), which was stated to be negligible. By taking the curl of Ampère's law (equation 1.21d), neglecting displacement currents, the Hall term can be expressed as

$$\mathbf{j} \times \mathbf{B} = \frac{1}{\mu_0} (\mathbf{B} \cdot \nabla) \mathbf{B} - \nabla \left(\frac{B^2}{2\mu_0} \right) \quad (1.24)$$

$$= \frac{1}{\mu_0} (\mathbf{B} \cdot \nabla) \mathbf{B} - \nabla P_{\text{mag}} \quad (1.25)$$

where the magnetic pressure, P_{mag} , is defined as $P_{\text{mag}} = B^2/2\mu_0$. The two terms on the right hand side represent two different forces. The first term corresponds to forces due to the curvature of the magnetic field, and is referred to as the magnetic tension force. The force is directed antiparallel to the field line radius of curvature, consequently acting to

reduce field line curvature and straighten magnetic field lines. The second term on the right hand side describes the contribution of the magnetic pressure, P_{mag} , which acts in the negative perpendicular direction of the magnetic pressure gradient. However, for most space plasma conditions, with some exceptions which will be discussed in the following section, the gradients in the magnetic pressure and curvature of field lines are negligibly small compared to the spatial scales considered. This allows the Hall term to be neglected in the generalised Ohm's law (equation 1.22).

1.2.4 Diffusion and the frozen-in-flux theorem

An important consequence arising from Ohm's law (equation 1.23) is the induction equation, describing the changes in the magnetic field, which will now be presented. By substituting for \mathbf{j} using Ampère's law (equation 1.21d), where displacement currents are neglected, and rearranging, Ohm's law becomes

$$\mathbf{E} = -\mathbf{v} \times \mathbf{B} + \frac{1}{\mu_0 \sigma} \nabla \times \mathbf{B} \quad (1.26)$$

Taking the curl of each side, and substituting for $\nabla \times \mathbf{E}$ using Faraday's law (equation 1.21c) gives

$$\frac{\partial \mathbf{B}}{\partial t} = \nabla \times (\mathbf{v} \times \mathbf{B}) + \frac{1}{\mu_0 \sigma} \nabla^2 \mathbf{B} \quad \text{Induction equation} \quad (1.27)$$

This is termed the induction equation, where the terms on the right hand side represent convection and diffusion of magnetic fields, respectively.

The second term of the induction equation (equation 1.27) corresponds to the diffusion of the magnetic field in a plasma. This describes the diffusive motion of the magnetic field, which acts to smooth out any local irregularities, as illustrated by Figure 1.6. The timescale over which magnetic diffusion occurs in a given plasma, τ_d , is

$$\tau_d = \mu_0 \sigma L^2 \quad (1.28)$$

where L is the characteristic length of the plasma.

For typical space plasmas, a collisionless medium can be assumed. For this case, the resistance acting on charge carriers is zero, and the electrical conductivity, σ tends to an infinite value ($\sigma \rightarrow \infty$). Therefore, the timescale of magnetic diffusion, τ_d , becomes infinitely long, as indicated by equation 1.28, and diffusion is a negligible process. For this

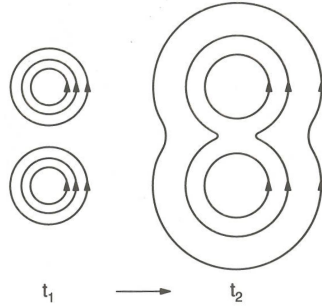


Figure 1.6: Schematic illustrating the diffusion of magnetic field lines [Baumjohann and Treumann, 1996].

approximation, the diffusion term in the induction equation (equation 1.27) becomes zero, leaving only the convection term:

$$\frac{\partial \mathbf{B}}{\partial t} = \nabla \times (\mathbf{v} \times \mathbf{B}) \quad \text{Frozen-in-flux condition} \quad (1.29)$$

This is the condition for frozen-in-flux [Alfvén, 1943]. Equation 1.29 implies that the magnetic field lines and plasma are constrained to move with each other, and forms the basis of the frozen-in-flux theorem. Figure 1.7 depicts a surface of plasma, embedded with a magnetic field. As the plasma moves, with a bulk velocity \mathbf{v} , and deforms in shape, due to the individual particle motions, the field lines also move in the same way. Alternatively, if the magnetic field energy dominates over the plasma particle energy, then the motion of magnetic field lines result in the corresponding distortions of the plasma surface. The result of the frozen-in-flux motion of plasma and magnetic field lines is that the magnetic flux through the surface remains constant. If this surface is considered as a cross-section of a flux tube, then it is inferred that the plasma and flux tube are constrained to move with each other.

If the frozen-in-flux theorem is considered in terms of particle motion, the individual particles move within the same flux tube, with gyromotions and bounce motions. However, a key assumption of MHD theory, from which the frozen-in-flux condition (equation 1.29) is derived, is that the motion of the individual particles is averaged over the gyromotions. Therefore, spatial and temporal variations in the electromagnetic field that are large compared to the gyroradii and period of gyromotions of the particles are assumed. Gradients in the magnetic field strength parallel to magnetic field lines and curvature of magnetic field

lines on scales comparable to particle gyroradii correspond to gradient and curvature drift, as discussed previously. These conditions represent a breakdown in the frozen-in-flux condition, and the plasma and magnetic field lines are no longer constrained to move together. The plasma particles are able to drift perpendicular to the magnetic field lines, and across magnetic flux tubes.

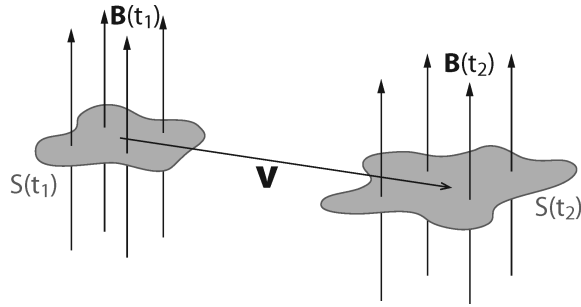


Figure 1.7: Diagram showing a surface of plasma, S , moving with bulk velocity \mathbf{u} , permeated by a magnetic field, \mathbf{B} , at times t_1 and t_2 . The surface represents a cross-section of a magnetic flux tube. (Figure adapted from Kivelson [1995a])

The frozen-in-flux condition (equation 1.29) arises from the assumption that a plasma is collisionless, such that the electrical conductivity is infinite ($\sigma \rightarrow \infty$). Using this approximation with Ohm's law (equation 1.23) gives

$$\mathbf{E} = -\mathbf{v} \times \mathbf{B} \quad (1.30)$$

which is an equivalent form of the frozen-in-flux condition. Equation 1.30 demonstrates the frame-dependency of electric fields, such that there are no electric fields present in a reference frame moving with the plasma ($\mathbf{v} = 0$). Furthermore, electric fields are directed purely perpendicular to \mathbf{v} and \mathbf{B} , with no component of \mathbf{E} parallel to the magnetic field existing for frozen-in-flux conditions.

The induction equation (equation 1.27) indicates that the diffusive motion and the convective motion (referring to motion with frozen-in-flow condition) both contribute to the plasma behaviour, for a non-infinitely conducting plasma. To assess the relative contributions of these terms, the magnetic Reynolds number, R_M , is used. From a consideration of the ratio of the convective term magnitude to the diffusion term magnitude, the magnetic Reynolds number can be expressed as

$$R_M = \mu_0 \sigma L v \quad (1.31)$$

where L is the characteristic length scale of variations in the plasma. For conditions where $R_M \gg 1$, the convective term dominates and the frozen-in-flow theorem is applicable. For the case of $R_M \sim 1$, the diffusion term cannot be neglected, and frozen-in-flow conditions are not present. Due to the large scale lengths, L , associated with magnetospheric plasmas and the solar wind, the magnetic Reynolds number is typically much greater than 1. Therefore, it can usually be assumed that the diffusion term is negligible and convective flows dominate.

1.3 Earth's magnetosphere

The properties of plasma in the context of a planetary magnetosphere will now be reviewed. The plasma environment of Earth, permeated by the approximately dipolar geomagnetic field, exhibits important structure and dynamic interactions with the solar wind.

At low altitudes (below ~ 60 km), the atmosphere of Earth is largely neutral. Incoming solar photons and energetic particle precipitation can ionise the atmospheric particles, which rapidly recombine, due to high densities corresponding to small mean free paths of the particles. For the Earth's atmosphere, solar EUV and UV photons are the primary source of ionisation, occurring on the dayside. At increased altitudes, the atmospheric neutral density reduces, and incoming solar radiation increases. The increasing ionising photon and particle precipitation and decreasing probability of recombination competes with the decreasing density of neutrals to be ionised with increasing altitude. Therefore, the density of ionised particles initially increases with increasing altitude, reaches a peak density, then decreases, as described by Chapman theory. This is illustrated in Figure 1.8 for electrons and a range of ion species, as well as the neutral atmospheric components for comparison. Note that the densities shown in Figure 1.8 correspond to daytime conditions, and are significantly reduced at nighttime, due to a decrease in the ionisation source. The transition region from the neutral atmosphere to a region dominated by ions and electrons is termed the ionosphere, and extends from approximately 60 - 600 km [Rishbeth, 1988].

The ionosphere can be considered as the base of the magnetosphere. The magnetosphere is the region above the ionosphere, where the atmosphere is ionised and, due to the decreased densities, approximately collisionless. This implies that the frozen-in-flux condition is satisfied, and the magnetic field lines and cold plasma are constrained to move together. The footprints of the quasi-dipolar geomagnetic field lines are embedded within the ionosphere,

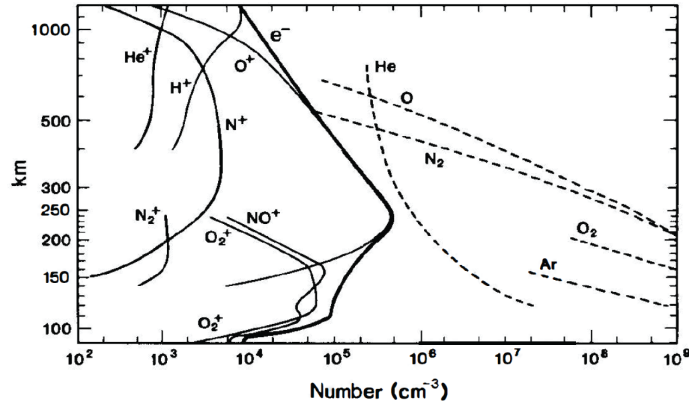


Figure 1.8: Density profiles for the ionised (solid) and neutral (dashed) species, indicating the composition in Earth's ionosphere under daytime conditions [Johnson, 1969; Luhmann, 1995].

and plasma generated by in the ionosphere fills the flux tubes, populating the magnetosphere. These magnetic field lines and plasma corotate with the Earth, in accordance with the frozen-in-flux theorem. The density of plasma in the magnetosphere ranges from the order $1 - 10^2 \text{ cm}^{-3}$, generally decreasing with altitude. The composition of this plasma is determined by the ions outflowing from the ionosphere. As lighter ions require less energy to overcome the gravitational binding, the magnetospheric plasma is composed predominantly of H^+ , with heavier ions such as He^+ and O^+ existing as secondary components. As stated, the magnetic field of Earth can be approximated as a dipole, such that the magnetic field strength at a given position is

$$|\mathbf{B}| = B_{\text{eq}} (1 + 3 \sin^2 \lambda)^{\frac{1}{2}} \frac{1}{R^3} \quad (1.32)$$

where λ is magnetic latitude, R is the radial distance in Earth radii (R_E), and B_{eq} is the equatorial magnetic field strength at the surface (approximately $31 \times 10^3 \text{ nT}$). Therefore, it is clear from equation 1.32, that the magnetic field strength in the magnetosphere decreases with radial distance, by a factor of $1/R^3$, and the magnetic field strength is greater at the magnetic poles in comparison to the equatorial plane.

1.3.1 Corotational flows

Considering a rotating atmosphere, the high frequency of collisions between ions and neutrals implies the rotation of the ionospheric plasma with the Earth. This transfers angular

momentum to the magnetic field lines, causing the flux tubes to corotate as well. At higher altitudes, the magnetic field energy dominates over the plasma energy, and the frozen-in-flux theorem indicates that the magnetospheric plasma must move with the field lines. The result is the corotation of the flux tubes and magnetospheric plasma with the Earth. As the magnetic field strength of the geomagnetic field is strong, the flows do not distort the field configuration, and interchange motion occurs. The magnetic field lines interchange positions as the field corotates, and the magnetic field remains constant at any given point, described by

$$\frac{\partial \mathbf{B}}{\partial t} = 0 \tag{1.33}$$

This is the interchange motion condition. The general corotational motion is illustrated in Figure 1.9, for the magnetic equatorial plane. The magnetic field, \mathbf{B} , is directed out of the plane, and the plasma is corotationally flowing around the Earth with a bulk velocity \mathbf{v} . The frozen-in-flux theorem implies the presence of an electric field, $\mathbf{E} = -\mathbf{v} \times \mathbf{B}$ (equation 1.30) directed radially inwards.

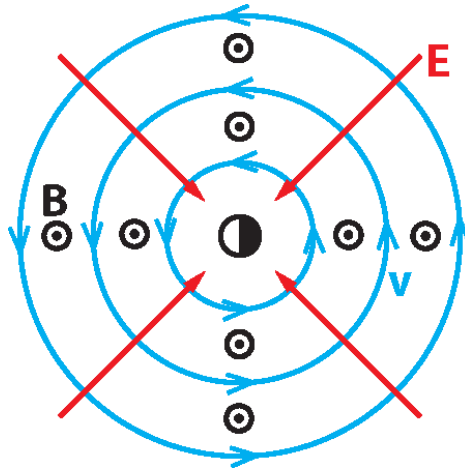


Figure 1.9: Schematic showing the relative directions of the magnetic field, \mathbf{B} , velocity, \mathbf{v} , and electric field, \mathbf{E} , for corotational flows of magnetospheric plasma and magnetic flux tubes. The diagram corresponds to the magnetic equatorial plane of the magnetosphere, with the Sun positioned to the left.

1.3.2 Solar wind-magnetosphere coupling

The magnetosphere is not an isolated system, and interacts with the solar wind. The solar wind is plasma streaming radially outwards from the surface of the Sun, due to the plasma pressure dominating over gravitational forces in the solar corona [Parker, 1958]. The Sun's magnetic field, in the absence of an outflowing solar wind, can be considered dipolar. In accordance with the frozen-in-flux theorem, and the magnetic field energy being relatively low in comparison to the plasma particle energy, the outflowing solar wind stretches the magnetic field lines radially outwards. As the solar wind streams away from the surface, carrying the magnetic field, and the footprints of the magnetic field lines corotate with the Sun, the magnetic field forms a spiral configuration. This is known as the Parker spiral [Parker, 1958], and further details can be found at Baumjohann and Treumann [1996] and Hundhausen [1995]. At a distance of 1 AU from the Sun, the solar wind flows at an average speed of approximately 450 km s^{-1} , with typical plasma densities of 5 cm^{-3} and IMF values of 5 nT [Baumjohann and Treumann, 1996]. The composition of the solar wind is mainly H^+ and He^{++} , and the solar wind flow is supersonic and super-Alfvénic. The solar wind and IMF are highly variable, exhibiting features associated with the level of solar activity at the time of upflow from the solar corona.

As the solar wind streams outwards, filling the solar system, it encounters the Earth's magnetosphere. Due to the frozen-in-flux conditions, the Earth's magnetospheric plasma and geomagnetic field are “frozen” together, and the solar wind and IMF are also “frozen” together. Therefore, the plasma must remain on their original magnetic flux tubes, and the solar wind and magnetospheric plasma cannot mix. The magnetosphere forms a cavity in the solar wind, as illustrated in Figure 1.10, where the boundary between the magnetospheric plasma and the solar wind flowing around the magnetosphere is called the magnetopause. Through a consideration of pressure balance at the boundary, it can be shown that the magnetopause nose is located at a sub-solar radial distance of approximately $10 R_E$ during typical conditions. A reduction in solar wind dynamic pressure away from the nose results in the flared shape of the magnetopause flanks. The shape of the magnetopause is extended in the anti-sunwards direction, forming the magnetotail. As the solar wind flow is supersonic, a shock wave is formed upstream of the magnetopause, which is known as the bow shock. The region between the bow shock and the magnetopause is the magnetosheath, consisting of the shocked, hot, and turbulent solar wind plasma.

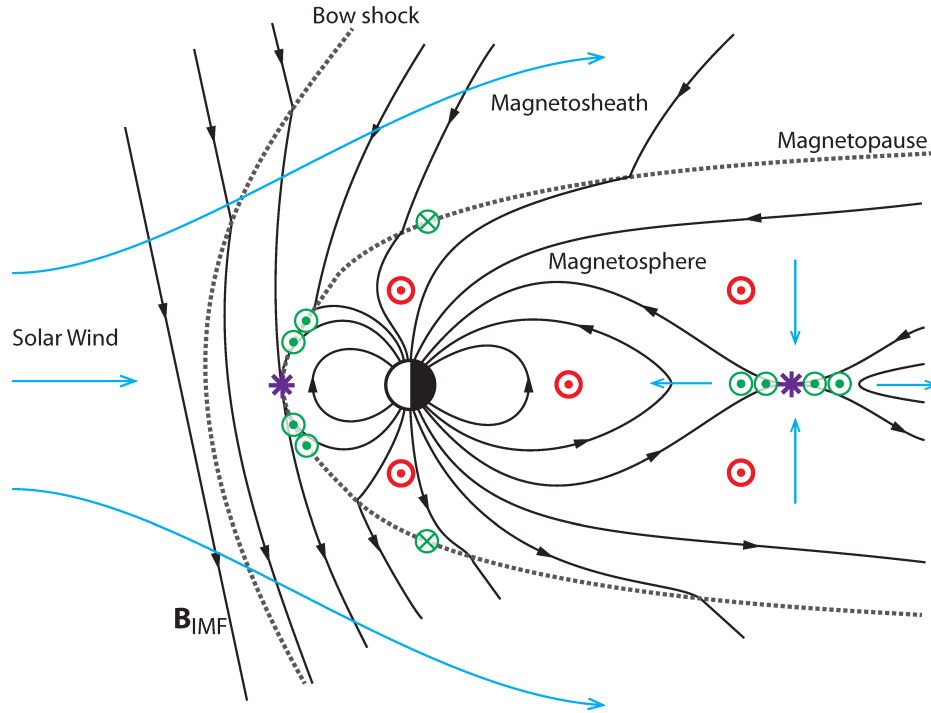


Figure 1.10: Illustration of the open magnetosphere model in the noon-midnight meridian plane (adapted from Hughes [1995]). The bow shock and magnetopause boundaries are indicated by dashed grey lines, the bulk plasma flow directions (blue), current flow directions (green), and electric field directions (red) are also shown. Low latitude reconnection takes place at the sub-solar point of the magnetopause under a southward directed IMF, \mathbf{B}_{IMF} , and reconnection also occurs in the tail region. Reconnection sites are represented by purple stars.

1.3.2.1 Chapman-Ferraro currents

At the magnetopause boundary, separating the IMF and the dipolar geomagnetic field, a gradient in the magnetic field is present. Therefore, due to Ampère's law (equation 1.21d), a current sheet must be formed at the boundary. The IMF is weak compared to the magnetospheric field, so the gradient in the magnetic field, \mathbf{B} , is directed Earthwards across the subsolar region of the magnetopause. Ampère's law indicates the current, \mathbf{j} , is parallel to $\nabla \times \mathbf{B}$, so the current across the magnetopause nose is directed duskwards. At higher latitudes, at the flanks of the magnetopause, the geomagnetic field points southwards, reversing the direction of the gradient. In these regions the current flows downwards. The direction of the magnetopause currents, known as the Chapman-Ferraro currents [Chapman,

1918; Chapman and Ferraro, 1930, 1931], are illustrated by the green vectors in Figure 1.10. These currents flow across the whole surface of the magnetopause, closing on themselves.

The effect of the Chapman-Ferraro currents flowing across the magnetopause boundary, is to generate a corresponding magnetic field. At the magnetopause nose, the magnetic field associated with the current is directed northwards, in the same direction as the magnetospheric dipolar magnetic field. Therefore, the contribution of the Chapman-Ferraro current is to compress the geomagnetic field, and increase the dipolar magnetic field strength. The compression is such that the magnetic field at the magnetopause is approximately twice the magnetic field strength of the undisturbed dipolar magnetic field.

The Chapman-Ferraro currents can be further understood by considering the particle motion at the magnetopause boundary. Figure 1.11 illustrates the motion of the solar wind particles, assumed to consist of protons and electrons, as they approach the magnetopause boundary, flowing with the solar wind. Note that in Figure 1.11, the magnetic field strength of the IMF has not been considered, as it is negligibly small in comparison to the geomagnetic field, and the particle gyroradii are relatively large. As solar wind particles encounter the geomagnetic field, the decrease in gyroradii of the ions and electron result in specular reflection at the magnetopause boundary. As apparent from Figure 1.11, a particle undergoes a half-gyration in the geomagnetic field, \mathbf{B} , being reflected from the magnetopause and travelling upstream in the solar wind. Note here that, for simplicity, it is being approximated that all solar wind particles travel at the same speed. As previously discussed, the sense of gyration is opposite for ions and electrons, due to the magnetic field force direction (equation 1.1). Therefore, a differential motion of the ions and electrons, as they encounter the magnetic field, corresponds to a flow of current, \mathbf{j} , directed duskwards. As the gyroradius is dependent on the particle mass (referring to equation 1.3), the ion gyroradius, r_{gi} , is larger than the electron gyroradius, r_{ge} , the ions penetrate further into the boundary. In addition, Figure 1.11 illustrates the finite width of the magnetopause, of the order of the ion gyroradius.

1.3.2.2 Dungey cycle and convective flows

The formation of the magnetopause arises as a consequence of the frozen-in-flux theorem implying that the solar wind plasma and magnetospheric plasma cannot mix. However, the frozen-in-flux condition requires variations in magnetic fields to be large in comparison with

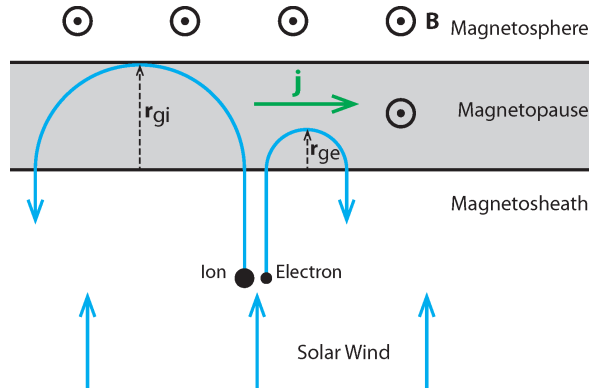


Figure 1.11: Diagram illustrating the motion of solar wind ions and electrons at the magnetopause boundary, corresponding to an intersection of the magnetopause nose in the equatorial plane (adapted from Baumjohann and Treumann [1996]). Ions and electrons exhibit gyromotion, with gyroradii r_{gi} and r_{ge} , respectively, as they encounter the geomagnetic field, \mathbf{B} . The resulting direction of the Chapman-Ferraro current, \mathbf{j} , is indicated.

the particle gyroradii. As discussed previously, magnetic field gradients at the magnetopause occur on length scales comparable to the particle gyroradii, indicated by the presence of the Chapman-Ferraro currents. Therefore, the frozen-in-flux condition breaks down, introducing an important concept known as magnetic reconnection. Figure 1.12 describes the reconnection process, occurring between anti-parallel magnetic field lines. Initially, consider the IMF and the magnetospheric magnetic field lines separated by the magnetopause boundary, where Chapman-Ferraro currents flow duskwards. In the magnetopause region, the spatial scale of magnetic field variations are small, and the decreased magnetic Reynolds number (equation 1.31) indicates that magnetic diffusion is not negligible and frozen-in-flux conditions are not satisfied. Magnetic diffusion acts to smooth out the gradients in the magnetic field, although the process is maintained in a steady state by the flow of magnetic flux towards the boundary, indicated by the flow vectors in Figure 1.12a, at the same rate of diffusion. As the anti-parallel field lines are compressed, a build-up of plasma would occur in the region, however, magnetic reconnection reconfigures the field line topology. Figure 1.12b indicates the presence of a reconnection point (purple star), where the superposition of the anti-parallel magnetic field lines results in a point of zero magnetic field strength. This is termed a magnetic neutral point. Figure 1.12 represents a plane intersecting the magnetopause, so the magnetic reconnection points lie along the surface of the magnetopause, forming a

line of reconnection referred to as a reconnection x-line. It is along the reconnection x-line that the reconnection processes occurs. Figure 1.12c illustrates the newly reconnected field line topology, where the IMF field lines are connected to the magnetospheric field lines, on either side of the reconnection point. Magnetic tension forces on the highly curved field lines act to accelerate the plasma away from the reconnection point, and the plasma outflow prevents a build up of plasma in the region. As the field lines contract and plasma outflow from the reconnection region occurs, the plasma inflow towards the region, and resulting magnetic reconnection, continues. A key consequence of the magnetic reconnection process is the mixing of plasma. According to the frozen-in-flux theorem, the solar wind plasma and magnetospheric plasma are confined to their corresponding magnetic field lines, and cannot mix. However, the newly reconnected field lines contains plasma originating from both the solar wind and magnetosphere. As the field lines leave the reconnection region, and the frozen-in-flux conditions are satisfied again, the solar wind plasma and magnetospheric plasma remain in the same magnetic flux tube, mixing through the parallel velocity motions. In addition, as the magnetic field lines contract, magnetic energy is converted into particle energy, accelerating and heating the plasma.

The magnetic reconnection process contribution to the large scale magnetospheric dynamics will now be introduced, referring to the magnetospheric configuration illustrated in Figure 1.10, corresponding to the case of southward IMF. Consider a geomagnetic field line at the dayside magnetopause. Initially, the field line has both ends connected to the magnetospheric field, and is referred to as a closed field line. However, at the dayside magnetopause boundary, magnetic reconnection occurs at the reconnection x-line (purple star), as previously discussed. The reconnection results in the reconfiguration of the magnetic field line, such that it has one end towards the geomagnetic field, and one end connected to the IMF. This field line is open. The newly reconnected field line at the magnetopause contracts, due to magnetic tension forces, and plasma flows away from the reconnection x-line. Note that frozen-in-flux conditions are satisfied everywhere in the magnetosphere, except for the reconnection sites. As one end of the field line is connected to the anti-sunward flowing IMF, the plasma flow causes the open field line to move anti-sunward, towards the nightside magnetosphere. This is illustrated by the flow of open field lines across the northern and southern hemispheres in Figure 1.10. These field lines become stretched, where kinetic energy associated with the solar wind flow is converted to magnetic energy, forming the elongated magnetotail. Magnetic field pressure forces in the tail pushes the field lines

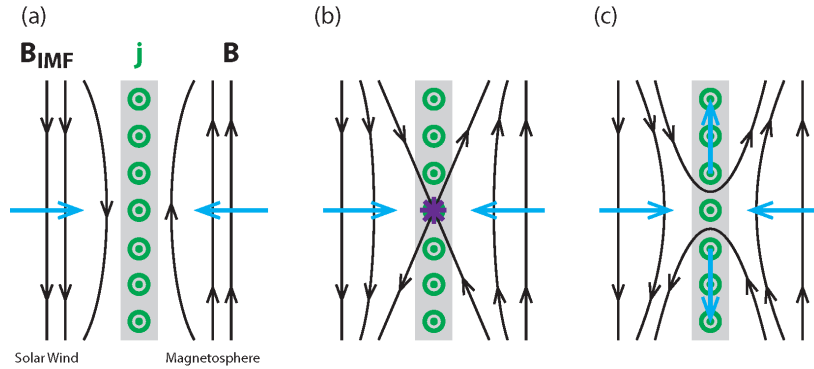


Figure 1.12: Reconnection process occurring between anti-parallel magnetic field lines, for the example of reconnection with southward IMF at the magnetopause, where each panel corresponds to a time step in the process. The IMF, \mathbf{B}_{IMF} , and magnetospheric dipole, \mathbf{B} , field lines are shown in the noon-midnight meridian. The solar wind plasma and magnetospheric plasma are separated by the magnetopause (grey region), where duskward Chapman-Ferraro currents, \mathbf{j} , (green vectors) are present. The blue vectors indicate the plasma flow vectors. Panel (a) illustrates the diffusion of field lines towards the magnetopause. Panel (b) describes the formation of a reconnection x-line, where a reconnection region is represented by a purple star. Panel (c) shows plasma outflow of newly reconnected magnetic field lines.

and plasma inwards to lower latitudes. In the central tail, the presence of anti-parallel field lines results in the formation of a tail current sheet and reconnection x-line (situated approximately 100 - 200 R_E downtail [Baumjohann and Treumann, 1996]), as indicated by Figure 1.10. Field lines reconnect in the tail region, and the plasma outflow from the reconnection region occurs. Earthwards of the tail reconnection x-line, field lines return to a closed configuration. Magnetic tension forces accelerates plasma Earthwards, such that the plasma and magnetic field lines move sunwards towards the dayside magnetopause. Assuming the solar wind conditions remain constant, the field line reconnects again at the dayside magnetopause, forming a cyclical motion of the field lines known as the Dungey cycle [Dungey, 1961]. Note that the flow of plasma within a magnetic field implies the presence of an electric field (equation 1.30), which is directed duskwards throughout the magnetosphere (red vectors in Figure 1.10). Mapping the motion of the field lines to the ionospheric footprints forms a dual-lobe convection cell, where open field lines flow anti-sunward across the polar cap, and return flow to the dayside occurs on closed field lines at lower latitudes. The boundary between the open and closed field lines is called the OCB

(Open Closed Boundary).

The rate of reconnection is highly dependent on the solar wind and IMF conditions, and the rate of reconnection at the magnetopause and at the magnetotail can vary independently. Therefore, the amount of open flux will increase when the dayside reconnection rate dominates, and decrease when nightside reconnection dominates [Cowley and Lockwood, 1992]. The IMF orientation is variable, and it is equally likely that the IMF is directed northwards. For this case the field lines are parallel at the magnetopause nose, thus a reconnection x-line is absent in this region. Instead, it is at high latitudes, on open field lines, that the field lines are anti-parallel at the magnetopause, and reconnection occurs [Dungey, 1963]. However, the Dungey cycle is most efficient under southwards IMF. Furthermore, the IMF can have components in the dawn-dusk direction. This introduces asymmetries in the magnetosphere, due to the torque of the IMF exerted on newly reconnected open field lines [Cowley, 1981a,b].

The motion of the magnetic field lines due to the Dungey cycle process is known as convective flows. At high latitudes, the field lines are open and convect anti-sunwards, towards the magnetotail. At low latitudes, the return flow is present, as illustrated in Figure 1.13, where field lines and plasma convect towards the dayside magnetopause following tail reconnection. As frozen-in-flux conditions are applicable, the plasma and flux tubes are frozen together, and an electric field is present (equation 1.30), which is directed duskwards.

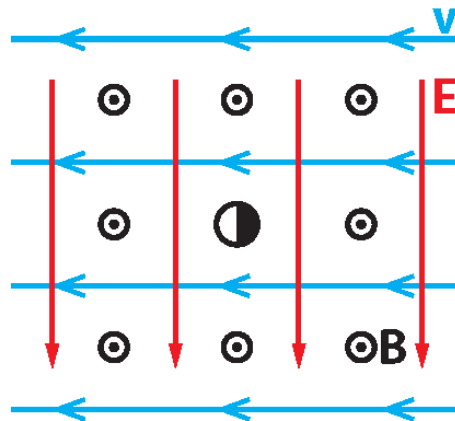


Figure 1.13: Schematic showing the relative directions of the magnetic field, \mathbf{B} , velocity, \mathbf{v} , and electric field, \mathbf{E} , for convective flows of magnetospheric plasma and closed magnetic flux tubes. The diagram corresponds to the magnetic equatorial plane of the magnetosphere, with the Sun positioned to the left.

1.3.3 Magnetospheric configuration

The contributions of corotation and solar wind-magnetosphere coupling determine the structure of the magnetosphere and features of the different regions. The key properties of the different magnetospheric regions will now be reviewed, referring to Figure 1.14.

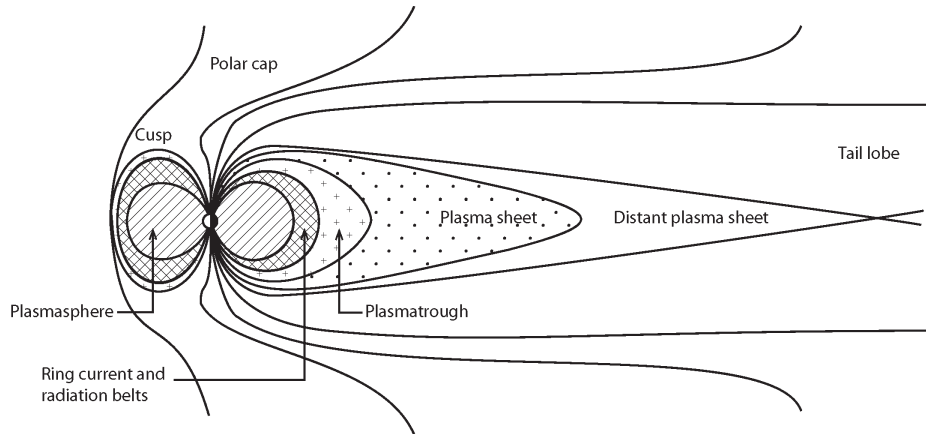


Figure 1.14: Diagram of the key plasma regions of the Earth's magnetosphere in the noon-midnight meridian plane (adapted from Wolf [1995]).

1.3.3.1 Cusp

At high latitudes, the motion of field lines is dominated by the convection cycle. Following reconnection at the dayside magnetopause, open field lines convect anti-sunward across the northern and southern polar cap, forming the cusp region and the open polar cap. As illustrated in Figure 1.14, the open field lines allow direct entry of magnetosheath plasma along field lines. Newly reconnected cusp field lines contract away from the reconnection region, and as magnetic energy is converted into plasma energy, the particles are heated and accelerated. For an increased energy and parallel velocity, a given particle will mirror in a region of increased magnetic field strength (referring to equation 1.6), corresponding to lower altitudes for the geomagnetic field. Therefore, the ionospheric region populated by the cusp field line footprints is characterised by increased electron precipitation, and ionospheric heating. As the field lines convect anti-sunward across the polar cap, hot particles with high flow speeds will quickly escape along the open field lines, whereas cooler particles will take

longer to escape. This corresponds to a decrease in temperature and flow speed with distance from the magnetopause.

The open field lines in the cusp region contain a mixture of magnetosheath plasma, mirroring at low altitudes then streaming away from the Earth, as well as ionospheric bulk ion flows streaming away from the Earth. The increased particle precipitation and ionospheric heating at the cusp footprints raises the ionospheric scale heights and causes upflow of the key ionospheric constituents (H^+ , He^+ , and O^+), where upflow is most significant for the O^+ species. This upflow is known as the “cleft ion fountain” [Lockwood et al., 1985a,b; Yau and Andre, 1997; Andre and Yau, 1997], descriptive of the flow being “swept” across the polar cap by the anti-sunward convection.

Furthermore, across the whole open polar cap region, an additional flow referred to as the “polar wind” is present [Axford, 1968; Nagai et al., 1984; Andre and Yau, 1997; Yau and Andre, 1997; Engwall et al., 2009; Li et al., 2012], where upflow of all ion species occurs. This upflow is due to the plasma pressure gradient along the open field line, as well as the formation of an ambipolar electric field parallel to the magnetic field. As electrons are highly mobile, they escape upwards along the magnetic field, which results in a charge separation and a corresponding electric field. This ambipolar electric field acts to accelerate ions upwards, forming the polar wind. The polar wind typically has energies less than a few eV, lower than the cleft ion fountain upflow, and a temperature of a fraction of an eV.

1.3.3.2 Tail lobes

As the field lines and plasma are convected to the nightside, the tail lobes are formed (Figure 1.14). The tail lobes are characterised by cold, low density plasma flowing away from the Earth, consisting predominantly of the cold ionospheric upflowing ions. These field lines are convected inwards, where nightside reconnection occurs, as previously discussed. The nightside reconnection process is associated with auroral bulk upflow [Andre and Yau, 1997; Yau and Andre, 1997], where these ionospheric upflows are dominated by the O^+ species. The upflows are thought to be driven by electron precipitation, due to the heated plasma following reconnection streaming parallel to field lines, and heating due to large convective electric fields in the ionosphere [Loranc et al., 1991; Wahlund et al., 1992; Wilson, 1994; Liu et al., 1995; Foster and Lester, 1996; Moore et al., 1996; Moore and Khazanov, 2010].

1.3.3.3 Plasma sheet

Following reconnection, the closed magnetic field region is referred to as the plasma sheet, as indicated in Figure 1.14. The plasma sheet is typically characterised by hot particles, with energies of the order of keV and densities of approximately $0.1 - 1 \text{ cm}^{-3}$ [Wolf, 1995].

Cold ionospheric plasma, a consequence of the cleft ion fountain, polar wind, and auroral bulk upflows, is transported to the plasma sheet through the convection motion of the field lines. Approximately 10% of the outflowing cold ions at high latitudes are lost to the solar wind due to the field-aligned velocity, whereas the remainder are transported to the closed magnetosphere through reconnection [Haaland et al., 2012a]. The transport efficiency of ionospheric plasma to the plasma sheet is strongly controlled by the rate of convection [Chappell et al., 1987; Chappell, 1988; Yau and Andre, 1997; Moore et al., 1999; Cully et al., 2003; Haaland et al., 2009; Kistler et al., 2010; Liao et al., 2010; Haaland et al., 2012a; Haaland et al., 2013], as under weak convection, the cold ions can travel further downtail before reaching the plasma sheet. An important feature of the ionospheric plasma transport is mass and velocity dispersion [Lockwood et al., 1985a,b,c; Chappell, 1988; Andre and Yau, 1997; Yau and Andre, 1997; Haaland et al., 2009; Maggiolo and Kistler, 2014]. This effect results in the heavier or colder ions entering the plasma sheet closer to the Earth in comparison to lighter or hotter ions.

1.3.3.4 Plasmasphere and plasmatrough

In addition to the convective motion, corotation is also present and contributes to the magnetospheric structure. It can be shown that convection dominates at larger radial distances from the Earth, and corotation is important at lower radial distances. Therefore, field lines at high invariant latitudes undergo the convective motion, as previously discussed, experiencing states of being open and closed magnetic fields. In contrast, field lines at low latitudes corotate, and remain closed. By summing the convective and corotational flows (illustrated in Figure 1.13 and Figure 1.9, respectively), it can be seen that the flow velocities, in the equatorial plane, are equal and opposite at a given radial distance along the dusk meridian. This radial distance is called the stagnation point, R_{SP} . Figure 1.15 illustrates the convection and corotation flow streamlines in the Earth's magnetic equatorial plane, indicating the position of the stagnation point. The flow streamline that passes through the stagnation point, the stagnation line, corresponds to the boundary between

corotation dominated flows at low radial distances, and convection dominated flows at large radial distances. The flow streamlines are more separated on the duskside, as the convective and corotation flows are in opposite directions, resulting in the asymmetric shape of the boundary.

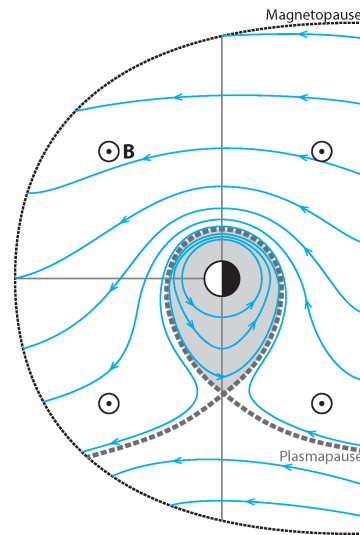


Figure 1.15: Diagram illustrating the combination of corotational flows (Figure 1.9) and convective flows (Figure 1.13) for the magnetic equatorial plane of the Earth's magnetosphere (adapted from Kavanagh et al. [1968] and Chappell [1972]). The directions of the flow vectors, \mathbf{v} , and magnetic field, \mathbf{B} , are shown. The magnetopause boundary is represented by the dashed black line, and the stagnation flow line, or plasmopause, is represented by the thick dashed grey line. The region within the plasmopause, the plasmasphere, is shaded light grey.

Figure 1.15 indicates that the region within the stagnation line remains closed and corotates with the Earth for steady-state conditions. As the field lines do not undergo the Dungey cycle, the field lines do not become open, removing a plasma loss process. Therefore, this region, referred to as the plasmasphere, exhibits high density, cold plasma, predominantly of ionospheric origin. The boundary containing the plasmasphere is the plasmopause, and the increased radial extent of the plasmopause on the duskside is often referred to as the “duskside plasmaspheric bulge”. The region outside the plasmopause is convection dominated, and is termed the plasmatrough. As the field lines undergo the Dungey cycle, they have been previously open, allowing loss of plasma as they convect across the polar cap. As a consequence, the number density is reduced outside the plasmasphere,

and observations of plasma number density indicate a sharp drop across the plasmopause into the plasmatrough [Carpenter, 1966; Chappell et al., 1970; Chappell, 1972; Carpenter and Anderson, 1992; Gallagher et al., 2000]. The position of the plasmasphere is highly variable, with the morphology and radial extent strongly dependent on the strength of the convective electric field [Carpenter, 1970; Chappell, 1972; Carpenter and Anderson, 1992; Gallagher et al., 2000; Lointier et al., 2013]. The plasmopause is typically located at average radial distances of 5 - 7 R_E [Darrouzet et al., 2013].

1.3.4 Current systems

A key feature of Earth's magnetosphere is the large scale current systems present, which respond strongly to internal dynamics and solar wind coupling. As mentioned above, magnetic field gradients on scales comparable to particles' gyroradii results in the generation of currents, due to the differential motions of ions and electrons. Magnetic field gradients across the magnetopause implies the presence of the Chapman-Ferraro currents, as discussed previously. The eastward directed currents are associated with a northwards magnetic field perturbation (see equation 1.21d), which acts to enhance the geomagnetic field. Furthermore, magnetic field gradients occur in the highly stretched magnetotail, resulting in the formation of tail currents. The tail current system is directed westwards across the centre of the magnetotail, and produces a magnetic perturbation that acts to increase the magnetic field strength for this region.

The key current system in the context of this study is the ring current, present in the inner magnetosphere, at a radial distance of approximately 6 R_E [Chapman and Ferraro, 1930, 1931; Singer, 1957; Daglis et al., 1999]. The ring current consists of hot ions and electrons, which are gradient-curvature drifting around the Earth. These particles are energetic enough such that the gyroradii (see equation 1.3) is comparable to both the gradient in the Earth's dipolar magnetic field perpendicular to \mathbf{B} and the radius of curvature of the magnetic field lines. As previously discussed, both of these factors result in the charge-dependent drift motion of particles, such that positively charged particles drift westwards, and negatively charged particles drift eastwards. This differential motion of the ions and electrons results in a current flow, directed westwards around the Earth. The radiation belts, a region of trapped, high energy particles, contribute significantly to the ring current [Van Allen et al., 1959]. The westwards ring current generates a magnetic field perturbation

which is southwards towards the Earth. Therefore, the ring current causes a local depression in the geomagnetic field. The strength of the ring current can be inferred from the magnitude of this depression, as will be discussed in a later section.

1.3.5 Plasma source and loss processes

The plasma populating the magnetosphere has two origins: the ionosphere and the solar wind. The ionospheric input into the magnetosphere has been previously discussed. At low latitudes, closed plasmaspheric flux tubes are filled by the diffusion of ionospheric plasma from lower altitudes. At higher altitudes, ionospheric outflow (polar wind, cleft ion fountain, and auroral bulk upflows) occurs across the polar cap, which is transported to the various magnetospheric regions, such as the plasma sheet and plasmatrough, through the convective motion of the flux tubes. Under general conditions, ionospheric outflow consists mostly of H^+ , whereas at high latitudes, the dayside cleft ion fountain and nightside auroral bulk upflows contain enhanced outflows of O^+ . These high latitude ion outflows are the main source of heavy ions in the magnetosphere. Previous studies have estimated the supply of ionospheric plasma, originating from observed high-latitude ionospheric upflows, to the key magnetospheric regions such as the plasma sheet and plasmatrough. The results show that the estimated densities agree reasonably well with observed densities in these regions, suggesting that ionospheric upflows are sufficient to populate the magnetosphere, and are the dominant plasma source. However, it is important to recognise that the outflow of ionospheric plasma at high latitudes and the transport to the plasma sheet is highly variable, responding strongly to solar wind driving [Young et al., 1982; Moore et al., 1999; Winglee, 2000; Korth et al., 2002; Kistler et al., 2006; Howarth and Yau, 2008; Haaland et al., 2009; Liao et al., 2010; Haaland et al., 2012a; Haaland et al., 2013; Li et al., 2012; Slapak et al., 2012] and incident photon flux [Young et al., 1982; Andre and Yau, 1997; Yau and Andre, 1997; Haaland et al., 2012b]. The process of open field lines at high latitudes, which are then closed via nightside reconnection, as part of the Dungey cycle allows entry of solar wind plasma into the magnetosphere. However, the dominant contribution of the ionospheric outflows implies the solar wind is a minor component in the magnetosphere. Similarly to ionospheric outflows, solar wind plasma is predominantly composed of H^+ ions, presenting difficulties in differentiating solar wind plasma from plasma originating from the ionosphere.

The plasma in the magnetosphere is also dependent on the loss processes that occur. The Dungey cycle implies a clear loss of particles to the solar wind when field lines become open, and also downtail when field lines reconnect on the nightside. Another important process that determines the density and properties of plasma in the magnetosphere is precipitation into the ionosphere, associated with the bounce motion of particles. Particles which have small pitch angles will have mirror points at low altitudes, deep in the ionosphere, where loss due to collisions is of increased probability. The loss cone is the range of pitch angles where loss due to ionospheric precipitation is highly probable. In a simplified sense, under steady state conditions, it is expected that particles with pitch angles in the loss cone are removed from the magnetosphere, and no further ionospheric precipitation occurs as the loss cone is empty. However, this is not the case for all regions of the magnetosphere. Pitch-angle scattering is a process where high frequency plasma waves change particle pitch angles through wave-particle interactions [Treumann and Baumjohann, 1997]. The pitch angle of a given particle can be altered and moved into the loss cone. Therefore, this phenomenon supplies plasma to the loss cone, such that it is no longer empty. Pitch-angle scattering results in an enhanced loss of particles through ionospheric precipitation and is an important process in the plasma sheet and intense ring current. An important feature of pitch-angle scattering is that the loss rate of electrons is greater in comparison to ions. Considering an ion and electron of the same energy, the electron will have a greater parallel velocity, so the bounce motion period is smaller compared to the ion. Therefore, the flux of electrons to the ionosphere is greater than the flux of ions, resulting in increased electron precipitation and shorter average lifetime of electrons.

Charge exchange is also an important process particular for particles contributing to the ring current. Although the process does not alter the density of plasma, it acts to reduce the energy of particles in the radiation belts, reducing the magnitude of the ring current. Considering an energetic radiation belt ion, X^+ , and a low energy neutral, Y , the charge exchange process can be described by



In this reaction, the energetic ion, X^+ , reacts with the low energy neutral, Y , resulting in a low energy ion, Y^+ and a energetic neutral, X . The energetic neutral is not confined to the geomagnetic field so quickly escapes from the magnetosphere. The energetic ion is replaced by a low energy ion, reducing the contribution to the ring current. Hot ring current ions

have typical lifetimes in the range of a couple of hours to days, before undergoing the charge exchange reaction, and becoming a cold ion.

1.4 Magnetospheric dynamics

The Earth's magnetosphere exhibits variations in the strength and configuration of the geomagnetic field and the magnetospheric current systems, which are referred to as geomagnetic activity. The variability and features are strongly controlled by the solar wind coupling to the magnetosphere. In particular, the dynamic pressure and orientation of the IMF are key contributing factors. Strong magnetic activity is observed during periods when the IMF has a significant southward component, driving strong convection in the magnetosphere through low latitude dayside reconnection. In particular, events such as substorms, magnetospheric convection events, and geomagnetic storms occur under these IMF conditions. These types of geomagnetic activity will be reviewed in this section, considering the response of the magnetosphere to the solar wind driving.

1.4.1 Steady magnetospheric convection events and substorms

As discussed in the previous section, the Dungey cycle describes the convective motion of magnetic field lines resulting from dayside and nightside reconnection. When the IMF has a southward component, low latitude reconnection occurs at the dayside magnetopause (Figure 1.10), where the IMF and geomagnetic field are antiparallel, creating open flux. In addition, reconnection occurs in the magnetotail, converting open flux to closed. If the rate of dayside and nightside reconnection are approximately equal for a sustained period of time, the rate of flux being opened and flux being closed are approximately balanced. This is known as a steady magnetospheric convection event [Sergeev et al., 1996; McPherron et al., 2005; Dejong et al., 2008; McPherron et al., 2008]. The polar cap is relatively stable in size, as the amount of open flux is constant, and strong convective flows are present in the magnetosphere.

However, dayside and nightside reconnection rates are not always equal in the magnetosphere. For these cases, a series of events associated with unbalanced reconnection rates can occur, termed magnetospheric substorms [McPherron et al., 1973; Russell and McPherron, 1973; Caan et al., 1977; McPherron, 1991, 1995; Baker et al., 1996; Baumjohann and

Treumann, 1996; McPherron et al., 2008]. A substorm can be considered in terms of 3 phases: growth phase, expansion phase, and recovery phase. These are illustrated below in Figure 1.16, and will now be described.

The substorm growth phase is associated with an enhanced dayside reconnection rate, usually initiated by a southward turning of the IMF, and a negligibly small nightside reconnection rate. The dominant dayside reconnection erodes the dayside magnetopause, transporting flux to the magnetotail. The open flux accumulates in the magnetotail, due to the lack of nightside reconnection, and the polar cap expands to low latitudes. The tail reconnection x-line is located at approximately 100-200 R_E , as indicated in the upper panel in Figure 1.16, and is known as the DNL (Distant Neutral Line). As a result of the compression of the magnetopause, the plasma pressure increases in the tail lobes. In addition, the enhanced dayside reconnection drives strong convective flows of closed flux tubes to the dayside magnetopause. The increased nightside plasma pressure and dayside rarefaction corresponds to a thinning of the plasma sheet and an inward motion of the tail current region [Coroniti and Kennel, 1972].

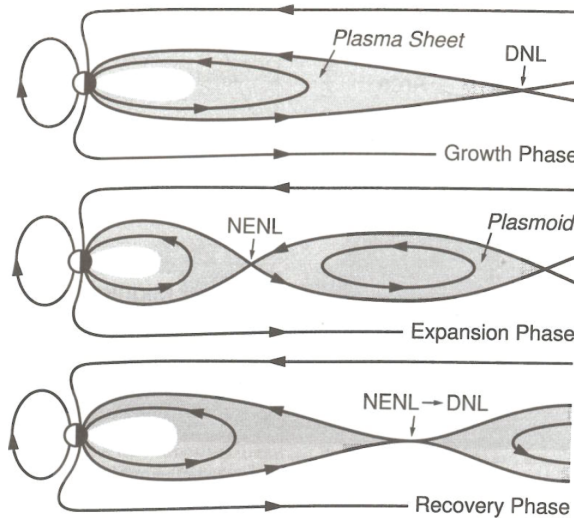


Figure 1.16: Schematic illustrating the geomagnetic configuration in the noon-midnight meridional plane for the 3 phases of the substorm process: growth phase (upper), expansion phase (middle), and recovery phase (lower) [Baumjohann and Treumann, 1996]. The radial location of the NENL and DNL reconnection x-lines in the magnetotail are indicated.

Towards the end of the growth phase, which typically lasts approximately 1 hour, the

formation of a NENL (Near-Earth Neutral Line) occurs in the central plasma sheet due to the highly stretched open magnetic field lines with a small vertical magnetic field component [Coroniti, 1985; Baker and McPherron, 1990]. This is an additional reconnection x-line in the tail region, located at approximately $30 R_E$ downtail. Reconnection begins slowly at the NENL, forming closed loops of magnetic field between the NENL and the DNL, as illustrated in Figure 1.16.

If reconnection continues until the last closed field lines connected to the DNL is reconnected at the NENL (see middle panel in Figure 1.16), then the expansion phase of a substorm is initiated, lasting approximately 70 minutes [Milan et al., 2007]. The parcel of plasma contained by the closed loops of magnetic field lines is termed a plasmoid, which is ejected tailwards, accelerated due to magnetic tension forces and a plasma pressure gradient. The ejection of the plasmoid and dipolarisation of the inner field lines, results in the region tailwards of the NENL collapsing. Explosive nightside reconnection is triggered at the NENL, with the sudden enhancement in the nightside reconnection rate rapidly closing the open flux in the magnetotail, corresponding to a significant reduction of the polar cap. This releases large amounts of energy, stored by the highly stretched tail field lines, injecting hot plasma into the plasma sheet. The enhanced nightside reconnection rate also corresponds to an intensification in particle precipitation, significantly increasing nightside auroral bulk upflows from the ionosphere.

Following the intense nightside reconnection, closing large amounts of open flux, the magnetosphere enters the recovery phase. The nightside reconnection rate gradually reduces, with a tailward motion of the NENL towards the DNL, as shown by the lower panel in Figure 1.16. The magnetosphere returns to the average configuration, with approximately balanced dayside and nightside reconnection rates. However, if the IMF remains southward, the recovery phase may coincide with the growth phase of a succeeding substorm.

1.4.2 Geomagnetic storms

Strong convective flows and enhanced supply of hot plasma sheet ions to the inner magnetosphere, associated with the occurrence of substorms or steady magnetospheric convection events during periods of southward IMF, can drive significant intensifications of the ring current. The sequence of events resulting in an enhanced ring current is known as a geomagnetic

storm [Chapman, 1918; Chapman and Bartels, 1940; Gonzalez et al., 1994; McPherron, 1995; Baumjohann and Treumann, 1996].

There are two key indices that are commonly used to measure the level of geomagnetic activity, associated with the occurrence of geomagnetic storms. As previously discussed, the ring current acts to reduce the strength of the geomagnetic field, and it is known that enhanced ring currents during geomagnetic storms results in significant reductions in the horizontal component of the global magnetic field relative to the average level [Chapman, 1918; Dessler and Parker, 1959; Sckopke, 1966]. The global variations in the horizontal field close to the magnetic equator can be represented by the Dst index, based on magnetic field observations at 4 ground based stations, evenly spaced in local time and approximately 25° from the magnetic equator [Sugiura and Poros, 1964; Sugiura and Kamei, 1991; Baumjohann and Treumann, 1996]. An alternative geomagnetic activity index is the SYM-H index, which is determined in a similar way as the Dst index, using observations from 6 ground based magnetic stations [Iyemori, 1990; Wanliss and Showalter, 2006]. Wanliss and Showalter [2006] demonstrates that the main difference between the hourly Dst index and the 1 minute resolution SYM-H index is the time resolution. Therefore, both the Dst index and the SYM-H index represent the strength of the ring current, and are appropriate proxies for the level of geomagnetic activity. Note that contributions to the magnetic perturbations from other currents systems result in an uncertainty in the magnetic indices, although these are minimised due to the location of the stations.

Figure 1.17 shows characteristic variations in the SYM-H index, representing a measure of the ring current strength, for a typical geomagnetic storm. Variations in the Dst index are observed to be characterised by the same features. Storms typically last multiple days and can generally be divided into 3 stages, based on the characteristic variations in the SYM-H index or Dst index trace, as labelled in Figure 1.17. These stages (the initial phase, the main phase, and the recovery phase) will now be discussed.

1.4.2.1 Initial phase

The initial phase is characterised by a small enhancement in the equatorial magnetic field (demonstrated by Figure 1.17), which is due to an increase in the solar wind dynamic pressure. Many magnetic storms correlate with the occurrence of a high speed solar wind parcel encountering the Earth's magnetosphere. The sudden increase in solar wind dynamic pressure at the Earth's magnetopause, acts to compress the magnetosphere, and thus enhance

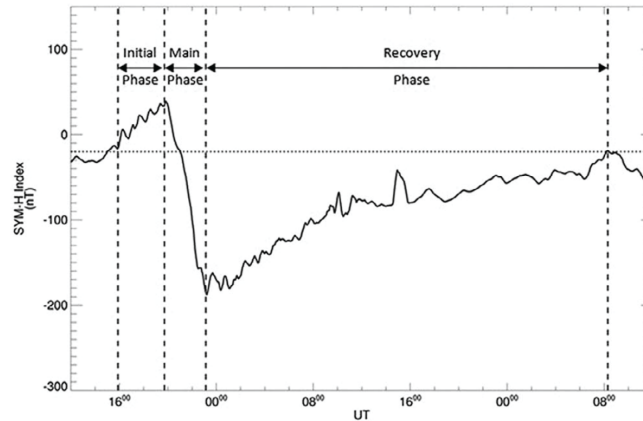


Figure 1.17: A SYM-H trace for a typical geomagnetic storm, with the initial phase, main phase, and recovery phase indicated [Hutchinson et al., 2011]. The horizontal dotted line represents the quiet time SYM-H value.

the Chapman-Ferraro magnetopause currents. The increased currents result in an increase in the associated positive magnetic field perturbations at the Earth's surface. This phase typically lasts approximately 4-16 hours.

1.4.2.2 Main phase

If there is a southward turning of the IMF, which lasts a substantial period of time, the main phase can be initiated. As previously discussed, southward IMF conditions drive enhanced convective flows in the magnetosphere, and are associated with an increased occurrence of substorms and steady magnetospheric convection events. The corresponding increase in nightside reconnection events heats the plasma sheet and increases transport to the ring current region. The continued supply of hot ions to the radiation belts, under southward IMF conditions, raises the average density and energy of the radiation belt population, thus increasing the strength of the ring current. The ring current intensity continues to increase, until the rate of plasma injection equals the rate of loss. As the energy of the ring current population is increased, the radius at which the particles gradient-curvature drift around the Earth decreases. Therefore, the ring current expands radially to lower L shells. Furthermore, the composition of the radiation belts exhibits significant increases in the concentration of heavy ions, particularly O^+ . Due to the strong convection flows and increased reconnection, the dayside cleft ion fountain and nightside bulk auroral upflows are

enhanced. This contributes to the increased energy of the plasma sheet as well as increasing the concentration of O^+ ions supplied to the inner magnetosphere. Overall, during the storm main phase, the enhanced ring current induces large magnetic field perturbations, opposing the main geomagnetic field, which results in a reduction of the magnetic field at the Earth's surface. This process is observed as a rapid decrease in the Dst index or SYM-H index, as shown by Figure 1.17. The main phase typically lasts approximately 1 day.

1.4.2.3 Recovery phase

The end of the main phase occurs when the IMF weakens or turns northward, reducing the convective flow strength and rates of reconnection. The supply of hot plasma to the radiation belts is reduced significantly, and plasma loss becomes dominant. As particles are lost, the ring current reduces, and the corresponding magnetic perturbations decrease. This is demonstrated by a reduction in the magnitude of the Dst index or SYM-H index (Figure 1.17) during the recovery phase of the storm, approaching the quiet time value. Radiation belt particles are predominantly lost through pitch angle scattering and charge exchange, as previously discussed. It is noted that the recovery phase, typically lasting several days, is initially characterised by a rapid reduction in the magnetic perturbation magnitude, followed by a more gradual recession, referring to Figure 1.17 for a typical example.

There are various explanations for the observed two-stage recovery phase. Akasofu et al. [1963] suggested that the differing decay times in magnetic field perturbations is due to the presence of two spatially separated ring current populations. Therefore, the radial dependence of neutral hydrogen density results in two different charge exchange lifetimes. Alternatively, it has been proposed that the feature corresponds to the rapid loss of O^+ from the ring current population, followed by the slower loss of protons, as the two atomic components have different decay times [Hamilton et al., 1988; Daglis, 1997]. Furthermore, an additional contribution to the initial rapid decay in the recovery phase has been attributed to the tail current magnetic field perturbations and particle losses to the dayside magnetopause through convective motions [Takahashi et al., 1990; Alexeev et al., 1996; Feldstein et al., 2000; Patra and Spencer, 2015].

1.5 ULF waves and FLRs

Waves play an important role in the magnetosphere, for the propagation of energy and transmitting information in the system, and are the result of perturbations to the system. The properties of waves in the magnetosphere will now be reviewed, focusing on ULF (Ultra Low Frequency) waves and the formation of FLRs (Field Line Resonances). The concepts reviewed in this section are discussed in further detail by: Hughes [1983]; Southwood and Hughes [1983]; Allan and Poulter [1992]; Kivelson [1995b]; Baumjohann and Treumann [1996]; Waters [2000]. MHD theory for the dispersion relation of waves in a cold plasma approximation show that there are 2 modes of waves present. These are the shear Alfvén wave mode and the fast magnetoacoustic wave mode. Some features of these wave modes, specifically the phase velocity, representing the velocity of the wave in the direction of propagation, and the group velocity, representing the velocity of energy propagation, are described by the Friedrichs diagrams in Figure 1.18. These Friedrichs diagrams are polar plots, describing the variations in the phase velocity and group velocity with the angle between the propagation wave vector and the background magnetic field, \mathbf{B} .

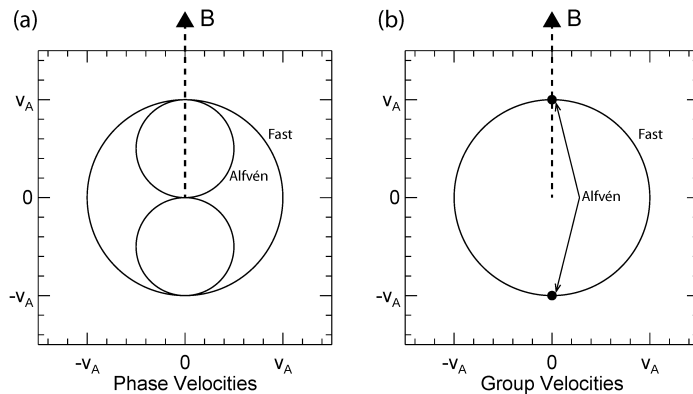


Figure 1.18: Friedrichs diagrams showing the (a) phase velocity and (b) group velocity for the Alfvén wave mode and the fast wave mode.

In the presence of a transverse displacement of a magnetic field line, the resulting magnetic tension force acts as a restoring force, allowing the propagation of transverse oscillations. This transverse wave mode is the Alfvén wave, where plasma density and magnetic field strength perturbations are perpendicular to the direction of propagation. Therefore, the presence of an Alfvén wave does not alter the magnetic field strength or plasma density.

The wave mode is field-guided, with energy propagation purely along the background magnetic field lines (Figure 1.18). The Alfvén wave mode has a group velocity and field-aligned phase velocity equal to the Alfvén speed, v_A , which is defined as

$$v_A = \sqrt{\frac{B^2}{\mu_0 \rho}} \quad (1.35)$$

where B is the magnetic field strength and ρ is the local plasma density. The presence of Alfvén waves in a plasma acts to reduce field line curvature of the background magnetic field.

The fast magnetoacoustic wave mode is a compressional wave, such that the propagation changes the local plasma density and magnetic field strength. The fast mode wave is produced by local perturbations in the total pressure, the sum of magnetic and thermal pressure, of the system. As shown in Figure 1.18a, the fast mode wave propagates isotropically in a cold plasma). Furthermore, the energy transfer by the propagation of a fast mode wave is also isotropic, independent of the background magnetic field direction, indicated by the group velocity (Figure 1.18b). Both the phase velocity and the group velocity are equal to the Alfvén speed (equation 1.35). The effect of fast mode waves is to reduce total plasma pressure gradients in the plasma, by transferring excess pressure as the wave radiates.

Of particular importance in the context of planetary magnetospheres are ULF waves, which have a frequency lower than the natural frequencies of the plasma (periods ranging from seconds to a few minutes [Jacobs et al., 1964]). The corresponding wavelengths are of the same order as magnetospheric scales, and are therefore strongly affected by the structure of the magnetosphere, exhibiting significant boundary effects. Pulsations in the Earth’s geomagnetic field, with frequencies within the ULF wave frequency range were first observed using ground magnetometers [Stewart, 1861], and Dungey [1954a,b] suggested that the pulsations were a result of the presence of MHD waves in the magnetosphere. These magnetic field oscillations are observed to occur at resonant frequencies for closed geomagnetic field lines, implying that the pulsations are the result of standing waves on the field lines, which are reflected at the ionospheric ends. This section will now discuss some of the key features of the standing wave formation.

1.5.1 Standing Alfvén wave formation

For an Alfvén wave travelling along a closed geomagnetic field line in the magnetospheric plasma, the wave energy propagates along the field line and is dissipated in the ionosphere by frictional forces. For an Alfvén wave that has a frequency equal to the field line resonant frequency, a standing wave is formed, referred to as a FLR (Field Line Resonance). The Alfvén waves are reflected by the ionosphere, where electric fields tend to zero due to the large ionospheric conductivities. The ionosphere acts as electric field nodes, and magnetic field antinodes, as illustrated by Figure 1.19. The FLR process is analogous to standing waves on a string.

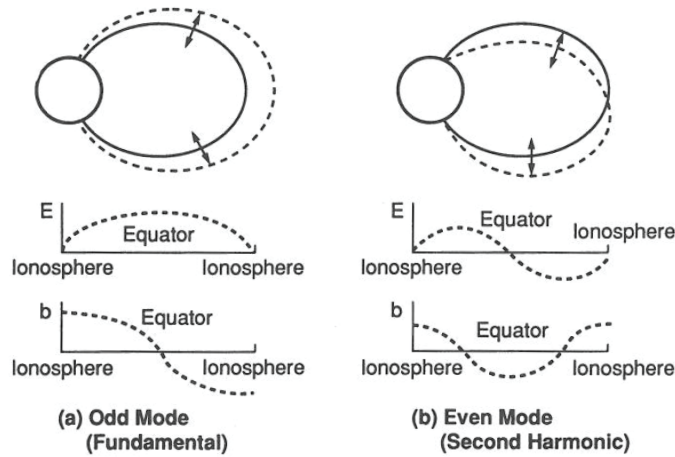


Figure 1.19: Schematics of (a) fundamental ($n = 1$) and (b) second harmonic ($n = 2$) FLR oscillations of a closed dipolar geomagnetic field line [Kivelson, 1995b]. The upper diagrams illustrate the field line displacements, with the dashed magnetic field lines representing displacements from the unperturbed solid magnetic field lines. The lower plots show the variation in the electric field perturbation, E , and magnetic field perturbation, b , along the magnetic field line.

It can be seen that for a given field line of length l , the allowed wavelengths of an Alfvén wave propagating parallel to the background magnetic field, λ_{\parallel} , are given by

$$\lambda_{\parallel} = \frac{2l}{n} \quad (1.36)$$

where n is the harmonic of the resulting standing wave. Therefore, the frequencies, f , that

satisfy these allowed wavelengths are

$$f = \frac{nv_A}{2l} \quad (1.37)$$

as the Alfvén wave has a field-aligned phase velocity equal to the Alfvén speed, v_A . Therefore, the FLR eigenfrequencies of a given magnetic field line is determined by the length of the field line between the ionospheres and the Alfvén speed, which is known to depend on the magnetic field strength and plasma mass density distribution along the field line (equation 1.35). Figure 1.19 provides an illustration of the magnetic field line displacements for the fundamental and second harmonic eigenfrequencies. Due to the variation of the magnetic field and plasma mass density across the magnetospheric field, a continuum of FLR eigenfrequencies exists.

Cummings et al. [1975] observed that the fundamental eigenfrequency is most commonly excited, and dominates over higher harmonics. In addition, two modes of the FLR oscillations exist. The toroidal mode represents azimuthal oscillations of complete magnetic field shells, whereas the poloidal mode refers to oscillations in the radial direction occurring in meridian planes. An observed FLR will often consist of both toroidal and poloidal components.

1.5.2 Wave energy sources

The FLR process involves the local excitation of a field line at the resonant eigenfrequency. The sources of energy that result in the formation of standing Alfvén waves in the closed magnetosphere are now presented, where the sources of wave energy are separated into two groups: convective flows and non-equilibrium particle distributions.

Convective flows involve the coupling of the fast mode and Alfvén mode, allowing energy transfer between the wave modes. Considering the presence of an Alfvén wave perturbation, it has been previously discussed that a low harmonic standing Alfvén wave will form on a field line that has a field line length comparable to the Alfvén wavelength. Consider an incoming fast mode wave from the magnetopause, isotropically propagating through the magnetosphere at the Alfvén speed (referring to Figure 1.18). Due to inhomogeneities in the dipole magnetic field, the fast mode wave will have a component of its group velocity aligned parallel to the magnetic field, allowing the transfer of energy from the fast mode to the Alfvén mode. As it propagates through the continuum of FLR eigenfrequencies,

there will be a coupling point, at which the fast mode phase velocity component along the field line is equal to the Alfvén mode phase velocity that corresponds to a standing Alfvén wave. The coupling of the perturbations results in energy transferring from the fast mode to the Alfvén mode, driving the FLR. The propagation of compressional fast mode waves in the magnetosphere can arise from Kelvin-Helmholtz instabilities at the magnetopause, fast mode waves entering the magnetosphere at the magnetopause nose or directly through the cusps, and from radial displacements of the magnetopause [Dungey, 1955; Southwood, 1974; Chen and Hasegawa, 1974; Hughes, 1983].

Alternatively, non-equilibrium particle distributions can act as a source of wave energy, driving FLRs in the magnetosphere. Enhancements in the plasma particle distribution can often occur as a result from injection of hot plasma sheet particles into the ring current region, and these particles can form a resonance with a ULF wave, causing wave growth [Southwood et al., 1969; Southwood, 1973; Tamao, 1978; Meerson and Sasorov, 1979; Southwood and Kivelson, 1982; Hughes, 1983]. Specifically, as the periods of ULF waves are comparable to particle bounce motion and drift motion periods, resonance with the bounce and drift motion can occur. This process, known as drift-bounce resonance, allows a transfer of energy from the particle phase space distribution to a wave, resulting in wave growth through the thermalisation of a non-equilibrium particle distribution.

Chapter 2

Literature Review

The aim of this statistical study is to determine an empirical model describing the spatial distribution of total plasma mass density in the closed magnetosphere. This chapter presents a review of previous studies examining the mass density distribution, assessing the key features and differences. Studies which have considered dependences in the mass density distribution with geomagnetic activity are also reviewed.

A key motivation for developing an empirical mass density model is to further understand the role of the magnetospheric plasma mass density in determining properties of FLRs. This chapter also presents a review of prior studies that have examined the spatial variations in field lines' resonant frequencies, based on both ground based and in-situ observations.

2.1 Statistical studies of magnetospheric mass density

Multiple studies providing empirical models of the mass density distribution in the closed magnetosphere exist [Gallagher et al., 2000; Takahashi et al., 2004; Berube et al., 2005; Denton et al., 2006; Takahashi and Denton, 2007; Maeda et al., 2009; Takahashi et al., 2014], which will now be discussed in further detail. Gallagher et al. [2000] presented the GCPM (Global Core Plasma Model), an amalgamation of previous models to provide a description of density distributions in the key magnetospheric regions. The resulting model is based on a range of in situ observations, including density measurements from the RIMS (Retarding Ion Mass Spectrometer) instrument on-board DE 1 [Gallagher et al., 1988] and electron density values derived from measurements of plasma characteristic frequencies by the SFR (Sweep

2.1 Statistical studies of magnetospheric mass density

Frequency Receiver) instrument on-board ISEE 1 [Carpenter and Anderson, 1992]. The results provide good spatial coverage and include dependences with geomagnetic activity, solar luminosity, average annual sunspot number and time, but this model is predominantly concerned with electron densities. The limited detail of the plasma ion composition, an important contributor to the mass density, is a key weakness of this model.

Subsequent studies by Berube et al. [2005], Maeda et al. [2009], and Takahashi et al. [2014] included contributions from ion composition, with some consideration of dependences with geomagnetic activity. In contrast to the in situ measurements used by Gallagher et al. [2000], these studies indirectly infer mass density values using ground magnetometer observations of field line resonance (FLR) frequencies [Berube et al., 2005; Maeda et al., 2009] and spacecraft observations of toroidal standing Alfvén waves [Takahashi et al., 2014]. These studies are based on relatively limited datasets. The study conducted by Maeda et al. [2009] examined equatorial mass density values in the plasmasphere and plasmatrough, estimated from CPMN (Circum-pan Pacific Magnetometer Network) magnetometer data. These results are based on only 19 events, providing a limited description of the mass density distribution. In contrast, the analysis of Berube et al. [2005] uses 5200 hours of data from the MEASURE (Magnetometers Along the Eastern Atlantic Seaboard for Undergraduate Research and Education) array of ground magnetometers, providing good statistical significance, but this covers a restricted L shell range from 1.7 to 3.1. In addition, this data only covers the dayside sector. Takahashi et al. [2014] utilises Geotail data covering a substantial time period of 11 years to determine mass density variations for an L shell range from 9 to 15. However, analysis is restricted to the dawn sector (0400 - 0800 MLT). The studies discussed so far [Gallagher et al., 2000; Berube et al., 2005; Maeda et al., 2009; Takahashi et al., 2014] all assume a power law dependence of mass density along field lines, as previously mentioned, where the power law form is used to map measurements to the equatorial plane to determine the equatorial distributions [Berube et al., 2005; Maeda et al., 2009]. This constitutes the main drawback of these studies. Although previous studies show that the mass density can be described by a power law dependence at lower L values (roughly $L \leq 6$) with relatively small field-aligned variations [Takahashi et al., 2004; Denton et al., 2006; Maeda et al., 2009], a different dependence is present for $L > 6$. Observations inferred that the mass density field-aligned distribution, for increased L , can be locally peaked at the magnetic equator, decreasing off-equator, and then increasing at higher latitudes [Takahashi et al., 2004; Denton et al., 2006; Takahashi and Denton, 2007; Denton et al., 2009].

Therefore, it is inappropriate to describe mass density variations along magnetic field lines using the power law form.

Although the models resulting from these studies provide a more accurate description of mass density variations, they are not without their limitations, which will now be reviewed. These studies use measurements of multiharmonic toroidal Alfvén wave frequencies to infer the field-aligned distribution of mass density. The inversion technique utilised to indirectly estimate the mass density makes several simplifying assumptions, and requires a functional form for the field-aligned dependence to be assumed. In addition, the datasets used all have limitations in terms of the spatial coverage provided. Takahashi et al. [2004] used CRRES data covering only 1200 - 1800 MLT (Magnetic Local Time), and whilst this dataset was extended by Denton et al. [2006] to a wider range, only 11% of the additional measurements lie outside this MLT sector. In contrast, Takahashi and Denton [2007] utilised GOES 5 magnetometer data to examine mass density variations with good MLT coverage over all sectors. However, this particular study was limited to field lines at geosynchronous orbit only, significantly restricting the L shell range of the resulting model. As well as spatial coverage, the temporal coverage of the data used can be assessed. All the datasets mentioned cover a short time interval, relative to the solar cycle, thus restricting the models in terms of variations with solar phase. Another key constraint of the models is the limited analysis of mass density variations with geomagnetic activity, with no details on other factors included.

2.2 Dependences on geomagnetic activity

A key aim of this study is to examine dependences of magnetospheric mass density distribution with geomagnetic activity. Previous models describing variations of mass density with geomagnetic activity have been produced [Menk et al., 1999; Gallagher et al., 2000; Takahashi et al., 2002; Berube et al., 2005; Denton et al., 2006; Takahashi et al., 2006; Maeda et al., 2009; Takahashi et al., 2010, 2014], although they are not without their limitations. Most of these studies indirectly infer the mass density on a field line from observations of harmonic standing Alfvén wave frequencies, either from spacecraft measurements [Takahashi et al., 2002; Denton et al., 2006; Takahashi et al., 2006, 2010, 2014] or ground-based magnetometer arrays [Menk et al., 1999; Berube et al., 2005; Maeda et al., 2009]. As detailed in the previous section, the method requires the assumption of a functional form describing the field-aligned distribution of mass density. Many of the mentioned studies assumed a power

law form to describe the field-aligned variations [Menk et al., 1999; Takahashi et al., 2002; Berube et al., 2005; Takahashi et al., 2006; Maeda et al., 2009; Takahashi et al., 2010, 2014], however previous observations indicate that this form does not account for a local peak in mass density at the magnetic equator [Takahashi et al., 2004; Denton et al., 2006; Takahashi and Denton, 2007; Denton et al., 2009]. Therefore, this choice of functional form may have introduced some inaccuracies to the results. Furthermore, it is also noted by Takahashi et al. [2014] that the detection of toroidal standing Alfvén waves is reduced at storm times, suggesting a possible observation bias for studies using this indirect technique. In contrast, the study conducted by Denton et al. [2006] accounted for the peaked field-aligned distribution of mass density, although the CRRES (Combined Release and Radiation Effects Satellite) dataset used in the study provides poor coverage over MLT. The spatial coverage is such that only 11% of the data lies outside of the 1200 - 1800 MLT sector.

All the studies mentioned previously in this section used an indirect inversion technique to infer the mass density of magnetospheric plasma. The GCPM (Global Core Plasma Model) [Gallagher et al., 2000], introduced in the previous section, provides the spatial distribution of density for the key magnetospheric regions, including variations with geomagnetic activity. The key limitation of the model is that the focus is mainly on electron density distributions, with restricted detail on the contribution of ion composition to the total mass density.

From a survey of existing mass density models, it is apparent that no sufficiently accurate description of the variations in the magnetosphere exists, with good spatial and temporal coverage, and a consideration of dependences on geomagnetic activity. This study aims to improve on previous models by using a larger dataset, providing statistically significant results with good spatial coverage. In addition, the dataset used comprises direct measurements, as opposed to indirectly inferring mass density values from magnetic field data.

2.3 FLR observations

A key focus of this study is to further understand the FLR process, and how standing Alfvén wave frequencies vary spatially, due to the magnetic field configuration combined with the mass density distribution. Furthermore, by assessing dependences on geomagnetic activity, the effects of various dynamical magnetospheric processes on the determination of

FLR frequencies can be examined. A summary of existing studies examining the variations in FLR frequencies is now detailed.

Among the first studies to consider the spatial distribution of FLR frequency was Obayashi and Jacobs [1958], where the latitudinal variation was assessed. Geomagnetic pulsations observed using ground-based magnetometers were analysed, for a period spanning about 80 days and covering a geomagnetic latitude range from approximately 40° to 60° . The results indicated that, although a large amount of scatter was present in the data, a clear increase in pulsation period with increasing latitude was observed. The latitude dependence was observed in following studies [Orr and Matthew, 1971; Samson et al., 1971], leading to a notable study conducted by Samson and Rostoker [1972].

Samson and Rostoker [1972] presented an analysis of Pc4 and Pc5 pulsations comprising approximately 185 hours of geomagnetic pulsation activity, observed using ground-based magnetometers covering latitudes from approximately 58° to 78° . The dataset was selected to cover periods of low geomagnetic activity, defined by Kp index values of less than 4. A linear trend in the data was identified, such that on average, the resonant pulsation period increased with latitude. The data is summarised below in Figure 2.1, which shows the fitted linear variation of the period with L value for the dataset, where data has been separated for the nightside sector (1730 - 0730 MLT) and the dayside sector (0730 - 1730 MLT). Previous observations are also indicated for comparison. As well as quantifying the L value dependence, some consideration of dependences on MLT is included, with results indicating the nightside FLR period is statistically greater than the dayside FLR period.

Variations in FLR pulsation period with MLT were further examined in studies by Yumoto et al. [1983] and Poulter et al. [1984]. Using ground-based observations obtained by the STARE (Scandinavian Twin Auroral Radar Experiment) radar and Slope Point radar, Poulter et al. [1984] identified 64 pulsation events, covering an interval of 1978 - 1980 and a latitude range of approximately 58° - 70° . The diurnal variation in average pulsation period was clearly identifiable, as illustrated in Figure 2.2, where periods were observed to maximise at dusk.

Following studies provided support for the observed latitudinal and MLT variations in FLR frequency [Glassmeier et al., 1984; Junginger and Baumjohann, 1984; Takahashi et al., 1984; Takahashi and McPherron, 1984; Engebretson et al., 1986; Mathie et al., 1999; Takahashi et al., 2004; Plaschke et al., 2008; Takahashi et al., 2015], using both ground-based and in-situ datasets. A study conducted by Takahashi et al. [2002] provided further

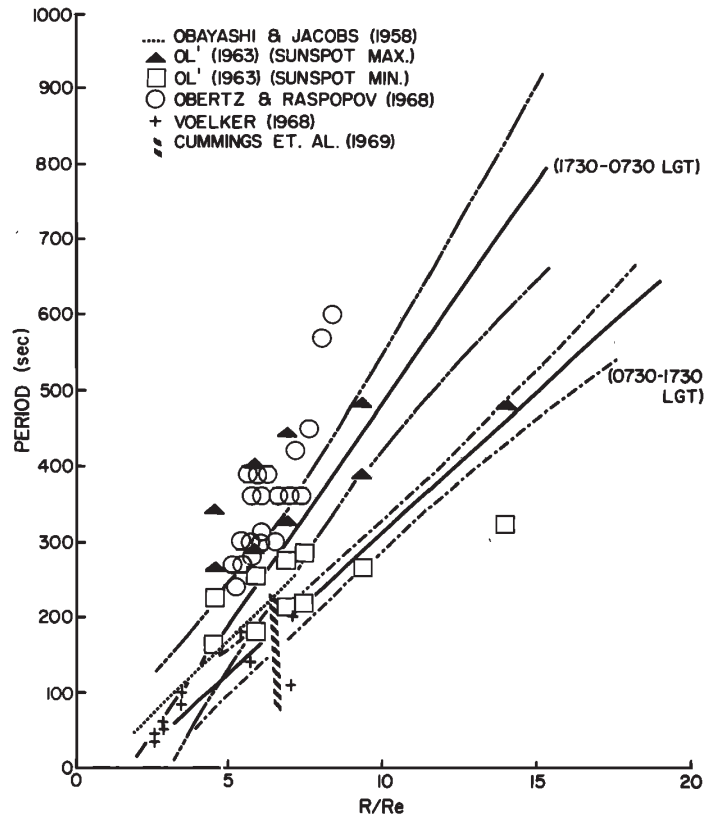


Figure 2.1: Resonant pulsation period (s) as a function of field line L value, from Samson and Rostoker [1972]. The solid lines show linear fits to data, separated into 1730 - 0730 MLT and 0730 - 1730 MLT sectors, and the dot-dash lines show the 95% confidence intervals. Previous observations of FLR periods are also indicated.

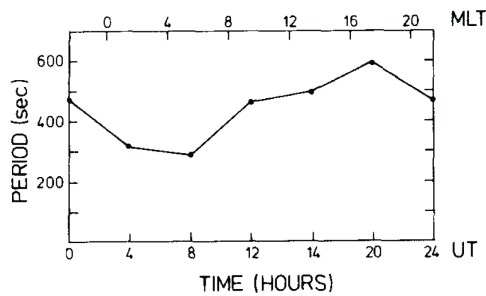


Figure 2.2: Average pulsation period (s) as a function of MLT and UT, observed by the STARE radars. Plot is taken from Poulter et al. [1984].

insight into the spatial variations of the resonant frequencies of field lines by presenting latitude-MLT maps. Using electric field and magnetic field observations from the AMPTE CCE (Active Magnetospheric Particle Tracer Experiment / Charge Composition Explorer), a dataset comprising of 3171 events was obtained. The contour map shown in Figure 2.3 was produced from statistical averages of the full dataset, illustrating L and MLT variations. A decrease in frequency with L shell, and frequency values minimising in the noon-dusk sector are the key observations encapsulated in the contour map.

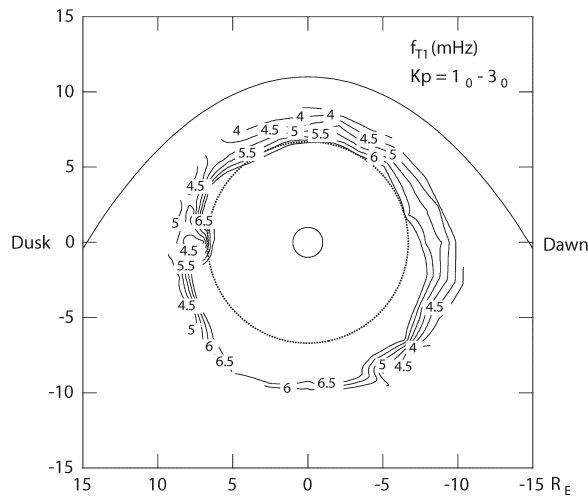


Figure 2.3: Contour map showing average frequency values (mHz) in the Earth’s magnetic equatorial plane, from Takahashi et al. [2002].

In a similar manner, Liu et al. [2009] presented a average map of field line resonant frequency distribution in L -MLT space, as shown in Figure 2.4. The map was based on observations of electric fields and magnetic fields obtained by THEMIS over the interval from November 2007 to December 2008. The average frequencies of Pc4 and Pc5 toroidal waves indicate a decreased frequency with L value and peak values located at approximately dawn (Figure 2.4), in agreement with prior studies.

The previously mentioned studies have focused on average spatial distributions, although, it is also of interest to understand how the spatial distributions of FLR frequencies vary with geomagnetic activity. The study by Takahashi et al. [2002], introduced above, considered the dependence of toroidal standing Alfvén wave frequencies with Kp index and solar wind activity. Figure 2.5 shows the average frequency variations with L value, where data has been binned for Kp index. Although the data included in Figure 2.5 is restricted to

the dawn sector (0400 - 0800 MLT), clear dependences on the level of geomagnetic activity is observed.

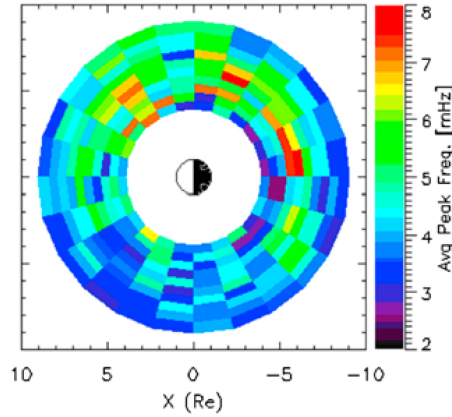


Figure 2.4: Intensity plot showing the average frequencies (mHz) of toroidal waves, in the Pc4 and Pc5 bands, plotted in the Earth's magnetic equatorial plane. Figure is taken from Liu et al. [2009].

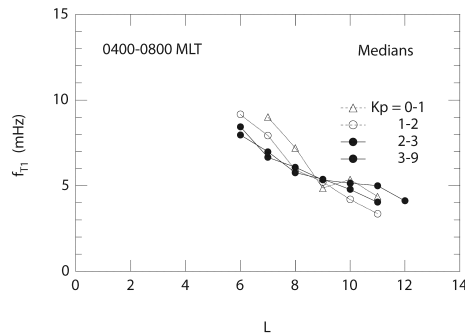


Figure 2.5: Frequency (mHz) as a function of L values, where each profile corresponds to a different Kp index bin, for data obtained in the 0400 - 0800 MLT sector. Figure is taken from Takahashi et al. [2002].

Overall, a review of previous studies indicates that there is a lack of large-scale, statistical studies of the FLR frequency distribution, including quantitative analyses of variations with geomagnetic activity. This introduces difficulties in providing any in-depth comparisons of the time-of-flight calculations to direct observations.

Chapter 3

Instrumentation and Data

3.1 Method

This study aims to determine an empirical model describing the spatial distribution of total plasma mass density in the closed magnetosphere. By combining spatial distributions of electron density, n_e , and average ion mass, m_{av0} , the corresponding spatial distribution of the total plasma mass density, ρ , is inferred from

$$\rho = n_e m_{av} \tag{3.1}$$

This method makes the reasonable assumptions that the magnetospheric plasma is quasi-neutral and the electron mass is negligible in comparison to the ion mass.

Measurements obtained by instruments on-board Cluster are utilised to examine spatial variations in the total plasma mass density for the closed magnetosphere. The method employed uses observations from the WHISPER (Waves of High frequency and Sounder for Probing of Electron density by Relaxation) instrument, providing total electron density, and the CODIF (ion Composition and Distribution Function analyser) instrument, providing average ion mass for ions in the energy range 0.025 - 40 keV/charge. The electron density and average ion mass datasets, obtained from the CAA (Cluster Active Archive) cover the time interval of 2001 - 2012, providing substantial data coverage for statistically significant spatial distributions. The key features of the Cluster spacecraft and details on the instruments used in this study are discussed in the following sections.

Although values of number densities for each ion species, provided by the CODIF instrument, could be used to measure plasma mass density, this distribution would be limited to the energy range covered by the CODIF instrument. In order to represent the full particle energy distribution of the magnetospheric plasma, this method of independently determining the number density and the average ion mass is chosen. This is because the technique used by the WHISPER instrument (described in more detail in the following section) provides measurements of the total electron density for the plasma. The average ion mass determined from measurements by the CODIF instrument also represents the total plasma reasonably assuming that the average ion mass is not a strong function of ion energy for the regions considered. This assumption is examined further in Chapter 4.

3.2 Cluster

Cluster comprises of four identical spacecraft (C1, C2, C3, and C4), which are arranged in a tetrahedral configuration. The polar orbits of the spacecraft crosses various key regions of the magnetosphere (see Escoubet et al. [1997a, 2013, 2015] for further details), and provides the necessary data coverage required for this study. Figure 3.1 shows a typical orbit trajectory for the Cluster spacecraft.

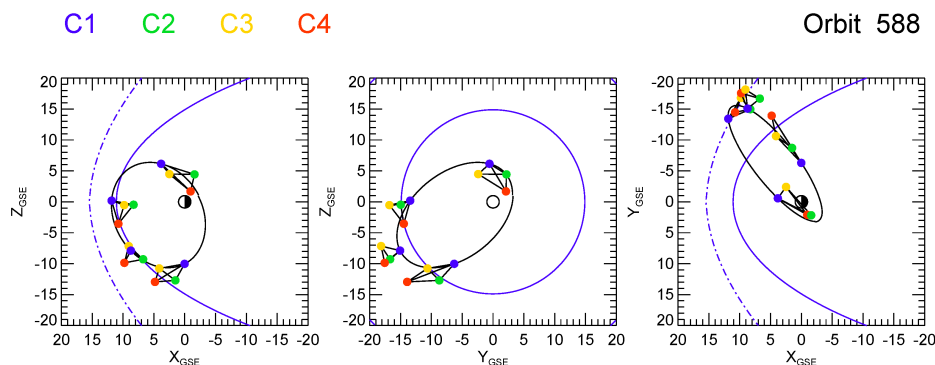


Figure 3.1: Cluster trajectory showing the spacecraft configuration for orbit 588 in each of the GSE (Geocentric Solar Ecliptic) coordinate planes. The four spacecraft positions are indicated at 15 minute intervals, where a scaling factor of 100 is used for the spacecraft separations. A key indicating the colour coding for the Cluster spacecraft is included. For reference, the average model position of the magnetopause and bow shock is shown by the blue solid and blue dashed lines, respectively.

The spacecraft were launched in 2000, with a 90° inclined polar orbit, an perigee of $4 R_E$, and a apogee of $19.6 R_E$. The orbital period of the spacecraft is approximately 57 hours. The orbit of the Cluster spacecraft was chosen to remain fixed in the inertial system, such that, due to the rotation of the Earth around the Sun, the spacecraft cross the key magnetospheric regions of scientific interest. The separation of the four spacecraft are variable, with the relative distance of the four spacecraft ranging between 20 km to 36000 km during the mission so far.

3.3 WHISPER

Electron density data is provided by the WHISPER instrument on-board all four of the spacecraft. WHISPER is a resonance sounder, that measures the total electron density of the local plasma using its active mode, through stimulation and detection of resonances at the local electron plasma frequency [Décréau et al., 1997]. Trotignon et al. [2003] describes the active mode operation, which involves a short (1 ms or less) wave transmission, using the EFW (Electric Field and Wave experiment) instrument antennae [Gustafsson et al., 1997], at a given frequency. A few ms after, the radio receiver is switched on, and the received signal is analysed by FFT (Fast Fourier Transform). The working frequency is then incremented, and the process repeated, to cover the expected range of the plasma frequency. A resonance is observed when the transmitted pulse frequency is close to a characteristic plasma frequency. By identifying the frequency location of the electron plasma frequency, f_{pe} , the electron plasma density, n_e , is directly inferred [Trotignon et al., 2001, 2003], using the relation

$$n_e = \frac{\epsilon_0 m_e}{e^2} (2\pi f_{pe})^2 \simeq \frac{1}{81} f_{pe}^2 \quad (3.2)$$

The frequency range covered by WHISPER restricts the electron density range of the measurements to within $0.25 - 80 \text{ cm}^{-3}$ [Trotignon et al., 2001]. The observations have a time resolution of one spacecraft spin (4 s).

The resonance sounding technique to observe electron density has been employed by previous instruments to monitor a range of plasma regions [Etcheto et al., 1983; Trotignon et al., 1986; Perraut et al., 1990; Stone et al., 1992a,b], due to its advantages of a high signal to noise ratio, reliable and accurate measurements, and ability to cover a large variety of plasma conditions [Décréau et al., 1997; Trotignon et al., 2003]. In addition, WHISPER has a further advantage by using an on-board FFT technique to analyse the frequency spectrum,

compared to previous resonance sounders that use the SFA (Swept Frequency Analyser) technique, providing higher time resolution [Décréau et al., 1997]. A disadvantage of the resonance sounding technique is that the measurements become unreliable for low density plasmas, where spacecraft photoelectrons can distort measurements [Pedersen et al., 2008] and the resonant frequencies are more difficult to detect. However, the resonance sounding method is suitable for the magnetospheric regions examined in this study, as will be explored in further detail in Chapter 4.

This instrument was chosen over particle experiments, in particular the electron analyser PEACE (Plasma Electron and Current Experiment) on-board Cluster, as the PEACE density estimates are sensitive to photoelectron contamination [Johnstone et al., 1997].

Another alternative method commonly used for measuring the total electron density is the spacecraft charging technique, which has been used before in large-scale systematic studies [Escoubet et al., 1997b; Johnson et al., 2001; Laakso et al., 2002a,b; Svenes et al., 2008; Haaland et al., 2012b]. This passive technique provides relatively high time resolution measurements [Pedersen et al., 2008], and can measure electron densities over many orders of magnitude [Laakso et al., 2002a] for long time intervals without major instrument degradation [Escoubet et al., 1997b]. However, Pedersen et al. [2008] notes that this technique relies on calibration by other experiments measuring electron density, such as WHISPER, on a yearly basis due to variations in solar radiation. In addition, there are limitations for low potentials, where the inferred electron density measurements can be overestimated.

3.4 CIS

The CIS (Cluster Ion Spectrometry) experiment, on-board all four spacecraft, consists of two different instruments: CODIF and HIA (Hot Ion Analyser). The key characteristics of these instruments are detailed below, and discussed further by Rème et al. [1997] and Rème et al. [2001]. A key point concerning these instruments is the contamination of the measurements due to penetrating energetic particles, most significant when the spacecraft cross the radiation belt region. This results in high levels of background noise, and is most significant for the HIA instrument. The consideration of the background contamination for the observations is discussed in Chapter 4.

3.4.1 CODIF

The CIS experiment includes the CODIF instrument, which is a high sensitivity, mass resolving spectrometer measuring the full three dimensional distribution functions of the key ion species in the energy range 0.025 - 40 keV/charge. The instrument combines ion energy per charge selection, by deflection in a rotationally symmetric toroidal electrostatic analyser, with a time-of-flight analysis. Integrals of the resulting distribution function, with a time resolution of one spacecraft spin (4 s), allow the ion density to be calculated for each of the ion species, specifically H^+ , O^+ , and He^+ . Although the CODIF instrument also measures the distributions functions of He^{++} ions, these are omitted from the dataset, as He^{++} density data is over-estimated due to strong contamination by H^+ ions. Using the densities, n_i , with the atomic mass, m_i , of each ion, i , the average ion mass, m_{av} , can be estimated from

$$m_{\text{av}} = \frac{\sum_i (n_i m_i)}{\sum_i n_i} \quad (3.3)$$

This study uses the ground calculated moments of the CODIF HS (High Sensitivity) data, limited to the MAG modes, as appropriate for the concerned regions (refer to Rème et al. [1997] for further details). It is also noted that data from the Cluster spacecraft C2 and C3 are not used (the CIS instrument is non-operational on C2 and there are instrumental issues with the CODIF sensor on C3), as summarised in Table 3.1

3.4.2 RPA mode

The CODIF instrument also includes an RPA (Retarding Potential Analyser) device, which is used for pre-acceleration to energies below 25 eV/charge. This extends the energy range to provide observations of ions with energies between 0.7 - 25 eV/charge (with respect to the spacecraft potential). The RPA device only operates when the instrument is in the RPA mode, which occurs approximately once per month. As the reduced operational frequency of the RPA mode, relative to the MAG modes, provides significantly less coverage, this study will examine spatial variations in average ion mass for CODIF MAG mode observations only.

	C1	C2	C3	C4
CODIF	Operations until 25 Oct. 2004	Not operational	One deficient MCP quadrant until switch-off on 11 Nov. 2009	Normal operations
HIA	Normal operations	Not operational	Normal operations until 11 Nov. 2009	Not operational

Table 3.1: Summary of CIS instrument status for all spacecraft (adapted from Dandouras et al. [2014]).

3.4.3 HIA

The HIA instrument is an ion energy spectrometer, which uses ion energy per charge selection by electrostatic deflection in a symmetrical quadrispherical analyser, with a fast imaging particle detection system. The measurements provide full three dimensional ion distribution functions for ions in the energy range 0.005 - 32 keV/charge, with a time resolution of one spacecraft spin (4 s). Unlike the CODIF instrument, the HIA instrument does not include a time-of-flight analysis, so does not provide mass resolved distribution functions. However, higher energy and angular resolution are obtained.

Measurements obtained by the HIA instrument, whilst operating in MAG modes, will be employed by this study. An additional point to note is that HIA data is unavailable from the Cluster spacecraft C2 and C4, as indicated in Table 3.1.

3.5 PEACE

The PEACE (Plasma Electron and Current Experiment), on-board all four Cluster spacecraft, provides full three dimensional distribution functions of electrons [Johnstone et al., 1997], covering the energy range 0.59 eV - 26.4 keV. The instrument consists of two ‘‘Top-Hat’’ electrostatic analysers, with differing geometric factors, which allow differing energy

ranges to be covered. Each analyser has a 180° field of view, and is mounted opposite to each other on the spacecraft. Therefore, on each spacecraft spin rotation, the instruments collect data from the full 4π solid angle. The full pitch angle range ($0^\circ - 180^\circ$) is covered, with 15° resolution, providing the electron pitch angle distribution used as part of the analysis of this study.

3.6 Ground magnetometer data

A key motivation of developing a mass density model for the closed magnetosphere, is the use of the model to estimate frequencies of standing Alfvén waves on closed geomagnetic field lines. This study tests the validity of estimated frequencies through a comparison with the average FLR frequencies observed by ground magnetometers. Data from fluxgate magnetometers in the IMAGE (International Monitor for Auroral Geomagnetic Effects) array are used. The IMAGE magnetometer array consists of 35 stations, located within 54 to 76 degrees magnetic latitude [Lühr, 1994]. The magnetic field measurements have a time resolution of 10 s. Figure 3.2 shows the locations of the stations for the IMAGE array in AACGM (Altitude Adjusted Corrected Geomagnetic) coordinates [Baker and Wing, 1989], for the region of interest. The IMAGE stations not used in the analysis of ground magnetometer data for this study have been excluded.

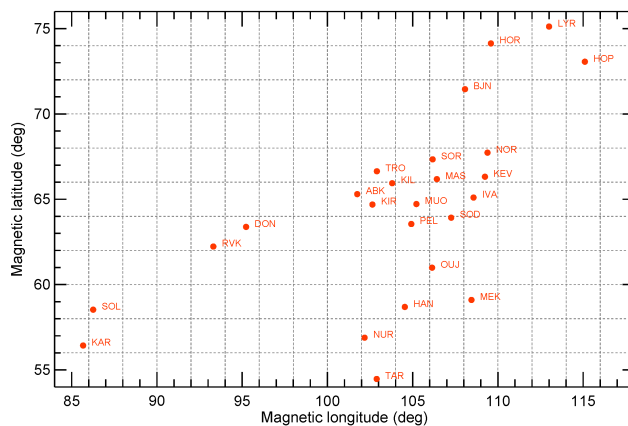


Figure 3.2: Ground magnetometer station locations in AACGM latitude and longitude coordinates, for the IMAGE magnetometer array. Stations are labelled by the station identification codes, and stations that are not utilised in the study have been excluded.

Chapter 4

Data Reduction

As discussed in the previous chapter, this study uses WHISPER and CODIF data to determine empirical models describing the spatial variations of total electron density and average ion mass. This chapter discusses the steps taken to process the data, obtained from the CAA, into reduced datasets, where the same technique is used for both WHISPER and CODIF datasets. Data and method verification tests that were undertaken to address key issues concerning the data usage are detailed.

4.1 Binning data

For each orbit, the data is binned by position into $0.5 \times 0.5 \times 0.5 R_E$ bins, in the GSM (Geocentric Solar Magnetospheric) coordinate system. The average value and average time of measurement for the observations in each bin of the orbit is determined, where the number of observations that are averaged in a bin typically ranges between 10 and 100. From the position of each bin, the corresponding MLT can also be found. Over all orbits between 2001 – 2012, the total number of passes through each bin is typically of the order 10^2 .

4.2 Field line tracing

4.2.1 Identifying the L value position

The next step taken is to determine the L value for each position bin, where the L value is the radial distance of the bin's field line in the magnetic equatorial plane. This is done

4.3 Removal of observations on open field lines

by tracing the field line corresponding to the bin's position and average measurement time, as predicted by the T96 magnetic field model [Tsyganenko, 1996], and defining the T96 magnetic equatorial position as the point of maximum radial distance along the field line. However, for cases where the angular difference between the field line midpoint position and the point of maximum radial distance exceeds 10° , then the field line midpoint of the field line is used instead. This technique accounts for the highly compressed dayside field lines, and it should be noted that the critical angular difference of 10° has been empirically chosen from an analysis of a variety of field line configurations. Figure 4.1 demonstrates the method for a sample of field lines. The T96 magnetic field model is parameterised by the solar wind dynamic pressure, IMF (Interplanetary Magnetic Field) B_y and B_z components, and the Dst index. The parameter values corresponding to the average measurement time of each bin was obtained from the NASA/Goddard Space Flight Center OMNI dataset through OMNIWeb, for the 1-min averaged solar wind parameters, and from the World Data Center for Geomagnetism (Kyoto) dataset, for hourly averaged Dst values.

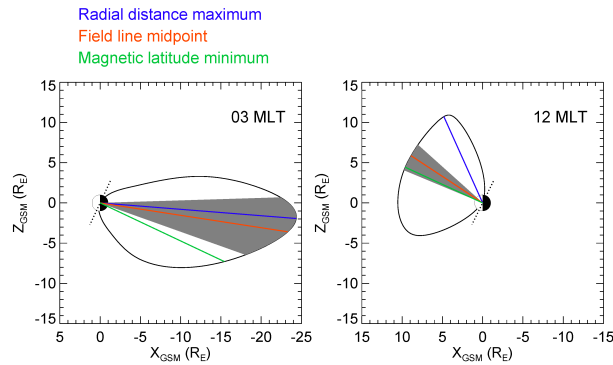


Figure 4.1: T96 magnetic field line configurations in the X-Z GSM plane, with the dotted line indicating the magnetic dipole axis. The vectors representing the maximum radial distance along the field line (blue line), the field line midpoint (red line), and the minimum in magnetic latitude along the field line (green line) are shown, with the grey shaded region covering $\pm 10^\circ$ magnetic latitude of the field line midpoint.

4.3 Removal of observations on open field lines

The procedure of determining the L values for each position bin allows any points where the field line is traced as open by the T96 magnetic field model to be discarded, as this

4.3 Removal of observations on open field lines

study is concerned only with the closed magnetosphere. However, there are inevitably some measurements on open field lines inaccurately modelled as closed field lines, which would contribute to some discrepancies in values taken near the magnetopause. In order to remove points corresponding to open field lines, a method adapted from Clausen et al. [2009] is employed, which will now be detailed. The top panel in Figure 4.2 shows an ion energy spectrogram obtained from CIS measurements using the HIA (Hot Ion Analyser) instrument [Rème et al., 1997], which illustrates the change in ion populations during a portion of the C1 spacecraft orbit. The spacecraft passes from the cusp region, through the OCB (Open-Closed Boundary), into the closed dayside magnetosphere, through perigee and then into the northern cusp region via the OCB again. It is apparent that open field lines near the OCB are characterised by relatively high ion fluxes at approximately 0.7 keV energies (see fourth panel for the DEF (Differential Energy Flux) profile at 0.7 keV), which can be used to distinguish between open and closed field lines near the boundary. However, high ion fluxes at this energy range are also observed near perigee, which correspond to closed field lines, so the DEF profile of ions at 0.02 keV (third panel) is used to differentiate between these situations. This is done by identifying where the DEF of ions at 0.02 keV and 0.7 keV (third and fourth panel respectively) exceed empirically defined critical values (dashed horizontal lines), which are indicated as red lines in the corresponding plots. From a comparison, points are defined as being on closed field lines if they have a DEF of ions at 0.7 keV below the critical value of $1 \times 10^7 \text{ keV cm}^{-2} \text{ s}^{-1} \text{ sr}^{-1} \text{ keV}^{-1}$ or a DEF of ions at 0.02 keV above $6 \times 10^6 \text{ keV cm}^{-2} \text{ s}^{-1} \text{ sr}^{-1} \text{ keV}^{-1}$, which is demonstrated in the second panel, where red (black) points correspond to open (closed) field line measurements. Therefore, using HIA/CIS ion energy flux measurements, it can be determined whether the spacecraft is situated on open or closed field lines, where DEF profiles at two energies are used to distinguish between flux peaks for open field lines and at perigee. This method is applied to all points in the datasets, discarding any points identified to be on open field lines, and the resulting datasets demonstrate a reduction in the fluctuation of values close to the OCB, as expected. It should be noted here that whilst Clausen et al. [2009] used data from the PEACE (Plasma Electron and Current Experiment) instrument on-board the Cluster satellite, we opted to use data from the HIA/CIS instrument instead, as this provides better data coverage over the required interval.

4.3 Removal of observations on open field lines

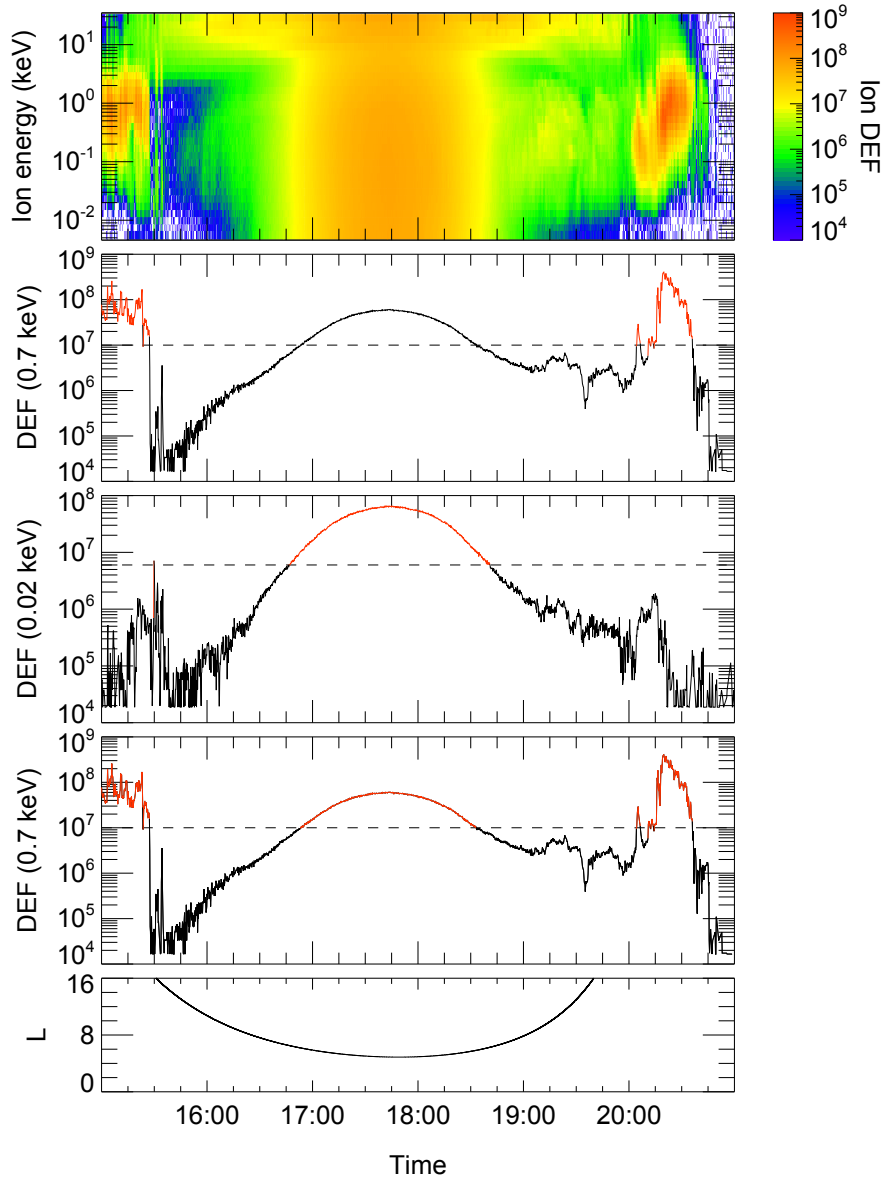


Figure 4.2: HIA/CIS ion energy flux data measured by C1 on 5 September 2002 (case study of Clausen et al., 2009). First panel: ion energy flux spectrogram. Second panel: DEF (Differential Energy Flux) profile for 0.7 keV ion energies, with the red line corresponding to field lines close to the magnetopause that have been identified as open. Third and fourth panels: DEF profiles corresponding to ion energies of 0.02 keV and 0.7 keV, respectively, where the red line indicates where the values exceed a threshold (indicated by horizontal dashed lines). Fifth panel: L values of the spacecraft position.

4.4 CODIF radiation belt contamination

An important aspect concerning the CODIF dataset that should be considered is the background contamination of the measurements due to penetrating energetic radiation belt particles. Although the effects of the background contamination are reduced due to the time-of-flight method of analysis used by CODIF (compared to HIA), a visual inspection of the energy-time spectrograms indicates that the occurrence of data contamination is not negligible. Furthermore, the background contamination effect is mass dependent, such that it is stronger for the O^+ ions [Mouikis et al., 2014]. This results in overestimated O^+ densities, and therefore overestimated average ion mass values, for observations with significant background contamination. Further details on the effect of the penetrating radiation belt particles on the CODIF measurements are described by Ganushkina et al. [2011], Kronberg et al. [2012], and Mouikis et al. [2014].

In order to identify where the CODIF data is significantly affected by the background contamination, a sample of representative passes through the radiation belt regions were assessed for signatures of contamination. This sample consisted of 38 passes in total, for a range of different seasons and orbit configurations. An example of the observed energy spectrograms during a perigee pass is shown in Figure 4.3, for the H^+ ions (first panel), He^+ ions (second panel), and O^+ ions (third panel). The fourth panel shows the ratio of count rates observed for O^+ to H^+ . The fifth panel shows variations in Dst index for reference, and the sixth panel shows the L value of the spacecraft position. This example shows a significant increase in count rates at lower L values (within vertical dashed lines), which is due to radiation belt contamination, and the fourth panel shows the contamination is stronger for O^+ ions compared to H^+ ions. For each case considered, the L values where the spectrograms showed features of radiation belt contamination were visually identified (see vertical dashed lines in Figure 4.3).

4.4 CODIF radiation belt contamination

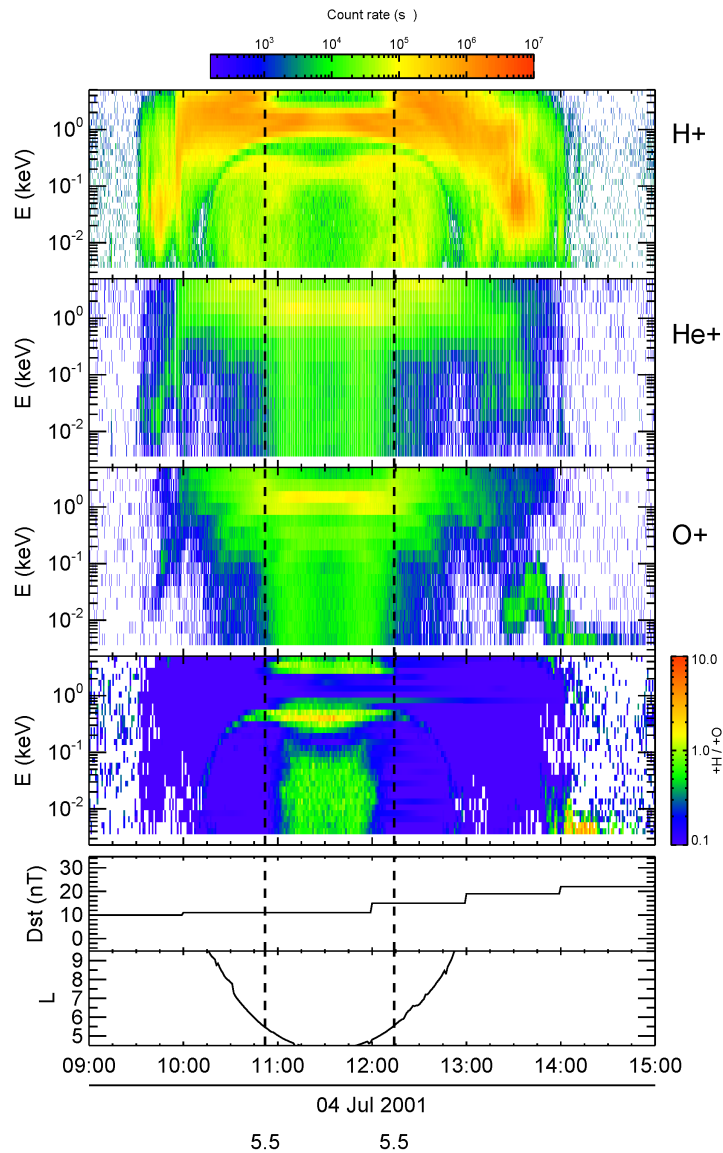


Figure 4.3: CODIF/CIS ion energy flux data measured by C1 on 4 July 2001. The first, second, and third panels show the energy flux spectrograms for the H^+ , He^+ , and O^+ ion species, respectively. The fourth panel shows the ratio of count rates of each time-energy bin for the O^+ and H^+ ion species (ratio of third and first panels). The fifth panel shows the hourly Dst index (nT) for the time interval, and the sixth panel shows the L values of the spacecraft position. The vertical dashed lines indicate the visually identified upper L values of observed contamination for the inbound and outbound spacecraft passes, where the labels below the panel indicate the corresponding L values.

Figure 4.4 shows the frequency of contamination of the CODIF data in this sample of 38 passes as a function of the spacecraft L value. It is clearly apparent that the contamination of data occurs more frequently at lower L values, where the spacecraft is more likely to encounter the radiation belts and the radiation belt particles are more energetic. Based on the inspection of the sample spacecraft passes, CODIF data obtained by the spacecraft at L values below 5.9 are not used in this study, due to the high occurrence of background contamination. Data obtained at $L \geq 5.9$ is less likely to be contaminated. For example, between $5.9 \leq L < 6.5$, on average 4% of the data in the sample is contaminated compared to an average of 64% for $4.5 \leq L < 5.9$. Therefore, restricting the CODIF data used to observations at L values at 5.9 or above will reduce the background contamination to a negligible effect.

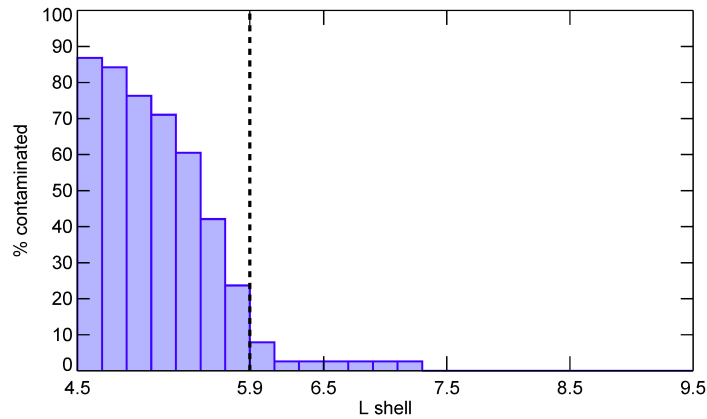


Figure 4.4: Histogram showing the percentage of cases where contaminated CODIF measurements, due to energetic radiation belt particles, were observed as a function of L shell. This is based on a representative sample of 38 passes through the radiation belt region. The vertical dashed line at $L = 5.9$ indicates the lower L shell boundary of CODIF data used in this study.

4.5 Method verification

This section addresses some key issues concerning the data used in the study. Firstly, the WHISPER total electron density data is tested to ensure that there is not a bias towards measurements in high density regions. The CODIF dataset is also examined, to determine whether the CODIF average ion mass data used is representative of the full ion population.

4.5.1 WHISPER usage

Laakso et al. [2002a] notes that the resonance sounding technique employed by WHISPER to measure the total electron density may not be suitable for tenuous plasmas where the density is extremely low. For these regions, such as in the polar cap, the plasma waves may not be identifiable from the spectra, and the total electron density cannot be determined. Therefore it is important to assess whether the WHISPER observations for the region considered in this study are systematically biased such that higher density measurements are preferentially obtained. Figure 4.5a shows the fraction of observations obtained by the WHISPER instrument binned for L value and MLT, with values within each bin averaged. The fraction of measurements is defined as the fraction of spacecraft passes through an L - MLT bin where WHISPER observations of the total electron density are obtained. In order to assess whether there is a significant systematic bias related to the capability of the WHISPER instrument to return measurements of the total electron density for nightside MLT sectors, the fraction of WHISPER observations shown in Figure 4.5a can be compared to the electron density distribution, as shown in Figure 4.5b. Figure 4.5b shows, using the same approach as Figure 4.5a, electron density observations binned for L value and MLT, where values in each bin are averaged. Figure 4.5b clearly shows that the total electron density observed by WHISPER shows reduced values on the dawnside compared to the duskside, noting that the details concerned with this feature will be discussed in section 5.4. A comparison between Figure 4.5a and Figure 4.5b does not seem to show an obvious bias of WHISPER preferentially returning observations for high density regions compared to low density regions. This can be assessed further by considering the correlation of the bins shown in Figure 4.5a and Figure 4.5b, and the results show that the Pearson's correlation coefficient for WHISPER fraction as a function of electron density is -0.07. This indicates that there is an extremely weak correlation between the two quantities (in fact, the sign of the correlation coefficient suggests increased WHISPER fractions in low density regions, opposite to the expected dependence). Therefore, there is no convincing evidence for a systematic bias in the WHISPER observations for the region considered in this study.

Furthermore, to assess whether the spatial variations in electron density observed by WHISPER are representative of the plasma, comparisons with PEACE (Plasma Electron and Current Experiment) and EFW (Electric Field and Waves) data have been performed for multiple case studies. The electron spectrometer, PEACE, provides direct measurements

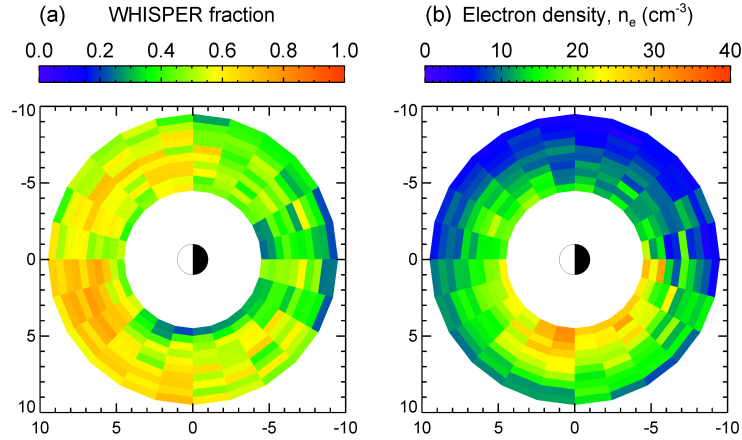


Figure 4.5: Polar plots showing distributions in L-MLT space, where values are binned for field line L value (using a bin width of 0.5) and MLT (using a bin width of 1 hour). The plots show the average of values within each bin. Panel (a) shows the fraction of the total spacecraft passes where WHISPER data is available. Panel (b) shows the distribution of total electron density, n_e , (cm^{-3}), as measured by WHISPER.

of the electron density for particles with energies in the range of 0.59 - 9.45 eV [Johnstone et al., 1997]. Conversely, the EFW instrument observes the spacecraft potential relative to the plasma [Gustafsson et al., 1997, 2001], which can be related to the local electron density using relations determined by Lybekk et al. [2012]. The spacecraft potential technique for monitoring electron density is ideal for tenuous plasma environments, and has been previously employed to observe regions such as the cusp and magnetotail lobes [Pedersen, 1995; Escoubet et al., 1997b; Laakso and Pedersen, 1998; Nakagawa et al., 2000; Scudder et al., 2000; Pedersen et al., 2001; Laakso et al., 2002a; Pedersen et al., 2008; Lybekk et al., 2012]. Figure 4.6 shows data obtained by C1 for the perigee pass of orbit 745, from the WHISPER, PEACE, and EFW instruments, for a representative case study. Figure 4.6a and Figure 4.6b shows electron density observations from WHISPER and PEACE, respectively, and Figure 4.6c shows spacecraft potential observations from EFW. The L value corresponding to the spacecraft position is indicated in Figure 4.6d, and the level of geomagnetic activity for the interval is described by the Dst index timeseries in Figure 4.6e. The WHISPER, PEACE, and EFW datasets were binned for L value, using a binsize of 0.2, averaged, and plotted as a function of L in Figure 4.6f, for the L range of interest. The solid coloured profiles

show the electron density variation as measured by WHISPER (green), PEACE (blue), and inferred values from EFW (red) using the Lybekk et al. [2012] relations. The dotted red profile shows the spacecraft potential observed by EFW, from which electron density values were inferred. It is noted that the magnitude of the spacecraft potentials observed here, representative for this region, are relatively small compared to the range of values typically used for the spacecraft potential technique, and lie outside the range appropriate for inferring electron densities. This suggests that the WHISPER instrument is more suitable, compared to the EFW instrument, for monitoring electron density for this region. Regardless, a comparison of the electron density profiles indicates generally good agreement between each instrument dataset, with similar L gradients. As expected, the magnitude of electron density observed by PEACE, corresponding to a restricted energy range, is lower than the total electron density measured by WHISPER. Overall, the representative example shown in Figure 4.6, provides evidence that the WHISPER dataset should provide a valid electron density spatial distribution for the region considered in this study.

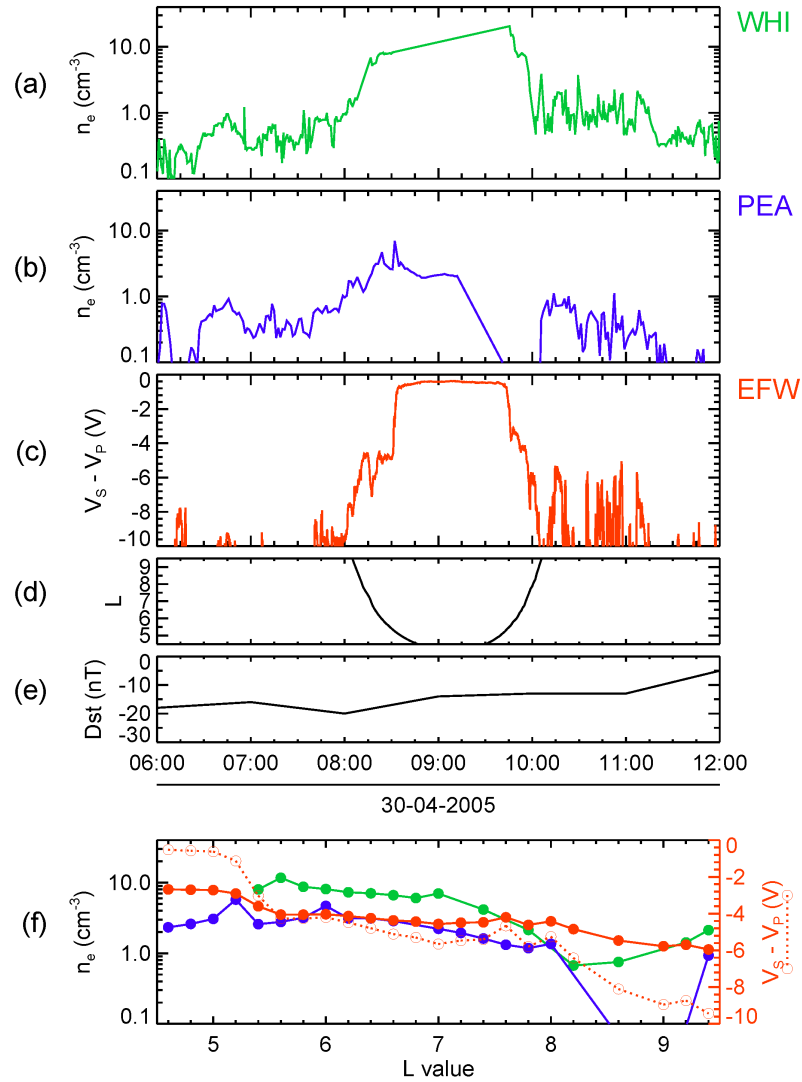


Figure 4.6: WHISPER (green), PEACE (blue), and EFW (red) observations obtained by C1 during the perigee pass of orbit 745. Panel (a) and panel (b) show electron density, n_e , (cm⁻³) timeseries for the WHISPER and PEACE instruments, respectively. Panel (c) shows the spacecraft potential, $V_S - V_P$, (V) timeseries. Panel (d) and panel (e) show the spacecraft L value and Dst index (nT) variation, respectively. For the observations of each instrument, the data are binned for L value, using a binsize of 0.2, and averaged (panel (f)). The solid profiles correspond to electron density, and the dotted profile corresponds to spacecraft potential. Electron density measurements for the EFW instrument were inferred from spacecraft potential measurements using relations from Lybekk et al. [2012].

4.5.2 CODIF usage

The assumption that the average ion mass dataset used is representative of the total plasma population in this region is tested as follows. The CODIF instrument includes the RPA (Retarding Potential Analyser) device [Rème et al., 1997]. When CODIF is operating in the RPA mode, ion densities in the energy range of 0.7 - 25 eV/charge (relative to the spacecraft potential) are provided. Therefore, densities measured using the RPA mode, and the corresponding calculated average ion mass, represent the cold population of plasma, which may be a significant population in this region. Figure 4.7 shows the correlation of ion density observations, and calculated average ion mass values, for data obtained in the MAG modes, corresponding to higher energy particles (0.025 - 40 keV/charge), and the RPA mode, corresponding to lower energy particles (0.7 - 25 eV/charge). Figure 4.7 also compares ion density observations to the total electron density measured by the WHISPER instrument. In total, 2419 values for the MAG modes, 236 values for the RPA modes, and 13697 values for the WHISPER instrument are obtained over the full time interval, where each value corresponds to data averaged in each position bin. The data is binned for L shell, using a binsize of 0.1, and the L shell of each bin is indicated by the colour of the point in Figure 4.7. Figure 4.7a-c show the correlation of ion densities of the key ion species (H^+ , O^+ , and He^+ , respectively) for the MAG mode and RPA mode of the CODIF instrument. It can be seen that the majority of the points for all of these panels (a,b,c) lie below the $y = x$ line, indicating that the densities observed by the MAG mode are, in general, greater compared to the densities observed by the RPA mode. This feature is further demonstrated by Figure 4.7d, which shows the corresponding total ion densities (summed over all ion species) for the MAG and RPA modes. The total ion density is observed to be increased for the MAG mode, representing the higher energy population, in comparison with the observed total ion density for the RPA mode, which measures the cold population. This indicates that, for the region considered here, the cold population, observed by the RPA mode of CODIF, is not the dominant population, and the hotter population, observed by the MAG mode constitutes a larger proportion of the total plasma. An analysis of case studies where the CODIF instrument on-board one spacecraft was operating in MAG mode while the CODIF instrument on-board another spacecraft was operating in RPA mode allowed a comparison of these two corresponding populations at approximately the same time. Although details

are not shown here for all case studies, an example is now briefly highlighted to support the findings.

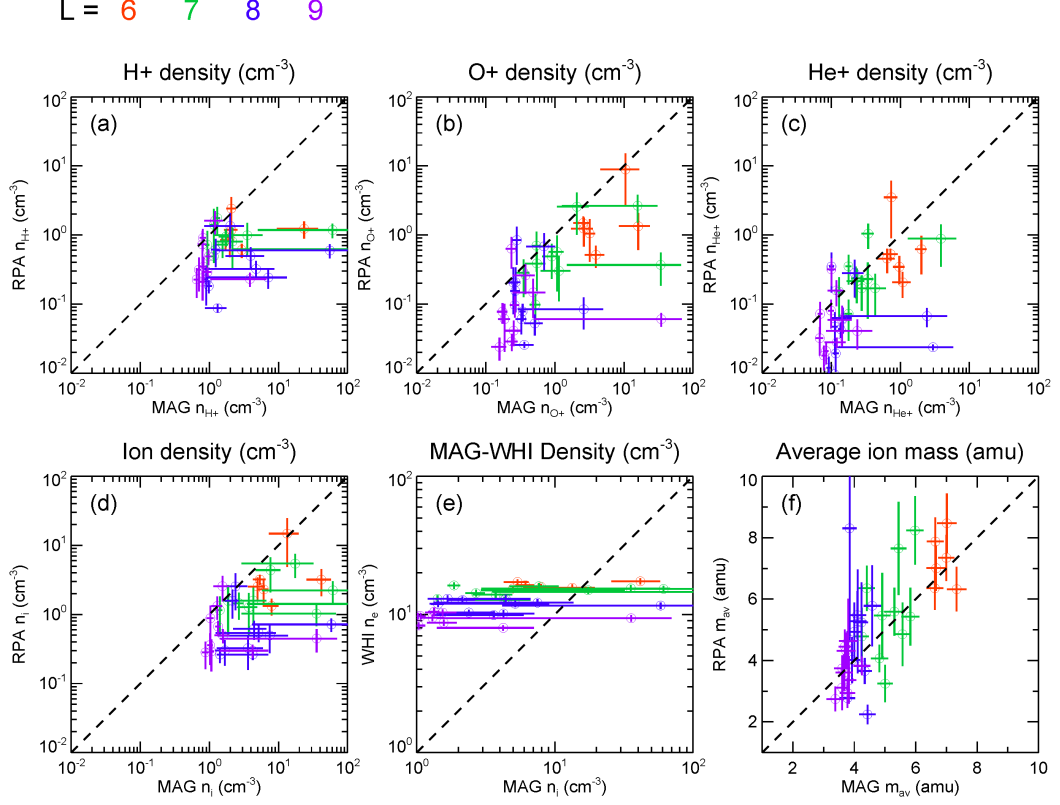


Figure 4.7: Plots showing correlations of CODIF measurements in the RPA (corresponding to 0.7 - 25 eV/charge energy range) and MAG (0.025 - 40 keV/charge energy range) modes, and WHISPER total electron density measurements. All data are binned for L value (represented by the colour of the points), with a binsize of 0.1, and the horizontal and vertical bars on each point correspond to the statistical standard error of the data in the L value bin. The dashed lines on each panel indicates $y = x$. Panels (a,b,c): correlation of H^+ , O^+ , and He^+ ion densities, n_{H^+} , n_{O^+} , and n_{He^+} , (cm^{-3}) respectively, measured by CODIF in the RPA and MAG modes. Panel (d): correlation of the total ion density, n_i , (cm^{-3}) measured by CODIF in the RPA and MAG modes. Panel (e): correlation of the total ion density, n_i , (cm^{-3}) measured by the CODIF in the MAG mode with the total electron density, n_e , (cm^{-3}) measured by WHISPER. Panel (f): correlation of average ion mass, m_{av} , (amu) values calculated from CODIF measurements in the RPA and MAG modes.

Figure 4.8 shows observations obtained by the CODIF instrument during the perigee pass through the dayside magnetosphere of orbit 356. The CODIF instrument was operating in MAG mode for C1 (blue), observing ions in the energy range of 0.025 - 40 keV/charge. Conversely, the CODIF instrument on-board C4 (red) was operating in RPA mode, where ion density observations correspond to the energy range of 0.7 - 25 eV/charge. Panel (a) shows the 1-minute averaged total ion density, n_i , and panel (b) shows the H^+ ion energy spectrogram, where both are observed by C1 in the MAG mode. Panel (c) and panel (d) show the corresponding ion density and H^+ energy spectrogram, respectively, observed by C4 operating in RPA mode. The position of C1 and C4 are indicated in panel (e), which shows the variation in L shell during the perigee pass. A comparison of the energy spectrograms shown in panel (b) and panel (d) appear to indicate that the cold population observed by the RPA mode is a continuation of the hot population observed by the MAG mode, with no separate cold population observed. This suggests that the cold and hot populations are of the same source. The corresponding spectrograms for He^+ ions and O^+ ions (not shown here) demonstrate the same feature. In order to directly compare ion density values, the observations shown in panel (a) and panel (c) are separately binned for L shell, using a binsize of 0.2, and observations in each bin are averaged. The binned data is plotted as a function of L shell in panel (f). It can be clearly seen that the ion densities corresponding to the MAG mode of the CODIF instrument are greater than the ion densities observed in the RPA mode. Therefore, this case study provides evidence for the hotter ion population, observed by the MAG mode, dominating relative to the colder ion population in the region considered by this study.

In order to assess the proportion of the total plasma that the MAG mode observes, the ion densities measured by the MAG mode are also compared to the total electron density measured by WHISPER, as shown by Figure 4.7e. From Figure 4.7e it can be seen that, as most of the points lie above the $y = x$ line, the ion densities observed by the MAG mode of CODIF are less than the electron densities observed by WHISPER. This is the expected result, as WHISPER instrument observes the total electron density of the plasma, whereas the CODIF instrument in the MAG mode observes only a proportion of this population. The notable feature of Figure 4.7e is that the proportion of the total density observed by the MAG mode is not insignificant, providing further evidence that the plasma observed by the MAG mode, with energies ranging between 0.025 - 40 keV/charge, is the major population for this region. Although it may still be argued that it would be inappropriate

to not consider the cold population further, Figure 4.7f demonstrates that the average ion mass values measured in the MAG mode can be reasonably used to represent the cold population measured in the RPA mode. Figure 4.7f shows the correlation of average ion mass values calculated from ion density observations in the MAG mode with corresponding values in the RPA mode. It is clear from Figure 4.7f that, across all L values shown, the points lie very close to the $y = x$ line. This indicates that the average ion mass values at lower energies, as measured by the RPA mode, are approximately equal to the average ion mass values measured in the MAG mode. Therefore, it appears that the ion composition of the plasma in the region considered is relatively uniform over the ion energies. This analysis has demonstrated that although CODIF is unable to observe some of the cold plasma population (due to spacecraft charging) and some of the hot plasma population (above the CODIF energy range), given the consistent values of average ion mass from the RPA mode energy range (0.7 - 25 eV/charge) and the MAG mode energy range (0.025 - 40 keV/charge), it is reasonable to consider that the average ion mass calculated from the MAG mode is generally representative of the total plasma population. It is important to recognise that there may be an additional cold plasma population in the plasma sheet at times, which cannot be observed due to spacecraft charging [Seki et al., 2003]. Due to the instrumental limitations of the CODIF instrument, the existence of an additional cold plasma sheet population is not accounted for in this study.

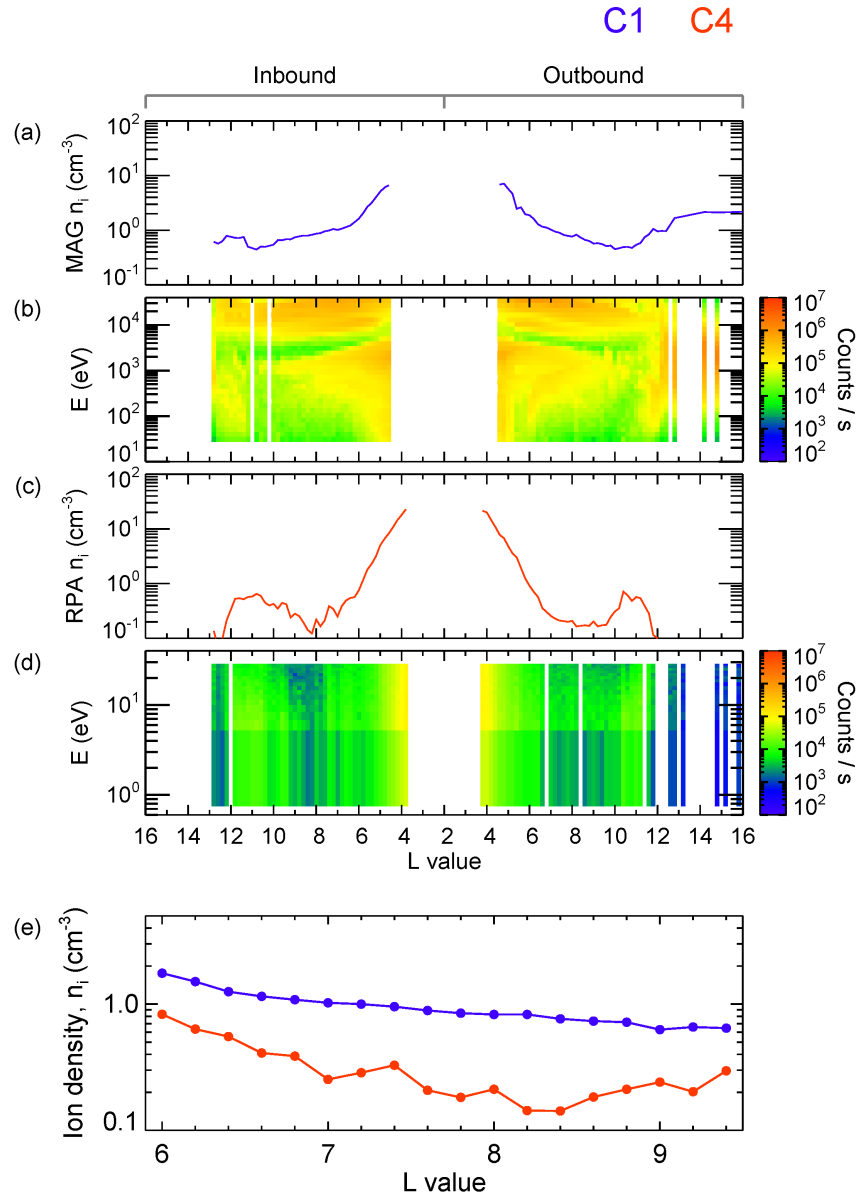


Figure 4.8: CODIF ion observations during the perigee pass of orbit 356, for C1 (blue) and C4 (red). Panel (a) and panel (b) show the total ion density, n_i , and H⁺ energy, E , spectrogram, respectively, observed by C1, where the CODIF instrument was operating in MAG mode. Panel (c) and panel (d) show the ion density and energy spectrogram, respectively, observed by C4, where the CODIF instrument was operating in RPA mode. Panel (e) shows the L values corresponding to the spacecraft positions. Panel (f) shows the ion density variation with L , corresponding to the observations shown in panel (a) and panel (c) binned for L value.

4.6 Reduced datasets

The resulting electron density and average ion mass datasets, binned for position with corresponding MLT and L values determined, and all measurements corresponding to open field lines removed, can now be examined.

4.6.1 Electron density

Variations with magnetic latitude and L value in the WHISPER dataset can be examined from the electron density distribution in the X-Z plane of the SM (Solar Magnetic) coordinate system (where the geomagnetic dipole axis is aligned with the Z axis). A coordinate transformation is used to determine the position in the SM coordinate system corresponding to each bin's position in the GSM coordinate system. The distribution of electron density is shown in Figure 4.9a in the X-Z plane, with the colour of each point representing the average value of the density measurements at that position (note that all measurements are now averaged over the number of orbit passes through the position bin). The measurement positions have been azimuthally mapped into the noon-midnight meridian, such that the radial distance from the Z axis is represented as the magnitude of the X position, and averaged separately over the dayside and nightside MLT sectors. All measurements in the southern hemisphere are also mapped to the corresponding position in the northern hemisphere, as it is assumed that the field-aligned distribution is symmetric about the magnetic equator. Note that spatial distributions of the data shown are binned with a binsize of $0.5 R_E$.

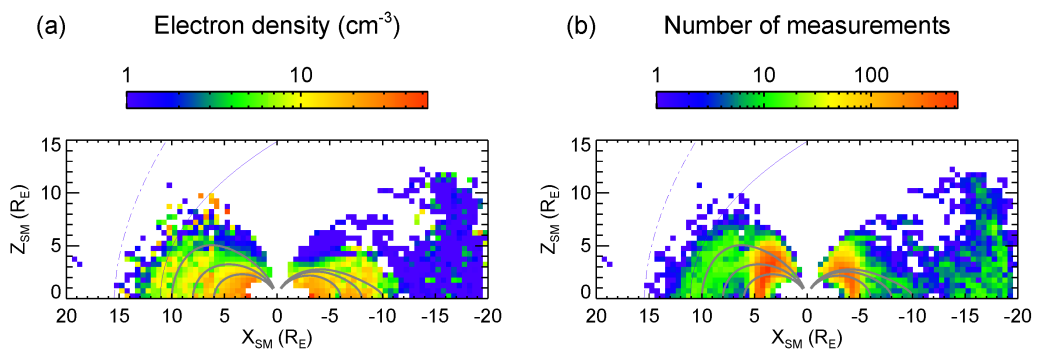


Figure 4.9: Spatial distribution of (a) average electron density (cm^{-3}) and (b) the number of measurements obtained by WHISPER in the X-Z plane (SM coordinate system).

In order to give an indication of the statistical significance of this spatial distribution, Figure 4.9b shows the equivalent spatial distribution of the number of measurements averaged over MLT in the X-Z SM plane.

It can be seen that there are sufficient measurements in the electron density dataset to provide a reliable spatial distribution over a significant range of L shells. More specifically, the electron density dataset provides sufficient spatial coverage along field lines in the region spanning $4.5 \leq L < 9.5$. This corresponds predominantly to the outer plasmasphere and plasmatrough, which will be the region considered in the following analysis for the electron density spatial distributions.

4.6.2 Average ion mass

As with the electron density dataset, the distribution of the average ion mass is shown in Figure 4.10a in the X-Z SM plane, illustrating variations with magnetic latitude and L value in the CODIF average ion mass dataset. As before, the values are averaged over MLT for the dayside and nightside sectors, and it is assumed that the field-aligned variations are symmetric about the magnetic equator, so values in the southern hemisphere are mapped to the northern. The corresponding distribution showing the number of measurements averaged at each position is included in Figure 4.10b. Note that the difference in equatorial coverage between the electron density and average ion mass data sets (Figure 4.9 and Figure 4.10 respectively) is due to the differing temporal coverage of the datasets. Due to instrumental issues of the CODIF instrument, the reduced average ion mass data is only available for times when Cluster's apogee was located at low latitudes.

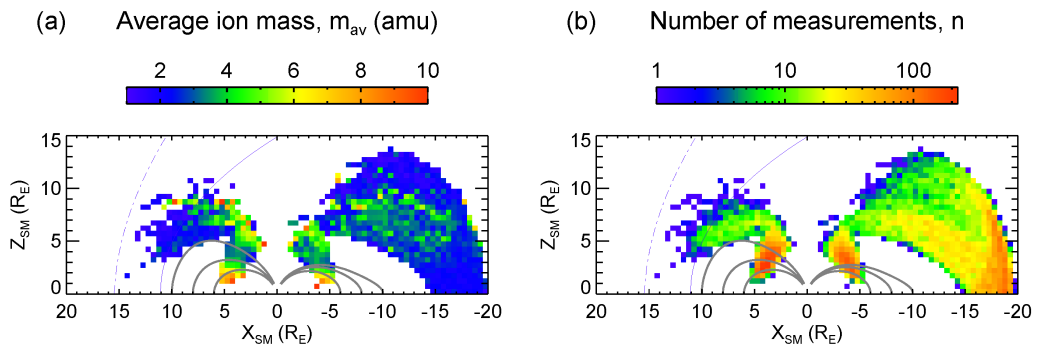


Figure 4.10: Spatial distribution of (a) average ion mass (amu) and (b) the number of measurements obtained by CODIF in the X-Z plane (SM coordinate system).

The CODIF measurements provide an average ion mass dataset covering $5.9 \leq L < 9.5$, which corresponds to the outer heavy ion torus and plasmatrough regions. Therefore, the average mass density distributions will be concerned with these magnetospheric regions. It is noted that for the L values covered by both WHISPER and CODIF data, the plasma under consideration also includes contributions from the near-Earth plasma sheet and the ring current plasma, as these populations can coexist in the region.

Chapter 5

Average Density Model

This chapter determines empirical models for the electron density and average ion mass, using the full datasets presented in Chapter 4, which are then combined to infer an empirical model for the total plasma mass density. As all data is used to produce the empirical models, the resulting distributions represent the average conditions of the closed magnetosphere. The analysis used to determine the models is presented, and features in the spatial distributions of electron density, average ion mass, and total mass density are discussed.

5.1 Field-aligned distribution of electron density

Variations in electron density along closed magnetospheric field lines are often assumed to follow a power law dependence. Cummings et al. [1969] is an example of this case, where assuming a dipolar field and hydrogen plasma, the electron density field-aligned distribution was modelled as a power law function. This model states that the electron density, n_e , at a radial distance R (R_E), on a field line with a maximum radial distance of L (R_E) is given by

$$n_e = n_{e0} \left(\frac{L}{R} \right)^\alpha \quad (5.1)$$

where n_{e0} is the electron density at $R = L$, and α is termed the power law index. This form implies that the electron density is a minimum at the magnetic equatorial position along the field line, and increases with magnetic latitude towards the ionospheric ends of the field line, assuming that α is positive. The rate at which the electron density increases depends on the magnitude of the power law index, α .

5.1 Field-aligned distribution of electron density

In order to determine the field-aligned distribution of electron density, the following analysis is conducted. The electron density data are binned for the field line L value and the normalised radial distance along the field line, R_{norm} , which is the radial distance at which the measurement was obtained, R (R_E), divided by the L value of the field line. The T96 magnetic field model is used here to determine the field line corresponding to each position bin, and the data are also binned for MLT in order to further examine the density dependence. The density variations along field lines are quantified by determining the most appropriate functional form to describe the field-aligned distribution. Then, using a least-squares fitting method to determine the best fitting function parameters, a hierarchical modelling approach is employed to define a model function that includes dependences on L value and MLT. As the function parameters vary on multiple levels (dependences on the L shell of the field line and MLT are expected), the hierarchical method separately fits to each of these levels, representing variations in the dataset as a whole. This statistical modelling method is described in detail by Clark and Gelfand [2006] and Tabachnick and Fidell [2006], but is now briefly summarised. Firstly, the best fit function parameters for the field-aligned profiles are determined for each L - MLT bin. For a given function parameter, the parameter can be expressed as $p_{\text{MLT},L}$. The first level considered is MLT variations. An assumed sinusoidal form function is fitted to the $p_{\text{MLT},L}$ values, considering each L bin separately, which provides $p_L(\text{MLT})$. The parameter now includes MLT dependences. The next level considered is L variations. A linear functional form is approximated to describe variations with L , and is fitted to the best fit sinusoidal function parameters from the previous fitting level. This provides the function parameter, $p(\text{MLT}, L)$, which is parameterised by L and MLT. This technique is utilised here as it provides a simple form for the function parameters, whilst encapsulating the key variations.

An example plot showing the electron density as a function of normalised radius is shown in Figure 5.1 for data corresponding to an L shell of 9 (data are binned for L using a binsize of 1.). Each point represents the average electron density value in the bin, where the normalised radius bin width is equal to 0.05, and the colour of the point corresponds to the number of averaged measurements in each bin, n . The vertical panels show the density data binned into 3 hour MLT intervals. The distribution of electron density values in each bin is indicated by the vertical grey line showing the range between the lower and upper quartile, with the short horizontal line representing the median value. As the profiles are

5.1 Field-aligned distribution of electron density

smoothed using a boxcar function, with a width of 3 bins, some points are shifted relative to the grey lines.

Figure 5.1 shows that at higher magnetic latitudes (equivalently, lower R_{norm} values), the distribution tends to resemble that of the expected power law (see equation 5.1), as evidenced by the blue curve, which represents a power law best fit described in more detail in the following subsection. However, at lower magnetic latitudes (higher R_{norm} values), close to the magnetic equatorial plane, a peak in electron density is often observed, which appears to have an MLT dependence. To account for the different dependences observed, the field-aligned distribution is separated into two regions, where the boundary between these regions is indicated by the vertical dotted line in Figure 5.1. The value of the normalised radius at the boundary between the two dependences is defined as $R_{\text{norm}} = 0.8$, which is determined from the mean value of R_{norm} where the average electron density is at a minimum for the field line distribution.

5.1.1 Power law model

For the high magnetic latitude region, a power law dependence is apparent, so the functional form of equation 5.1 is chosen to describe the field-aligned distribution. Using a least-squares fitting method, weighted by the number of measurements in each bin, the best fit parameters (n_{e0} and α) in equation 5.1 are determined for each field-aligned distribution. Variations in the best fit parameters are then quantified to include dependences with L and MLT, providing a hierarchical model for a power law field-aligned distribution. The resulting power law model (equation 5.2a, with model parameters given by equations 5.2c and 5.2d) is shown as the solid blue line in Figure 5.1. This model has also been extrapolated into the lower latitude region for comparison, as illustrated by the dashed blue line, clearly illustrating that the power law does not provide a valid description close to the magnetic equator. Although some MLT sectors do not appear to represent the best fit with minimum deviations from the data (e.g. first panel in Figure 5.1), this is due to the hierarchical technique employed. As mentioned previously, the model fits shown are results of fits at multiple levels, accounting for variations with L and MLT, as well as R_{norm} .

The functions used for all model parameters are chosen to include a sinusoidal term, so that the circular form describes the MLT dependence. The phase term of the sinusoidal component indicates the location of the peak of the parameter in degrees of MLT eastwards

5.1 Field-aligned distribution of electron density

from the midnight meridian, and an amplitude term is included to determine the magnitude of the MLT dependence. Both the phase and amplitude terms are linear functions of L . An offset, which is also a linear function of L , is added to the sinusoidal term, to represent the mean value of the parameter across all MLT. The functional forms chosen to represent the MLT and L dependences have been chosen as they were the simplest forms that described the observed variations in the data, minimising the number of free parameters. Note that when fitting for the model parameters, if no clear L dependence in the data was observed, the L dependence was removed from the relevant functional form.

The key features of the power law dependence, and the variations with L and MLT, are discussed in section 5.4.

5.1 Field-aligned distribution of electron density

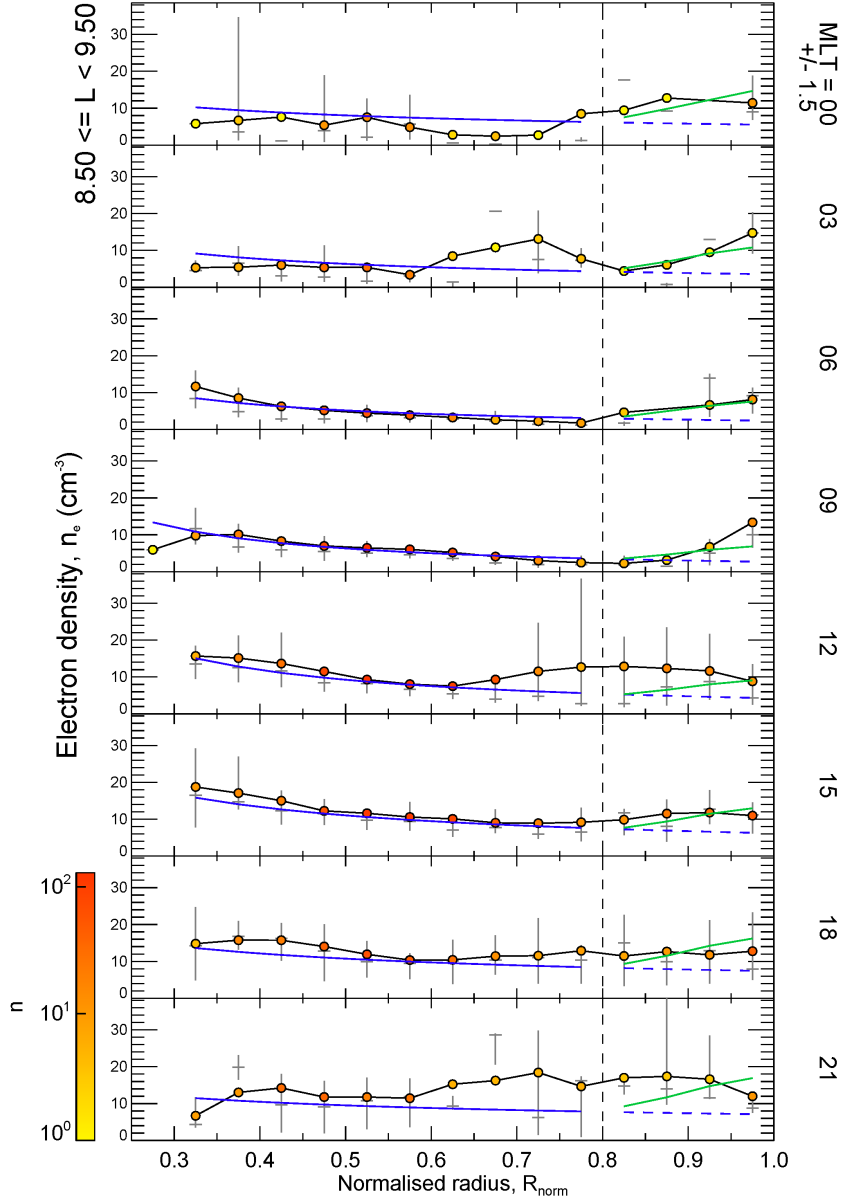


Figure 5.1: Electron density, n_e , (cm^{-3}) plotted as a function of normalised radius, R_{norm} , for $8.5 \leq L < 9.5$ at 3 hour MLT intervals, where the colour of each point indicates the number of WHISPER measurements, n , averaged in each bin. The upper and lower quartiles of the distribution of points averaged in each bin is shown by the grey line, intersected by a short horizontal line at the median value. The vertical dashed line indicates the boundary between the power law and Gaussian dependences. The blue line represents the best fitting power law dependence, where the dashed blue line is the extrapolated dependence. The green line represents the best fitting Gaussian function.

5.1.2 Gaussian model

The localised peak in electron density in the lower latitude region indicates that a power law dependence is not an appropriate form to describe the variations in this region, as can be seen from the difference between the extrapolated power law model and observed electron density in Figure 5.1 close to the magnetic equator (at $R_{\text{norm}} > 0.8$). For this region, a Gaussian function is chosen to represent the electron density peak. The width of the peak is fixed to 0.1 and the position to $R_{\text{norm}} = 1.0$ (i.e. at the magnetic equatorial plane), in order to reduce the number of free parameters in the fitting. An offset, equal to n_{e0} from the power law model defined in equation 5.2c, is added to the Gaussian function. This is done so that the electron density given by the Gaussian function is representing an enhancement compared to the background power law model, extrapolated into the lower latitude region. This region is modelled by fitting a Gaussian function to the field-aligned distributions, using a least-squares method weighted by the number of measurements in each bin, and quantifying the parameters' dependence on L and MLT. The resulting model for this region is indicated in Figure 5.1 by the solid green line, and is shown in equation 5.2b, where n_{e0} and a (peak height above n_{e0}) are defined in equations 5.2c and 5.2e. Further discussion of the dependences present in this model are included in section 5.4.

The power law and Gaussian models can now be combined to form the model for the electron density distribution along field lines, with dependences on L and MLT included, as summarised below in equation 5.2:

$$n_e = n_{e0} R_{\text{norm}}^{-\alpha} \quad R_{\text{norm}} \leq 0.8 \quad (5.2a)$$

$$= a \exp \left[-\frac{1}{2} \left(\frac{R_{\text{norm}} - 1.0}{0.1} \right)^2 \right] + n_{e0} \quad R_{\text{norm}} > 0.8 \quad (5.2b)$$

$$n_{e0} = 35.0 - 3.35L + (9.38 - 0.756L) \cos(15\text{MLT} + 76.) \quad (5.2c)$$

$$\alpha = -0.173 + 0.113L + 0.412 \cos(15\text{MLT} + 81.9 + 16.0L) \quad (5.2d)$$

$$a = -1.24 + 0.944L + 2.92 \cos(15\text{MLT} + 40.) \quad (5.2e)$$

Overall, Figure 5.1 shows the model defined by equation 5.2 presents a reasonable fit to the data profiles. This is representative of the full dataset, and deviations between the model profiles and the data profiles can be typically be attributed to the low number of

5.1 Field-aligned distribution of electron density

measurements within a bin, as the fitting method is weighted by observation frequency. However, the data profile shown in Figure 5.1 for the 1200 MLT bin, shows a non-negligible deviation for $R_{\text{norm}} \sim 0.8$, despite significant sampling of the region. The enhancement of total electron density is not accurately described by the model, and is discussed further in section 5.4.

The azimuthally mapped spatial distribution (averaging separately over dayside and nightside MLT sectors) predicted by the resulting model is shown in Figure 5.2a and Figure 5.2b in the X-Z SM plane, including the distribution where the equatorial peak is neglected by using the extrapolated power law form for the lower latitude region (Figure 5.2a). A comparison of the two forms of the model show that the inclusion of the Gaussian function to represent the localised peak results in significant enhancements in electron density at low latitudes, as expected, particularly for large L values with the effect being stronger on the nightside.

The spatial distribution in the T96 magnetic equatorial plane predicted by the electron density model is shown in Figure 5.3a and Figure 5.3b, illustrating MLT and L dependences. Figure 5.3a corresponds to the extrapolated power law model and Figure 5.3b corresponds to the combination of the power law and Gaussian functions. A comparison of the distributions further illustrate how the use of the Gaussian function, accounting for the localised peak in electron density, results in increased values overall compared to the extrapolated power law form. The spatial features shown in Figure 5.2a,b and Figure 5.3a,b are discussed in section 5.4.

5.1 Field-aligned distribution of electron density

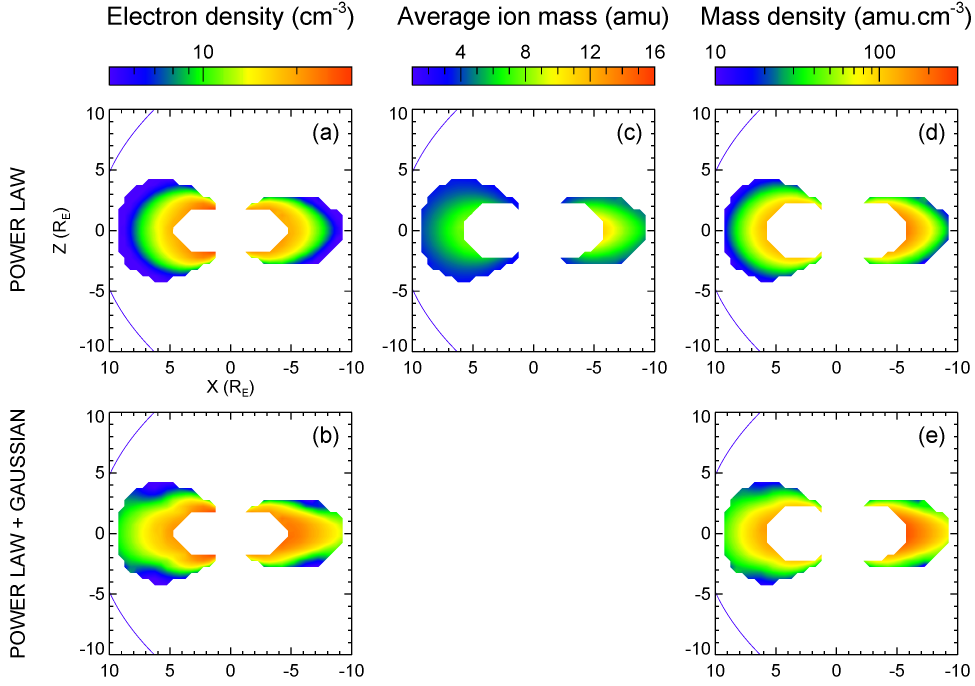


Figure 5.2: Spatial distribution in the X-Z SM plane using the field-aligned models for (a,b) electron density and (c) average ion mass, defined by equation 5.2 and equation 5.3, respectively. These models are combined to determine the corresponding distribution for (d,e) the plasma mass density. The distributions using both the extrapolated power law form (upper row) and Gaussian function (lower row) for the low latitude electron density dependence are shown for comparison. Note that the scales have been adjusted relative to the data plots (Figure 4.9 and Figure 4.10) to focus on the most relevant regions. The T96 magnetic field model used in this case corresponds to spring equinox, with a solar wind dynamic pressure of 2nPa.

5.1 Field-aligned distribution of electron density

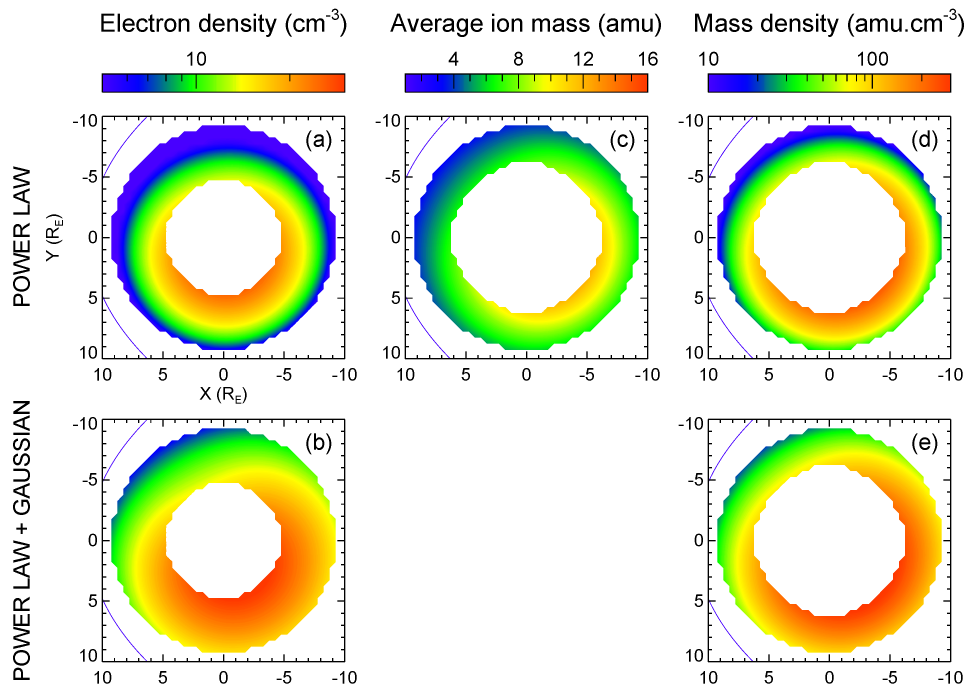


Figure 5.3: The spatial distribution of (a,b) electron density, (c) average ion mass and (d,e) mass density in the T96 magnetic equatorial plane, in the same format as Figure 5.2.

5.2 Field-aligned distribution of average ion mass

Using the same approach as for the electron density dataset (see section 5.1), the CODIF dataset is binned by L , MLT, and normalised radius, R_{norm} , in order to examine the distribution of average ion mass, m_{av} , along geomagnetic field lines. An example plot showing the average ion mass as a function of normalised radius is shown in Figure 5.4 for an L shell of 7 (note that, unlike Figure 5.1, Figure 5.4 uses logarithmic scales in order to linearise power law dependences). It can be seen from this example that the average ion mass tends to maximise towards the magnetic equator and decreases off-equator, in contrast to the electron density results and in agreement with the results of previous studies [Takahashi et al., 2004; Denton et al., 2006]. It can also be noted that, compared to the electron density field-aligned profiles, the average ion mass profiles provide less coverage across R_{norm} , so the resulting field-aligned model has to be extrapolated along the field lines.

To describe this field-aligned dependence, a power law form is chosen, as shown in equation 5.3:

$$m_{\text{av}} = m_{\text{av}0} R_{\text{norm}}^{-\beta} \quad (5.3a)$$

$$m_{\text{av}0} = 16.4 - 1.32L + (7.12 - 0.665L) \cos(15\text{MLT} + 32.) \quad (5.3b)$$

$$\beta = -2.13 + 0.223L + (2.26 - 0.218L) \cos(15\text{MLT} + 219.) \quad (5.3c)$$

where $m_{\text{av}0}$ is the average ion mass at the magnetic equatorial point of the field line, and β is the power law index. However, unlike the electron density case, the power law index, β , is allowed to be negative. This results in a distribution where the average ion mass is a maximum at the magnetic equator and decreases towards the ionospheric ends of the magnetic field lines, as desired. The previously described least-squares fitting method (see section 5.1) is employed to determine the best fit parameters ($m_{\text{av}0}$ and β), providing the average ion mass model describing field-aligned variations, shown in equation 5.3. This model is represented in Figure 5.4 as the solid blue line. As before, variations on L shell and MLT are quantified in the model. The features of the parameters are discussed in further detail in section 5.4. It is noted from Figure 5.4 that, for the 0300 MLT bin, the model profile displays larger average ion mass values along the field compared to the data profile. This is a feature apparent for all 0300 MLT bins across all L bins considered here, and is attributed to the sinusoidal form chosen to represent the MLT variations. The MLT variations of average

5.2 Field-aligned distribution of average ion mass

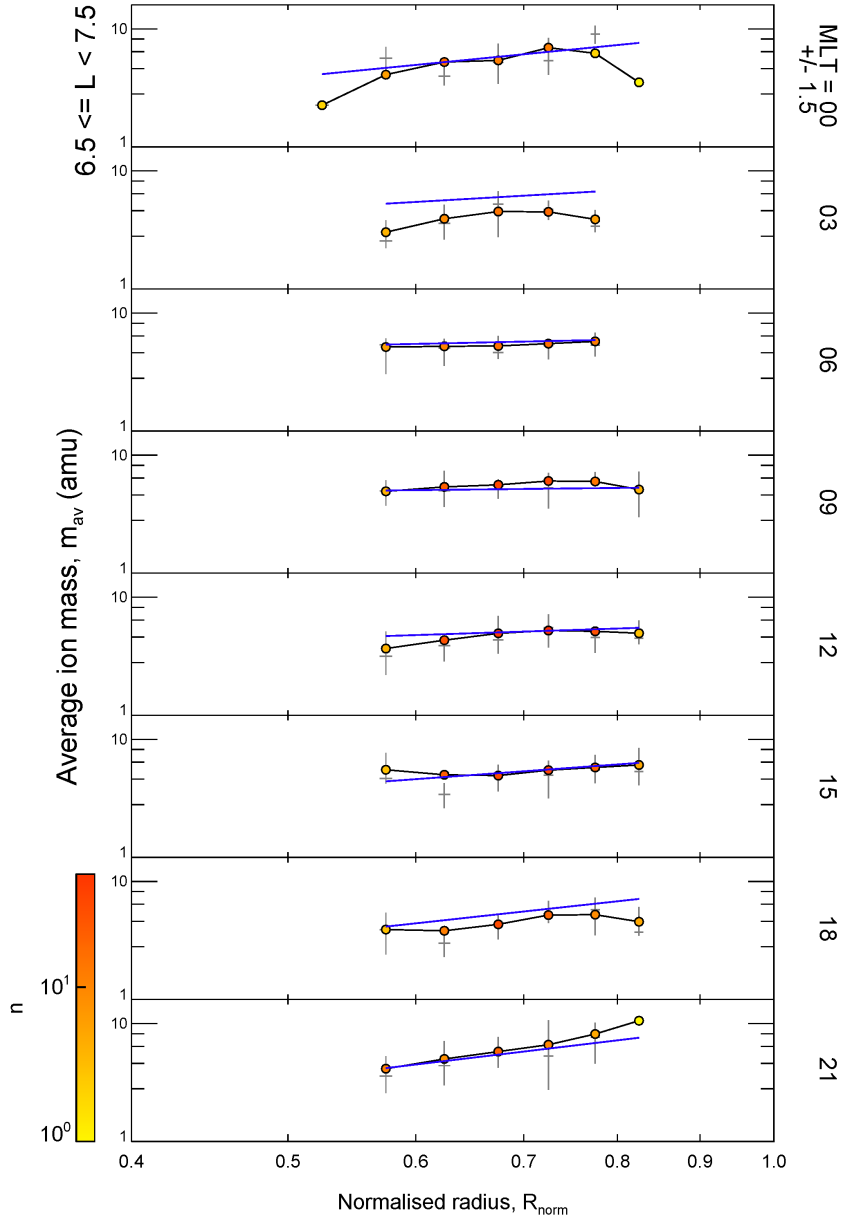


Figure 5.4: Average ion mass, m_{av} , (amu) plotted as a function of normalised radius, R_{norm} , for $6.5 \leq L < 7.5$ at 3 hour MLT intervals, where the colour of each point indicates the number of CODIF measurements, n , averaged in each bin. The upper and lower quartiles of the distribution of points averaged in each bin is shown by the grey line, intersected by a short horizontal line at the median value. The blue line represents the best fitting power law dependence.

ion mass are not fully described by the assumed circular variation, although the deviations do not appear large enough to significantly affect the overall results. It is highlighted here, that simple functional forms are chosen to concisely describe the key macroscopic features of the average ion mass distribution and the total electron density distribution, such that small scale features are not fully resolved by the resulting model.

Equation 5.3, representing the average ion mass distribution along magnetic field lines, is used to examine the azimuthally mapped spatial distribution in the X-Z SM plane. This is shown in Figure 5.2c. In addition, the spatial distribution in the T96 magnetic equatorial plane, predicted by the field-aligned average ion mass model, is also shown in Figure 5.3c. The spatial features shown in Figure 5.2c and Figure 5.3c are examined in section 5.4.

5.3 Mass density model

Using the empirically determined field-aligned distribution models for electron density (equation 5.2 discussed in section 5.1) and average ion mass (equation 5.3 discussed in section 5.2), a model describing the spatial distribution of the plasma mass density can be inferred. It is recognised that the average ion mass model represents the ion composition for a subset of the total population, although the analysis discussed in section 4 indicates the average ion mass is consistent with lower energies, and is an appropriate estimate for the total plasma population. This is done using equation 3.1, and, from the range of L shells where both WHISPER and CODIF data coverage exist, the model represents the region covered by $5.9 \leq L < 9.5$. Firstly, the combination of the electron density and average ion mass models to provide the mass density distribution in the X-Z SM plane is presented in Figure 5.2d and Figure 5.2e, where all values have been azimuthally mapped and averaged over MLT. As mentioned previously, both forms of the electron density model at low latitudes are considered for comparison. It can be seen from Figure 5.2e that the contribution of the localised electron density peak at the magnetic equatorial plane results in a clear enhancement of mass density compared to the case where this is neglected (Figure 5.2d), particularly at larger L values.

The corresponding mass density distribution in the T96 equatorial plane is shown in Figure 5.3d and Figure 5.3e, demonstrating dependences with L and MLT. As expected, the use of the Gaussian function to represent the electron density equatorial peak results in comparatively enhanced mass density values. It can also be noted here that the contribution

of the ion composition in this region is also an important factor in determining the mass density distribution, as shown by Figure 5.2 and Figure 5.3. The spatial distributions of mass density shown in Figure 5.2d,e and Figure 5.3d,e are discussed in further detail in section 5.4.

5.4 Discussion

The empirical field-aligned models for electron density and average ion mass, presented in section 5.1 and section 5.2, include dependences on both L and MLT. The features apparent in the models will now be discussed in further detail, providing information on the processes influencing the mass loading of field lines in the outer plasmasphere, plasmatrough and near-Earth plasma sheet regions of the closed magnetosphere.

5.4.1 Electron density

Cummings et al. [1969] first modelled the field-aligned electron density distribution as a power law form (equation 5.1), assuming a dipolar field and hydrogen plasma. The power law index, α , is an important parameter, as it determines the rate at which electron density increases towards the ionospheric ends of the field line. For a diffusive equilibrium model, where the hydrostatic approximation is assumed, the number density along a flux tube is proportional to the magnetic field strength, which implies a power law index within the range of 0.5-1.0 [Takahashi et al., 2004]. This diffusive equilibrium model is appropriate for high density regions, such as the plasmasphere, where the hydrostatic approximation is valid. Low-density regions, such as the plasmatrough, can be suitably represented by a collisionless plasma model, which corresponds to a power law index of approximately 4 [Takahashi et al., 2004]. Observational evidence of a power law dependence for the field-aligned electron density distribution in the plasmatrough shows that the variation has a form between that predicted by the diffusive equilibrium model and that predicted by the collisionless model [Goldstein et al., 2001; Denton et al., 2002, 2004]. For example, Denton et al. [2002] observed a power law index of 1.6-2.1 for the plasmatrough.

It can be seen from equation 5.2d that the power law index, α is modelled to include the observed dependences on both MLT and L . These variations are illustrated in Figure 5.5a, which shows the value of α as a function of MLT and L . Equation 5.2d and Figure 5.5a

show that α is assumed to have a linear dependence on L with a sinusoidal variation, where the amplitude is independent of L . However, the phase has an L dependence, such that the peak in α moves from approximately noon towards dawn with increasing L . Dependences of the power law index with MLT have also been reported from previous studies, such as Denton et al. [2002, 2015]. This result is consistent with the assumption that the power law form models the loading of electron density along field lines from the ionosphere. Due to electron outflows from photoionisation at the ionosphere by incident solar radiation, the electron density is at a maximum at the ionospheric ends of the field line, and decreases away from this region towards the equator. Therefore, the electron outflow will be greater on the dayside field lines, compared to the nightside field line footprints with reduced insolation, so the density at the footprints will be greater on the dayside. Consequently, this results in an increased magnitude of the gradient in electron density from the ends of the field line towards the magnetic equator for dayside field lines, so the observed α value should be greater for the dayside MLT sector. This is consistent with the determined value for the model α parameter.

Another feature of the α parameter is that the mean value of the variation is modelled to represent the observed increase of α with L , in agreement with previous findings [Denton et al., 2002]. This is expected to be due to an increase in flux tube volume with L , such that the total electron density across the field lines is reduced. Therefore, for increased L values, the gradient in electron density from the end of a field line towards the magnetic equatorial plane will be increased in magnitude (i.e. a greater decrease in electron density moving away from the ionosphere), resulting in an increased α value. This feature of the α dependence is demonstrated in Figure 5.5a, where it can be seen that the magnitude of α increases with L . For the region modelled, α is approximately 0.4-1.0, which is markedly lower compared to other results previously mentioned (e.g. Denton et al. [2002]).

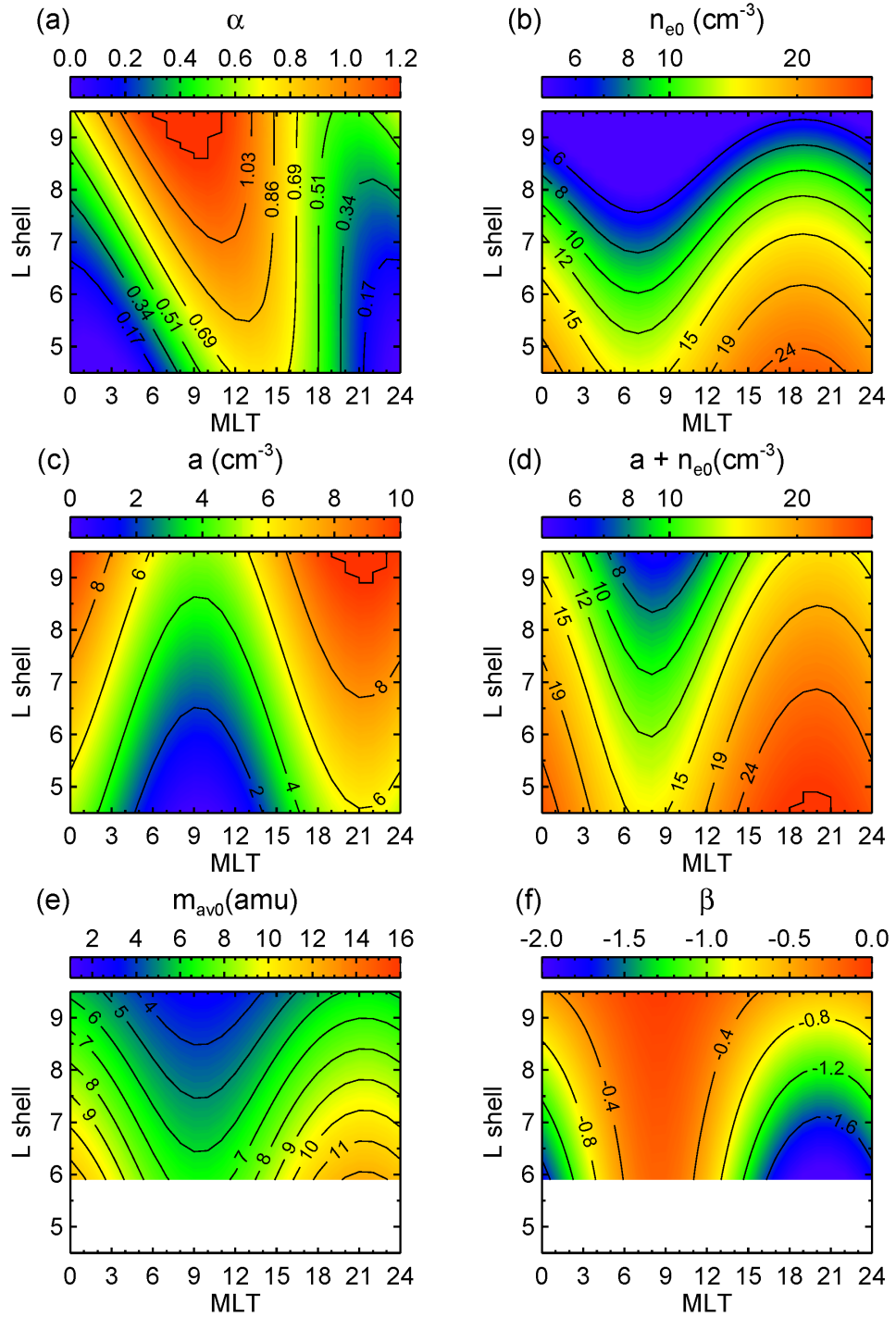


Figure 5.5: Contour plots showing the variation of the electron density and average ion mass model parameters (as defined in equations 5.2 and 5.3, respectively) with L value and MLT.

It is also assumed that n_{e0} has a sinusoidal MLT variation, with the amplitude of the variation dependent on L , as illustrated by Figure 5.5b showing n_{e0} as a function of MLT and L . In this case the phase of the sinusoidal variation was observed to be independent of L . The MLT dependence of n_{e0} is found to have a maximum at approximately 1800 MLT, which is expected to be due to the ‘plasmaspheric bulge’ [Carpenter, 1966; Chappell et al., 1970]. This MLT dependence results in generally increased electron densities towards the duskside (in agreement with Sheeley et al. [2001]), which is clearly identified in Figure 5.5b as well as Figure 5.3a. However, it should be noted that our model is based on the full dataset, averaged over all solar wind and geomagnetic conditions. This results in a blurring of the MLT variations presented in the equatorial distributions, as the ‘plasmaspheric bulge’ shape and location is highly variable and dependent on various processes [Carpenter, 1970; Chappell, 1972; Carpenter and Anderson, 1992; Gallagher et al., 2000; Lointier et al., 2013; Katus et al., 2015].

The amplitude of the MLT variation of n_{e0} decreases with L shell, shown by Figure 5.5b and equation 5.2c. As mentioned above, the MLT dependence is due to the plasmaspheric bulge. Therefore, at increased L shells, further away from the plasmasphere boundary, the amplitude of the MLT variation is reduced.

In addition, the mean value of n_{e0} , averaged over sinusoidal variations, is found to decrease with the L value of the field line (apparent in Figure 5.5b), as previously observed [Carpenter and Anderson, 1992; Goldstein et al., 2001; Sheeley et al., 2001; Denton et al., 2002, 2004; Berube et al., 2005; Ozhogin et al., 2012]. This could be a result of increased flux tube volume with increasing L value, such that the electron refilling from the ionosphere is distributed over a greater volume and results in generally decreased electron density values. The flux tube length is also increased so, due to the average lifetime of the electrons, the flux tube will take longer to be fully replenished by the ionospheric source, and on average will contain fewer electrons close to the magnetic equator. This is in agreement with Denton et al. [2004], where results indicated that the time associated with flux tube refilling is increased with increasing L shell.

However, as discussed in section 5.1, the power law model is not an appropriate description of the density close to the magnetic equator. Instead a Gaussian function, with an offset of n_{e0} , is chosen to represent the distribution in this region, where the peak height a varies with L and MLT. As with the previous parameters, the peak height relative to the background power law distribution, a , is assumed to have a sinusoidal variation, with a

constant phase, as shown by Figure 5.5c. It can be seen that a increases with L , such that the contribution of the Gaussian distribution at the magnetic equatorial plane increases for larger L . The MLT dependence of a is such that the equatorial enhancement is strongest towards nightside field lines. Figure 5.5d shows the dependences of the total peak height, $a + n_{e0}$, on L and MLT. The peak of this variation is located at approximately 1800MLT, due to the MLT dependence of the n_{e0} parameter (compare panels b and d in Figure 5.5). It can also be seen from Figure 5.5d that the average value of the total peak height, $a + n_{e0}$, decreases with increasing L value, where the decrease is dominated by the n_{e0} dependence previously discussed.

It is important to consider that the equatorial region at high L values, corresponding to observations of the equatorial peak, is only sampled in the later half of the time period covered by the WHISPER dataset. This is due to variations in the orbital configuration, as the perigee gradually moved to higher latitudes throughout the time period considered in this study. In order to assess whether the observed equatorial enhancement is a consequence of the temporal variation in coverage, the field line distribution of electron density is examined further in Figure 5.6. The first panel of Figure 5.6 presents an example of the equatorial enhancement, observed for data within $8.5 \leq L < 9.5$ and 06 ± 1.5 MLT, and this L - MLT bin was chosen as a suitable case for further analysis. The second panel of Figure 5.6 shows PEACE observations of the electron DNF (Differential Number Flux). The energy - pitch angle spectrogram shows an average of DNF observations obtained by the PEACE instrument onboard the C1 spacecraft for the full time interval (2001 - 2012), for positions corresponding to $R_{\text{norm}} > 0.8$ within the L - MLT bin. Therefore, the results describe electrons in the equatorial enhancement region. It can be seen that for a given energy bin, the DNF distribution is not isotropic, and values are peaked for pitch angles close to 90° . This is known as a pancake pitch angle distribution, and referring to the particle distribution function for a collisionless plasma, implies that the number density of particles increases for decreasing magnetic field strength. This implies the electron density approaches a maximum at the equatorial point of a field line, where the magnetic field is weakest, in agreement with the peaked field-aligned distribution observed in the WHISPER dataset. As the pitch angle distribution shown in the second panel of Figure 5.6 is based on complete energy - pitch angle spectrograms obtained by PEACE, the peaked field-aligned distribution of electron density can be attributed to an intrinsic property of the plasma, and therefore the result provides support for the validity of the observed equatorial enhancement.

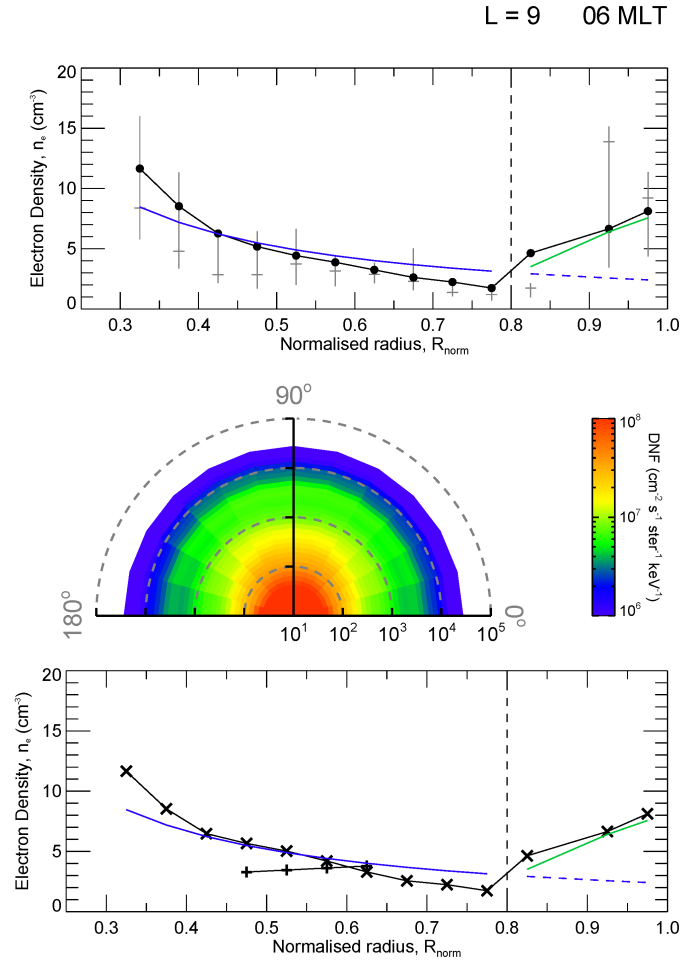


Figure 5.6: Data corresponding to $8.5 \leq L < 9.5$ and 06 ± 1.5 MLT. The first and third panels show the averaged WHISPER observations of electron density, n_e , plotted as a function of normalised radius, R_{norm} , using the same format as Figure 5.1. The first panel corresponds to averaged values over the full WHISPER dataset, reproduced for convenience from Figure 5.1. The third panel shows the field-aligned profile for data obtained before October 2004, represented by the plus symbols, and data obtained following October 2004, represented by the cross symbols. The second panel shows the average electron DNF (Differential Number Flux), $\text{cm}^{-2} \text{s}^{-1} \text{ster}^{-1} \text{keV}^{-1}$, observed by the PEACE instrument onboard the C1 spacecraft, in an energy - pitch angle spectrogram. The radial and angular position of a given bin corresponds to the energy and pitch angle, respectively.

The field-aligned distribution of electron density can be further tested by separating the dataset into two intervals, depending on the time of observation. The first interval covers the time period prior to October 2004, and the second interval covers observations obtained following October 2004. Therefore, the later time period corresponds to an interval during which the equatorial regions at high L values was sampled, unlike the earlier time period. The reason for selecting October 2004 as the boundary between the two time periods is that the first interval corresponds to the temporal coverage of the CODIF dataset. The third panel shows the variation in electron density along a field line for the two intervals, where the first interval is indicated by the plus symbols and the second interval corresponds to the cross symbols. It can be concluded that the two profiles exhibit similar values in the region where there is concurrent data coverage, and in addition, the peaked distribution remains for the second time interval. Therefore, the equatorial enhancement, apparent in the first panel of Figure 5.6, is not a consequence of averaging data from different times, and the analysis indicates that the peaked distribution close to the magnetic equator is a valid feature. It is also important to note that the same features were present in the other L - MLT bins as for the case shown in Figure 5.6. Furthermore, the variations in the prominence of an equatorial enhancement with MLT, and the initial decrease in electron density moving away from the magnetic equator forming a peaked distribution, would be unexplained assuming the peak was a false result due to temporal variations in spatial coverage.

A possible explanation for the observed electron density peak near the magnetic equator in this dataset could be the contribution of solar wind - magnetosphere coupling as an electron source (e.g. plasma entering the closed magnetosphere in the equatorial region, via the plasma sheet, through nightside reconnection processes). This peak is observed for the upper L values of the considered region, where the electron input by photoionisation at the ionosphere becomes comparable to the solar wind - magnetosphere coupling source. The density peak becomes increasingly prominent with increasing L value, towards the plasma sheet region, due to the decreased background power law densities (representing a decreasing ionospheric contribution). This explanation also supports the MLT dependence of the height of the peak, as the ionospheric electron source is correlated with solar illumination, and so the dominance of the plasma sheet source is expected to be apparent for nightside field lines, where the plasma sheet becomes an important plasma source. Flux tubes on the nightside are observed to have a decreased ionospheric plasma contribution due to reduced solar

illumination, and plasma entry into the closed magnetosphere by reconnection primarily occurs on the nightside, increasing the contribution of the plasma sheet population.

Previous studies examining the electron density distribution along field lines in the plasmatrough region have observed a power law dependence with a density minimum at the magnetic equator [Décréau et al., 1986; Olsen et al., 1987; Olsen, 1992; Denton et al., 2002, 2004], in contradiction with the results of this dataset. However, Gallagher et al. [2000] reported an increase in the sum of the H^+ and He^+ densities within approximately 20° of the magnetic equator, which, assuming quasi-neutrality, implies a corresponding maximum in electron density. This assumes that the contribution of other ion species in terms of number density is negligible, which is reasonable for the higher L shells (see Figure 5.3c). A possible localised peak was also examined by Denton et al. [2006], who concluded, from an analysis of CRRES plasma wave data, that there is no convincing evidence for a local peak in electron density near the magnetic equator. However, the results show insufficient data at low latitudes for large L shells. In addition, Denton et al. [2006] noted a small peak for $L=8-9$, but argues that at this range the magnetic latitude coverage is not complete, the magnetic field model is unreliable, and large statistical errors are present. In contrast to the evidence suggesting an electron density minimum, a case study conducted by Denton et al. [2009] observed a plasmatrough field line distribution of electron density with a localised peak at the magnetic equator, decreasing to a minimum value at a magnetic latitude of approximately 12.5° , then increasing steeply away from the magnetic equator. This appears to be the only conclusive observation of a peaked distribution in agreement with this empirical model.

As mentioned in section 5.1, the resulting model describes a generally representative description of the distribution of electron density along closed field lines. However, as shown by Figure 5.1, a localised enhancement in total electron density is observed in the data profile at R_{norm} for the 1200 MLT bin for $8.5 \leq L < 9.5$, which is not encapsulated by the relatively simple functional form of the model. The 1200 MLT bin of Figure 5.1 shows that the median values (horizontal grey lines) of the data within the R_{norm} bin are in close agreement with the model profile, and the relatively large upper quartile values compared to the lower quartile values (referring to extent of the grey vertical lines) suggest an asymmetric distribution of electron density values within the bins. It is postulated here that a possible cause of the enhanced mean values in the region is due to an additional plasma population located close the dayside magnetopause at $R_{\text{norm}} \sim 0.8$. This may be

due to the energetic gradient-curvature drifting plasma, as previous studies have shown that compression of the dayside magnetosphere results in a localised maximum in magnetic field strength at noon within $\sim 1 - 2 R_E$ of the magnetopause, which can cause bifurcation of drift shells in this region [Mead, 1964; Shabanskiy and Antonova, 1969; Öztürk and Wolf, 2007]. Although further analysis of this feature is outside the scope of this study, the process would be expected to enhance the density in this region.

5.4.2 Average ion mass

The resulting field-aligned variations for average ion mass, presented in section 5.2, models the distribution to be a maximum towards the magnetic equator, and decreasing off-equator. Although there are no models (to our knowledge) describing the field-aligned distribution of average ion mass in quantitative detail, previous studies of the plasma mass density distribution along magnetic field lines suggest that the average ion mass should be locally peaked at the magnetic equator [Takahashi et al., 2004; Denton et al., 2006], in agreement with our field-aligned distribution. Although, these studies assumed a power law form for the electron density, neglecting any number density contribution to an equatorial peak in mass density, the previously discussed case study by Denton et al. [2009] suggests that an equatorial enhancement in the average ion mass might still be expected in this region. The preferential concentration of heavy ions at the magnetic equatorial plane is expected due to the centrifugal force acting more effectively on heavier ions [Denton et al., 2006, 2009], assuming similar temperatures for the ion species, and was described by Lemaire and Gringauz [1998] in terms of an effective gravitational potential well at the magnetic equator.

A key source of heavy ions in the region covered by the dataset, determining the variations of the average ion mass field-aligned distribution with L and MLT, is the plasma sheet population. As mentioned in section 5.4.1, the observation of a localised enhancement in electron density close to the magnetic equatorial plane, most prominent at larger L values on the nightside, was inferred as the contribution of the plasma sheet population. This provides evidence of plasma sheet particles below $L = 9.5$, within the region considered for the average ion mass dependences. It is known that enhanced ionospheric outflows of heavy ions occur in the cusp and nightside auroral regions [Shelley et al., 1972, 1982; Lockwood et al., 1985a,b,c; Chappell et al., 1987; Chappell, 1988; Andre and Yau, 1997; Yau and Andre, 1997; Peterson et al., 2008; Liao et al., 2010]. This plasma, which has an

increased relative concentration of heavy ions, is convected into the plasma sheet and then Earthwards, populating the closed magnetosphere [Chappell et al., 1987; Chappell, 1988; Yau and Andre, 1997; Cully et al., 2003; Dandouras et al., 2005; Kistler et al., 2010; Liao et al., 2010; Mouikis et al., 2010; Haaland et al., 2012a; Haaland et al., 2013; Kronberg et al., 2012]. The plasma sheet particles enter the inner magnetosphere on the nightside region, acting to increase the average ion mass for nightside MLT sectors. Therefore, it is expected that the plasma sheet population contributes to the average ion mass distribution, and the convection of plasma sheet ions into the considered region acts to preferentially enhance the average ion mass in the nightside closed magnetosphere.

The field-aligned distribution of average ion mass is modelled using a power law form (equation 5.3a), with a negative power law index, β , to represent a maximum in average ion mass at the magnetic equatorial plane, as discussed in section 5.2. Figure 5.5e (showing m_{av0} as a function of MLT and L) illustrates the dependences of the empirically modelled equatorial average ion mass parameter, m_{av0} , as defined by equation 5.3b. The equatorial average ion mass parameter, m_{av0} , (equation 5.3b) combines a linear function in L with a sinusoidal component. Equation 5.3b shows that the mean value of m_{av0} , averaged over all MLT sectors, decreases linearly with L value. The decrease of the equatorial average ion mass with increased L values is illustrated by Figure 5.3c and Figure 5.5e. This feature of the average ion mass distribution is in agreement with previous observations [Mouikis et al., 2010; Ohtani et al., 2011; Maggiolo and Kistler, 2014], and is thought to result from the mass dispersion of outflowing ionospheric ions. The heavy ions in the closed magnetosphere predominantly originate from ionospheric outflows at high latitudes. As the plasma is convected into the plasma sheet, mass dispersion occurs, such that low energy O^+ ions enter the closed magnetosphere at lower L values compared to lighter ions [Lockwood et al., 1985a,c; Chappell, 1988; Andre and Yau, 1997; Yau and Andre, 1997; Haaland et al., 2009; Maggiolo and Kistler, 2014]. This results in an L gradient of O^+ concentration, such that the average ion mass increases towards lower L values. Therefore, the observed L shell dependence of m_{av0} (see Figure 5.5e) is a consequence of the plasma sheet properties.

Equation 5.3b includes a sinusoidal component for the model parameter m_{av0} , which describes variations of equatorial average ion mass with MLT. Figure 5.3c and Figure 5.5e clearly show that the MLT dependence is such that m_{av0} approaches a maximum at approximately 2200 MLT, so the equatorial average ion mass is higher in the evening sector compared to the morning sector. This feature can be attributed to plasma sheet convection

into the inner magnetosphere. Plasma sheet particles convect into the considered region from the nightside, such that the corresponding average ion mass enhancement will be predominantly localised to nightside MLT sectors. Furthermore, as plasma is convected Earthwards from the nightside plasma sheet, energetic ions drift westward in the inner magnetosphere forming the ring current population. During substorms and steady magnetospheric convection events, increased electron precipitation and ionospheric heating results in an increased O^+ concentration of upflowing ions that are injected into the inner magnetosphere [Lockwood et al., 1985a,b; Shelley et al., 1972, 1982; Kronberg et al., 2012; Chappell et al., 1987; Li et al., 2012; Yau and Andre, 1997; Andre and Yau, 1997; Chappell, 1988; Peterson et al., 2008; Liao et al., 2010]. Therefore, the occurrence of substorms and steady magnetospheric convection events act to preferentially enhance the average ion mass in the premidnight sector compared to the postmidnight sector, and contributes to the observed MLT asymmetry of m_{av0} . Furthermore, this process may be responsible for the overestimation of average ion mass by the model at 0300 MLT (see Figure 5.4), previously highlighted in section 5.2.

The function describing the model parameter m_{av0} (equation 5.3b) also includes an observed L shell dependence for the amplitude of the MLT variation. It can be seen from Figure 5.5e, that the amplitude of the MLT variation decreases with L value. As the MLT asymmetry arises as a consequence of heavy ions originating from the plasma sheet, the MLT dependence is expected to be most significant in the region of enhanced heavy ion concentration. This occurs towards the lower L values, as previously mentioned.

Equation 5.3c defines the power law index, β , which includes a linear function, describing the dependence of the power law index (averaged over all MLT sectors) on L , and a sinusoidal component representing the MLT variations. The dependences on L and MLT are illustrated in Figure 5.5f. It can be seen that β linearly becomes less negative for increased L values, moving away from the average ion mass enhancement. More negative β values at lower L values indicate a steep decrease in average ion mass values away from the magnetic equatorial plane, which is expected to be due to the large enhancement in heavy ions at the magnetic equator due to the effects of the centrifugal force acting on the ions. An additional consideration for decreasing β with increasing L value is the corresponding increase in the flux tube volume and length. Considering ionospheric ions with similar lifetimes, the increased flux tube volume and length means that fewer heavy ions will be concentrated at the magnetic equatorial plane, resulting in flatter field-aligned distributions.

The sinusoidal MLT variation of the power law index, β , shown by equation 5.3c, indicates that the most negative values are located at approximately 2100 MLT, which is clearly shown in Figure 5.5f. This is due to a decreased up-welling of ionospheric O^+ ions on the nightside field lines, as a result of reduced photoionisation from solar radiation [Young et al., 1982; Lennartsson, 1989; Stokholm et al., 1989]. This causes the values to decrease more rapidly from the equatorial enhancement towards the ionospheric ends for nightside field lines, thus causing a steeper field-aligned distribution, represented by a more negative power law index.

Furthermore, the plasma sheet contribution acts to increase the gradient along nightside field lines, relative to the dayside. As previously discussed, the average ion mass enhancement due to both this feature is greatest for nightside MLT sectors compared to the dayside (see Figure 5.3c and Figure 5.5e). The increase in the relative concentration of heavy ions in the equatorial region of flux tubes in the nightside region corresponds to an increased gradient in average ion mass along the field line. The result is a more negative power law index, β , value on nightside field lines than dayside field lines, where the average ion mass is reduced.

The discussion of the average ion mass distribution has mainly focused on the contribution of the plasma sheet population, which is convected into the closed magnetosphere. However, an additional source of heavy ions, which will influence the average ion mass of the plasma in this region, is the heavy ion torus. The heavy ion torus is a region of enhanced O^+ densities located just outside the plasmasphere, with no corresponding enhancement for the densities of light ions [Chappell, 1982; Horwitz et al., 1984, 1986; Roberts et al., 1987; Comfort et al., 1988; Berube et al., 2005; Darrouzet et al., 2009; Nosé et al., 2011, 2015]. The increased O^+ concentration will clearly correspond to an increase in the average ion mass of the plasma in the heavy ion torus. The expected L value position of the heavy ion torus typically ranges from $L \sim 4.5 - 6.5$ [Nosé et al., 2011], with decreasing heavy ion enhancements, indicating the outer edge of the torus, observed at $L \sim 6 - 8$ [Lee and Angelopoulos, 2014]. It has been proposed that the heavy ion torus is the result of the interaction between the plasmasphere and the ring current [Horwitz et al., 1986; Roberts et al., 1987; Nosé et al., 2011]. This interaction is expected to be most intense in the evening region, just beyond the duskside bulge region [Roberts et al., 1987; Burch et al., 2001]. As only the outer edge of the heavy ion torus coincides with the L range considered by this study, it is expected that the heavy ion torus contribution is minor in comparison with the

plasma sheet contribution for this region. Nevertheless, the heavy ion torus acts to increase the average ion mass at lower L values in the dusk MLT sectors, further intensifying the average ion mass enhancement shown in Figure 5.3c.

5.4.3 Mass Density

Previous studies have observed that the field-aligned dependence of mass density, reviewed in Chapter 2, is expected to have a relatively flat profile (small power law index) for lower L values [Takahashi et al., 2004; Denton et al., 2006; Maeda et al., 2009]; whereas at larger L values, previous studies find the distribution is locally peaked at the magnetic equatorial plane, decreases off-equator and then increases again towards the ionospheric ends of the field lines [Takahashi et al., 2004; Denton et al., 2006; Takahashi and Denton, 2007; Denton et al., 2009]. As presented in section 5.3, the electron density and average ion mass models are combined to determine the distribution of the mass density in the region of $5.9 \leq L < 9.5$. Therefore, this resulting mass density model includes contributions of the plasma number density and ion composition to the spatial variations. The distribution of mass density along field lines, and variations with L value and MLT are now discussed, considering the high latitude and equatorial regions separately.

By combining the electron density and average ion mass field-aligned empirical models (equation 5.2 and equation 5.3), the field-aligned profiles of mass density can be determined (see Figure 5.2 and Figure 5.3 for the resulting spatial distributions). Examples of the field-aligned profiles of mass density are shown in Figure 5.7. The left (right) panels show profiles for $L = 6$ ($L = 9$), and the upper (lower) panels show profiles for 1200 MLT (0000 MLT). A comparison of these panels illustrate the dependences of the mass density field-aligned distribution with MLT and L . The corresponding profiles predicted by the electron density and average ion mass models (defined by equation 5.2 and equation 5.3) are also included in Figure 5.7, which illustrate the contributions of the plasma number density and ion composition to the mass density field-aligned distribution.

The results indicate that the high latitude region ($R_{\text{norm}} \leq 0.8$) generally demonstrates a power law dependence of field-aligned mass density. For dayside field lines (see upper panels of Figure 5.7) the off-equator high-latitude region shows an increasing mass density towards the ionospheric ends of the field line, indicating a power law dependence with a positive power law index, similar to the electron density field-aligned distribution. As for

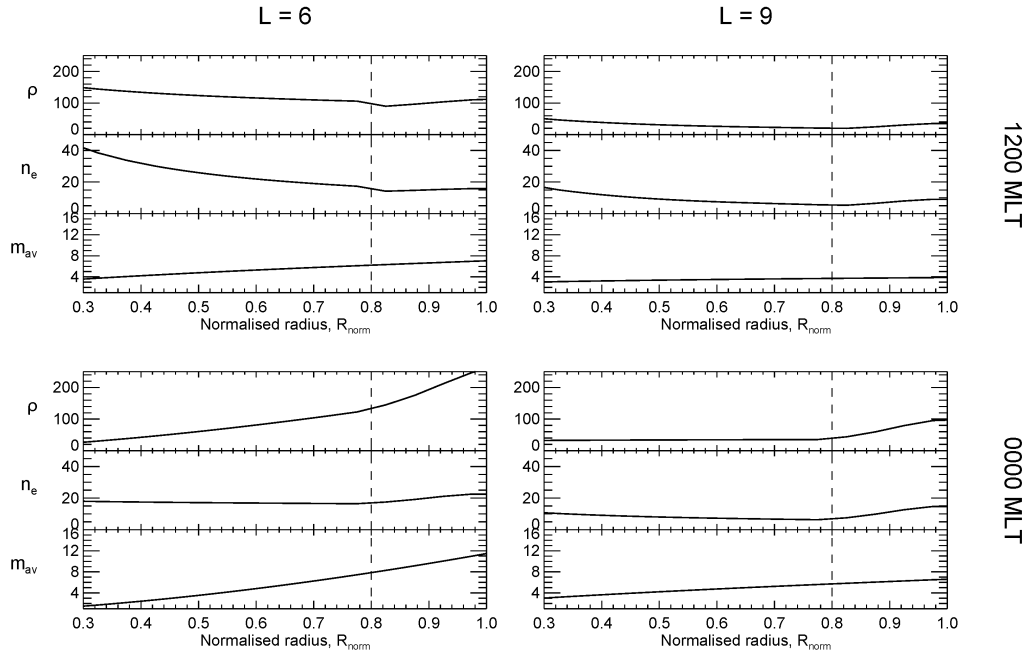


Figure 5.7: Panels showing the mass density, ρ , ($\text{amu}\cdot\text{cm}^{-3}$), electron density, n_e , (cm^{-3}) as defined by equation 5.2, and average ion mass, m_{av} (amu) as defined by equation 5.3, plotted as a function of normalised radius, R_{norm} . The left (right) panels show profiles for $L = 6$ ($L = 9$) and the upper (lower) panels show profiles for 1200 MLT (0000 MLT). The vertical dashed lines on each panel indicates the boundary between the power law and Gaussian dependences, corresponding to the electron density model.

the electron density, the power law index is shown to become more positive for larger L values on the dayside (note that a comparison of the upper panels of Figure 5.7 does not clearly illustrate this feature, as the power law index actually represents the logarithmic gradient and linear axes have been used here), corresponding to steeper mass density profiles in the high latitude region, in agreement with previous studies [Denton et al., 2006; Maeda et al., 2009]. The close correlation of the mass density field line distribution form with the observed electron density indicates that the mass density distribution at high latitudes along closed dayside field lines is dominated by the number density.

In contrast, the high latitude region of the nightside field lines exhibits differing features. Referring to the lower panels of Figure 5.7, the field line profile at lower L values show the mass density decreasing towards the ends of the field line, represented by a negative power

law index similarly to the average ion mass distribution. Moving to larger L values, the profile becomes flatter, as the power law index increases and becomes positive for this region. This results in a distribution where the mass density increases slightly towards the ionospheric ends of the field lines, in agreement with the observed electron density field line distribution. Therefore, it can be inferred that the nightside mass density distribution at high latitudes is dominated by the ion composition at lower L values, and becomes increasingly dominated by the number density at larger L values. As for the dayside field lines, the increase in the power law index is roughly consistent with previous studies [Denton et al., 2006; Maeda et al., 2009], although these studies constrain the power law index to be positive. This approach considers negative power law index values to account for the effects of the centrifugal force on heavy ions.

The consideration of the profiles shown in Figure 5.7 indicate that the number density is generally the dominant factor in determining the high latitude field-aligned distribution of mass density. An exception to this is at lower L values on nightside MLT sectors (see lower left panel of Figure 5.7), where the ion composition appears to be the dominant contribution to the mass density. This is expected to correspond to the presence of the average ion mass enhancement at the lower L values, and referring to Figure 5.5e and Figure 5.5f, the average ion mass field line profile is steepest (most negative power law index) with a peak in the equatorial average ion mass at approximately 2130 MLT. Therefore, in the nightside region at lower L values, the plasma is relatively O^+ rich and the ion composition has a significant contribution to the mass density. Moving away from this average ion mass enhancement, the relative concentration of O^+ ions decreases and the field line profiles become flatter, resulting in a decreased contribution of the ion composition.

The resulting mass density field-aligned distribution also presents some notable features for the low latitude equatorial region (at $R_{\text{norm}} > 0.8$), illustrated in the example profiles shown in Figure 5.7. The combination of the localised electron density peak with the average ion mass, which approaches a maximum towards the magnetic equatorial plane, provides a peaked mass density distribution at the equator, as expected. The low latitude peak, in comparison to the expected low latitude distribution extrapolated from the high latitude region, is observed to become increasingly prominent at larger L values, in agreement with previous findings [Takahashi et al., 2004; Denton et al., 2006; Takahashi and Denton, 2007; Denton et al., 2009]. This can be attributed to the contribution of the plasma number density, as the localised electron density peak height (relative to the background power law

distribution) increases with L , which is illustrated by a comparison of the predicted mass density distributions shown in Figure 5.2. It can be seen that the mass density distribution corresponding to the use of the Gaussian function at low latitudes, as opposed to the extrapolated power law dependence, results in noticeably increased values near the magnetic equatorial plane at larger L values. This contradicts previous studies [Takahashi et al., 2004; Denton et al., 2006; Takahashi and Denton, 2007], where the equatorial mass density peak has predominantly been associated with a low latitude enhancement of heavy ions, under the assumption that the electron density follows a power law dependence. Whereas the results of this study appear to indicate that a localised peak in the number density is also a significant factor to the mass density in this region.

The variations of mass density in the equatorial plane are also worthwhile discussing. Figure 5.3 illustrates the L dependence of the inferred mass density model, with high mass density plasma present at low L values, due to the average ion mass enhancement and high number density plasma. The mass density decreases with L value, which is attributed to decreasing plasma number density as a result of larger flux tube volume and length. The composition of the plasma also becomes less O^+ dominated, resulting in decreasing mass density. In general, the decrease in mass density with L is in agreement with previous models [Takahashi et al., 2004; Denton et al., 2006; Maeda et al., 2009; Min et al., 2013; Takahashi et al., 2014].

Figure 5.3 demonstrates the MLT dependence of the mass density model. It can be seen that the equatorial mass density approaches a maximum in the evening sector. By considering the electron density enhancement at approximately 1900 MLT, due to the duskside plasmaspheric bulge region, and the average ion mass enhancement due to the plasma sheet population present for nightside field lines, it is clear that the mass density enhancement in this region is due to a combination of both features. Therefore, the variation in mass density with MLT is due to contributions from both the number density and ion composition.

Overall, an empirical model describing the spatial distribution of mass density along closed field lines for $5.9 \leq L < 9.5$ has been obtained, including dependences on L and MLT. The resulting model indicates key similarities and differences with previous models [Gallagher et al., 2000; Takahashi et al., 2004; Berube et al., 2005; Denton et al., 2006; Takahashi and Denton, 2007; Maeda et al., 2009; Takahashi et al., 2014]. Due to the relatively large dataset employed and the choice of methodology, the mass density model provides a more valid and representative description of the total mass density distribution compared

to previous models. In particular, a more accurate model of number density variations, accounting for the localised enhancement close to the magnetic equator, and the inclusion of the ion composition contribution to the mass density, provide notable improvements over previous models.

Chapter 6

Geomagnetic Variations

As presented in Chapter 5, empirical models describing the spatial distribution of electron density and average ion mass in the closed magnetosphere were determined from WHISPER and CODIF observations. The models were combined to infer a corresponding model for the total plasma mass density, which covered all MLT sectors for L values in the range of $5.9 \leq L < 9.5$. As the models were based on an average of the full WHISPER and CODIF datasets, the resulting distributions represent the average conditions of the magnetosphere. In this chapter, the models are developed to understand how the spatial distributions of electron density, average ion mass, and total mass density vary with geomagnetic activity. Using a similar approach as used in Chapter 5, the field-aligned distributions of electron density and average ion mass are modelled, accounting for variations with geomagnetic activity, as well as L and MLT. In the same way as before, the models are combined, and a model describing the spatial distribution of plasma mass density is obtained, which includes dependences with geomagnetic activity. This chapter is concluded with a discussion on how the models vary with geomagnetic activity, and the information they provide on the associated magnetospheric processes.

6.1 Binning data for Dst index

The electron density and average ion mass datasets are used to examine the distribution along magnetic field lines. Whereas the previous analysis (Chapter 5) compared data at different MLT and L values, this study also compares data at different levels of geomagnetic

activity. To represent the level of geomagnetic activity, the hourly averaged Dst index is chosen, and the Dst index value is determined for each position bin. It is known that geomagnetic storms are characterised by a significant reduction in the horizontal component of the global magnetic field relative to the average level [Chapman, 1918], as a result of an enhanced ring current during the main phase [Dessler and Parker, 1959; Sckopke, 1966]. The Dst index represents the magnitude of these global variations of the horizontal field close to the magnetic equator. Therefore, Dst index is an appropriate proxy for the level of geomagnetic activity in the magnetosphere.

For each dataset (WHISPER observations of electron density and CODIF observations of average ion mass), the variations along magnetic field lines are modelled. The same functional forms as used in the average model, previously discussed in Chapter 5, are used to describe the field aligned variations. In order to quantify the distribution, the least-squares hierarchical fitting technique [Clark and Gelfand, 2006; Tabachnick and Fidell, 2006] is employed. This approach fits to the multiple levels (L value, MLT, and Dst index) that the function parameter is expected to vary with, representing variations in the dataset as a whole.

The initial step in analysing the field-aligned variations of each dataset is to bin the data for the normalised radial distance along the magnetic field line, R_{norm} , which is the radial distance at which the measurement was obtained, R (R_E), divided by the L value of the field line. The T96 magnetic field model is used here to determine the field line corresponding to the measurement, and a bin width of 0.05 is used for the normalised radius. The data is also binned for each level included in the multi-level fitting technique. The L value bin width used is 1., and the MLT bin width used is 3 hours. The distribution of data with respect to Dst index needs to be considered when choosing a bin width for the Dst index level. Figure 6.1 shows the frequency, representing the number of measurements, for a range of Dst index values. It is identified that the majority of data lies between -100 to 10 nT, where this range corresponds to moderately disturbed to typical quiet time conditions. Therefore, only data within this range was selected, avoiding extreme values distorting the variations. The data is then divided into 6 bins for Dst index, as indicated by the colour coding in Figure 6.1. It is noted that the bin widths vary with Dst index, such that bins at lower Dst index values have a increased bin width. This was done to ensure that each bin contained a sufficient number of data points for the fits to remain statistically reliable, as

it is apparent in Figure 6.1 that the frequency is significantly decreased at largely negative Dst index values.

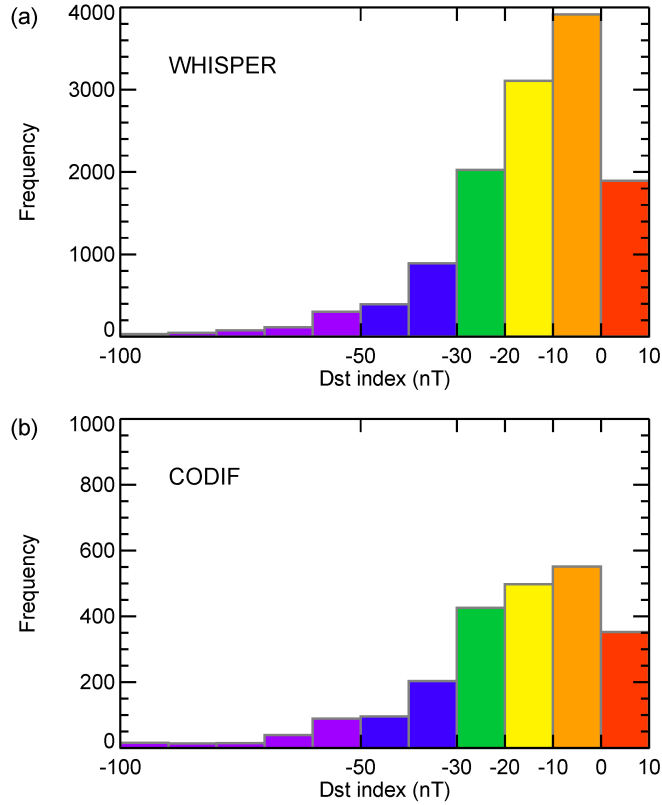


Figure 6.1: Histograms showing the distribution of the number of data points with Dst index (nT) for (a) electron density data from WHISPER and (b) average ion mass data from CODIF. The differing colours of the bars indicate the division of the datasets into 6 bins for Dst index.

6.2 Field-aligned distribution of electron density

By plotting the electron density, n_e , as a function of normalised radius, R_{norm} the field-aligned dependence is illustrated. An example plot is shown in Figure 6.2, for $5.5 \leq L < 6.5$ and 0900 MLT, where the points indicate the average electron density value in the normalised radius, R_{norm} , bin. The profiles have been smoothed using a boxcar function, with a width of 3 bins. Each panel corresponds to a different bin of Dst index, referring to Figure 6.1. As previously discussed in Chapter 5, it has been shown that the field line dependence of electron

6.2 Field-aligned distribution of electron density

density can be separated into two regions, where the boundary between these dependences is defined at $R_{\text{norm}} = 0.8$ (indicated by the vertical grey dashed line in Figure 6.2). At high latitudes ($R_{\text{norm}} \leq 0.8$) the electron density generally increases towards the ends of the field line, corresponding to a power law distribution. At low latitudes ($R_{\text{norm}} > 0.8$), a peak in electron density close to the magnetic equatorial plane is often observed, which is represented by a Gaussian distribution. Using the same functional forms as the average model, a least-squares fitting method, weighted by the number of points in each bin, is used to determine the best fit function parameters for each field-aligned profile. The function parameters are the electron density at the magnetic equatorial point on the field line, n_{e0} , the power law index, α , and the peak height above n_{e0} , a . The hierarchical approach includes dependences on L , MLT, and Dst index in the best fit parameters, providing the required functions. The power law model is given by equation 6.1a, and the Gaussian model is given by equation 6.1b. The model parameters (n_{e0} , α , and a) are defined by equations 6.1c, 6.1d and 6.1e. The field line distribution predicted by the model is shown by the overplotted solid coloured lines in Figure 6.2. The empirical electron density model describes variations in the L range of $4.5 \leq L < 9.5$, and covers all MLT.

$$n_e = n_{e0} R_{\text{norm}}^{-\alpha} \quad R_{\text{norm}} \leq 0.8 \quad (6.1a)$$

$$= a \exp \left[-\frac{1}{2} \left(\frac{R_{\text{norm}} - 1.0}{0.1} \right)^2 \right] + n_{e0} \quad R_{\text{norm}} > 0.8 \quad (6.1b)$$

$$n_{e0} = 10^{1.60+0.00667D_{st}} (1 - 0.0952L) + 3.68 \cos(15\text{MLT} + 83.0 - 1.18D_{st}) \quad (6.1c)$$

$$\alpha = 0.211 + 0.0616L + 0.423 \cos(15\text{MLT} + 223.) \quad (6.1d)$$

$$a = 10^{0.785+0.00681D_{st}} + 3.47 \cos(15\text{MLT} + 324.) \quad (6.1e)$$

Consistent with the average model, the functional form used to describe the model parameters include a sinusoidal term, where the phase and amplitude represent MLT dependences, combined with an offset term, defining the mean value of a parameter across all MLT. The amplitude, phase, and offset parameters are all allowed to be functions of L value and Dst index. The dependences of the resulting electron density model (equation 6.1) will be discussed in detail in section 6.6. It is also noted that when fitting for the model parameters, if no dependence on L or Dst index was clearly observed in the data, the dependence was removed from the relevant functional form.

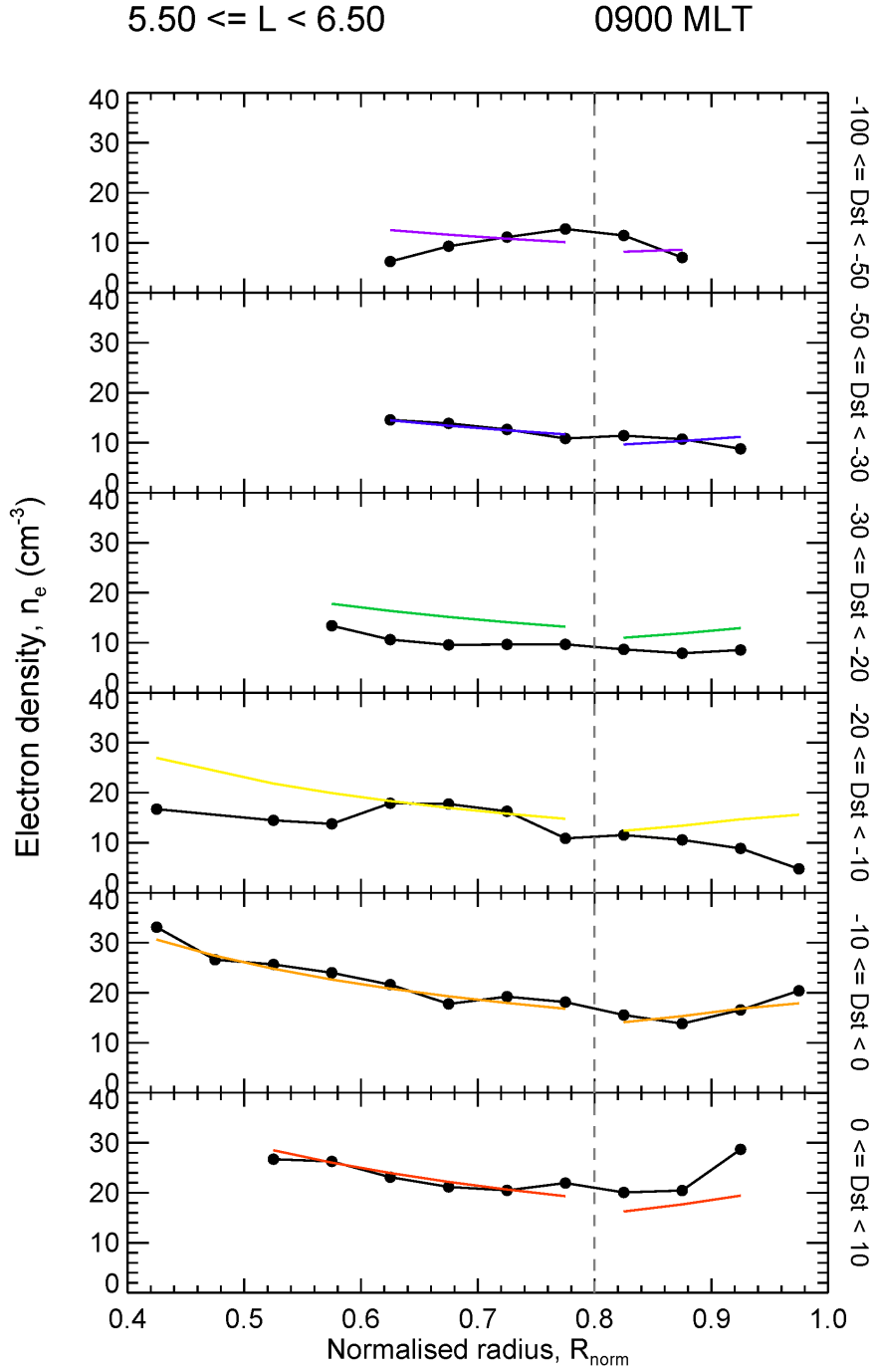


Figure 6.2: Electron density, n_e , (cm^{-3}) plotted as a function of normalised radius, R_{norm} , for $5.5 \leq L < 6.5$ and 0900 MLT. The panels display data for each Dst index (nT) bin (as defined in Figure 6.1). The vertical dashed line indicates the boundary between the power law and Gaussian dependences, and the overplotted coloured lines represent the best fitting functions to the overall dataset.

The spatial distribution predicted by the resulting model is shown in the left panels of Figure 6.3, where values are mapped azimuthally to the X-Z plane and averaged separately over dayside and nightside MLT sectors. The SM (Solar Magnetic) coordinate system is used here, where the geomagnetic dipole axis is aligned with the Z axis, in order to clearly illustrate variations with L value and magnetic latitude. The panels show the distribution at four values of Dst index, chosen to indicate variations between disturbed and quiet conditions. In addition, the left panels of Figure 6.4 show the distribution of electron density predicted by the model (equation 6.1) in the T96 magnetic equatorial plane. Each panel corresponds to a different value of the Dst index, using the same Dst index values as in Figure 6.3. Figure 6.3 and Figure 6.4 demonstrate some clear dependences of the electron density spatial distribution on Dst index, which are examined further in section 6.6.

6.3 Field-aligned distribution of average ion mass

Using the same method as for the electron density model discussed above (section 6.2), the field-aligned distribution of average ion mass is now examined. Figure 6.5 shows an example plot for $6.5 \leq L < 7.5$ and 1200 MLT, where each panel shows the average ion mass, m_{av} , as a function of normalised radius, R_{norm} (smoothed using a boxcar function of width 3), for each Dst index bin. Note that, unlike the electron density plots in Figure 6.2, logarithmic scales are used for both axes, which linearises power law dependences. As discussed in Chapter 5, the field line dependence of average ion mass can be represented by a power law function with a negative power law index, describing the average ion mass maximising towards the magnetic equator and decreasing off-equator. A function of this form is least-squares fitted to the data, with the fitting weighted by the number of data points in each bin. Using the hierarchical fitting approach, the function parameters (the average ion mass at the magnetic equatorial point of the field line, m_{av0} , and the power law index, β) are obtained, with dependences on L value, MLT and Dst index included. The resulting model for the field-aligned distribution of average ion mass is given by equation 6.2a, with the function parameters defined by equations 6.2b and 6.2c. The model field-aligned variations are illustrated by the overplotted solid coloured lines in Figure 6.5. The model covers all MLT values in the region of $5.9 \leq L < 9.5$.

6.3 Field-aligned distribution of average ion mass

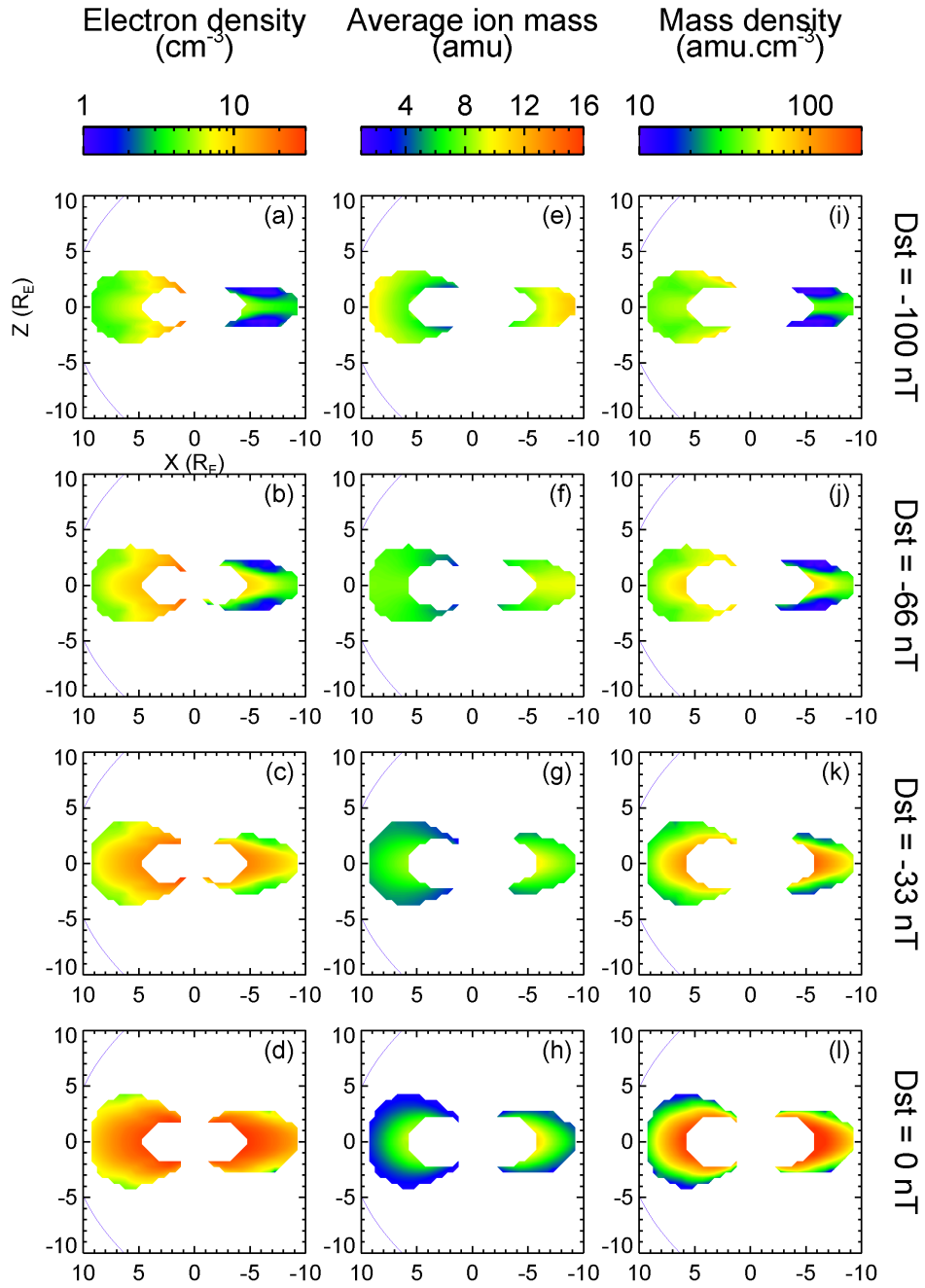


Figure 6.3: Spatial distribution in the X-Z SM plane using the field-aligned models for (a-d) electron density and (e-h) average ion mass, defined by equation 6.1 and equation 6.2, respectively. The models are combined to infer the corresponding total mass density distributions (i-l). Each vertical panel shows the distribution for a different value of the Dst index (nT). The T96 magnetic field model used corresponds to spring equinox, with a solar wind dynamic pressure of 2 nPa. The expected locations of the magnetopause under these conditions are included as the blue solid lines for reference.

6.3 Field-aligned distribution of average ion mass

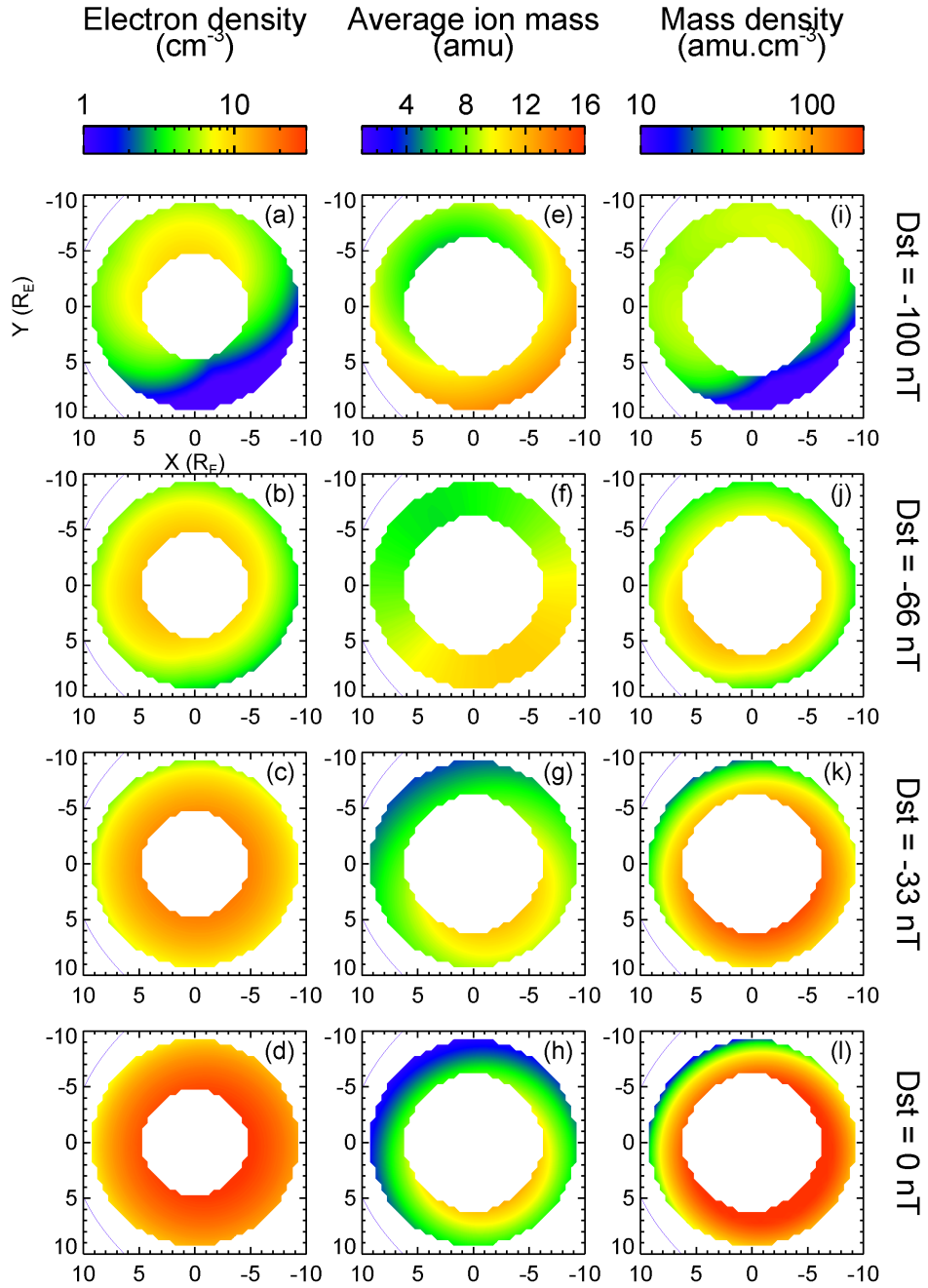


Figure 6.4: Same format as Figure 6.3, for the spatial distribution in the T96 magnetic equatorial plane.

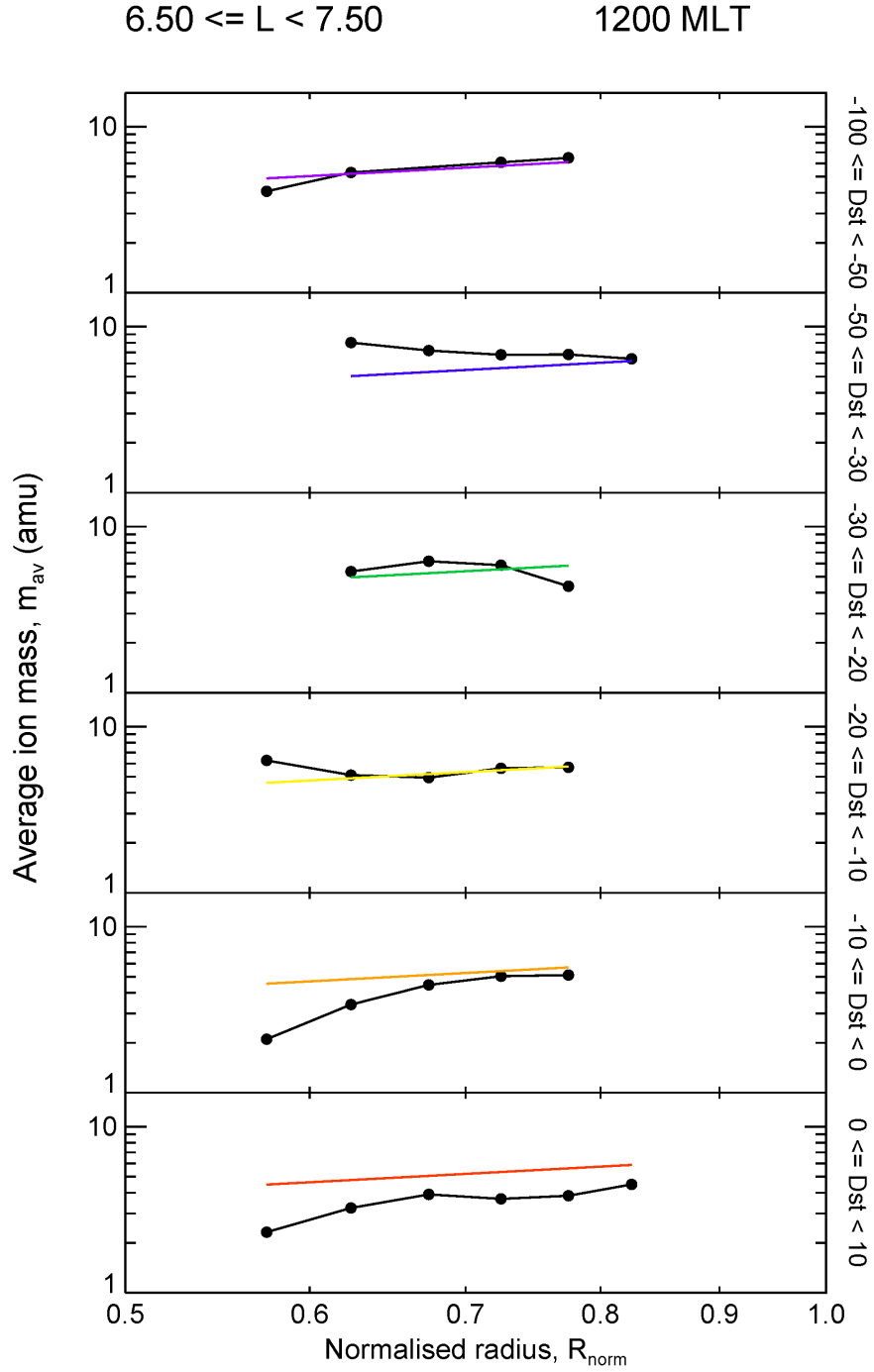


Figure 6.5: Average ion mass, m_{av} , (amu) plotted as a function of normalised radius, R_{norm} , for $6.5 \leq L < 7.5$ and 0900 MLT. The panels display data for each Dst index (nT) bin (as defined in Figure 6.1). The overplotted coloured lines represent the best fitting functions to the overall dataset.

$$m_{\text{av}} = m_{\text{av}0} R_{\text{norm}}^{-\beta} \quad (6.2a)$$

$$m_{\text{av}0} = 19.4 + 0.164D_{st} - (1.62 + 0.0247D_{st})L + 2.52 \cos(15\text{MLT} + 61.) \quad (6.2b)$$

$$\beta = -1.91 + 0.165L + (0.851 + 0.00559D_{st}) \cos(15\text{MLT} + 270.) \quad (6.2c)$$

This empirical model for the field-aligned distribution of the average ion mass is used to determine the spatial distribution in the X-Z SM plane, as shown in the middle panels of Figure 6.3. As for the electron density distribution, the values are mapped to the plane, separately averaging over the dayside and nightside MLT sectors, and each panel shows the distribution at a different value of the Dst index. The corresponding distributions of average ion mass in the T96 magnetic equatorial plane are shown in the middle panels of Figure 6.4. The features apparent in Figure 6.3 and Figure 6.4 are discussed in section 6.6.

6.3.1 Cusp enhancement

It is known that during disturbed conditions, heavy ion outflows occur at high latitudes [Shelley et al., 1972, 1982; Lockwood et al., 1985a,b,c; Chappell et al., 1987; Chappell, 1988; Andre and Yau, 1997; Yau and Andre, 1997; Peterson et al., 2008; Liao et al., 2010]. Figure 6.6 and Figure 6.7 show the average ion mass distribution described by the model (equation 6.2), mapped close to the field line footprints in the ionosphere. The values are plotted for a range of 3 hour MLT intervals, in the plane normal to the magnetic equatorial plane. Figure 6.6 shows the model average ion mass values for a Dst index of 0 nT, and Figure 6.7 represents the corresponding values for a Dst index equal to -100 nT. It has been assumed that the field-aligned dependence observed in the CODIF dataset can be extrapolated along the whole field line. Although this cannot be shown to be a reasonable assumption, the purpose of the distributions shown in Figure 6.6 and Figure 6.7 is to provide estimates on the relative magnitudes of the heavy ion compositions, not to represent the true values of average ion mass in the region. There are clear differences between the distributions of average ion mass in Figure 6.6 and Figure 6.7, which will be assessed in section 6.6.

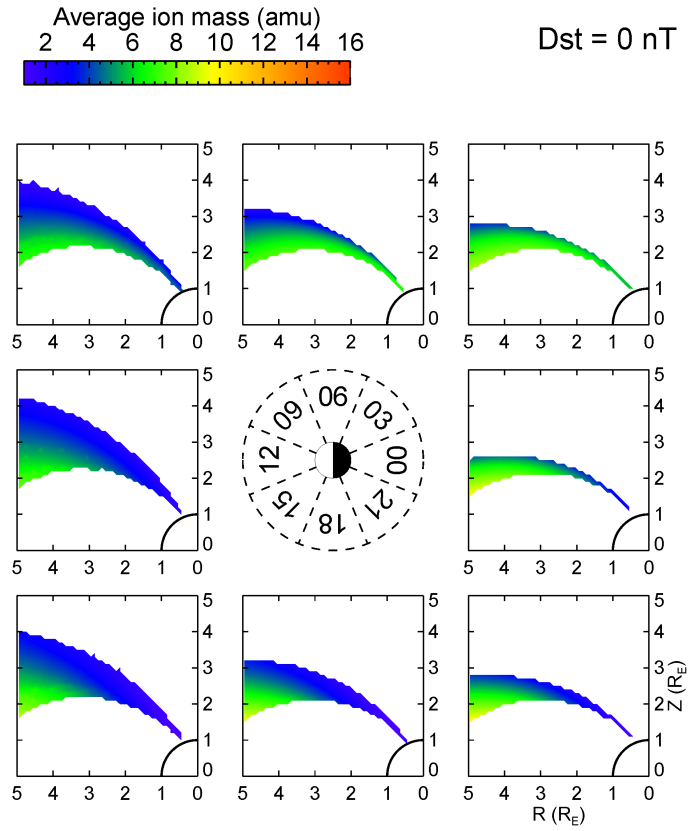


Figure 6.6: Each panel shows the spatial distribution of average ion mass (amu) for a different MLT sector using the field-aligned model (equation 6.2) for $Dst = 0$ nT. The central diagram indicates the MLT sectors of the surrounding panels. The x axes correspond to the radial distance in the magnetic equatorial plane, R (R_E), and the z axes correspond to the Z SM coordinate (R_E). The unfilled quarter circles represent the Earth.

6.4 Mass density model with Dst index dependence

Using the same approach as for the average model (Chapter 5), the empirical models for the field line distribution of electron density (equation 6.1 presented in section 6.2) and average ion mass (equation 6.2 presented in section 6.3), are combined, using equation 3.1, to infer the corresponding model for the total plasma mass density including dependences in Dst index. Due to the spatial coverage of the WHISPER and CIS datasets, this mass density model represents plasma in the region covered by $5.9 \leq L < 9.5$, for all MLT.

This resulting model is used to examine variations in the X-Z SM plane for a range of Dst

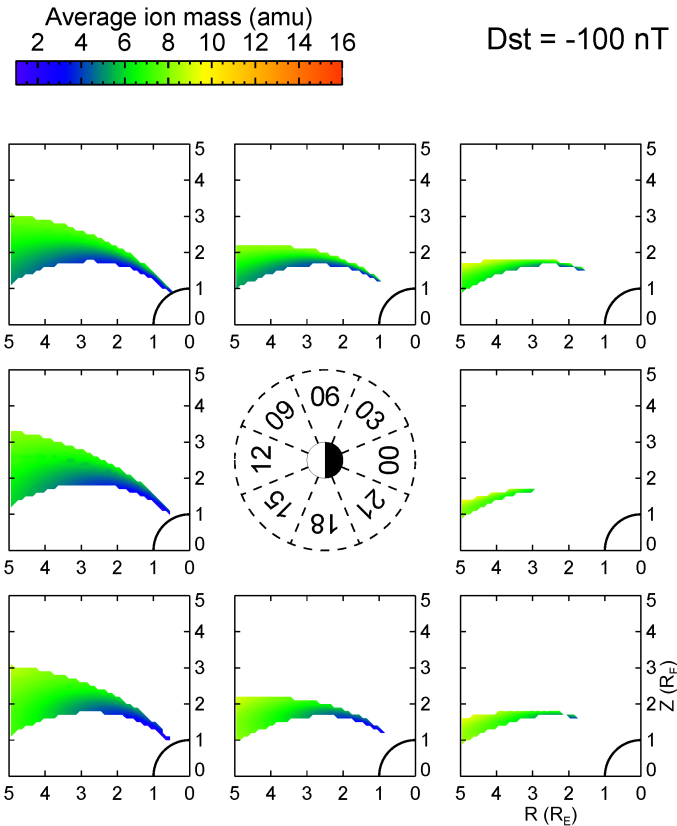


Figure 6.7: Same format as Figure 6.6, but for Dst = -100 nT

index values, as shown in the right panels of Figure 6.3, where values have been azimuthally mapped and averaged over MLT. In addition, the corresponding spatial distribution in the T96 magnetic equatorial plane for each of these values of Dst index is shown in the right panels of Figure 6.4. The dependences of mass density on Dst index, illustrated by the distributions in Figures 6.3 and 6.4, are discussed in the following section.

6.5 Dependences on Kp index

Although the mass density model presented in section 6.4 is parameterised by Dst index, many other studies use Kp index as a proxy for the level of geomagnetic activity [Menk et al., 1999; Gallagher et al., 2000; Takahashi et al., 2002; Denton et al., 2006; Takahashi et al., 2006, 2010, 2014]. The Kp index is determined from the mean value of geomagnetic

field disturbances observed at 13 subauroral stations [Bartels et al., 1939; Thomsen, 2004]. The disturbances relate to large-scale ring current variations, due to the contribution of low latitude stations, and variations in auroral current systems, observed by stations located at higher latitudes. Therefore, the Kp index provides a global measure of magnetospheric disturbances due to a larger range of current systems. To allow for comparisons of the mass density model for different parametrisations, the same approach was used to assess variations in the data with Kp index.

Figure 6.8 shows the distribution of WHISPER electron density data (panel (a)) and CODIF average ion mass data (panel (b)) with Kp index. The datasets were binned for Kp index, as indicated by the coloured bars in Figure 6.8, where data with a Kp index greater than 4 were not included due to the low number of data points available. The same hierarchical modelling technique, as detailed in section 6.2 and section 6.3, was applied to the field-aligned distributions of each dataset, except variations with Kp index were modelled, as opposed to variations with Dst index.

6.5.1 Field-aligned distribution of electron density

The resulting model for the field-aligned distribution of electron density, n_e , is shown in equation 6.3. The electron density model covers all MLT sectors in the region of $4.5 \leq L < 9.5$. The same functional form as before was used (equation 6.1), where a power law distribution represents the higher latitude region of field lines (equation 6.3a), and a Gaussian function is used to describe the equatorial region (6.3b). The model parameters for the electron density model (equatorial electron density, n_{e0} , power law index, α , and relative peak height, a) were quantified to include dependences on L , MLT, and Kp index, and are defined by equation 6.3c, equation 6.3d, and equation 6.3e.

$$n_e = n_{e0} R_{\text{norm}}^{-\alpha} \quad R_{\text{norm}} \leq 0.8 \quad (6.3a)$$

$$= a \exp \left[-\frac{1}{2} \left(\frac{R_{\text{norm}} - 1.0}{0.1} \right)^2 \right] + n_{e0} \quad R_{\text{norm}} > 0.8 \quad (6.3b)$$

$$n_{e0} = 48.5 - 7.43K_p - (4.66 - 0.695K_p)L + (4.99 - 0.394K_p) \cos(15\text{MLT} + 52.5 + 22.K_p) \quad (6.3c)$$

$$\alpha = 0.00352 + 0.101L + 0.395 \cos(15\text{MLT} + 216.) \quad (6.3d)$$

$$a = 7.04 - 1.32K_p + 3.14 \cos(15\text{MLT} + 5.) \quad (6.3e)$$

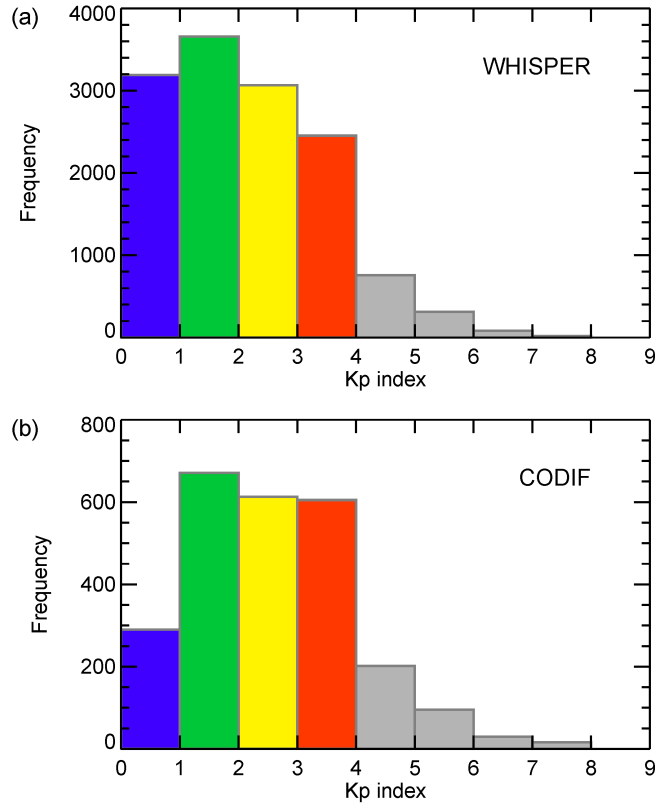


Figure 6.8: Histograms showing the distribution of the number of data points with Kp index for (a) electron density data from WHISPER and (b) average ion mass data from CODIF. The differing colours of the bars indicate the division of the datasets into 4 bins for Kp index.

Using equation 6.3, the spatial distribution of electron density is plotted in the left panels of Figure 6.9, where values are mapped azimuthally to the X-Z SM plane, averaging separately over dayside and nightside MLT sectors. Each vertical panel shows the electron density distribution at a different Kp index value, as labelled, to illustrate variations in the spatial distribution with Kp index. In addition, the electron density spatial distribution, as defined by equation 6.3, mapped to the T96 magnetic equatorial plane, is shown in the left panels of Figure 6.10. Both Figure 6.9 and Figure 6.10 show notable variations in the electron density spatial distribution with Kp index, which are discussed in section 6.6.

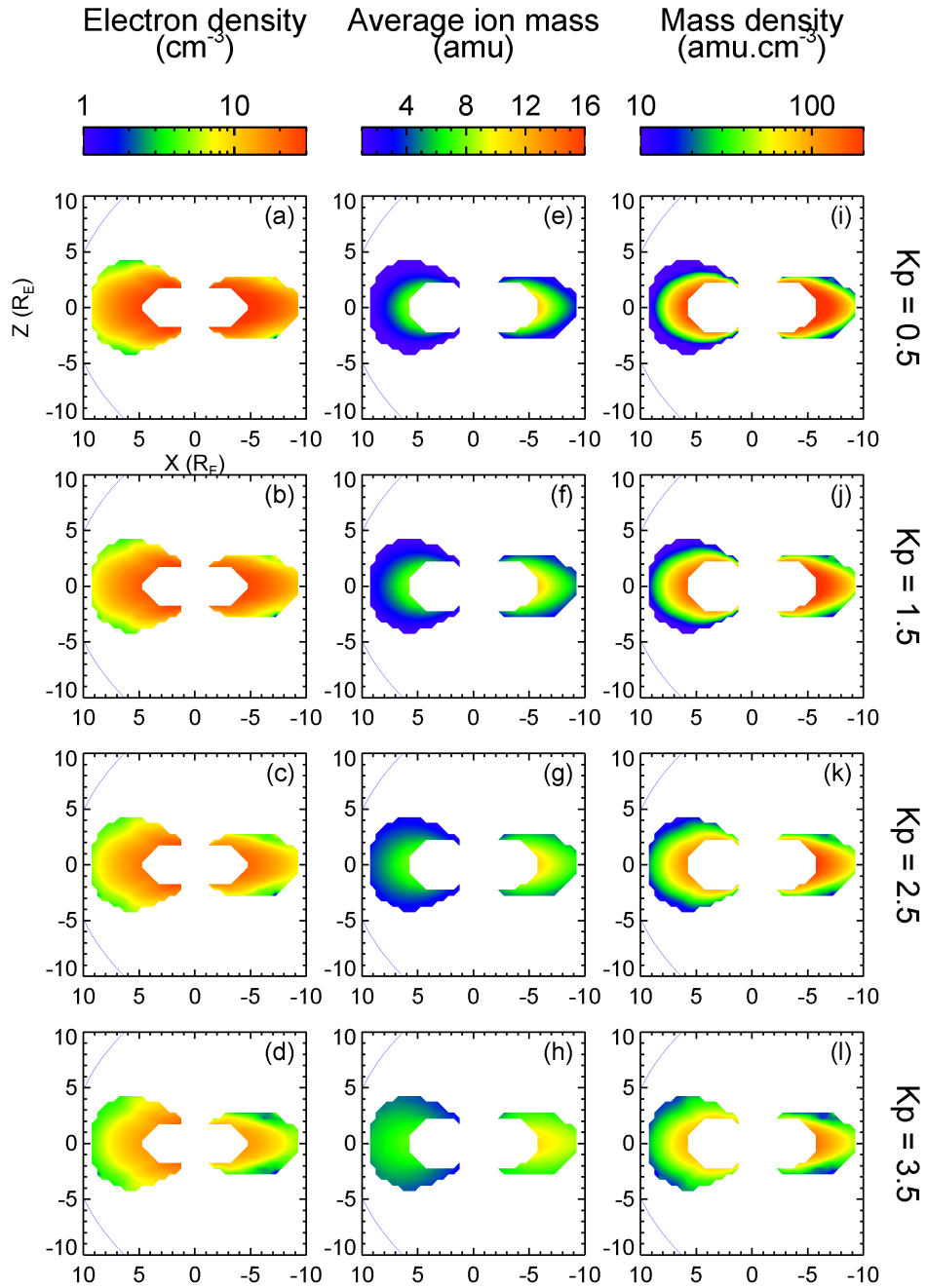


Figure 6.9: Spatial distribution in the X-Z SM plane using the field-aligned models for (a-d) electron density and (e-h) average ion mass, defined by equation 6.3 and equation 6.4, respectively. The models are combined to infer the corresponding total mass density distributions (i-l). Each vertical panel shows the distribution for a different value of the Dst index (nT). The T96 magnetic field model used corresponds to spring equinox, with a solar wind dynamic pressure of 2 nPa. The expected locations of the magnetopause under these conditions are included as the blue solid lines.

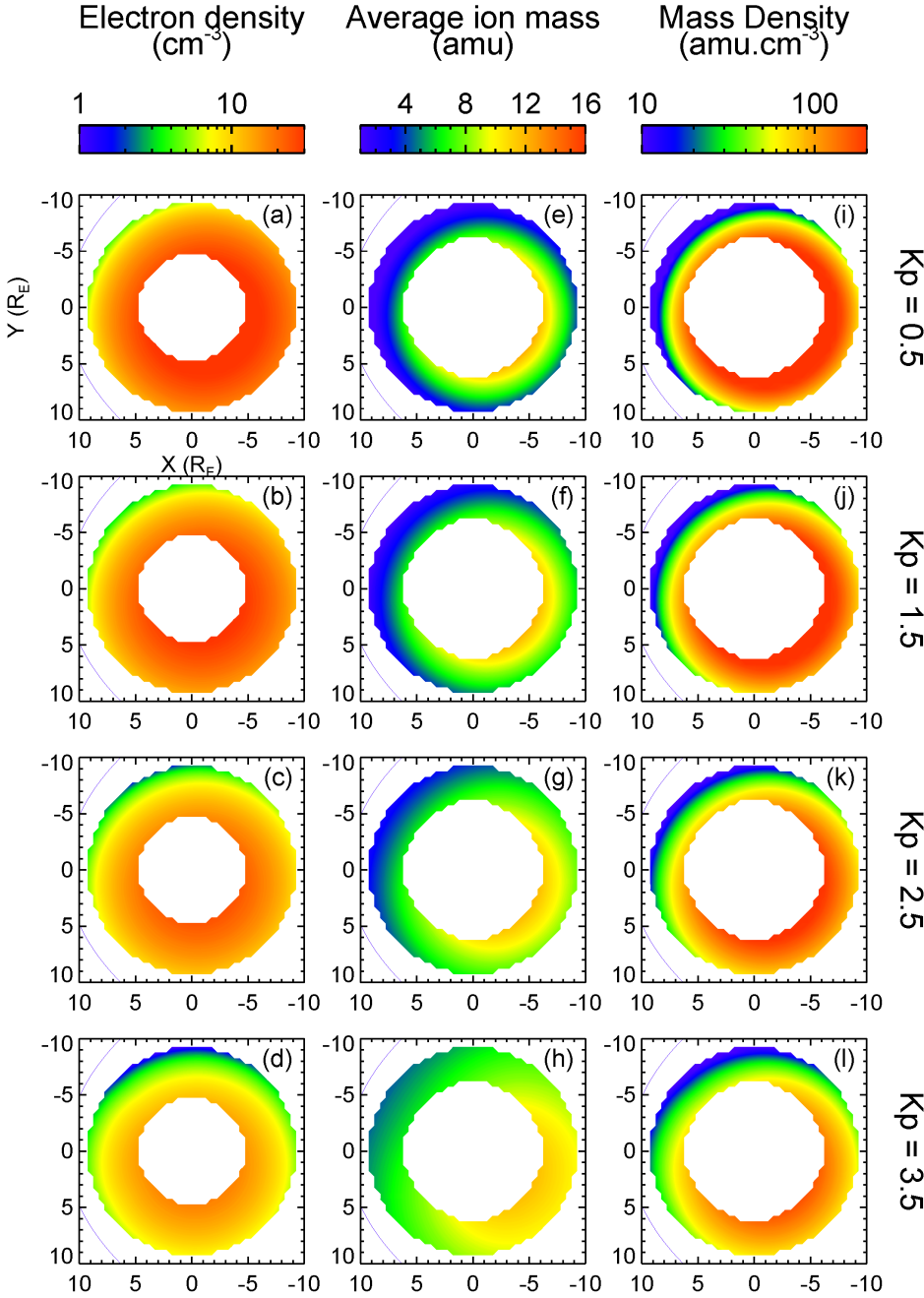


Figure 6.10: Same format as Figure 6.9, for the spatial distribution in the T96 magnetic equatorial plane.

6.5.2 Field-aligned distribution of average ion mass

The corresponding model for field-aligned variations in average ion mass, m_{av} , using the same power law functional form as previously (equation 6.2), is given by

$$m_{av} = m_{av0} R_{norm}^{-\beta} \quad (6.4a)$$

$$m_{av0} = 25.3 - 3.78K_p - (2.62 - 0.600K_p) L + 2.75 \cos(15MLT + 31.) \quad (6.4b)$$

$$\beta = -2.18 + 0.188L + 1.03 \cos(15MLT + 270.) \quad (6.4c)$$

where m_{av0} is the average ion mass at the magnetic equatorial point of the field line, and β is the power law index. The model parameters (m_{av0} and β) include dependences on L , MLT, and Kp index, and are described by equation 6.4a and equation 6.4c. The average ion mass model covers all MLT sectors in the region of $5.9 \leq L < 9.5$.

Using the average ion mass model, defined by equation 6.4, the spatial distribution is plotted for a range of Kp index values. The middle panels of Figure 6.9 show the distribution of average ion mass mapped azimuthally to the X-Z SM plane. In addition, the spatial distribution of average ion mass in the T96 magnetic equatorial is shown in the middle panels of Figure 6.10. Differences in the spatial distributions for varying Kp index values are assessed in section 6.6.

6.5.3 Mass density model with Kp index dependence

Similarly to the Dst index dependent mass density model, the models describing the field-aligned distributions of electron density (equation 6.3) and average ion mass (equation 6.4) are combined, using equation 3.1. The resulting mass density model includes dependences on L , MLT, and Kp index, and represents all MLT sectors for the closed magnetosphere between $5.9 \leq L < 9.5$. The corresponding spatial distributions mapped to the X-Z SM plane and in the T96 magnetic equatorial plane are shown in the right panels of Figure 6.9 and Figure 6.10, respectively. The range of panels show the mass density distribution at various Kp index values.

The total plasma mass density, and correspondingly electron density and average ion mass, show important variations with Kp index. The dependences on Kp index will be compared to the corresponding Dst dependent models, providing information on how using a different proxy for the level of geomagnetic activity affects the spatial distributions. This discussion is presented in section 6.6.

6.6 Discussion

This section will now discuss the key features of the empirical Dst dependent models for electron density and average ion mass, and the inferred mass density model. As the previous chapter examined the dependences of the electron density, average ion mass and total mass density on L value and MLT in detail (Chapter 5), this discussion will predominantly focus on the dependences of the field line distributions on Dst index. Furthermore, the effect of quantifying variations with Kp index, as opposed to Dst index, is also considered. This will provide an understanding of how the spatial distributions vary with geomagnetic activity, due to changes in the mass loading processes in the closed regions of the outer plasmasphere, plasmatrough, and near-Earth plasma sheet.

6.6.1 Electron Density

Using the same functional form as the average model (equation 5.2), the field line distribution of electron density at high latitudes is described using a power law function (equation 6.1a). This form gives a field line distribution where the electron density is a minimum at the magnetic equatorial point, and increases towards the ionospheric ends of the field line (where the power law index is constrained to be a position value). The power law form represents the contribution of the ionosphere as a plasma source, loading the flux tubes through photoionisation by incident solar radiation. This results in a distribution where the electron density along a field line approaches a maximum towards the ionosphere, and decreases moving away from this plasma source. The model parameters for the power law function (equation 6.1a) are the power law index, α , (equation 6.1d) and the electron density at the magnetic equatorial point of the field line, n_{e0} (equation 6.1c), which both contain information on how the power law field-aligned distribution varies with L , MLT, and Dst index.

The power law index, α , (equation 6.1d) describes the gradient of the electron density decrease away from the ionosphere. As previously identified, the power law index is observed to linearly increase in value with L shell, which is attributed to the increase in flux tube volume and length, resulting in a decreased total electron density across the flux tube. Therefore, the decrease in electron density moving away from the ionosphere, along field lines, will be greater, corresponding to an increased value of α .

A dependence of the power law index, α , on MLT is also observed, indicated by the sinusoidal component in equation 6.1d, in agreement with the average model (equation 5.2d) and previous studies [Denton et al., 2002]. The MLT dependence is such that α is peaked at approximately dawn. As discussed in Chapter 5, the dayside field line footprints have an increased flux of solar radiation incident, so the electron density will be increased at the ionospheric source, compared to the nightside field lines. This feature can be understood by considering the changes in the electron density along a flux tube that is corotating through all MLT sectors. In the nightside, the ionospheric refilling rates are minimised, resulting in depleted flux tubes. As the depleted flux tube corotates into the dawn sector, the electron density at the ionospheric ends of the field lines is increased to the dayside level, due to increased insolation. The electron density along the whole field line is increased as the flux tube moves through the dayside region, due to increased refilling from the ionospheric source. When the flux tube enters the nightside region, refilling rates return to the nightside level, and electron density along the field line is decreased due to loss processes dominating. Therefore, it can be seen that the gradient in electron density will be greatest at dawn, as the electron density is high at the ionospheric ends of a field line, but moving away from the ionosphere, the electron density is low due to the time spent in the nightside region. This results in the power law index maximising at approximately dawn, in agreement with these observations.

The power law index is not observed to demonstrate any statistically significant or coherent dependences on Dst index. However, results from previous studies suggest that refilling rates from the ionospheric plasma source vary with geomagnetic activity, which could imply changes in the power law index. Plasmaspheric electron density has been observed to decrease with increased Kp index (representing more disturbed conditions), which was attributed to reduced refilling rates [Young et al., 1982; Denton et al., 2002; Laakso et al., 2002b; Denton et al., 2004]. This is expected to result in decreased electron density at the field line ends, reducing the power law index during disturbed conditions. In direct contrast, Su et al. [2001] observed increased refilling rates from the ionosphere during periods of high magnetic activity. In this case, the power law index would be increased during disturbed conditions. However, this view does not consider the changes in loss processes with geomagnetic activity, which would determine the electron density along the field line away from the ionosphere, and influence the value of the power law index. Therefore, it is

unclear whether the lack of observed dependence of the power law index on Dst index is representative.

The power law function (equation 6.1a) is also parameterised by the electron density at the magnetic equatorial point on the field line, n_{e0} , (equation 6.1c). This parameter is observed to show some important dependences with Dst index, which will now be discussed and compared to previous studies. The mean value of n_{e0} over all MLT (the offset component of equation 6.1c) includes dependences on both L value and Dst index. The L shell variation is such that the equatorial electron density decreases with increased L value, as observed in the previous study and in agreement with multiple previous observations [Carpenter and Anderson, 1992; Goldstein et al., 2001; Sheeley et al., 2001; Denton et al., 2002, 2004; Berube et al., 2005; Ozhogin et al., 2012]. As discussed in Chapter 5, this is expected to be due to the increased flux tube volume and length with L , so the total density of plasma along the field lines will be reduced.

This study observes that with decreased values of Dst index, the electron density logarithmically decreases across all L shells (illustrated by a comparison of the left panels in Figure 6.3) and that the gradient of the L profile becomes flatter, consistent with previous findings [Chappell, 1972; Young et al., 1982; Denton et al., 2002; Laakso et al., 2002a; Denton et al., 2004; Reinisch et al., 2004; Denton et al., 2014]. This is as expected, as previous studies indicate that during the main phase of a geomagnetic storm, an increased convective electric field results in an earthwards motion of the plasmapause [Grebowsky, 1970; Chappell, 1972; Chen and Wolf, 1972; Berchem and Etcheto, 1981; Horwitz et al., 1984; Loto'aniu et al., 1999; Gallagher et al., 2000; Sheeley et al., 2001; Su et al., 2001; Laakso et al., 2002b; O'Brien and Moldwin, 2003; Dent et al., 2006; Grew et al., 2007; Thaller et al., 2015]. This is thought to be caused by a southward turning of the IMF (Interplanetary Magnetic Field) at main phase commencement, which initiates an increase in dayside magnetopause reconnection and increases the strength of the convective electric field [Cowley, 1982; Echer et al., 2008; Milan et al., 2009; Yermolaev et al., 2010]. An earthwards motion of the plasmapause at decreased Dst values would correspond to the electron density at each L value being decreased compared to the quiet time conditions, in agreement with these observations. An increased convective electric field would also correspond to a flattened L profile and reduced electron densities in the plasmatrough, as the convective field acts to erode the plasmatrough. Furthermore, O'Brien and Moldwin [2003] have shown that the enhanced ring current during disturbed conditions can also result in the erosion of the plasmasphere

through non-convective processes. During the subsequent recovery phase of a geomagnetic storm, characterised by increasing Dst values, the plasmapause moves outwards to the quiet time position at higher L values, and filling of the depleted new plasmaspheric flux tubes with cold ionospheric plasma increases the electron densities to their original level [Chappell, 1972; Horwitz et al., 1984; Comfort et al., 1988; Dent et al., 2006].

Although convective erosion is expected to dominate the loss of lower energy electrons (< 100 keV), studies have shown that wave-particle interactions and magnetopause shadowing are important loss mechanisms for energetic electrons (> 100 keV) that act to decrease densities during storm times [Fu et al., 2011]. The injection of particles from the plasma sheet during southward IMF conditions can lead to significant particle energy anisotropies, which are unstable to pitch-angle scattering by various plasma waves, such as EMIC (Electromagnetic Ion Cyclotron), plasmaspheric hiss, and whistler mode chorus waves [Kennel and Petschek, 1966; Reeves et al., 2003; Thorne et al., 2013; Fu et al., 2011; Millan and Thorne, 2007; Summers et al., 2007]. This results in loss to the atmosphere. Magnetopause shadowing becomes important during storm times, as an enhanced ring current causes electrons to drift radially outwards in order to conserve the third adiabatic invariant associated with the gradient-curvature drift motion. This process results in electrons that were previously on closed drift paths moving onto open drift paths, such that they are consequently lost to the magnetopause [Li et al., 1997; Reeves et al., 2003; Shprits et al., 2006; Millan and Thorne, 2007; Fu et al., 2011; Turner et al., 2012].

An additional contribution to decreasing electron densities with decreasing Dst index could be variations in the refilling rates from the ionosphere. As previously mentioned, it has been observed that the refilling rates are lower during geomagnetically active periods [Young et al., 1982; Denton et al., 2002; Laakso et al., 2002b; Denton et al., 2004]. This change would result in flux tubes being relatively depleted compared to quiet time conditions. However, it is noted that Su et al. [2001] observed a differing dependence, where refilling rates are higher during periods of increased geomagnetic activity, contradicting these results.

Equation 6.1c also includes a sinusoidal component for n_{e0} , demonstrating observed MLT dependences. The key feature of the MLT variation is that the peak in the n_{e0} parameter is observed to move from approximately dusk to noon with decreased Dst values. As the average model observed, the MLT asymmetry in n_{e0} is thought to be due to the presence of a ‘plasmaspheric bulge’, such that the electron density is generally increased towards the dusk sector for average quiet conditions [Carpenter, 1966; Chappell et al., 1970;

Sheeley et al., 2001; O'Brien and Moldwin, 2003; Thaller et al., 2015]. Therefore, the Dst dependence suggests that this duskside bulge is observed to rotate sunwards from the dusk region to noon during periods of increased geomagnetic activity. As the duskside bulge is a result of the cancellation of the corotational and convective electric fields, an increased convective field during the main phase is expected to affect features of the bulge region. Chappell [1972] explains, through a consideration of the direction of the convective flows, that an increased convective field acts to erode plasmaspheric flux tubes from the afternoon region (the erosion is most efficient in this region, where the convective flow streamlines are almost perpendicular to the plasmopause). These high density detached flux tubes are then convected sunwards, increasing the electron density in the noon sector, and forming a plasmaspheric plume that extends into the morning sector [Elphic et al., 1996; Ober et al., 1997; Burch et al., 2001; Sandel et al., 2001; Su et al., 2001; Goldstein and Sandel, 2005; Grew et al., 2007; Borovsky and Denton, 2008; Walsh et al., 2013; Katus et al., 2015; Thaller et al., 2015]. Therefore, this process supports the observed Dst dependence of n_{e0} and previous observations of the plasmaspheric bulge rotating towards noon [Nishida, 1966; Carpenter, 1970; Chappell, 1972; Higel and Lei, 1984; Moldwin et al., 1994; Elphic et al., 1996; Gallagher et al., 1998, 2000; Su et al., 2001; Laakso et al., 2002a; Katus et al., 2015; Thaller et al., 2015].

As identified by the average model, a localised peak in electron density is observed for the low latitude region of the field-aligned distribution. This feature is not accurately described by the power law function, so a Gaussian function with an offset of n_{e0} is used to model this region (equation 6.1b). This electron density peak is thought to be a result of solar wind - magnetosphere coupling, acting as a source of plasma in the closed magnetosphere, in addition to the ionospheric source previously discussed. The height of this peak at the magnetic equatorial point on a field line relative to the background power law value, a , is defined by equation 6.1e, where the sinusoidal component represents variations with MLT. The amplitude and phase of the MLT dependence were found to show no observable correlations with L value or Dst index. In agreement with the previous average model, the peak of a is located in the nightside MLT sector, which supports the proposition that nightside reconnection may be acting as a plasma source in the closed magnetosphere.

The average value of a over all MLT sectors, includes dependences on Dst index (see equation 6.1e). It is noted here that, unlike the average model, no statistical trends of a with L could be identified; the reason for this is currently unclear. However, this parameter

is observed to have a logarithmic dependence on Dst index, such that a decreases with decreasing Dst index. As with the previously discussed n_{e0} parameter, the decrease could be a result of increased convective erosion in the plasmatrough acting to deplete the flux tubes of plasma. As this plasma population is not thought to be directly originating from an ionospheric source, the decrease in a could be expected to be independent of variations in the ionospheric refilling rates. However, if the source of this plasma is from closure of open tail field lines by nightside reconnection, then refilling rates may have an effect. These open field lines will contain both ionospheric and solar wind plasma, so a reduced ionospheric source during disturbed conditions [Young et al., 1982; Denton et al., 2002; Laakso et al., 2002b; Denton et al., 2004] could result in decreased densities on the tail flux tubes. Therefore, the total input of plasma on the nightside will also be reduced.

As shown by equation 6.1e, the a parameter represents the electron density at the magnetic equatorial point relative to the background power law value, n_{e0} . Therefore, the observed electron density at the magnetic equatorial plane will be equal to $a + n_{e0}$, corresponding to the distributions shown in the left panels of Figure 6.4. It can clearly be seen from a comparison of panels a-d in Figure 6.4, that the equatorial electron density decreases with decreased Dst index. As previously discussed, both the n_{e0} and a parameters are reduced during the main phase of a geomagnetic storm, so this dependence is in agreement with the expected result. Another feature of the equatorial distributions is the strong MLT variations. During quiet times, the electron density is peaked towards the dusk sector, indicating that the MLT variation is dominated by the power law distribution (n_{e0} maximises at approximately dusk, as shown by equation 6.1c). However, at decreased Dst index values, corresponding to high levels of geomagnetically active conditions, the left panels of Figure 6.4 show that the peak in electron density moves from dusk towards noon. This represents the sunward motion of the plasmaspheric bulge, previously discussed, resulting from the contribution of the power law n_{e0} parameter. In addition, a relative enhancement is apparent at approximately dawn. This is caused by the Gaussian function (peaked in the postmidnight sector, as shown by equation 6.1e) contribution becoming comparable to the background power law, acting to shift the MLT peak towards dawn.

6.6.2 Average Ion Mass

The field-aligned distribution of average ion mass is modelled using a power law form function, where the power law index is allowed to be negative, as discussed in section 6.3. This functional form provides a distribution where the average ion mass maximises towards the magnetic equatorial point on the field line. As discussed for the average model (Chapter 5), this represents the effects of the centrifugal force, which acts more effectively on the heavier ions [Lemaire and Gringauz, 1998; Takahashi et al., 2004; Denton et al., 2006, 2009]. The resulting model is defined by equation 6.2, and is parameterised by the equatorial average ion mass, m_{av0} , and the power law index, β .

The average ion mass at the equatorial point on a field line, m_{av0} , is described by the sinusoidal function in equation 6.2b. Results from the average model observed an MLT asymmetry in the average ion mass distribution, with enhanced values on the nightside, peaking in the evening sector. In addition, an L dependence in m_{av0} described increasing values of average ion mass with decreasing L . These features of the distribution were attributed to the plasma sheet population. Enhanced ionospheric outflows of heavy ions are known to occur at high latitudes, in the cusp and auroral zone [Shelley et al., 1972, 1982; Lockwood et al., 1985a,b; Chappell et al., 1987; Chappell, 1988; Andre and Yau, 1997; Yau and Andre, 1997; Peterson et al., 2008; Liao et al., 2010; Li et al., 2012]. The convection of the plasma, which has an increased relative concentration of heavy ions, to the plasma sheet and then Earthwards to the closed magnetosphere, populates the nightside region [Chappell et al., 1987; Chappell, 1988; Yau and Andre, 1997; Cully et al., 2003; Dandouras et al., 2005; Kistler et al., 2010; Liao et al., 2010; Mouikis et al., 2010; Haaland et al., 2012a; Haaland et al., 2013; Kronberg et al., 2012]. Due to mass dispersion effects, heavier ions are convected to lower L values compared to lighter ions, resulting in an L shell gradient of average ion mass [Lockwood et al., 1985a,b; Chappell, 1988; Andre and Yau, 1997; Yau and Andre, 1997; Haaland et al., 2009; Maggiolo and Kistler, 2014]. It was also noted that an additional minor contribution to the average ion mass distribution is the presence of a heavy ion torus located just outside the plasmasphere, enhancing the average ion mass values in this region [Chappell, 1982; Horwitz et al., 1984, 1986; Roberts et al., 1987; Comfort et al., 1988; Berube et al., 2005; Darrouzet et al., 2009; Nosé et al., 2011, 2015]. In agreement with a proposed formation mechanism of the heavy ion torus, an interaction between the plasmasphere and ring current, the corresponding heavy ion enhancement is greatest in the

evening MLT sectors [Horwitz et al., 1986; Roberts et al., 1987; Burch et al., 2001; Nosé et al., 2011].

The dependences of the equatorial average ion mass, m_{av0} , as shown by equation 6.2b, are illustrated in Figure 6.4e-h. In terms of the MLT dependence of m_{av0} , no coherent variations with Dst index could be identified from the data. The sinusoidal variations are in good agreement with the average model, with m_{av0} peaking in the evening sector. Although, it is also noted that, in contrast with the average model, no discernible L dependence in the amplitude of the MLT variations was apparent in the data analysis, and consequently, a dependence was not quantified. However, it was observed that the sinusoidal offset term in equation 6.2b, representing m_{av0} averaged over MLT variations, demonstrated significant dependences with Dst index. The L gradient increases with decreased Dst index, to the extent that the gradient becomes positive for active geomagnetic conditions. Therefore, m_{av0} decreases with increasing L value for quiet times (Figure 6.4h), whereas m_{av0} increases with increasing L value for disturbed times (Figure 6.4e). In addition, the intercept of the linear dependence decreases with decreased Dst index (equation 6.2b). The overall result is a significant increase in m_{av0} at the higher L values of the model L range ($L \gtrsim 6.5$), and a small decrease in m_{av0} at the lower L values ($L \lesssim 6.5$), over all MLT sectors. This feature is in agreement with multiple previous studies [Young et al., 1982; Takahashi et al., 2006; Maeda et al., 2009; Nosé et al., 2009; Moukikis et al., 2010; Ohtani et al., 2011; Maggiolo and Kistler, 2014], and can be attributed to the increased O^+ concentration of the plasma sheet population. Increased magnetic activity causes increased heating of the atmosphere and ionosphere, a result of the dissipation of auroral currents and $E \times B$ drifts, resulting in a rise in the ion and neutral scale heights. As O^+ ions have a relatively low scale height, they react more strongly to changes in magnetic activity compared to other ions [Young et al., 1982]. In addition, an increase in magnetic activity can also increase ionisation by auroral electrons, where the precipitating electrons are deposited at altitudes where oxygen is the dominant species [Young et al., 1982]. Therefore, both changes in the scale height and ionisation by auroral electrons have effects that are most significant for O^+ ions [Young et al., 1982; Kronberg et al., 2012], resulting in enhanced O^+ concentrations for ionospheric outflows in the cusp and nightside auroral regions. The outflowing plasma at high latitudes is convected through the lobes to the plasma sheet, and to the nightside inner magnetosphere [Yau et al., 1985; Lennartsson and Shelley, 1986; Ebihara et al., 2006; Kistler et al., 2006; Haaland et al., 2009; Liao et al., 2010; Yau et al., 2012; Denton et al., 2014; Maggiolo and Kistler, 2014].

This process supports the observed increase in m_{av0} with increased geomagnetic activity, most significantly at higher L values towards the plasma sheet (Figure 6.4e-h).

As mentioned previously, the heavy ion torus also contributes to the m_{av0} dependence on Dst index, although the L range of the model covers only the outer regions of the heavy ion torus, so the contribution to the average ion mass is minor compared to the plasma sheet population. It has been suggested by Nosé et al. [2011] that during the storm main phase, the strong convective fields result in the erosion of the heavy ion torus, due to the formation of a plasmaspheric plume extending to the dayside magnetopause [Elphic et al., 1996; Ober et al., 1997; Sandel et al., 2001; Goldstein and Sandel, 2005; Grew et al., 2007; Borovsky and Denton, 2008; Walsh et al., 2013] and acceleration by magnetic field dipolarisation, accelerating O^+ ions and forming the O^+ -rich ring current. This feature correlates with the m_{av0} dependence on Dst index at lower L , where values decrease slightly for disturbed conditions (Figure 6.4e-h). The interactions between the expanding plasmasphere and ring current in the recovery phase of a storm are thought to repopulate the heavy ion torus, a feature of the quiet inner magnetosphere [Nosé et al., 2011].

The modelled field-aligned distribution of the average ion mass is also dependent on the power law index, β , defined by equation 6.2c, where the magnitude represents the gradient of the decrease in average ion mass moving away from the magnetic equator along a field line. Equation 6.2c shows that the parameter is described using a sinusoidal function, to include MLT dependences, with an offset defining the value of β averaged over MLT variations.

As for the average model, the β parameter, averaged over MLT, is observed to linearly become less negative with increasing L value, as represented by the offset terms in equation 6.2c. This feature was attributed to the increasing magnetic field flux tube volume and length at increased L . Equation 6.2c shows that no dependence on Dst index is included for the model β parameter offset term, which is due to a lack of consistent variations with Dst index in the data.

As shown by equation 6.2c, the power law index, β , is observed to demonstrate dependences with MLT, indicated by the sinusoidal component. The phase of the sinusoidal term is such that the most negative β values at a particular L value are observed at dusk, in good agreement with the average model. In this region, there will be reduced upwelling of ionospheric O^+ ions, due to reduced solar illumination [Young et al., 1982; Lennartsson, 1989; Stokholm et al., 1989], resulting in a larger gradient along the field line. Furthermore, the convection of the O^+ -rich plasma sheet population acts to enhance the equatorial average

ion mass for nightside MLT sectors, and steepen the field-aligned gradient. The phase of the sinusoidal term is observed to show no coherent dependences on Dst index, implying that the MLT location of the power law index minima is independent of geomagnetic activity.

The amplitude of the MLT dependence of β is shown to depend on Dst index (see equation 6.2c). However, it is noted that the amplitude term does not include a linear dependence on L value, unlike the average model, as no identifiable variations were present in the data. The geomagnetic activity dependence is such that the amplitude is observed to decrease and the gradient in L becomes flatter with decreased Dst index values. This corresponds to the dawn-dusk asymmetry in β reducing, and its variation with L also reducing. As previously mentioned, during disturbed conditions, enhanced ionospheric outflows of O^+ ions at high latitudes convect, through the plasma sheet, to the inner magnetosphere. This increases the average ion mass across all MLT sectors (Figure 6.4). Therefore, this will act to reduce the diurnal variations and decrease the amplitude of the MLT dependence of β .

6.6.2.1 Cusp enhancement

The spatial distribution of average ion mass has been shown to vary strongly with Dst index, as illustrated by the middle panels of Figure 6.3 and Figure 6.4. The features of the average ion mass model indicate that during disturbed conditions, enhanced heavy ion outflows occur at high latitudes, and strongly influence the spatial distribution of average ion mass in the closed magnetosphere. By mapping the average ion mass values close to the ionosphere, the distributions shown in Figure 6.6 and Figure 6.7 are provided. These figures provide some detail on heavy ion outflows on the field lines corresponding to the spatial distributions shown in Figure 6.3 and Figure 6.4. As mentioned previously, it has been assumed that the field-aligned distribution defined by equation 6.2 can be extrapolated to high latitudes along the field line, which is an unjustified assumption. Therefore, the average ion mass values are not expected to be a valid representation of this region, but the analysis of Figure 6.6 and Figure 6.7 is intended to provide some information on the relative magnitudes of heavy ion outflows.

Figure 6.6 shows the average ion mass values for a Dst index value equal to 0 nT, which corresponds to quiet geomagnetic conditions, and Figure 6.7 shows the average ion mass values at a Dst index value equal to -100 nT, representing relatively active conditions. Each panel of Figure 6.6 and Figure 6.7 is an average of values for each MLT sector, as labelled. A

comparison of Figure 6.6 and Figure 6.7 indicates that for disturbed conditions, the average ion mass increases across all MLT sectors. The key feature is a significant enhancement in values for the nightside MLT sector in Figure 6.7. Furthermore, it can be seen that for quiet conditions, the values decrease with increasing latitude (Figure 6.6). In contrast, for active intervals, this dependence reverses, resulting in an increase in average ion mass with increasing latitude, as illustrated in Figure 6.7. This provides support for the expected enhancement in heavy ion outflows at high latitudes during geomagnetically active condition [Shelley et al., 1972, 1982; Lockwood et al., 1985a,b; Chappell et al., 1987; Chappell, 1988; Andre and Yau, 1997; Yau and Andre, 1997; Peterson et al., 2008; Liao et al., 2010; Li et al., 2012]. These heavy ion outflows are then convected into the inner magnetosphere, providing the spatial distributions of average ion mass shown in Figure 6.3e-h and Figure 6.4e-h.

6.6.3 Mass Density

By combining the electron density and average ion mass empirical models, using equation 3.1, a model describing the variations of the total mass density along closed field lines can be inferred, which includes dependences on L value, MLT and Dst index. As discussed in Chapter 3, this empirical modelling approach accounts for the contributions of both the number density and ion composition of the plasma. The spatial distributions predicted by this mass density model for various values of Dst index are shown in the right panels of Figure 6.3 and Figure 6.4, mapped to the X-Z SM plane and T96 magnetic equatorial plane respectively, where it is clearly illustrated that the mass density varies significantly with geomagnetic activity. The field-aligned distribution of the mass density is now discussed, specifically focusing on the variations with Dst index. For additional details on the dependences on L and MLT, refer to Chapter 5.

Figure 6.11 shows the field line profiles at multiple Dst index values, and comparing for different MLT and L values. The first feature that is apparent from Figure 6.11 is the mass density along the full field line, in general, decreases with decreasing Dst index, except for the morning MLT sector at high L values (see upper two right panels in Figure 6.11). This indicates that the Dst variations are generally dominated by changes in the plasma number density, as the electron density is observed to decrease during geomagnetically active conditions (as discussed in section 6.6.1). However, for high L values in the morning sector (upper two right panels), this dependence reverses, such that the mass density along the

field line for all MLT is observed to slightly increase with decreasing Dst index. In this case, the ion composition is the dominant factor, where the increasing relative concentration of O^+ ions during disturbed conditions acts to increase the mass density despite the decreased number density. This feature may be a result of the relative enhancement in electron density at approximately dawn for disturbed conditions (Figure 6.4a), expected to be due to the plasma sheet population, as previously discussed. As the number density decrease is not as significant in this region, compared to lower L shells and other MLT sectors, the ion composition variations dominate, resulting in the mass density increase.

The general decrease in mass density during decreased Dst index is also apparent from the spatial distributions shown in Figure 6.3 and Figure 6.4. This feature is a somewhat unexpected result, which will now be examined in further detail. Previous statistical studies have observed the mass density to increase in this region during geomagnetically disturbed periods, in particular Takahashi et al. [2002, 2006, 2010] and Min et al. [2013]. These observations were interpreted as a result of the injection of heavy ions into the closed magnetosphere during the main phase of a storm, causing high relative concentrations of O^+ ions. The increased average ion mass was thought to dominate over the relatively weak reductions in electron density, and act to increase the plasma mass density. Although it was noted by Takahashi et al. [2006] and Min et al. [2013] that the mass density enhancements were relatively short lived and weakly correlated with Dst index. The studies [Takahashi et al., 2002, 2006, 2010; Min et al., 2013] all indirectly inferred the equatorial total mass density values from spacecraft observations of toroidal standing Alfvén wave harmonic frequencies. Using the MHD wave equation (see equation 1 of Takahashi et al. [2010]) combined with a numerical magnetic field model, the mass density was determined by choosing the value that gives an eigenfrequency matching the observed frequency. In order to estimate the equatorial mass density using this method, a function describing the field-aligned dependence of mass density must be assumed. These studies all used a power law function to represent the distribution along magnetic field lines, however, previous studies have shown that this form does not represent an observed peak in mass density close to the magnetic equator [Takahashi et al., 2004; Denton et al., 2006; Takahashi and Denton, 2007; Denton et al., 2009]. The localised peak is also observed in this study (see Figure 6.11), as well as the average model. However, as the mass density contribution to determining the field line frequency is mainly at the equator, where the magnetic field is weakest, the estimated

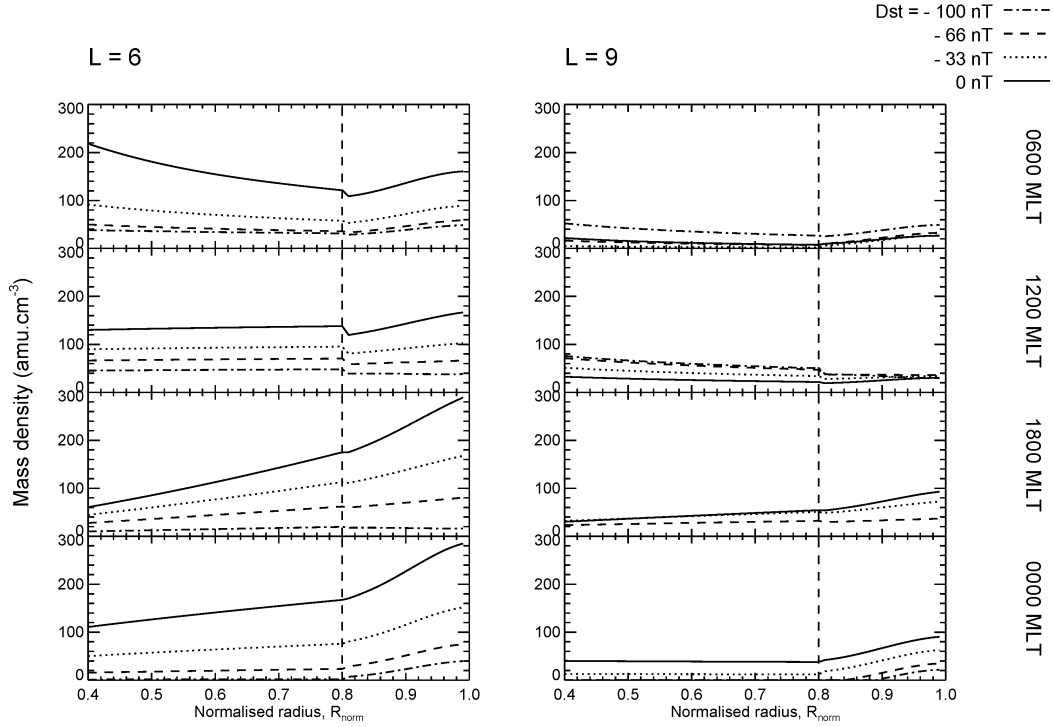


Figure 6.11: Panels showing the mass density ($\text{amu}\cdot\text{cm}^{-3}$) as a function of the normalised radius, R_{norm} . The mass density values are calculated by combining the electron density (equation 6.1) and average ion mass (equation 6.2) field-aligned models using equation 3.1. Each panel shows the field line distribution at a different value of the Dst index (nT), as indicated by the linestyle. The left (right) panels show profiles for $L = 6$ ($L = 9$), and the vertical panels show profiles for multiple MLT values. The vertical dashed lines on each panel indicate the boundary separating the power law and Gaussian form field-aligned dependence for the electron density model.

equatorial mass density should not differ significantly from the true value. In addition, these inaccuracies would not be expected to reverse the dependence on geomagnetic activity.

In contrast, other studies have observed decreased mass densities associated with geomagnetically active conditions [Menk et al., 1999; Dent et al., 2006; Denton et al., 2006;

Menk et al., 2014], in agreement with this model. Denton et al. [2006] used ratios of observed toroidal standing Alfvén wave frequency harmonics with a Monte Carlo fit to infer field line distributions of mass density at different Dst index values. Unlike the previously mentioned studies, the equatorial peak in the mass density distribution was accounted for, assuming a polynomial form to represent field-aligned variations. Denton et al. [2006] found that at high latitudes, away from the magnetic equatorial plane, the mass density decreased with decreased Dst index. This resulted in a more peaked distribution for disturbed conditions. This feature was attributed to an increased ring current and reduced plasmaspheric density (as previously discussed in section 6.6.1). However, the equatorial mass density showed little variation with Dst index, unlike the results presented here. Although it should be noted that Denton et al. [2006] compared only two samples of the mass density observed at different Dst index, and that the inversion technique employed required a functional form describing the field-aligned distribution to be assumed. A study conducted by Menk et al. [1999, 2014] also observed decreased mass density during disturbed conditions. The plasmaspheric mass density was inferred from ground-based observations of FLR frequencies for different Kp values, where the Kp index represents the level of geomagnetic activity. Menk et al. [1999, 2014] found that the mass density was increased during low Kp intervals, corresponding to quiet conditions. This feature was attributed to the refilling of the plasmasphere in the recovery phase and following storms, which caused the mass density to be increased compared to storm times, where the plasmasphere is depleted. Furthermore, Dent et al. [2006] presented measurements of the total plasma mass density, inferred from ground magnetometer observations of FLR frequencies, showing an overall depletion of the total plasma mass density during a geomagnetic storm period. The analysis indicated that, although an enhancement in the heavy ion population occurred, when combined with a decrease in number density, the overall effect was reduced values in plasma mass density across all L shells examined ($2.3 \geq L \leq 6.3$) during disturbed conditions. Therefore, there is evidence both in agreement and in opposition to the observed decrease in mass density at low L values, but the reasons for these differences are unclear at present.

Figure 6.11 also illustrates variations in the shape of the field line profiles with geomagnetic activity. Note that the dependence of profile shape on L and MLT during quiet conditions are examined for the average model (Chapter 5), and will not be discussed in detail here, instead focusing on the variations on Dst index. Firstly, the high latitude region (left of dashed vertical lines) will be considered, where power law dependences are observed,

with the electron density model following a positive power law index (equation 6.1) and the average ion mass following a negative power law index (equation 6.2). It has been shown that the power law indices (equation 6.1d and equation 6.2c) do not demonstrate any strong dependences on Dst index, and therefore, the difference between profiles shown in Figure 6.11 are predominantly due to variations in the equatorial values (equation 6.1c and equation 6.2b). It is clear from Figure 6.11, that the high latitude region is characterised by a decrease in mass density values during disturbed conditions, for the majority of L values and MLT sectors. As mentioned above, this is due to the decreased number density dominating over ion composition variations for disturbed conditions. The exception is for field lines at higher L values in the morning sector, referring to the upper two left panels of Figure 6.11, where an increase in mass density during disturbed conditions is shown. As previously discussed, this increase is due to the ion composition contribution dominating over the number density contribution.

The lower latitude region is also seen to vary with geomagnetic activity, as shown by the profiles in Figure 6.11. In this region, the electron density is locally peaked above the background power law distribution, where the relative peak height reduces during disturbed conditions, as described by equation 6.1. The average ion mass also approaches a maximum towards the magnetic equator (equation 6.2), so the resulting mass density distribution is expected to be peaked in this region, as shown by the average model and multiple others [Takahashi et al., 2004; Denton et al., 2006; Takahashi and Denton, 2007; Denton et al., 2009]. Consistent with the previous discussion, the peak decreases during disturbed conditions across all regions, except for the morning sector at higher L values (upper two left panels in Figure 6.11), where the peak height slightly increases. As discussed, this feature is attributed to the magnitude of electron density depletion being reduced in this region, such that the increase in average ion mass is the dominant contribution to the total plasma mass density.

6.6.4 Comparison to parametrisation with Kp index

Although the dependences of mass density on geomagnetic activity have been quantified using Dst index as a proxy for the level of magnetic field disturbances, it was mentioned previously (section 6.5) that many studies choose to use Kp index instead [Menk et al., 1999; Gallagher et al., 2000; Takahashi et al., 2002; Denton et al., 2006; Takahashi et al., 2006, 2010, 2014]. The key difference between Dst index and Kp index is attributed to

the location of the magnetometer stations, from which the magnetic field disturbances are observed. Whereas Dst index is a result of observations taken at low latitudes, Kp index is based on observations at a larger range of latitudes. Therefore, the variations in Dst index are largely dependent on the ring current intensity, and the variations in Kp index are controlled by the auroral current systems in addition to the ring current.

In order to understand how using Kp index as a proxy for the level of geomagnetic activity orders the data, the variations in the field-aligned distributions of electron density and average ion mass were quantified, including dependences with Kp index. The corresponding mass density model was inferred, and the resulting spatial distributions are shown in Figure 6.9 and Figure 6.10. These can be directly compared to the spatial distributions for the Dst dependent models shown in Figure 6.3 and Figure 6.4. Although a detailed comparison of the quantitative differences between model parameters is outside of the scope of this study, some key features will be highlighted.

The same functional form for the electron density field-aligned distributions was chosen for both the Dst dependent model (equation 6.1) and the Kp dependent model (equation 6.3), and both electron density models cover $4.5 \leq L < 9.5$. The power law form, used to represent variations at high latitudes, is parameterised by the electron density at the magnetic equatorial plane, n_{e0} , and the power law index, α . A comparison of the n_{e0} model parameter for the Dst dependent model (equation 6.1c) and the Kp dependent model (equation 6.3c) indicates that a steeper decrease in n_{e0} with increased activity for the Dst model. Furthermore, the gradient of n_{e0} with L value decreases at a stronger rate with respect to Dst index than Kp index. In terms of n_{e0} dependences on MLT, both models demonstrate the peak MLT location moving to earlier MLT values, although the rotation is greater for the Dst dependent model. The power law form is also parameterised by the power law index. Both the Dst dependent model α (equation 6.1d) and the Kp dependent model α (equation 6.3d) do not include any dependence on geomagnetic activity, as no coherent variations could be identified from the dataset. The electron density model also includes a Gaussian function to describe a peak in electron density localised to the magnetic equatorial plane (equation 6.1b and equation 6.3b). The peak height relative to the background power law distribution, a , is defined by equation 6.1e for the Dst dependent model, and equation 6.3e for the Kp dependent model. Both model a parameters show the same variation with geomagnetic activity, with negligible deviations in values between them. Overall, the electron density model exhibits stronger dependences on Dst index compared to Kp index, where

the associated variations in electron density are attributed to increased convective flows in the closed magnetosphere with increasingly active geomagnetic conditions.

The average ion mass was also modelled including dependences on both Dst index and Kp index, covering closed field lines within $5.9 \leq L < 9.5$. The power law form was used for both (equation 6.2 and equation 6.4), which is parameterised by the average ion mass at the magnetic equatorial point of a field line, m_{av0} , and the power law index, β . The m_{av0} model parameter demonstrates a stronger increase in m_{av0} at low L values, and a stronger decrease in m_{av0} at high L values, when parameterised with Dst index (equation 6.2b) compared to Kp index (equation 6.4b). This feature is illustrated through a comparison of the middle panels of Figure 6.4 and Figure 6.10. Referring to the α parameter, no dependence on Kp index was quantified, as no clear variations could be identified from the dataset (equation 6.4c). However, the Dst dependent model observed dependences in the amplitude of α MLT variations when parameterised with Dst index (equation 6.2c). Therefore, the average ion mass models suggest that dependences in plasma ion composition with geomagnetic activity are stronger with respect to Dst index, compared to Kp index.

Using the same method as for the Dst dependent model, the electron density (equation 6.3) and average ion mass models (equation 6.4) are combined to infer an empirical model for the total plasma mass density, including dependences on Kp index. The model describes the total plasma mass density distribution for closed field lines, over all MLT sectors in the region of $5.9 \leq L < 9.5$. As for the Dst model, the combination of decreased plasma number density and increased heavy ion concentration, results in decreased total mass density for disturbed conditions. This indicates the dominance of number density variations compared to ion composition. It has been identified that variations in both electron density and average ion mass are stronger when parameterised with Dst index than Kp index. Therefore, dependences in the total plasma mass density are correspondingly stronger for Dst index compared to Kp index, as expected. It can be concluded from the comparison that the Dst index is a better proxy for storm-related variations and convective flows in the closed magnetosphere than the Kp index. This is thought to be due to the Dst index being predominantly controlled by the ring current, so it is more effective at isolating storm-related magnetic field perturbations. In contrast, the Kp index includes larger contributions from other current systems, such as auroral current systems. The inclusion of additional current systems, affected by non-storm related processes, act to smooth the variations in electron

density and average ion mass, when using Kp index as a proxy for geomagnetic activity [O'Brien and Moldwin, 2003].

Further analysis, not included here, involved examining the dependence of the electron density, average ion mass, and total plasma mass density spatial distributions on IMF orientation. Using the same empirical modelling technique as for the average model (Chapter 5), data were binned for prolonged northward IMF intervals and southward IMF intervals. The resulting distributions during northward IMF conditions generally indicated increased electron densities, decreased average ion mass, and an overall increase in total plasma mass density. In comparison to the expected distributions using the Dst models and Kp models, the electron density, average ion mass, and mass density values were in close agreement, with some deviations attributed to the formation of a cold dense plasma sheet under northward IMF [Terasawa et al., 1997; Fujimoto et al., 1998; Wing et al., 2002; Thomsen et al., 2003; Hasegawa et al., 2004; Li et al., 2005; Øieroset et al., 2005; Wing et al., 2005; Lavraud et al., 2006a,b; Wing et al., 2006; Imber et al., 2007; Nagata et al., 2007, 2008; Wang et al., 2010]. The results for southward IMF conditions showed decreased electron densities, increased average ion mass, and a slight overall decrease in the total plasma mass density, compared to the average model. The dependences are in significant agreement with the Dst models and Kp models, for the corresponding level of geomagnetic activity. This indicates that the variations under southward IMF conditions are due to the same processes under an enhanced geomagnetic activity, namely enhanced convective flows towards the dayside magnetopause and increased heavy ion outflows.

In addition, previous studies have shown that the electron density and ion composition, and therefore the total plasma mass density, in the closed magnetosphere has a solar cycle dependence. It has been observed that during times of increased solar activity, the number density is enhanced and the average ion mass is increased, relative to low solar activity periods [Young et al., 1982; Horwitz et al., 1986; Comfort et al., 1988; Lennartsson, 1989; Lawrence et al., 1999; Su et al., 2001; Nosé et al., 2009; Mouikis et al., 2010; Denton et al., 2011]. This is due to increased solar flux resulting in increased photoionisation in the ionosphere. Using the Cluster dataset of electron density and average ion mass observations, dependences on solar flux were examined. However, due to a significant change in orbital configuration during solar minimum, the coverage of electron density data along field lines is not uniform with solar activity. Furthermore, the average ion mass dataset does not cover the full solar minimum phase, due to CODIF instrumental issues. Consequently, due to the

constraints of the datasets, quantifying the field-aligned dependence of electron density and average ion mass with solar activity was not possible. However, the initial analysis suggested that variations of electron density and average ion mass with F10.7 cm flux, an indicator of solar activity, were relatively minor compared to spatial variations and variations with geomagnetic activity.

Chapter 7

Applications

The empirical models developed in Chapter 5 and Chapter 6 describe the spatial distribution of total plasma mass density in the closed magnetosphere, and considers variations with geomagnetic activity. The mass density distributions provide information on the structure of the magnetosphere, and has important implications for various dynamical processes. In this chapter, the role of plasma mass density in determining frequencies of standing Alfvén waves on closed field lines is examined, exploring spatial and geomagnetic variations. The empirical mass density models are employed to estimate the frequencies, using the time-of-flight method. Furthermore, the validity of the estimated frequencies are assessed through a comparison with average FLR frequencies observed by ground magnetometers.

7.1 Time-of-flight method

The FLR process involves the formation of a standing Alfvén wave on a closed geomagnetic field line, as detailed in section 1.5. Considering the propagation of an Alfvén wave along a given magnetic field line, the resonant eigenfrequencies are determined by the field line length and the Alfvén speed (equation 1.37). The Alfvén speed (equation 1.35) is a function of local plasma mass density and magnetic field strength, so will vary significantly along closed field lines. Taking this into account, the resonant fundamental mode frequency, f , of a given field line can be approximated using the time-of-flight technique [Warner and Orr, 1979]

$$\frac{1}{f} = 2 \int \frac{ds}{v_A} \quad (7.1)$$

where the integral is taken over the field line length. This technique requires assumptions of the magnetic field line length, and field-aligned variations of the magnetic field strength and plasma mass density, which determine the Alfvén speed distribution along the field line (equation 1.35). Using a simple dipolar magnetic field model combined with a radial power law mass density model, this technique is demonstrated in Figure 7.1, where the time-of-flight approach was applied to multiple field lines covering a range of L values and all MLTs. The radial power law mass density model is defined to have a mass density of 100 cm^{-3} at $L = 4$, decreasing with radial distance in the equatorial plane with a r^{-4} dependence, as used in previous studies [Warner and Orr, 1979; Wild et al., 2005]. The mass density model is based on OGO (Orbiting Geophysical Observatories) observations of H^+ densities, presented in a study by Chappell [1972]. Figure 7.1 shows the frequencies calculated using equation 7.1 plotted at the field lines position in the dipole magnetic equatorial plane (left panel) and the field line footprint latitude (right panel), considering field lines with L values covering $4 \leq L < 10$. The choice of magnetic field model and mass density model used to produce the results shown in Figure 7.1 are clearly very simplistic, neglecting any local time variations, but are included here to illustrate the time-of-flight technique.

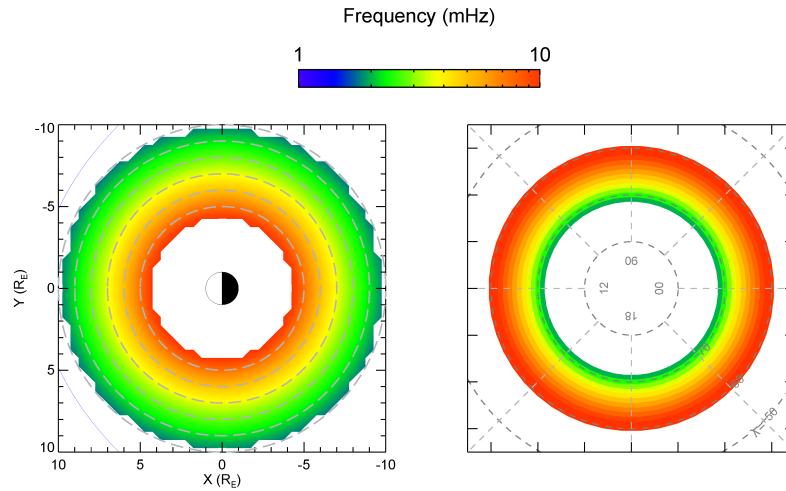


Figure 7.1: Field line oscillation frequency calculated using the time-of-flight approximation, where a dipole magnetic field model and a radial power law mass density model were employed. The left panel shows the frequencies mapped to the field lines' position in the magnetic equatorial plane. The right panel shows the frequencies mapped to the AACGM latitude and MLT of the field line footprints in the northern hemisphere.

An alternative method in determining the resonant frequency for a given field line is using the Singer et al. [1981] method, where the MHD wave equation is numerically solved using a fourth-order Runge-Kutta algorithm [Waters et al., 1995]. In a study conducted by Wild et al. [2005] the estimated frequencies using the time-of-flight approximation (equation 7.1) were directly compared to frequencies calculated using the Singer et al. [1981] method, where the T96 magnetic field model and a radial power law mass density model were used for both. The T96 magnetic field model at spring equinox, with an input dynamic pressure value of 2 nPa, was used. Although the time-of-flight technique is relatively simplistic compared to the Singer et al. [1981] method, Wild et al. [2005] showed that the frequencies were in good agreement up to field line footprint latitudes above approximately 75° , where the estimates diverged. As the empirical mass density models cover field lines with footprints well below 75° , the simpler and quicker time-of-flight approximation is chosen over the Singer et al. [1981] method to estimate the resonant frequencies.

7.1.1 Wild et al. [2005] study

Previous studies have explored estimating standing Alfvén wave eigenfrequencies using the time-of-flight approximation with realistic magnetic field models. Wild et al. [2005] presented an assessment of field line eigenfrequencies calculated using equation 7.1, employing the T96 magnetic field model and a simple radial power law mass density model, for high latitude closed geomagnetic field lines. The results indicated that the use of the realistic T96 magnetic field model, compared to previous calculations using more simplistic magnetic field models [Warner and Orr, 1979; Lee and Lysak, 1990], provides more representative estimates of the eigenfrequencies. The use of the T96 magnetic field model provides a more realistic description of local time variations, field configuration at high latitudes, and dependences on geomagnetic activity and solar wind conditions.

Estimates of field line fundamental model frequencies are shown in Figure 7.2, corresponding to the T96 magnetic field model and the radial power law mass density model used in Figure 7.1. A comparison of Figure 7.1 and Figure 7.2 clearly illustrates the effects of using a more realistic magnetic field model on the calculated frequencies. Local time variations in the magnetic field configuration are represented as variations in the frequency with MLT.

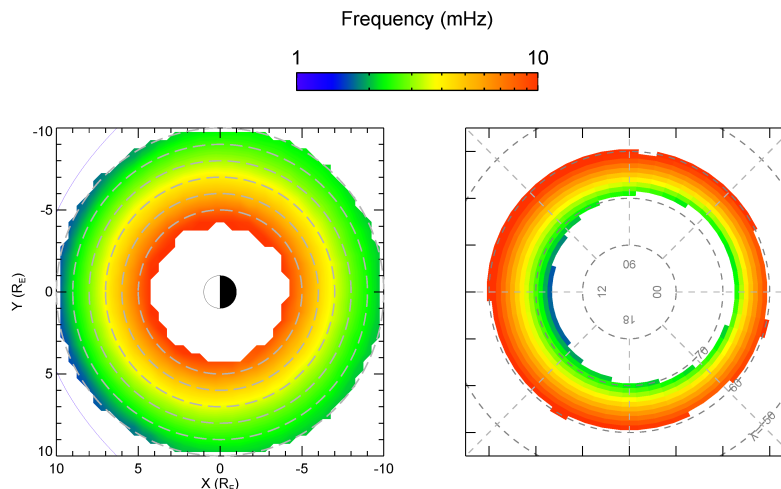


Figure 7.2: Same format as Figure 7.1, where the time-of-flight calculated frequencies correspond to the use of the T96 magnetic field model and a radial power law mass density model.

However, the mass density model used in the time-of-flight approximation for calculating the frequencies shown in Figure 7.2 is highly simplistic. It has been shown that the magnetospheric mass density distribution contains strong variations with MLT, responds strongly to a range of dynamical processes in the magnetosphere, and cannot be described validly with a simple radial power law mass density model (see Chapter 5 and Chapter 6). As the local Alfvén velocity depends on the plasma mass density (equation 1.35), the resonant frequency for a given field line will depend on the mass density distribution along the field line, as well as the magnetic field. Therefore, the time-of-flight analysis of field line resonant frequencies presented by Wild et al. [2005] can be further refined by including the empirical mass density models developed previously (Chapter 5 and Chapter 6) to account for the mass density contribution, in addition to a realistic magnetic field model. This forms the basis of the following study.

7.2 Results

The time-of-flight technique is now applied to calculate the resonant frequencies for a range of field lines, using the T96 magnetic field model and the empirical mass density models presented in Chapter 5 and Chapter 6. The models involved separately modelling field-aligned variations of total electron density and average ion mass, using WHISPER and

CODIF observations respectively. The electron density models and average ion mass models included variations with L and MLT, and the combination of the models (using equation 3.1) provide corresponding mass density models covering all MLT and L values in the region of $5.9 \leq L < 9.5$. The models are based on the full datasets, for the time interval of 2001 - 2012.

7.2.1 Average mass density model

Figure 7.3 presents the resonant frequencies calculated with the time-of-flight approximation for a range of field lines, using the T96 magnetic field model and the average mass density model, presented in Chapter 5. The T96 magnetic field model used here corresponds to spring equinox, with a dynamic pressure of 2 nPa. For comparison, the frequencies have been calculated using both forms of the electron density model: the power law form (upper panels), and the use of the Gaussian function at low latitudes (lower panels). The left panels show the frequencies plotted at the field lines' position in the magnetic equatorial plane, and the right panels show the frequencies plotted at the field lines' footprint position. The spatial coverage of field lines shown is restricted by the L range of the mass density model used ($5.9 \leq L < 9.5$).

Figure 7.3 shows some differences in the time-of-flight calculations, which are further illustrated in Figure 7.4 and Figure 7.5, showing latitude profiles and MLT profiles for the calculated frequencies. The grey profiles represent the time-of-flight calculated frequencies using the radial power law mass density model. The green profiles correspond to the empirical mass density model, where the Gaussian function was used at low latitudes in the electron density model. The blue profiles correspond to the empirical mass density model, where a power law form was extrapolated and used at low latitudes. Many models using the power law form for plasma number density are based on spacecraft observations, which are used to fit for the equatorial electron density model parameter, n_{e0} , using a power law function (equation 5.2a). Assuming the power law index is described by equation 5.2d, electron density observations obtained by a spacecraft at high latitudes, where the power law dependence is observed, would correspond to a equatorial electron density value of n_{e0} under a power law distribution. In contrast, for a spacecraft located in the magnetic equatorial plane, the observed equatorial electron density would be equal to $n_{e0} + a$, due to the localised enhancement. Therefore, assuming a power law form for the field-aligned electron

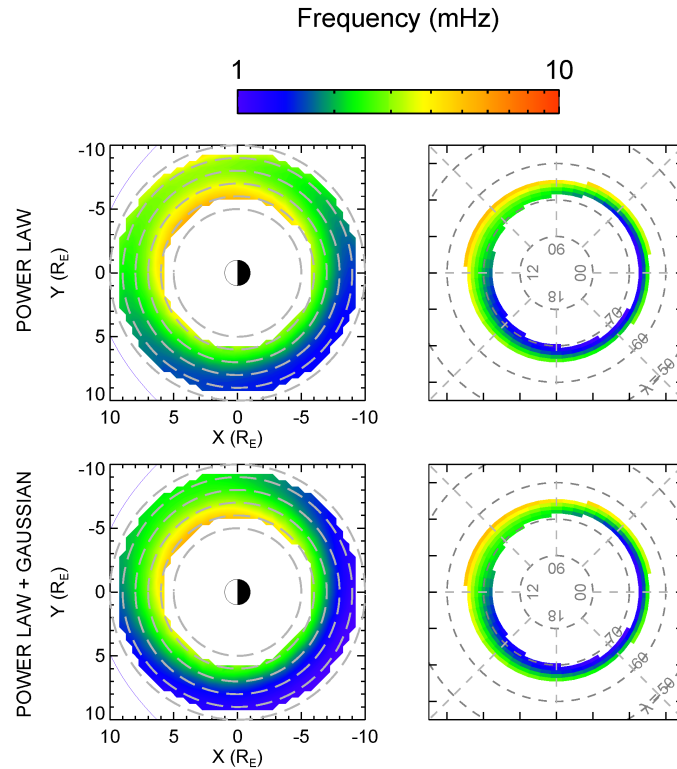


Figure 7.3: Same format as Figure 7.1, where the time-of-flight calculated frequencies correspond to the use of the T96 magnetic field model and the empirical average mass density model (a combination of the electron density model defined by equation 5.2 and the average ion mass model defined by equation 5.3, as discussed in Chapter 5). The frequencies using both the extrapolated power law form (upper row) and Gaussian function (lower row) for the low latitude electron density dependence are shown for comparison.

density can produce two models with different equatorial values, due to spacecraft locations. The corresponding mass density models were used to calculate the field line resonant frequencies using the time-of-flight technique, as represented by the blue profiles in Figure 7.4 and Figure 7.5. The blue solid profiles correspond to the power law form using an equatorial electron density equal to n_{e0} , representing results for high-latitude spacecraft observations, and the blue dashed profiles correspond to the power law form using an equatorial electron density equal to $n_{e0} + a$, representing results for equatorial spacecraft observations. The parameters n_{e0} and a are defined by equation 5.2c and equation 5.2e, respectively. The

time-of-flight calculations shown in Figure 7.4 and Figure 7.5 indicate several clear differences in estimated frequencies depending on the choice of mass density model, which will be discussed further in the following section.

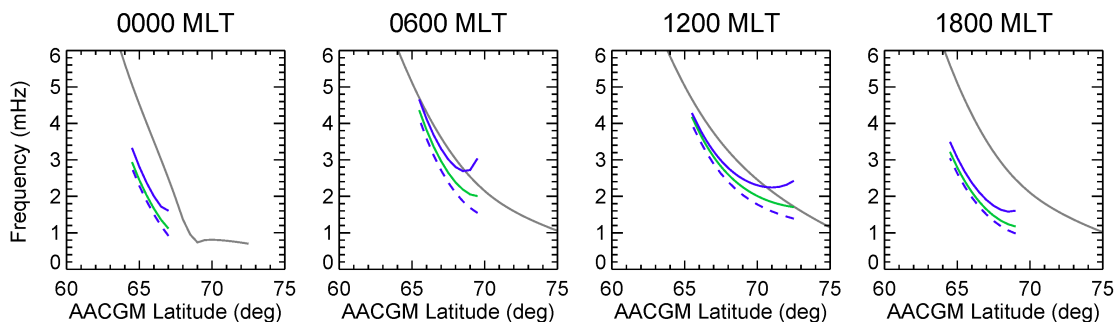


Figure 7.4: Field line oscillation frequency as a function of AACGM latitude, calculated using the time-of-flight approximation with the T96 magnetic field model and various mass density models (as indicated by the profile colours). The grey lines correspond to a radial power law mass density model, and the green and blue lines correspond to the empirical mass density model (a combination of the electron density model defined by equation 5.2 and the average ion mass model defined by equation 5.3, as discussed in Chapter 5). The blue lines show calculated frequencies using the extrapolated power law form for the low latitude electron density dependence, based on hypothetical spacecraft observations of electron density off-equator (solid) and in the equatorial plane (dashed). The green solid lines show calculated frequencies using the Gaussian function for the low latitude electron density dependence. Each panel corresponds to field lines at different MLTs, as indicated.

7.2.2 Dependence on geomagnetic activity

Time-of-flight calculations are also computed for the empirical mass density model including dependences with geomagnetic activity, presented in Chapter 6. As for the average model, the Dst model combines an empirical electron density model (equation 6.1) and empirical average ion mass model (equation 6.2), describing field-aligned variations, which are both parameterised by Dst index. The resulting mass density model describes Dst index variations from -100 nT to 10 nT.

Using the same approach as before, the time-of-flight approximation provides estimated

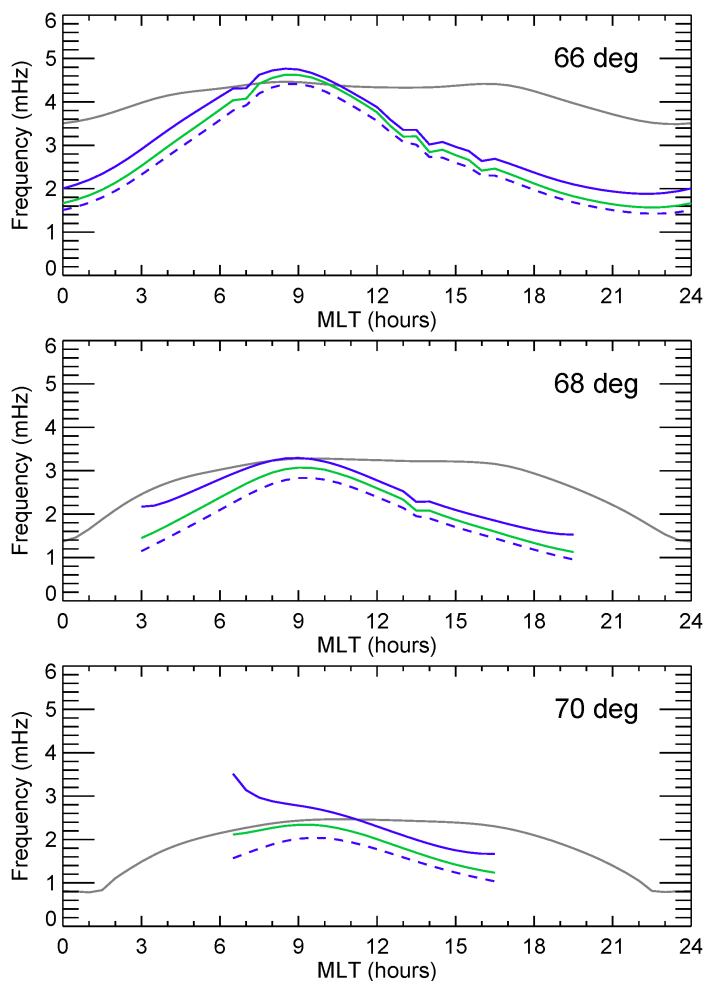


Figure 7.5: Field line oscillation frequency as a function of MLT, calculated using the time-of-flight approximation with the T96 magnetic field model and various mass density models (as indicated by the profile colours). The same colour coding is used as in Figure 7.4. Each panel corresponds to field lines at different AACGM latitude, as indicated.

Alfvén wave frequencies, assuming magnetic field and mass density models (equation 7.1). Figure 7.6 shows the estimated frequencies for a range of field lines covering all MLTs and $5.9 \leq L < 9.5$. Each row represents a different value of Dst index, used in the magnetic field model and mass density model, where both models are parameterised by Dst index. The T96 magnetic field was set to spring equinox conditions. Dst index values from -100 nT to 0 nT have been considered, representing geomagnetically active conditions to quiet conditions,

respectively. The left panels of Figure 7.6 show the frequencies plotted at the field lines' position in the magnetic equatorial plane and the right panels show the frequencies plotted at the field lines' ionospheric footprint. Note that the footprint latitude coverage shown in the right panels of Figure 7.6 varies with Dst index due to the mapping of field lines, as the inner magnetospheric field lines expand during times of enhanced ring current.

In order to compare frequency variations with Dst index more quantitatively, latitude profiles and MLT profiles are included in Figure 7.7 and Figure 7.8. The coloured profiles correspond to the use of the Dst mass density model at different values of Dst index, as labelled, and the grey profile corresponds to the use of the average mass density model, for comparison.

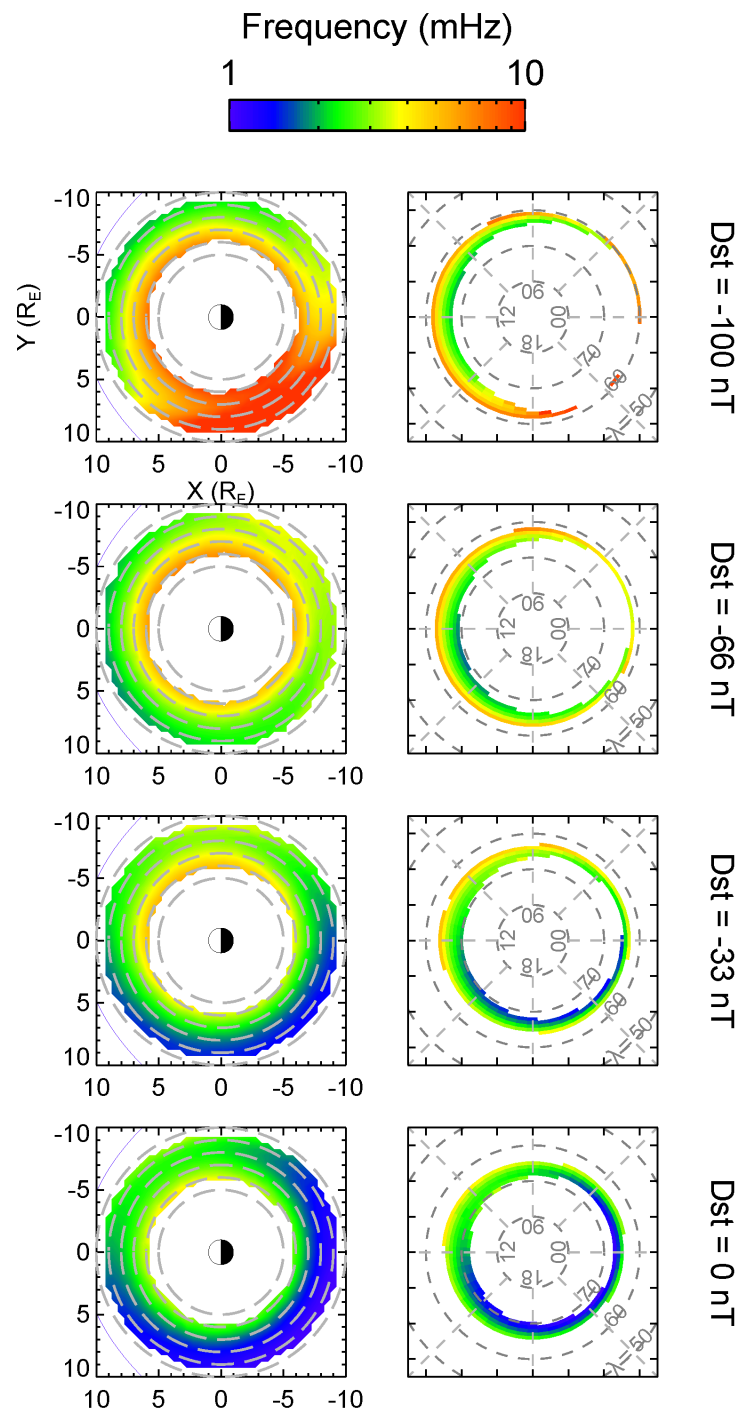


Figure 7.6: Same format as Figure 7.1, where the time-of-flight calculated frequencies correspond to the use of the T96 magnetic field model and the empirical Dst-dependent mass density model (a combination of the electron density model defined by equation 6.1 and the average ion mass model defined by equation 6.2, as discussed in Chapter 6). Each row corresponds to frequencies calculated for different values of the Dst index.

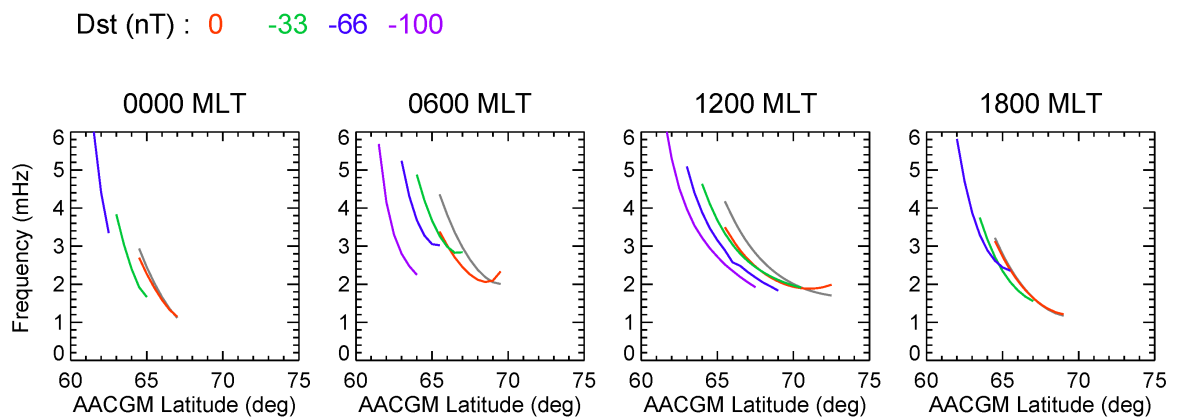


Figure 7.7: Same format as Figure 7.4, where frequencies are calculated using the time-of-flight approximation with the T96 magnetic field model and various mass density models (as indicated by the profile colours). The grey profiles correspond to the empirical average mass density model (a combination of the electron density model defined by equation 5.2 and the average ion mass model defined by equation 5.3, as discussed in Chapter 5). The red, green, blue, and purple profiles correspond to the use of various Dst index values with the empirical Dst-dependent mass density model (a combination of the electron density model defined by equation 6.1 and the average ion mass model defined by equation 6.2, as discussed in Chapter 6). The legend above the panels indicates the colour coding of the profiles using the empirical Dst-dependent mass density model.

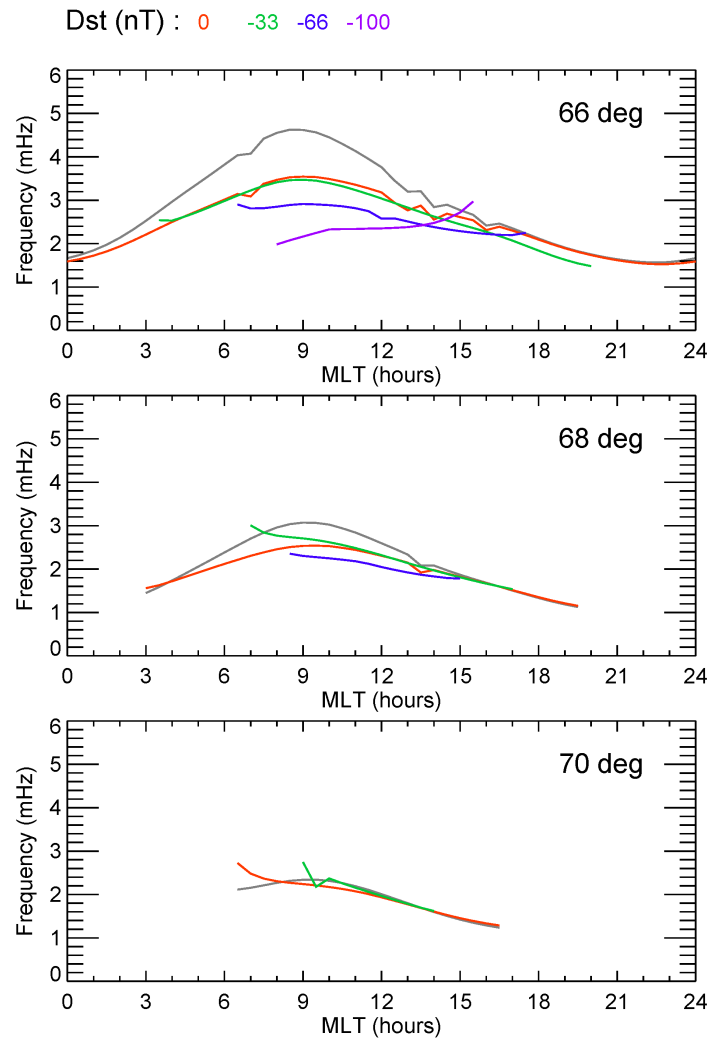


Figure 7.8: Same format as Figure 7.5, where frequencies are calculated using the time-of-flight approximation with the T96 magnetic field model and various mass density models (as indicated by the profile colours). The same colour coding is used as in Figure 7.7.

7.3 Discussion

The results of the time-of-flight calculations indicate several features and differences in profiles through using various mass density models. The contribution of the mass density models in estimating standing Alfvén wave frequencies will now be discussed.

7.3.1 Average mass density model

The aim of the time-of-flight analysis is to improve the estimates of Wild et al. [2005], where a simple radial power law mass density model was used with the realistic T96 magnetic field model. Through a comparison of the frequency profiles corresponding to the radial power law mass density model (solid grey) and the empirical mass density model (solid green), shown in Figure 7.4 and Figure 7.5, the contribution of the mass density distribution to standing Alfvén wave frequencies can be assessed. Figure 7.4 shows the frequency variation with footprint latitude. In agreement with multiple previous FLR observations and time-of-flight calculations, the estimated frequency for the radial power law mass density model (solid grey profile) is observed to decrease with increasing footprint latitude, across all MLT sectors (see also Figure 7.2), which is a feature attributed to the magnetic field contribution, as field line length increases and magnetic field strength decreases for increasing footprint latitude [Obayashi and Jacobs, 1958; Orr and Matthew, 1971; Samson et al., 1971; Samson and Rostoker, 1972; Yumoto et al., 1983; Glassmeier et al., 1984; Poulter et al., 1984; Engebretson et al., 1986; Mathie et al., 1999; Takahashi et al., 2002, 2004; Wild et al., 2005; Plaschke et al., 2008; Liu et al., 2009; Takahashi et al., 2015]. This feature is also observed for the profile corresponding to the empirical mass density model (solid green). As shown in Figure 5.3, the mass density is observed to decrease with increasing L value, which acts to increase the Alfvén speed (equation 1.35) and therefore, increase the standing Alfvén wave frequency (equation 7.1). The overall combination of the magnetic field and mass density variations is demonstrated by the empirical mass density model profile (solid green) in Figure 7.4, and the decrease in frequency with increasing latitude indicates that magnetic field variations are the dominant contribution.

Figure 7.5 illustrates the frequency variations with MLT, and it can be seen that the profile corresponding to the use of the radial power law mass density model (solid grey) demonstrates strong dependences with MLT, with frequency values maximising on the day-side. The diurnal variation in standing Alfvén wave frequency is a feature observed in pre-

vious studies [Yumoto et al., 1983; Junginger and Baumjohann, 1984; Poulter et al., 1984; Takahashi et al., 1984; Takahashi and McPherron, 1984; Mathie et al., 1999; Plaschke et al., 2008; Liu et al., 2009; Takahashi et al., 2015]. The radial power law mass density model profiles only include MLT asymmetries for the magnetic field contribution, and assumes the plasma mass density contribution has no MLT dependence. Therefore, the magnetic field results in higher frequencies on the dayside, where the magnetic field lines are shortest and the magnetic field strength maximises [Mathie et al., 1999; Wild et al., 2005]. By replacing the radial power law mass density model with the empirical mass density model, plasma mass density contributions to the MLT asymmetry in time-of-flight frequencies are included. The solid green profile in Figure 7.5 demonstrates the MLT dependences of the estimated frequencies using the empirical mass density model, which similarly to the use of the radial power law mass density model (solid grey profile), exhibits strong MLT dependences, although the peak frequency MLT location is shifted towards dawn and the lowest values are present towards dusk. This is due to the mass density values maximising in the evening sector, as a result of the plasmaspheric bulge and average ion mass enhancement (Figure 5.3), which acts to decrease the time-of-flight calculated frequencies [Junginger and Baumjohann, 1984; Takahashi et al., 2015]. Furthermore, the mass density contribution increases the MLT asymmetry of the frequency profiles, a feature observed through a comparison of the solid grey profiles and solid green profiles in Figure 7.5. It is noted that the frequency MLT asymmetry is greatest for lower latitudes (upper panel), corresponding to strongest mass density MLT asymmetries (Figure 5.3).

A comparison of the profiles corresponding to the empirical mass density model (green profile) and the radial power law mass density model (grey profile), in Figure 7.4 and Figure 7.5, indicate some large deviations, such that the empirical mass density model profile consistently displays lower frequency values. This suggests that the radial power law mass density model tends to underestimate mass density values compared to the empirical mass density model (equation 7.1 and equation 1.35). The reason for this could be due to the radial power law mass density model neglecting contributions of heavy ions to the total plasma mass density, whereas the empirical mass density model accounts for ion composition variations. The average ion mass model clearly indicates that it is inappropriate to assume a H^+ plasma for this region, and O^+ ions are a significant factor (Figure 5.3), which act to increase the total plasma mass density.

Overall, Figure 7.4 and Figure 7.5 demonstrate that the use of a realistic empirical mass density model, as opposed to a simple radial power law mass density model, refines the time-of-flight calculations. The consideration of ion composition and MLT asymmetries in the empirical mass density model provide further features in the spatial variations in field lines' resonant frequency, resulting in decreased frequency values, enhanced MLT asymmetries, and frequency values peaking at earlier MLTs compared to the use of a radial power law mass density model. This indicates that the mass density distribution represents a significant contribution to determining the resonant frequency of a field line, and using a simplified power law mass density model can produce large deviations in the calculated frequencies.

7.3.1.1 Contribution of equatorial enhancement

A key feature of the empirical mass density model is the inclusion of an observed localised enhancement in number density at the magnetic equatorial plane, neglected by previous models. As mentioned in Chapter 5, previous studies assume plasma number density follows a power law form along closed magnetic field lines, such that the number density maximises at the field line ionospheric footprint and approaches a minimum at the magnetic equatorial plane. The empirical model for total electron density (equation 5.2) found that although this distribution is appropriate for high latitudes, close to the magnetic equatorial point of a field line, a statistically significant localised enhancement in total electron density is observed. This was described by including a Gaussian form function at low latitudes (equation 5.2b). Figure 7.3 shows time-of-flight calculations corresponding to electron density models using the power law form extrapolated to low latitudes (upper panels) and using the Gaussian function at the equatorial region (lower panels). A comparison of the estimated frequencies presents some notable differences, indicating that the equatorial enhancement in plasma number density represents a non-negligible contribution in determining standing Alfvén wave frequencies. This will now be examined further, through a consideration of the latitude and MLT profiles.

Figure 7.4 shows differences between frequencies calculated using the empirical mass density model (green profile) and the empirical power law forms (blue profiles). As previously mentioned, the solid blue profiles are intended to represent hypothetical results for high-latitude spacecraft observations, and the dashed blue profiles represent hypothetical results for equatorial spacecraft observations. The solid blue profiles, representing a power

law electron density distribution with an equatorial value of n_{e0} , is larger than the dashed blue profiles, representing a power law electron density distribution with an equatorial value of $n_{e0} + a$. This is expected, because the dashed blue profile corresponds to larger number density values, and hence larger mass density values compared to the solid blue profile, across the full field line length. Therefore, as shown by equation 7.1 and equation 1.35, the decreased Alfvén speeds result in decreased standing Alfvén wave frequencies for a given field line. Figure 7.4 shows the green solid profile, corresponding to use of the empirical mass density model accounting for the equatorial enhancement in plasma number density, has frequency values above the blue dashed profile and below the blue solid profile. This is due to the number density values from the electron density model. Considering the corresponding electron density values used for each profile, the solid blue profile neglects the equatorial enhancement and provides values less than the solid green profile. On the other hand, the dashed blue profile does not account for the decrease in electron density away from the peak in the Gaussian region, assuming a power law form across the full field line, and provides values higher than the solid green profile. Therefore, the resulting mass density values for the solid blue profile will be less than the solid green profile, and the mass density values for the dashed blue profile will be greater than the solid green profile. The time-of-flight calculations shown in Figure 7.4 show that the solid blue profiles overestimate the resonant frequency and the dashed blue profiles underestimate the resonant frequency, through a comparison with the solid green profiles. Therefore, by assuming a power law form for the plasma number density, deviations from the corresponding observed peaked number density distribution occurs. Figure 7.4 indicates that the deviations are negligible at lower latitudes for the range considered here, and increase at higher latitudes. This is due to the observed equatorial enhancement in electron density becoming increasingly prominent at larger L values, attributed to the presence of the nightside plasma sheet population.

In addition to the latitude profiles (Figure 7.4), the MLT profiles shown in Figure 7.5 also demonstrate that the solid blue profile shows frequency values greater than the solid green profile, and the dashed blue profile shows frequency values lower than the solid green profile. The difference between the values is smallest at approximately noon and greatest towards nightside MLT sectors. This is due to the relative height of the equatorial number density enhancement being greatest for nightside MLT sector, corresponding to the presence of the plasma sheet population. Therefore, the blue profiles under/over-estimate frequencies most significantly for nightside MLT sectors. It can be concluded, from Figure 7.4 and Figure 7.5,

that using a power law form for number density in the low latitude region can result in large deviations compared to including a Gaussian form function to account for the equatorial number density enhancement, particularly at high L values for nightside MLT sectors.

7.3.2 Dependence on geomagnetic activity

The previous analysis has established that the use of an empirical mass density model provides more realistic estimations of standing Alfvén wave frequencies. However, the average mass density model, developed from averages over the full datasets, does not describe variations with geomagnetic activity. Time-of-flight calculations using the T96 magnetic field model and the mass density model including dependences with geomagnetic activity, presented in Chapter 6, where both models are parameterised by Dst index, are now assessed to explore how the magnetic field and mass density contributions to standing Alfvén wave frequencies vary with geomagnetic activity levels.

The study conducted by Wild et al. [2005] examined variations in resonant frequencies with Dst index, using the T96 magnetic field model and a radial power law mass density model, revealing the contribution of magnetic field changes in the time-of-flight calculations. The results showed that with increasingly negative Dst index values, the time-of-flight frequencies decreased, which is expected to be due to the magnetic field expanding and weakening as a result of an enhanced ring current.

Including the Dst-dependent mass density model in the time-of-flight calculations, representing a more realistic mass density distribution that includes dependences on geomagnetic activity levels, provides the frequency estimates shown in Figure 7.6. Considering the mass density dependence on Dst index independently, the combination of decreased number density and increased average ion mass during disturbed conditions was observed to result in generally decreased plasma mass density values, in comparison to quiet times, for the region considered (Chapter 6). A decrease in plasma mass density implies a corresponding increase in Alfvén speed (equation 1.35), and therefore, an increase in field lines' resonant frequencies (equation 7.1). Overall, for increasing levels of geomagnetic activity, the magnetic field changes act to decrease standing Alfvén wave frequencies [Wild et al., 2005], and the mass density changes act to increase standing Alfvén wave frequencies. The combination of these two competing variations provide the dependences shown in Figure 7.7 and Figure 7.8. The profiles in Figure 7.7 and Figure 7.8 show that, for a given footprint latitude, the estimated

frequencies decrease for increasingly negative Dst index values. Therefore, the results of the time-of-flight calculations indicate that during enhanced ring current conditions, the resonant frequencies of field lines, in the footprint latitude range considered, is decreased compared to periods of low geomagnetic activity. This provides evidence for magnetic field variations dominating over mass density variations, resulting in decreased frequencies for increasing ring current energy. Furthermore, comparing the frequencies corresponding to the average mass density model (grey profile) and the frequencies for quiet conditions (red profile), there is good agreement between the values. This is expected, as the average model represents the typical magnetospheric conditions.

Direct measurements of FLR frequencies support the time-of-flight calculations, where decreased frequencies are observed during disturbed conditions [Obertz and Raspopov, 1968; Warner and Orr, 1979; Engebretson and Cahill, 1981; Takahashi et al., 2002]. However, some previous observations (e.g. Takahashi et al. [2002]) have interpreted a decrease in frequencies as a corresponding increase in plasma mass density, as it is known that heavy ion concentration is increased during storm times (see section 6.6.2). The results of Chapter 6 indicate that a reduction in the number density during disturbed conditions results in an overall decrease in plasma mass density, outweighing the average ion mass variations, and that the decrease in standing Alfvén wave frequency is solely due to magnetic field variations. It is highlighted that changes in both the magnetic field and mass density require consideration when indirectly inferring mass density variations with geomagnetic activity.

Another notable feature of the time-of-flight calculations is the MLT location of minimum frequency values varies with Dst index, as apparent from Figure 7.6 and Figure 7.8. For quiet times, the time-of-flight frequencies approach a minimum in the evening MLT sector. For increasing Dst index, representing increasing levels of geomagnetic activity, the MLT location shifts to earlier MLT sectors, towards noon. This dependence was not present in the calculations of Wild et al. [2005], and therefore, can be attributed solely to the mass density contributions. The Dst mass density model shows that due to the sunward rotation of the plasmaspheric bulge, the MLT location of peak mass density values moves from dusk to noon (Chapter 5, in particular Figure 6.4). As increased mass density values correspond to decreased Alfvén speed (equation 1.35), and therefore decreased time-of-flight frequencies (equation 7.1), the MLT dependence of the estimated frequencies is a direct consequence of the mass density variations.

7.4 A comparison to ground magnetometer observations

In order to assess the validity of the time-of-flight calculations detailed previously, a comparison to observed FLR frequencies would prove useful. As reviewed in Chapter 2, there is a lack of large-scale, statistical studies of the FLR frequency distribution, which introduces difficulties in comparing the time-of-flight calculations to direct observations. Consequently, a statistical analysis of FLR frequencies, observed by ground magnetometers in the IMAGE array, is conducted here. The formation of standing Alfvén waves on closed geomagnetic field lines excites resonant oscillations of the field line, which can be observed in corresponding magnetic field perturbations on the ground. Toroidal standing Alfvén waves drive perturbations in the north-south direction, or x-component, at the ground, and by identifying the frequency of the perturbations, the natural frequency of the relevant field line is obtained. This section aims to identify the standing Alfvén wave frequencies of field lines, using ground magnetometer observations, and determine the variations in average frequency with L and MLT. The distribution of average frequencies can then be compared to the calculated time-of-flight frequencies.

The IMAGE ground magnetometer array, introduced in Chapter 3, is utilised here. The dataset employed in this study comprises observations obtained between 2001 - 2012, corresponding to the same time period as the Cluster dataset used for the mass density model. In order to routinely identify resonant oscillations in the observed north-south magnetic field component, B_x , an automated FLR identification method was developed, which will now be detailed.

7.4.1 Automated FLR identification

The crossphase technique [Waters et al., 1991] is chosen to identify resonant toroidal oscillations. Consider field line oscillations monitored by two ground magnetometer stations, latitudinally separated and approximately located along the same meridian, in the presence of a fast mode wave driving wave. The fast mode wave consists of a continuum of frequencies. For each station, the corresponding field line will resonate independently at its eigenfrequency, determined by the field line length, as well as the variation in magnetic field strength and plasma mass density along the field line (equation 7.1). Due to the variation in eigenfrequency with latitude, field lines located at the northern station and southern station will resonate with slightly different frequencies. This is illustrated in the top panel

7.4 A comparison to ground magnetometer observations

of Figure 7.9, showing a peak in amplitude at frequency ω_N , corresponding to the northern station, and a peak in amplitude at frequency ω_S , corresponding to the southern station. Assuming a linear variation in the resonant frequency, evaluating the crossphase between the B_x components from the two stations provides the crossphase difference function. The crossphase difference function will be peaked at the eigenfrequency corresponding to the field line located at the midpoint of the two stations considered, as illustrated in the bottom panel of Figure 7.9. Therefore, using the B_x component from two closely spaced stations, the resonant frequency of the midpoint field line can be determined via the crossphase technique. The crossphase technique makes some notable assumptions. Magnetic field lines are approximated as uncoupled, such that the oscillations are purely toroidal; only damping through ionospheric dissipation is present; and the coupling between the fast mode and toroidal wave mode is identical for all field lines. Despite the simplifying assumptions, the method has proved relatively robust for identifying FLR frequencies. It remains reliable at low signal strengths and is less sensitive to amplitude variations compared to alternative techniques [Waters et al., 1995].

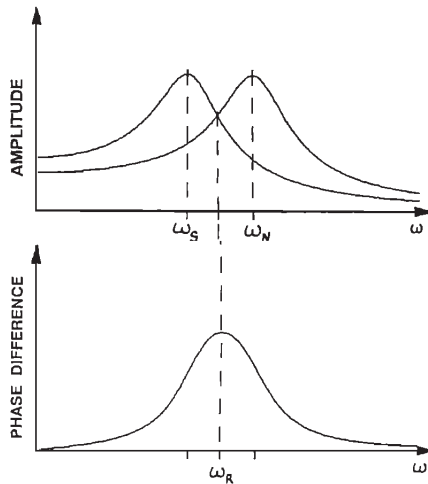


Figure 7.9: Schematic plots considering a resonant field line oscillation at frequency ω_N and a separate resonant field line oscillation at frequency ω_S [Waters et al., 1991]. The amplitude response (top panel) and crossphase difference (bottom panel) as a function of frequency, ω , are shown.

The crossphase technique is implemented in this study as part of an automated identification method. The automated method is demonstrated in Figure 7.10, which shows a

7.4 A comparison to ground magnetometer observations

representative sample of IMAGE data obtained between 00:00 - 12:00 UT on 10 November 2006, for the Abisko (ABK) and Tromsø (TRO) ground magnetometer stations. The steps taken to identify resonances and the frequencies of resonant oscillations in the B_x data are now detailed, where the relevant panels corresponding to each step of the process are as numbered on the right in Figure 7.10.

1. Taking the magnetic field data for two ground magnetometer stations that are closely spaced in latitude, the B_x timeseries are bandpass filtered between 100 s to 1000 s. Figure 7.10 shows the filtered B_x data from (a) ABK and (b) TRO.

2. Using a 40 minute sliding window, incremented by 10 minutes, the power spectrum and crossphase spectrum between the two B_x timeseries were computed, following Waters et al. [1991]. The spectra for the sample considered here are shown in Figure 7.10c and Figure 7.10d.

3. A defining feature of a FLR is a relatively stable oscillation with time, so in order to neglect variations on small timescales, hourly averages of the power and crossphase spectrum are calculated for each frequency bin. This is illustrated in Figure 7.10e and Figure 7.10f. Furthermore, frequency bins with an average power below the corresponding median hourly power are excluded and plotted as black. This is done because crossphase values with a small power are essentially random, and add noise to the spectrum.

4. The next step follows from the automated method of Berube et al. [2003]. The t statistic, defined as the mean crossphase divided by the crossphase standard deviation, is calculated for each hourly frequency bin. The resulting spectrum is shown in Figure 7.10g for the sample considered. The t statistic is low for bins consisting of large crossphase fluctuations, and consequently, it is useful for identifying stable, non-random, peaks in crossphase. All bins where $t \leq 1$ are plotted as black for the t statistic spectrum shown in Figure 7.10g. Values where $t \leq 1$ have a standard deviation greater than the mean crossphase, and the significance of the associated crossphase is low [Press, 1992; Berube et al., 2003]. This condition will be detailed further in the next step.

5. The final step of the method identifies the frequency associated with the peak hourly crossphase value (i.e. the frequencies of the peak crossphase values in Figure 7.10f), taking each hour interval individually. The frequencies for this sample are plotted in Figure 7.10h for each hour interval, shown by the horizontal black and grey lines. In order to identify whether the peak in crossphase at the frequency is associated with an FLR, the value of the t statistic corresponding to the frequency bin for the corresponding hour interval is

7.4 A comparison to ground magnetometer observations

consulted. Provided the t statistic meets the criterion $t > 1$, the frequency is validated as corresponding to a FLR, and plotted as black in Figure 7.10h. If the criterion is not met, an FLR has not been identified. The frequency is considered not valid and plotted as grey.

Therefore, this method enables the automated identification of FLRs, and the field line eigenfrequencies, from simultaneous B_x observations at two latitudinally separated ground magnetometer stations. For the sample shown in Figure 7.10, the crossphase spectrum shows a clear enhancement in the crossphase at a frequency of approximately 4 mHz (panel (c)), which can be visually identified as evidence of an FLR. The automated method identifies valid frequencies across this time interval (Figure 7.10h), in reasonable agreement with a visual identification. In addition, Figure 7.10h shows calculated frequencies using the time-of-flight approximation, assuming the T96 magnetic field model and the empirical average mass density model (see Chapter 5). The solar wind dynamic pressure, IMF B_y , IMF B_z , and Dst index values at the observation times are inputted into the T96 magnetic field model. A comparison of the frequencies identified using the automated method are in encouraging agreement with the time-of-flight estimates.

7.4 A comparison to ground magnetometer observations

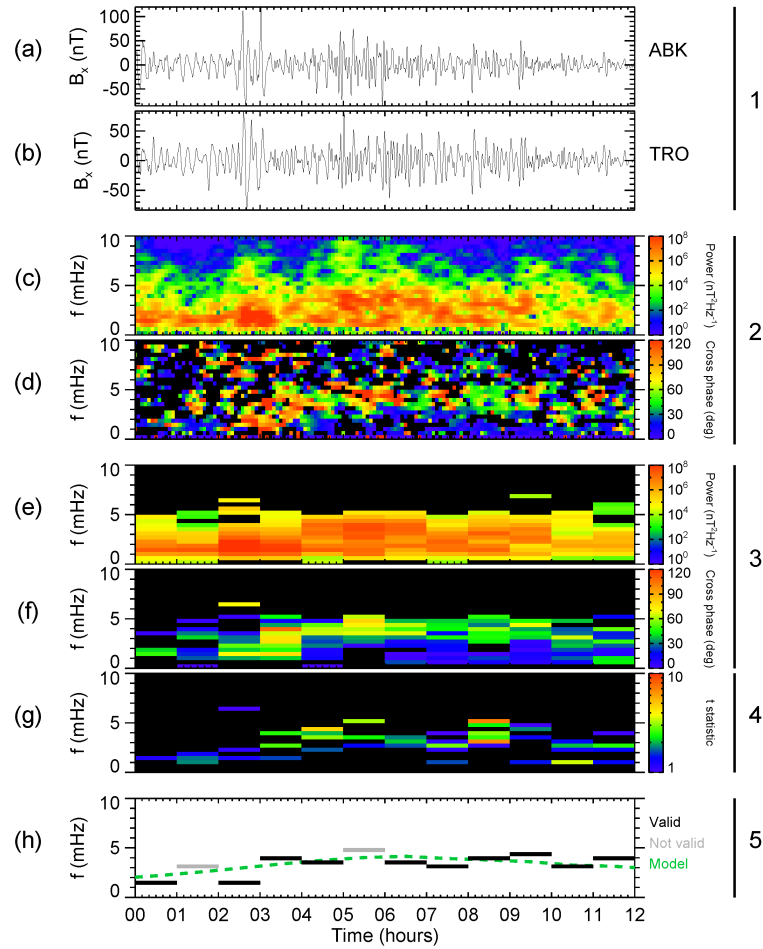


Figure 7.10: Magnetic field data for 10 November 2006, illustrating the automated FLR identification method. Panel (a) and panel (b) show B_x data (nT) from Abinsko (ABK) and Tromsø (TRO), respectively, bandpass filtered between 100 s to 1000 s. Panel (c) and panel (d) show the power ($\text{nT}^2 \text{Hz}^{-1}$) spectrum and crossphase (deg) spectrum, computed from the ABK and TRO data. Panel (e) and panel (f) show the corresponding power and crossphase spectra, where hourly averages have been taken for each frequency bin. Frequency bins corresponding to a hourly power value below the hourly median power are plotted as black. Panel (g) shows the t statistic spectrum, defined as the mean crossphase divided by the crossphase standard deviation. Values where $t \leq 1$ are plotted as black. Panel (h) shows frequency (mHz) values corresponding to the peak hourly crossphase, for each hour interval. Frequencies that meet the $t > 1$ criterion are validated and plotted as black, otherwise frequencies are not valid and plotted as grey. The green dashed line shows frequencies calculated under the time-of-flight approximation, assuming the T96 magnetic field model, and the empirical average mass density model presented in Chapter 5.

7.4.2 Statistical analysis of ground magnetometer observations

The automated FLR identification method is used in this study to examine the average variations in field line eigenfrequencies. Multiple station pairings were manually selected, with suitable separations and covering a range of latitudes. The magnetic latitude locations of the station pairs are shown in Figure 7.11a, with the midpoint magnetic latitude indicated by the red points. The choice of station pairs was influenced by the station separation. Closer station spacing results in smaller crossphase peak values at the resonant frequency, whereas greater spacing results in increased noise in the crossphase spectrum due to lower coherence [Waters et al., 1995; Menk et al., 1999]. Previous studies suggest an optimum station separation of approximately 110 km in latitude [Menk et al., 2004; Chi et al., 2013]. Although ideal station spacing is restricted by the station locations of the arrays, the station pairs used in this study is reasonable. Furthermore, latitudinal coverage is limited at the higher latitudes of the range considered, due to the station locations, although it remains sufficient. For each station pair, the automated FLR identification method was applied to the simultaneous B_x observations, for all data obtained within the time period of 2001 - 2012. This provides a database of FLR frequency observations for each station pair.

Figure 7.11 shows the results from the analysis. Panel (a) shows the station pairs used, indicating the station magnetic latitudes and midpoint magnetic latitudes. Panel (c) shows the frequencies, binned for MLT and averaged, and panel (d) shows the corresponding number of detected FLRs, identified via the automated method. Each row of data shown in Figure 7.11c and Figure 7.11d represent observations from the station pair in the same row of Figure 7.11a, where station pairs have been ordered from top to bottom in decreasing midpoint latitude. Clear dependences in the average frequency distribution with MLT and latitude are apparent from Figure 7.11c. These features correspond to an average over all geomagnetic conditions, and can be compared to time-of-flight calculations assuming the average mass density model. For reference, the time-of-flight calculations using the average mass density model (Chapter 5) are included in Figure 7.11b, where each row shows estimates for field lines at the corresponding midpoint AACGM latitude shown in Figure 7.11a. The latitudinal coverage of the time-of-flight calculations in Figure 7.11b is restricted by the L shell range of the mass density model ($5.9 \leq L < 9.5$).

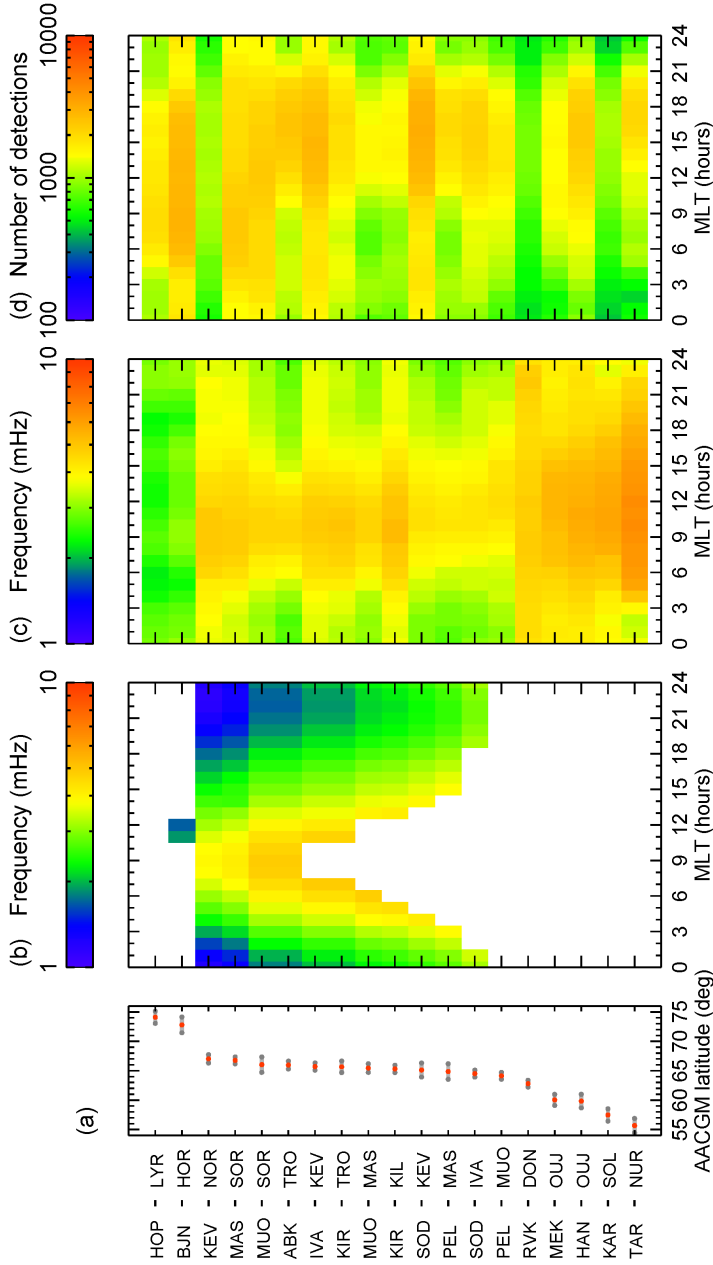


Figure 7.11: Panel (a) shows the station ACGM latitudes (degrees) (grey points) and midpoint ACGM latitude (red points) for the station pairs used in the IMAGE data analysis, with station identification codes labelled on the left of the panel. Panel (b) shows time-of-flight calculated frequencies (mHz) employing the empirical average mass density model and the T96 magnetic field model at spring equinox. The average frequency (mHz) and number of detections using the automated FLR identification method are shown in panel (c) and panel (d), respectively, where values have been binned for MLT (hours). Following the same format as panel (a), each row corresponds to a station pairing, where the midpoint ACGM latitude was used for the time-of-flight calculations.

7.4 A comparison to ground magnetometer observations

It can be seen from Figure 7.11c that the field line eigenfrequency tends to decrease with increasing latitude, in agreement with the time-of-flight calculations (Figure 7.11b). In order to present a more quantitative comparison of the time-of-flight calculations and ground magnetometer analysis, the latitudinal dependences are explored further in Figure 7.12. Figure 7.12 shows eigenfrequency variations with magnetic latitude, where each panel displays a different MLT, as labelled. The green profiles represent the time-of-flight calculations, assuming the T96 magnetic field model and the average mass density model (Chapter 5), corresponding to results shown in Figure 7.12b and Figure 7.3. For comparison, time-of-flight calculations using the T96 magnetic field model, but with the simple radial power law mass density model (Figure 7.2), is shown by the grey profiles. Figure 7.12 also includes the IMAGE observations, shown by the purple points, where each point represents a station pair from the selection detailed in Figure 7.11a. The purple points are plotted at the midpoint magnetic latitude, and the mean frequency value in the relevant MLT bin, corresponding to Figure 7.11. The error bars indicate the upper and lower quartile of frequency values in the MLT bin. The results shown in Figure 7.12 show that, in general, the time-of-flight calculations are in reasonable agreement with the average frequencies observed in the ground magnetometer dataset. Furthermore, the time-of-flight calculations based on the average mass density model appear to provide estimates closer to the ground magnetometer FLR observations, in comparison to the time-of-flight calculations using the radial power law mass density model. This suggests that the time-of-flight calculations are improved through the use of a more realistic mass density model. The difference is particularly apparent for 1800 MLT (fourth panel of Figure 7.12), an MLT sector where the mass density is strongly influenced by the plasmaspheric bulge and enhanced heavy ion population. These features are encapsulated in the empirical mass density model, unlike the simple radial power law mass density model, such that the resulting time-of-flight calculations demonstrate better agreement with the IMAGE FLR observations in this region.

In addition to latitudinal features, Figure 7.11c also shows MLT asymmetries in the frequency of standing Alfvén waves observed in the IMAGE dataset. Frequencies peak in the morning MLT sector, in agreement with the time-of-flight calculated frequencies (Figure 7.11b, Figure 7.3, and Figure 7.5). Figure 7.13 compares the MLT variations in field line eigenfrequency, for the time-of-flight calculations (green profiles and grey profiles), and the average ground magnetometer observations (purple profile), where the colour coding used is as in Figure 7.12. A representative sample of station pairs are shown. Each panel

7.4 A comparison to ground magnetometer observations

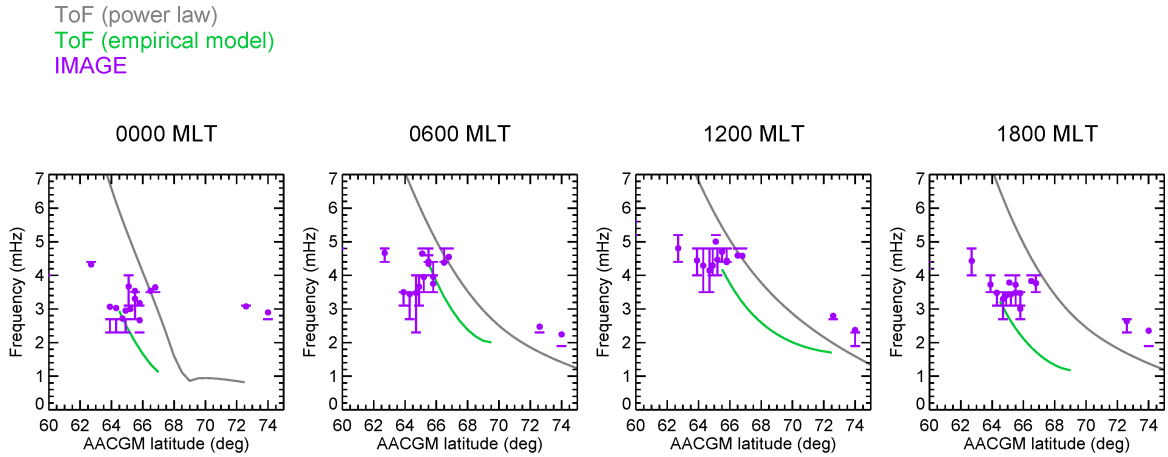


Figure 7.12: Field line oscillation frequency (mHz) as a function of AACGM latitude (degrees), where each panel corresponds to field lines at different MLT (hours) values, as labelled. Time-of-flight calculated frequencies are shown by the green profiles and the grey profiles. The T96 magnetic field model is used, and the green profile corresponds to use of the empirical mass density model, whereas the grey profile corresponds to use of a simple radial power law mass density model. The average frequencies identified in the ground magnetometer dataset are shown by the purple points, where each point corresponds to a different station pairing, and are plotted at the midpoint latitude between stations. The error bars on the purple points indicate the upper and lower quartile values.

corresponds to a different station pair from those shown in Figure 7.11a, and the midpoint latitude is labelled on the right of each panel for reference. The results shown in Figure 7.13 provide further evidence that the time-of-flight calculations are improved through using the empirical average mass density model, as opposed to the radial power law mass density model. The estimated frequencies corresponding to the empirical average mass density model (green profile) tend to have values closer to the average FLR frequencies (purple profile), than estimated frequencies using the radial power law mass density model (grey profile).

However, it is important to note that at higher latitudes, some deviations are apparent. The time-of-flight estimates using the empirical mass density model (green profile) appear to be consistently lower compared to the average IMAGE observations, evident from both Figure 7.12 and Figure 7.13. It is noted that the station pair coverage of IMAGE ground magnetometer stations is relatively sparse for the higher magnetic latitudes considered here,

7.4 A comparison to ground magnetometer observations

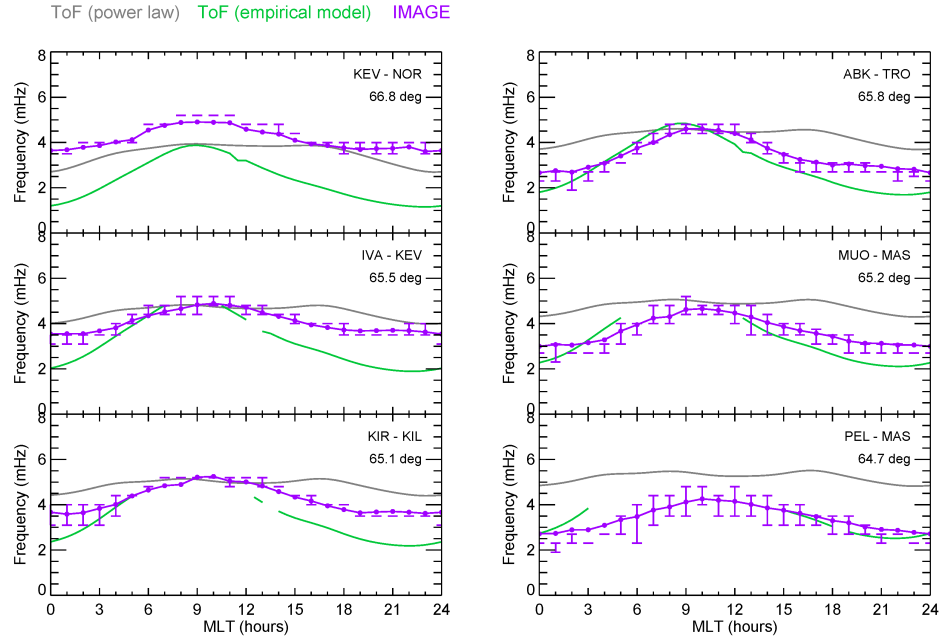


Figure 7.13: Field line oscillation frequency (mHz) as a function of MLT (hours), where each panel corresponds to a different station pair used in the ground magnetometer data analysis, as labelled. The purple profiles correspond to the average frequency observed for the station pair, with upper and lower quartile values indicated by the error bars. Using the midpoint AACGM latitude of the station pair, frequencies are calculated using the time-of-flight approximation, as shown by the green profiles and the grey profiles, assuming the T96 magnetic field model. The green profiles correspond to the use of the empirical mass density model, and the grey profiles correspond to the use of a simple radial power law mass density model.

in comparison to station pairs located at magnetic latitudes of approximately 65 degrees. Furthermore, due to the restricted station coverage, station spacing deviates slightly from ideal separation. As a consequence, the statistical significance of the average frequencies observed in the IMAGE dataset is reduced for the higher latitude station pairs shown in Figure 7.11, Figure 7.12, and Figure 7.13. An additional consideration is that the automated FLR identification method may be biased due to the choice of window size used for determining the crossphase spectrums. The window size may suppress detection of low frequency FLRs, and bias the observed FLR frequency distribution.

Overall, a comparison of the time-of-flight calculations and average frequencies observed by IMAGE indicate encouraging agreement in the values, as well as agreement in latitudinal

7.4 A comparison to ground magnetometer observations

and local time dependences. Furthermore, by using the more realistic empirical average mass density model, the time-of-flight estimates appear to provide values closer to the ground magnetometer observations, than calculations using a simple radial power law mass density model. Therefore, it can be concluded that the time-of-flight estimates here provide valid frequency estimates, relative to previous estimates using a simple mass density model.

The results obtained here have scope for improvement and further study. A key restriction of the IMAGE data analysis is the latitudinal coverage of ground magnetometer stations, which imposes limitations on the statistical significance of the average frequency distributions observed. An area of future work will involve extending the analysis to include data from additional ground magnetometer arrays, such as CARISMA (Canadian Array for Realtime Investigations of Magnetic Activity), in order to improve the latitudinal coverage. In addition, a possible suppression of low frequency FLR detection in the automated FLR identification method requires examination. The dataset of observed frequencies, identified using the automated method, can also be analysed further to understand variations and dependences of field line eigenfrequencies with geomagnetic conditions and solar wind driving. This will allow the validity of time-of-flight calculations using the Dst mass density model (Chapter 6) to be assessed.

Chapter 8

Conclusions and Future Work

This study has examined the spatial distribution of the total plasma mass density in the closed magnetosphere using Cluster observations. The total plasma mass density is a fundamental parameter of the magnetosphere, determining the propagation of wave modes and energy transfer, and the spatial distribution provides valuable insight into the morphology and dynamics of the terrestrial magnetosphere.

Using observations obtained by the WHISPER and CODIF instruments on-board Cluster, empirical models describing the field-aligned distribution of electron density and average ion mass along closed geomagnetic field lines were obtained, including dependences with L shell and MLT. The data spans a time interval from approximately 2001 – 2012, and represents the region of $5.9 \leq L < 9.5$, corresponding to the outer plasmasphere, plasmatrough, and near-Earth plasma sheet. A key result obtained is the presence of a localised peak in electron density close to the magnetic equator in the electron density model, neglected by many previous models. Furthermore, the average ion mass model indicates the presence of heavy ions expected to originate from high-latitude ionospheric outflows. The resulting models are combined to infer the spatial distribution of the plasma mass density, providing information on the plasma mass loading processes occurring in this region, and their dependences with L and MLT. Notable differences between this model and previous empirical models are the size and coverage of the underlying datasets, the inclusion of the ion composition contribution to determining mass density, and that a localised enhancement in the plasma number density close to the magnetic equatorial plane is accounted for.

The analysis was furthered by assessing variations in the electron density, average ion

mass, and total plasma mass density with geomagnetic activity. Using the same approach as the average model, dependences with Dst index, as well as L value and MLT, were quantified in the field-aligned distributions for electron density and average ion mass. The combination of the models provide information on how plasma mass density varies between quiet and geomagnetically disturbed conditions, and how the spatial distribution changes. The results illustrate the effects of various storm-related magnetospheric dynamics on the spatial distributions of electron density, average ion mass and total mass density. The key findings of this analysis include the observed decrease in mass density during disturbed conditions for the majority of field lines, a result contradicting previous observations, which indicates the dominance of changes in the number density over ion composition variations. An exception to this dependence is the observed enhancement in the total plasma mass density for the morning sector at higher L values. This feature corresponds to a relatively less dramatic reduction in number density in this region, such that the increase in average ion mass dominates.

The mass density models developed demonstrate the strong dependences of number density and ion composition with L , MLT, and geomagnetic disturbances, indicating that simplistic power law models developed by previous studies are not representative of the field-aligned mass density distribution. The direct in-situ data used to observe both number density and ion composition, allow the distribution along closed field lines to be modelled without prior assumption of a functional form. This is a key advantage over the inversion technique used in previous studies, where spacecraft measurements of multiharmonic toroidal Alfvén wave frequencies are used to indirectly infer the field-aligned distribution, assuming a functional form. However, the inversion technique provides a distribution along a full field line at a given time, whereas the method used here, produces a statistical average over many observations. An area of future work could involve using the realistic functional forms for the field-aligned distribution developed here, combined with the inversion methodology, to provide a more representative and valid description of magnetospheric mass density variations.

The final part of this study explored a possible application of the empirical mass density models. Using a time-of-flight technique, the frequencies of standing Alfvén waves were estimated, employing the T96 magnetic field model and the empirical mass density models. This represents an improvement on the estimates of Wild et al. [2005], where the T96 magnetic field model was used in conjunction with a relatively simplistic power law mass density

model. The results showed significant deviations in calculated frequencies through the use of a more realistic mass density model. Furthermore, the effect of including the equatorial enhancement in number density was examined, and the variations with geomagnetic activity were assessed. A key result was the observed decrease in field line eigenfrequency with increasing geomagnetic activity, in agreement with direct observations of field line oscillations. Although previous studies attributed this to a decrease in magnetic field strength combined with an increase in mass density, this analysis showed the mass density actually increases. However, this feature is masked by the dominating magnetic field variations. The study is concluded by testing the validity of the time-of-flight calculations through a comparison to ground magnetometer observations of FLRs. An automated FLR detection method was developed, and applied to an IMAGE dataset covering a time period of 2001 – 2012, to determine the average FLR frequency distribution in L -MLT space. The results show that a closer agreement with the FLR frequencies is observed through the use of the realistic mass density model, as opposed to a simple power law mass density model, in the time-of-flight calculations.

A clear area of future work is further analysis of the IMAGE FLR observations, to determine variations in the spatial distribution of FLR frequency with Dst index. This will allow the time-of-flight calculations, based on the Dst mass density model, to be compared to the ground magnetometer observations. Furthermore, extending the analysis to include CARISMA ground magnetometer observations will improve latitudinal coverage.

References

- Akasofu, S.-I., S. Chapman, and B. Venkatesan (1963), The Main Phase of Great Magnetic Storms, *J. Geophys. Res.*, *68*, 3345–3350, doi:10.1029/JZ068i011p03345. 38
- Alexeev, I. I., E. S. Belenkaya, V. V. Kalegaev, Y. I. Feldstein, and A. Grafe (1996), Magnetic storms and magnetotail currents, *J. Geophys. Res.*, *101*, 7737–7748, doi:10.1029/95JA03509. 38
- Alfvén, H. (1943), On the Existence of Electromagnetic-Hydrodynamic Waves, *Arkiv for Astronomi*, *29*, 1–7. 14
- Allan, W., and E. M. Poulter (1992), ULF waves-their relationship to the structure of the Earth's magnetosphere, *Reports on Progress in Physics*, *55*, 533–598, doi:10.1088/0034-4885/55/5/001. 39
- Andre, M., and A. Yau (1997), Theories and Observations of Ion Energization and Outflow in the High Latitude Magnetosphere, *Space Sci. Rev.*, *80*, 27–48, doi:10.1023/A:1004921619885. 27, 28, 31, 98, 99, 100, 116, 130, 134
- Axford, W. I. (1968), The polar wind and the terrestrial helium budget, *J. Geophys. Res.*, *73*, 6855–6859, doi:10.1029/JA073i021p06855. 27
- Baker, D. N., and R. L. McPherron (1990), Extreme energetic particle decreases near geostationary orbit - A manifestation of current diversion within the inner plasma sheet, *J. Geophys. Res.*, *95*, 6591–6599, doi:10.1029/JA095iA05p06591. 35
- Baker, D. N., T. I. Pulkkinen, V. Angelopoulos, W. Baumjohann, and R. L. McPherron (1996), Neutral line model of substorms: Past results and present view, *J. Geophys. Res.*, *101*, 12,975–13,010, doi:10.1029/95JA03753. 33

- Baker, K. B., and S. Wing (1989), A new magnetic coordinate system for conjugate studies at high latitudes, *J. Geophys. Res.*, *94*, 9139–9143, doi:10.1029/JA094iA07p09139. 58
- Bartels, J., N. H. Heck, and H. F. Johnston (1939), The three-hour-range index measuring geomagnetic activity, *Terrestrial Magnetism and Atmospheric Electricity*, *44*(4), 411–454, doi:10.1029/TE044i004p00411. 119
- Baumjohann, W., and R. Treumann (1996), *Basic Space Plasma Physics*, Imperial College Press. v, vi, vii, 2, 7, 14, 19, 22, 24, 33, 34, 36, 39
- Berchem, J., and J. Etcheto (1981), Experimental study of magnetospheric convection, *Advances in Space Research*, *1*, 179–184, doi:10.1016/0273-1177(81)90104-6. 126
- Berube, D., M. B. Moldwin, and J. M. Weygand (2003), An automated method for the detection of field line resonance frequencies using ground magnetometer techniques, *Journal of Geophysical Research (Space Physics)*, *108*, 1348, doi:10.1029/2002JA009737. 163
- Berube, D., M. B. Moldwin, S. F. Fung, and J. L. Green (2005), A plasmaspheric mass density model and constraints on its heavy ion concentration, *J. Geophys. Res.*, *110*, A04212, doi:10.1029/2004JA010684. 44, 45, 46, 47, 93, 101, 105, 126, 130
- Borovsky, J. E., and M. H. Denton (2006), Effect of plasmaspheric drainage plumes on solar-wind/magnetosphere coupling, *Geophys. Res. Lett.*, *33*, L20101, doi:10.1029/2006GL026519. 1
- Borovsky, J. E., and M. H. Denton (2008), A statistical look at plasmaspheric drainage plumes, *Journal of Geophysical Research (Space Physics)*, *113*, A09221, doi:10.1029/2007JA012994. 128, 132
- Burch, J. L., D. G. Mitchell, B. R. Sandel, P. C. Brandt, and M. Wüest (2001), Global dynamics of the plasmasphere and ring current during magnetic storms, *Geophys. Res. Lett.*, *28*, 1159–1162, doi:10.1029/2000GL012413. 101, 128, 131
- Caan, M. N., R. L. McPherron, and C. T. Russell (1977), Characteristics of the association between the interplanetary magnetic field and substorms, *J. Geophys. Res.*, *82*, 4837–4842, doi:10.1029/JA082i029p04837. 33

- Carpenter, D. L. (1966), Whistler studies of the plasmopause in the magnetosphere: 1. Temporal variations in the position of the knee and some evidence on plasma motions near the knee, *J. Geophys. Res.*, *71*, 693–709, doi:10.1029/JZ071i003p00693. 30, 93, 127
- Carpenter, D. L. (1970), Whistler evidence of the dynamic behavior of the duskside bulge in the plasmasphere, *J. Geophys. Res.*, *75*, 3837–3847, doi:10.1029/JA075i019p03837. 30, 93, 128
- Carpenter, D. L., and R. R. Anderson (1992), An ISEE/Whistler model of equatorial electron density in the magnetosphere, *J. Geophys. Res.*, *97*, 1097–1108, doi:10.1029/91JA01548. 30, 45, 93, 126
- Chapman, S. (1918), An Outline of a Theory of Magnetic Storms, *Royal Society of London Proceedings Series A*, *95*, 61–83, doi:10.1098/rspa.1918.0049. 20, 36, 108
- Chapman, S., and J. Bartels (1940), *Geomagnetism*, no. v. 1 in The International series of monographs on physics, Clarendon Press. 36
- Chapman, S., and V. C. A. Ferraro (1930), A New Theory of Magnetic Storms., *Nature*, *126*, 129–130, doi:10.1038/126129a0. 21, 30
- Chapman, S., and V. C. A. Ferraro (1931), A new theory of magnetic storms, *Terrestrial Magnetism and Atmospheric Electricity (Journal of Geophysical Research)*, *36*, 77, doi:10.1029/TE036i002p00077. 21, 30
- Chappell, C. R. (1972), Recent satellite measurements of the morphology and dynamics of the plasmasphere., *Rev. Geophys.*, *10*, 951–979, doi:10.1029/RG010i004p00951. vii, 29, 30, 93, 126, 127, 128, 144
- Chappell, C. R. (1982), Initial observations of thermal plasma composition and energetics from Dynamics Explorer-1, *Geophys. Res. Lett.*, *9*, 929–932, doi:10.1029/GL009i009p00929. 101, 130
- Chappell, C. R. (1988), The terrestrial plasma source - A new perspective in solar-terrestrial processes from Dynamics Explorer, *Reviews of Geophysics*, *26*, 229–248, doi:10.1029/RG026i002p00229. 28, 98, 99, 100, 116, 130, 134

- Chappell, C. R., K. K. Harris, and G. W. Sharp (1970), The morphology of the bulge region of the plasmasphere, *J. Geophys. Res.*, *75*, 3848, doi:10.1029/JA075i019p03848. 30, 93, 127
- Chappell, C. R., T. E. Moore, and J. H. Waite, Jr. (1987), The ionosphere as a fully adequate source of plasma for the earth's magnetosphere, *J. Geophys. Res.*, *92*, 5896–5910, doi:10.1029/JA092iA06p05896. 28, 98, 99, 100, 116, 130, 134
- Chen, A. J., and R. A. Wolf (1972), Effects on the plasmasphere of a time-varying convection electric field, *Planetary and Space Science*, *20*, 483–509, doi:10.1016/0032-0633(72)90080-3. 126
- Chen, L., and A. Hasegawa (1974), A theory of long-period magnetic pulsations: 1. Steady state excitation of field line resonance, *J. Geophys. Res.*, *79*, 1024–1032, doi:10.1029/JA079i007p01024. 43
- Chi, P. J., et al. (2013), Sounding of the plasmasphere by Mid-continent MAgnetoSeismic Chain (McMAC) magnetometers, *Journal of Geophysical Research (Space Physics)*, *118*, 3077–3086, doi:10.1002/jgra.50274. 166
- Clark, J., and A. Gelfand (2006), *Hierarchical Modelling for the Environmental Sciences : Statistical methods and applications: Statistical methods and applications*, Oxford biology, Oxford University Press, UK. 79, 108
- Clausen, L. B. N., T. K. Yeoman, R. C. Fear, R. Behlke, E. A. Lucek, and M. J. Engebretson (2009), First simultaneous measurements of waves generated at the bow shock in the solar wind, the magnetosphere and on the ground, *Ann. Geophys.*, *27*, 357–371, doi:10.5194/angeo-27-357-2009. ix, 61, 62
- Comfort, R. H., I. T. Newberry, and C. R. Chappell (1988), Preliminary statistical survey of plasmaspheric ion properties from observations by DE 1/RIMS, *Washington DC American Geophysical Union Geophysical Monograph Series*, *44*, 107–114, doi:10.1029/GM044p0107. 101, 127, 130, 141
- Coroniti, F. V. (1985), Explosive tail reconnection - The growth and expansion phases of magnetospheric substorms, *J. Geophys. Res.*, *90*, 7427–7447, doi:10.1029/JA090iA08p07427. 35

- Coroniti, F. V., and C. F. Kennel (1972), Changes in magnetospheric configuration during the substorm growth phase, *J. Geophys. Res.*, *77*, 3361, doi:10.1029/JA077i019p03361. 34
- Cowley, S. W. H. (1981a), Magnetospheric asymmetries associated with the y-component of the IMF, *Planet. Space Sci.*, *29*, 79–96, doi:10.1016/0032-0633(81)90141-0. 25
- Cowley, S. W. H. (1981b), Magnetospheric and ionospheric flow and the interplanetary magnetic field, in *The Physical Basis of the Ionosphere in the Solar-Terrestrial System*, pp. (4–1)–(4–14), AGARD-CP-295. 25
- Cowley, S. W. H. (1982), The causes of convection in the earth’s magnetosphere - A review of developments during the IMS, *Reviews of Geophysics and Space Physics*, *20*, 531–565, doi:10.1029/RG020i003p00531. 126
- Cowley, S. W. H., and M. Lockwood (1992), Excitation and decay of solar wind-driven flows in the magnetosphere-ionosphere system, *Annales Geophysicae*, *10*, 103–115. 25
- Cully, C. M., E. F. Donovan, A. W. Yau, and H. J. Opgenoorth (2003), Supply of thermal ionospheric ions to the central plasma sheet, *Journal of Geophysical Research (Space Physics)*, *108*, 1092, doi:10.1029/2002JA009457. 28, 99, 130
- Cummings, W. D., R. J. O’Sullivan, and P. J. Coleman, Jr. (1969), Standing Alfvén waves in the magnetosphere, *J. Geophys. Res.*, *74*, 778, doi:10.1029/JA074i003p00778. 78, 90
- Cummings, W. D., C. Countee, D. Lyons, and W. Wiley (1975), The dominant mode of standing Alfvén waves at the synchronous orbit, *Journal of Geophysical Research*, *80*(25), 3705–3708, doi:10.1029/JA080i025p03705. 42
- Daglis, I. A. (1997), The role of magnetosphere-ionosphere coupling in magnetic storm dynamics, *Washington DC American Geophysical Union Geophysical Monograph Series*, *98*, 107–116, doi:10.1029/GM098p0107. 38
- Daglis, I. A., R. M. Thorne, W. Baumjohann, and S. Orsini (1999), The terrestrial ring current: Origin, formation, and decay, *Reviews of Geophysics*, *37*, 407–438, doi:10.1029/1999RG900009. 30

- Dandouras, I., et al. (2005), Multipoint Observations of Ionic Structures in the Plasmasphere by CLUSTER-CIS and Comparisons With IMAGE-EUV Observations and With Model Simulations, *Washington DC American Geophysical Union Geophysical Monograph Series*, 159, 23. 99, 130
- Dandouras, I., A. Barthe, and the CIS Team (2014), User Guide to the CIS measurements in the Cluster Active Archive (CAA), *Tech. rep.*, CAA-EST-UG-CIS 3.3. xx, 57
- Darrouzet, F., et al. (2009), Plasmaspheric Density Structures and Dynamics: Properties Observed by the CLUSTER and IMAGE Missions, *Space Sci. Rev.*, 145, 55–106, doi:10.1007/s11214-008-9438-9. 101, 130
- Darrouzet, F., V. Pierrard, S. Benck, G. Lointier, J. Cabrera, K. Borremans, N. Y. Ganushkina, and J. D. Keyser (2013), Links between the plasmopause and the radiation belt boundaries as observed by the instruments CIS, RAPID, and WHISPER onboard Cluster, *Journal of Geophysical Research (Space Physics)*, 118, 4176–4188, doi:10.1002/jgra.50239. 30
- Décrou, P. M. E., D. Carpenter, C. R. Chappell, J. Green, and J. H. Waite, Jr. (1986), Latitudinal plasma distribution in the dusk plasmaspheric bulge - Refilling phase and quasi-equilibrium state, *J. Geophys. Res.*, 91, 6929–6943, doi:10.1029/JA091iA06p06929. 97
- Décrou, P. M. E., et al. (1997), Whisper, a Resonance Sounder and Wave Analyser: Performances and Perspectives for the Cluster Mission, *Space Sci. Rev.*, 79, 157–193, doi:10.1023/A:1004931326404. 54, 55
- Dejong, A. D., A. J. Ridley, and C. R. Clauer (2008), Balanced reconnection intervals: four case studies, *Annales Geophysicae*, 26, 3897–3912, doi:10.5194/angeo-26-3897-2008. 33
- Dent, Z. C., I. R. Mann, J. Goldstein, F. W. Menk, and L. G. Ozeke (2006), Plasmaspheric depletion, refilling, and plasmopause dynamics: A coordinated ground-based and IMAGE satellite study, *Journal of Geophysical Research (Space Physics)*, 111, A03205, doi:10.1029/2005JA011046. 126, 127, 136, 137
- Denton, R. E., J. Goldstein, J. D. Menietti, and S. L. Young (2002), Magnetospheric electron density model inferred from Polar plasma wave data, *J. Geophys. Res.*, 107, 1386, doi:10.1029/2001JA009136. 90, 91, 93, 97, 125, 126, 127, 129

- Denton, R. E., J. D. Menietti, J. Goldstein, S. L. Young, and R. R. Anderson (2004), Electron density in the magnetosphere, *J. Geophys. Res.*, *109*, A09215, doi:10.1029/2003JA010245. 90, 93, 97, 125, 126, 127, 129
- Denton, R. E., K. Takahashi, I. A. Galkin, P. A. Nsumei, X. Huang, B. W. Reinisch, R. R. Anderson, M. K. Sleeper, and W. J. Hughes (2006), Distribution of density along magnetospheric field lines, *J. Geophys. Res.*, *111*, A04213, doi:10.1029/2005JA011414. 44, 45, 46, 47, 87, 97, 98, 102, 103, 104, 105, 118, 130, 135, 136, 137, 138
- Denton, R. E., et al. (2009), Field line distribution of density at L=4.8 inferred from observations by CLUSTER, *Ann. Geophys.*, *27*, 705–724, doi:10.5194/angeo-27-705-2009. 45, 47, 97, 98, 102, 104, 130, 135, 138
- Denton, R. E., M. F. Thomsen, K. Takahashi, R. R. Anderson, and H. J. Singer (2011), Solar cycle dependence of bulk ion composition at geosynchronous orbit, *J. Geophys. Res.*, *116*, A03212, doi:10.1029/2010JA016027. 141
- Denton, R. E., K. Takahashi, M. F. Thomsen, J. E. Borovsky, H. J. Singer, Y. Wang, J. Goldstein, P. C. Brandt, and B. W. Reinisch (2014), Evolution of mass density and O+ concentration at geostationary orbit during storm and quiet events, *Journal of Geophysical Research (Space Physics)*, *119*, 6417–6431, doi:10.1002/2014JA019888. 126, 131
- Denton, R. E., K. Takahashi, J. Lee, C. K. Zeitler, N. T. Wimer, L. E. Litscher, H. J. Singer, and K. Min (2015), Field line distribution of mass density at geostationary orbit, *Journal of Geophysical Research (Space Physics)*, *120*, 4409–4422, doi:10.1002/2014JA020810. 91
- Dessler, A. J., and E. N. Parker (1959), Hydromagnetic theory of geomagnetic storms, *J. Geophys. Res.*, *64*, 2239–2252, doi:10.1029/JZ064i012p02239. 36, 108
- Dungey, J. W. (1954a), Electrodynamics of the outer atmosphere, *Pennsylvania State University Ionosphere Research Laboratory Science Report*, *69*. 40
- Dungey, J. W. (1954b), The propagation of Alfvén waves through the ionosphere, *Pennsylvania State University Ionosphere Research Laboratory Science Report*, *57*. 40
- Dungey, J. W. (1955), Electrodynamics of the Outer Atmosphere, in *Physics of the Ionosphere*, p. 229. 43

- Dungey, J. W. (1961), Interplanetary Magnetic Field and the Auroral Zones, *Physical Review Letters*, *6*, 47–48, doi:10.1103/PhysRevLett.6.47. 24
- Dungey, J. W. (1963), Structure of the exosphere, or adventures in velocity space, in *Geophysics: The Earth's Environment*, edited by C. DeWitt, J. Hieblot, and A. Lebeau, pp. 505–550, Gordon and Breach, New York. 25
- Ebihara, Y., M. Yamada, S. Watanabe, and M. Ejiri (2006), Fate of outflowing suprathermal oxygen ions that originate in the polar ionosphere, *Journal of Geophysical Research (Space Physics)*, *111*, A04219, doi:10.1029/2005JA011403. 131
- Echer, E., W. D. Gonzalez, B. T. Tsurutani, and A. L. C. Gonzalez (2008), Interplanetary conditions causing intense geomagnetic storms ($Dst \leq -100$ nT) during solar cycle 23 (1996–2006), *Journal of Geophysical Research (Space Physics)*, *113*, A05221, doi:10.1029/2007JA012744. 126
- Elphic, R. C., L. A. Weiss, M. F. Thomsen, D. J. McComas, and M. B. Moldwin (1996), Evolution of plasmaspheric ions at geosynchronous orbit during times of high geomagnetic activity, *Geophys. Res. Lett.*, *23*, 2189–2192, doi:10.1029/96GL02085. 128, 132
- Engebretson, M. J., and L. J. Cahill (1981), Pc5 pulsations observed during the June 1972 geomagnetic storm, *J. Geophys. Res.*, *86*, 5619–5631, doi:10.1029/JA086iA07p05619. 160
- Engebretson, M. J., L. J. Zanetti, T. A. Potemra, and M. H. Acuna (1986), Harmonically structured ULF pulsations observed by the AMPTE CCE magnetic field experiment, *Geophys. Res. Lett.*, *13*, 905–908, doi:10.1029/GL013i009p00905. 48, 155
- Engwall, E., A. I. Eriksson, C. M. Cully, M. André, R. Torbert, and H. Vaith (2009), Earth's ionospheric outflow dominated by hidden cold plasma, *Nature Geoscience*, *2*, 24–27, doi:10.1038/ngeo387. 27
- Escoubet, C. P., R. Schmidt, and M. L. Goldstein (1997a), Cluster - Science and Mission Overview, *Space Sci. Rev.*, *79*, 11–32, doi:10.1023/A:1004923124586. 53
- Escoubet, C. P., A. Pedersen, R. Schmidt, and P. A. Lindqvist (1997b), Density in the magnetosphere inferred from ISEE 1 spacecraft potential, *J. Geophys. Res.*, *102*, 17,595–17,610, doi:10.1029/97JA00290. 55, 67

- Escoubet, C. P., M. G. G. T. Taylor, A. Masson, H. Laakso, J. Volpp, M. Hapgood, and M. L. Goldstein (2013), Dynamical processes in space: Cluster results, *Annales Geophysicae*, *31*, 1045–1059, doi:10.5194/angeo-31-1045-2013. 53
- Escoubet, C. P., A. Masson, H. Laakso, and M. L. Goldstein (2015), Recent highlights from Cluster, the first 3-D magnetospheric mission, *Annales Geophysicae*, *33*, 1221–1235, doi:10.5194/angeo-33-1221-2015. 53
- Etcheto, J., G. Belmont, P. Canu, and J. G. Trotignon (1983), Active sounder experiments on GEOS and ISEE, in *ESA Special Publication, ESA Special Publication*, vol. 195, edited by W. R. Burke, pp. 39–46. 54
- Feldstein, Y. I., L. A. Dremukhina, U. Mall, and J. Woch (2000), On the two-phase decay of the Dst-variation, *Geophys. Res. Lett.*, *27*, 2813–2816, doi:10.1029/2000GL003783. 38
- Foster, C., and M. Lester (1996), Observations of nightside auroral plasma upflows in the F-region and topside ionosphere, *Annales Geophysicae*, *14*, 1274–1283, doi:10.1007/s00585-996-1274-1. 27
- Fu, H. S., J. B. Cao, B. Yang, and H. Y. Lu (2011), Electron loss and acceleration during storm time: The contribution of wave-particle interaction, radial diffusion, and transport processes, *Journal of Geophysical Research (Space Physics)*, *116*(A15), A10210, doi:10.1029/2011JA016672. 127
- Fujimoto, M., T. Terasawa, T. Mukai, Y. Saito, T. Yamamoto, and S. Kokubun (1998), Plasma entry from the flanks of the near-Earth magnetotail: Geotail observations, *J. Geophys. Res.*, *103*, 4391–4408, doi:10.1029/97JA03340. 141
- Gallagher, D. L., P. D. Craven, and R. H. Comfort (1988), An empirical model of the earth's plasmasphere, *Advances in Space Research*, *8*, 15–21, doi:10.1016/0273-1177(88)90258-X. 44
- Gallagher, D. L., P. D. Craven, and R. H. Comfort (1998), A simple model of magnetospheric trough total density, *J. Geophys. Res.*, *103*, 9293–9298, doi:10.1029/97JA03665. 128
- Gallagher, D. L., P. D. Craven, and R. H. Comfort (2000), Global core plasma model, *J. Geophys. Res.*, *105*, 18,819, doi:10.1029/1999JA000241. 30, 44, 45, 46, 47, 93, 97, 105, 118, 126, 128, 138

- Ganushkina, N. Y., I. Dandouras, Y. Y. Shprits, and J. Cao (2011), Locations of boundaries of outer and inner radiation belts as observed by Cluster and Double Star, *Journal of Geophysical Research (Space Physics)*, *116*, A09234, doi:10.1029/2010JA016376. 63
- Glassmeier, K. H., H. Volpers, and W. Baumjohann (1984), Ionospheric Joule dissipation as a damping mechanism for high latitude ULF pulsations - Observational evidence, *Planet. Space Sci.*, *32*, 1463–1466, doi:10.1016/0032-0633(84)90088-6. 48, 155
- Goldstein, J., and B. R. Sandel (2005), The Global Pattern of Evolution of Plasmaspheric Drainage Plumes, *Washington DC American Geophysical Union Geophysical Monograph Series*, *159*, 1. 128, 132
- Goldstein, J., R. E. Denton, M. K. Hudson, E. G. Miftakhova, S. L. Young, J. D. Menietti, and D. L. Gallagher (2001), Latitudinal density dependence of magnetic field lines inferred from Polar plasma wave data, *J. Geophys. Res.*, *106*, 6195–6202, doi:10.1029/2000JA000068. 90, 93, 126
- Gonzalez, W. D., J. A. Joselyn, Y. Kamide, H. W. Kroehl, G. Rostoker, B. T. Tsurutani, and V. M. Vasyliunas (1994), What is a geomagnetic storm?, *J. Geophys. Res.*, *99*, 5771–5792, doi:10.1029/93JA02867. 36
- Grebowsky, J. M. (1970), Model study of plasmopause motion, *J. Geophys. Res.*, *75*, 4329–4333, doi:10.1029/JA075i022p04329. 126
- Grew, R. S., F. W. Menk, M. A. Clilverd, and B. R. Sandel (2007), Mass and electron densities in the inner magnetosphere during a prolonged disturbed interval, *Geophys. Res. Lett.*, *34*, L02108, doi:10.1029/2006GL028254. 126, 128, 132
- Gustafsson, G., et al. (1997), The Electric Field and Wave Experiment for the Cluster Mission, *Space Sci. Rev.*, *79*, 137–156, doi:10.1023/A:1004975108657. 54, 67
- Gustafsson, G., et al. (2001), First results of electric field and density observations by Cluster EFW based on initial months of operation, *Annales Geophysicae*, *19*, 1219–1240, doi:10.5194/angeo-19-1219-2001. 67
- Haaland, S., B. Lybekk, K. Svenes, A. Pedersen, M. Förster, H. Vaith, and R. Torbert (2009), Plasma transport in the magnetotail lobes, *Annales Geophysicae*, *27*, 3577–3590, doi:10.5194/angeo-27-3577-2009. 28, 31, 99, 130, 131

- Haaland, S., et al. (2012a), Estimating the capture and loss of cold plasma from ionospheric outflow, *Journal of Geophysical Research (Space Physics)*, *117*, A07311, doi:10.1029/2012JA017679. 28, 31, 99, 130
- Haaland, S., K. Svenes, B. Lybekk, and A. Pedersen (2012b), A survey of the polar cap density based on Cluster EFW probe measurements: Solar wind and solar irradiation dependence, *J. Geophys. Res.*, *117*, A01216, doi:10.1029/2011JA017250. 31, 55
- Haaland, S., et al. (2013), *Cold Ion Outflow as a Source of Plasma for the Magnetosphere*, pp. 341–354, American Geophysical Union, doi:10.1029/2012GM001317. 28, 31, 99, 130
- Hamilton, D. C., G. Gloeckler, F. M. Ipavich, B. Wilken, and W. Stuedemann (1988), Ring current development during the great geomagnetic storm of February 1986, *J. Geophys. Res.*, *93*, 14,343–14,355, doi:10.1029/JA093iA12p14343. 38
- Hasegawa, H., M. Fujimoto, T.-D. Phan, H. Rème, A. Balogh, M. W. Dunlop, C. Hashimoto, and R. TanDokoro (2004), Transport of solar wind into Earth’s magnetosphere through rolled-up Kelvin-Helmholtz vortices, *Nature*, *430*, 755–758, doi:10.1038/nature02799. 141
- Higel, B., and W. Lei (1984), Electron density and plasmopause characteristics at 6.6 R_E - A statistical study of the GEOS 2 relaxation sounder data, *J. Geophys. Res.*, *89*, 1583–1601, doi:10.1029/JA089iA03p01583. 128
- Horwitz, J. L., R. H. Comfort, and C. R. Chappell (1984), Thermal ion composition measurements of the formation of the new outer plasmasphere and double plasmopause during storm recovery phase, *Geophys. Res. Lett.*, *11*, 701–704, doi:10.1029/GL011i008p00701. 101, 126, 127, 130
- Horwitz, J. L., R. H. Comfort, L. H. Brace, and C. R. Chappell (1986), Dual-spacecraft measurements of plasmasphere-ionosphere coupling, *J. Geophys. Res.*, *91*, 11,203–11,216, doi:10.1029/JA091iA10p11203. 101, 130, 131, 141
- Howarth, A., and A. W. Yau (2008), The effects of IMF and convection on thermal ion outflow in magnetosphere-ionosphere coupling, *Journal of Atmospheric and Solar-Terrestrial Physics*, *70*, 2132–2143, doi:10.1016/j.jastp.2008.08.008. 31
- Hughes, W. J. (1983), Hydromagnetic waves in the magnetosphere, *Reviews of Geophysics and Space Physics*, *21*, 508–520, doi:10.1029/RG021i002p00508. 39, 43

- Hughes, W. J. (1995), The magnetopause, magnetotail, and magnetic reconnection, in *Introduction to Space Physics*, edited by M. G. Kivelson and C. T. Russell, pp. 227–287, Cambridge University Press. vi, 20
- Hundhausen, A. J. (1995), The solar wind, in *Introduction to Space Physics*, edited by M. G. Kivelson and C. T. Russell, pp. 91–128, Cambridge University Press. 19
- Hutchinson, J. A., D. M. Wright, and S. E. Milan (2011), Geomagnetic storms over the last solar cycle: A superposed epoch analysis, *Journal of Geophysical Research (Space Physics)*, *116*, A09211, doi:10.1029/2011JA016463. vii, 37
- Imber, S. M., S. E. Milan, and B. Hubert (2007), Observations of significant flux closure by dual lobe reconnection, *Annales Geophysicae*, *25*, 1617–1627, doi:10.5194/angeo-25-1617-2007. 141
- Iyemori, T. (1990), Storm-time magnetospheric currents inferred from mid-latitude geomagnetic field variations, *Journal of Geomagnetism and Geoelectricity*, *42*, 1249–1265. 36
- Jacobs, J. A., Y. Kato, S. Matsushita, and V. A. Troitskaya (1964), Classification of geomagnetic micropulsations, *Journal of Geophysical Research*, *69*(1), 180–181, doi:10.1029/JZ069i001p00180. 40
- Johnson, C. Y. (1969), Ion and neutral composition of the ionosphere., *Annals of the IQSY*, *5*, 197–213. v, 17
- Johnson, M. T., J. R. Wygant, C. Cattell, F. S. Mozer, M. Temerin, and J. Scudder (2001), Observations of the seasonal dependence of the thermal plasma density in the Southern Hemisphere auroral zone and polar cap at 1R_E, *J. Geophys. Res.*, *106*, 19,023–19,034, doi:10.1029/2000JA900147. 55
- Johnstone, A. D., et al. (1997), Peace: a Plasma Electron and Current Experiment, *Space Sci. Rev.*, *79*, 351–398, doi:10.1023/A:1004938001388. 55, 57, 67
- Junginger, H., and W. Baumjohann (1984), Resonant harmonic Alfvén waves in the magnetosphere - A case study, *J. Geophys. Res.*, *89*, 10,757–10,762, doi:10.1029/JA089iA12p10757. 48, 156

-
- Katus, R. M., D. L. Gallagher, M. W. Liemohn, A. M. Keesee, and L. K. Sarno-Smith (2015), Statistical storm time examination of MLT-dependent plasmopause location derived from IMAGE EUV, *Journal of Geophysical Research (Space Physics)*, *120*, 5545–5559, doi:10.1002/2015JA021225. 93, 128
- Kavanagh, L. D., Jr., J. W. Freeman, Jr., and A. J. Chen (1968), Plasma flow in the magnetosphere, *J. Geophys. Res.*, *73*, 5511–5519, doi:10.1029/JA073i017p05511. vii, 29
- Kennel, C. F., and H. E. Petschek (1966), Limit on stably trapped particle fluxes, *Journal of Geophysical Research*, *71*(1), 1–28, doi:10.1029/JZ071i001p00001. 127
- Kistler, L. M., et al. (2006), Ion composition and pressure changes in storm time and nonstorm substorms in the vicinity of the near-Earth neutral line, *Journal of Geophysical Research (Space Physics)*, *111*(A10), A11222, doi:10.1029/2006JA011939. 31, 131
- Kistler, L. M., C. G. Mouikis, B. Klecker, and I. Dandouras (2010), Cusp as a source for oxygen in the plasma sheet during geomagnetic storms, *Journal of Geophysical Research (Space Physics)*, *115*, A03209, doi:10.1029/2009JA014838. 28, 99, 130
- Kivelson, M. G. (1995a), Physics of space plasmas, in *Introduction to Space Physics*, edited by M. G. Kivelson and C. T. Russell, pp. 27–57, Cambridge University Press. v, 2, 3, 15
- Kivelson, M. G. (1995b), Pulsations and magnetohydrodynamic waves, in *Introduction to Space Physics*, edited by M. G. Kivelson and C. T. Russell, pp. 330–355, Cambridge University Press. vii, 39, 41
- Korth, A., R. H. W. Friedel, F. Frutos-Alfaro, C. G. Mouikis, and Q. Zong (2002), Ion composition of substorms during storm-time and non-storm-time periods, *Journal of Atmospheric and Solar-Terrestrial Physics*, *64*, 561–566, doi:10.1016/S1364-6826(02)00013-5. 31
- Kronberg, E. A., S. E. Haaland, P. W. Daly, E. E. Grigorenko, L. M. Kistler, M. Fränz, and I. Dandouras (2012), Oxygen and hydrogen ion abundance in the near-Earth magnetosphere: Statistical results on the response to the geomagnetic and solar wind activity conditions, *Journal of Geophysical Research (Space Physics)*, *117*(A16), A12208, doi:10.1029/2012JA018071. 63, 99, 100, 130, 131

- Laakso, H., and A. Pedersen (1998), Ambient Electron Density Derived from Differential Potential Measurements, *Washington DC American Geophysical Union Geophysical Monograph Series*, 102, 49. 67
- Laakso, H., R. Pfaff, and P. Janhunen (2002a), Polar observations of electron density distribution in the Earth's magnetosphere. 1. Statistical results, *Ann. Geophys.*, 20, 1711–1724, doi:10.5194/angeo-20-1711-2002. 55, 66, 67, 126, 128
- Laakso, H., R. Pfaff, and P. Janhunen (2002b), Polar observations of electron density distribution in the Earth's magnetosphere. 2. Density profiles, *Ann. Geophys.*, 20, 1725–1735, doi:10.5194/angeo-20-1725-2002. 55, 125, 126, 127, 129
- Lavraud, B., et al. (2006a), Evidence for newly closed magnetosheath field lines at the dayside magnetopause under northward IMF, *Journal of Geophysical Research (Space Physics)*, 111, A05211, doi:10.1029/2005JA011266. 141
- Lavraud, B., M. F. Thomsen, S. Wing, M. Fujimoto, M. H. Denton, J. E. Borovsky, A. Aasnes, K. Seki, and J. M. Weygand (2006b), Observation of two distinct cold, dense ion populations at geosynchronous orbit: local time asymmetry, solar wind dependence and origin, *Annales Geophysicae*, 24, 3451–3465, doi:10.5194/angeo-24-3451-2006. 141
- Lawrence, D. J., M. F. Thomsen, J. E. Borovsky, and D. J. McComas (1999), Measurements of early and late time plasmasphere refilling as observed from geosynchronous orbit, *J. Geophys. Res.*, 104, 14,691–14,704, doi:10.1029/1998JA900087. 141
- Lee, D. H., and R. L. Lysak (1990), Effects of azimuthal asymmetry on ULF waves in the dipole magnetosphere, *Geophysical Research Letters*, 17(1), 53–56, doi:10.1029/GL017i001p00053. 145
- Lee, J. H., and V. Angelopoulos (2014), On the presence and properties of cold ions near Earth's equatorial magnetosphere, *Journal of Geophysical Research (Space Physics)*, 119, 1749–1770, doi:10.1002/2013JA019305. 101
- Lemaire, J. F., and K. I. Gringauz (1998), *The Earth's Plasmasphere*, Cambridge University Press, Cambridge, UK. 98, 130

- Lennartsson, W. (1989), Energetic (0.1- to 16-keV/e) magnetospheric ion composition at different levels of solar F10.7, *J. Geophys. Res.*, *94*, 3600–3610, doi:10.1029/JA094iA04p03600. 101, 132, 141
- Lennartsson, W., and E. G. Shelley (1986), Survey of 0.1- to 16-keV/e plasma sheet ion composition, *J. Geophys. Res.*, *91*, 3061–3076, doi:10.1029/JA091iA03p03061. 131
- Li, K., et al. (2012), On the ionospheric source region of cold ion outflow, *Geophys. Res. Lett.*, *39*, L18102, doi:10.1029/2012GL053297. 27, 31, 100, 130, 134
- Li, W., J. Raeder, J. Dorelli, M. Øieroset, and T. D. Phan (2005), Plasma sheet formation during long period of northward IMF, *Geophys. Res. Lett.*, *32*, L12S08, doi:10.1029/2004GL021524. 141
- Li, X., et al. (1997), Multisatellite observations of the outer zone electron variation during the November 34, 1993, magnetic storm, *Journal of Geophysical Research: Space Physics (19782012)*, *102*(A7), 14,123–14,140, doi:10.1029/97JA01101. 127
- Liao, J., L. M. Kistler, C. G. Mouikis, B. Klecker, I. Dandouras, and J.-C. Zhang (2010), Statistical study of O⁺ transport from the cusp to the lobes with Cluster CODIF data, *Journal of Geophysical Research (Space Physics)*, *115*, A00J15, doi:10.1029/2010JA015613. 28, 31, 98, 99, 100, 116, 130, 131, 134
- Liu, C., J. L. Horwitz, and P. G. Richards (1995), Effects of frictional ion heating and soft-electron precipitation on high-latitude F-region upflows, *Geophysical Research Letters*, *22*(20), 2713–2716, doi:10.1029/95GL02551. 27
- Liu, W., T. E. Sarris, X. Li, S. R. Elkington, R. Ergun, V. Angelopoulos, J. Bonnell, and K. H. Glassmeier (2009), Electric and magnetic field observations of Pc4 and Pc5 pulsations in the inner magnetosphere: A statistical study, *Journal of Geophysical Research (Space Physics)*, *114*(A13), A12206, doi:10.1029/2009JA014243. viii, 50, 51, 155, 156
- Lockwood, M., J. H. Waite, Jr., T. E. Moore, C. R. Chappell, and M. O. Chandler (1985a), The cleft ion fountain, *J. Geophys. Res.*, *90*, 9736–9748, doi:10.1029/JA090iA10p09736. 27, 28, 98, 99, 100, 116, 130, 134

- Lockwood, M., J. H. Waite, Jr., T. E. Moore, C. R. Chappell, and J. F. E. Johnson (1985b), A new source of suprathermal O⁺ ions near the dayside polar cap boundary, *J. Geophys. Res.*, *90*, 4099–4116, doi:10.1029/JA090iA05p04099. 27, 28, 98, 100, 116, 130, 134
- Lockwood, M., T. E. Moore, J. H. Waite, Jr., C. R. Chappell, and J. L. Horwitz (1985c), The geomagnetic mass spectrometer - Mass and energy dispersions of ionospheric ion flows into the magnetosphere, *Nature*, *316*, 612, doi:10.1038/316612a0. 28, 98, 99, 116
- Lointier, G., F. Darrouzet, P. M. E. Décréau, X. Vallières, S. Kouglbléno, J. G. Trotignon, and J.-L. Rauch (2013), Refilling process in the plasmasphere: a 3-D statistical characterization based on Cluster density observations, *Ann. Geophys.*, *31*, 217–237, doi:10.5194/angeo-31-217-2013. 30, 93
- Loranc, M., W. B. Hanson, R. A. Heelis, and J.-P. St.-Maurice (1991), A morphological study of vertical ionospheric flows in the high-latitude F region, *Journal of Geophysical Research: Space Physics*, *96*(A3), 3627–3646, doi:10.1029/90JA02242. 27
- Loto'aniu, T. M., C. L. Waters, B. J. Fraser, and J. C. Samson (1999), Plasma mass density in the plasmatrough: Comparison using ULF waves and CRRES, *Geophys. Res. Lett.*, *26*, 3277–3280, doi:10.1029/1999GL003641. 126
- Luhmann, J. G. (1995), Ionospheres, in *Introduction to Space Physics*, edited by M. G. Kivelson and C. T. Russell, pp. 183–202, Cambridge University Press. v, 17
- Lühr, H. (1994), The IMAGE magnetometer network, in *STEP International*, vol. 4, pp. 4–6, USSCO. 58
- Lybekk, B., A. Pedersen, S. Haaland, K. Svenes, A. N. Fazakerley, A. Masson, M. G. G. T. Taylor, and J.-G. Trotignon (2012), Solar cycle variations of the Cluster spacecraft potential and its use for electron density estimations, *Journal of Geophysical Research (Space Physics)*, *117*, A01217, doi:10.1029/2011JA016969. x, 67, 68, 69
- Maeda, N., S. Takasaki, H. Kawano, S. Ohtani, P. Decreau, J. Trotignon, S. Solovye, D. Baishev, and K. Yumoto (2009), Simultaneous observations of the plasma density on the same field line by the CPMN ground magnetometers and the Cluster satellites, *Adv. Space Res.*, *43*, 265–272, doi:10.1016/j.asr.2008.04.016. 44, 45, 46, 47, 102, 103, 104, 105, 131

- Maggiolo, R., and L. M. Kistler (2014), Spatial variation in the plasma sheet composition: Dependence on geomagnetic and solar activity, *Journal of Geophysical Research (Space Physics)*, *119*, 2836–2857, doi:10.1002/2013JA019517. 28, 99, 130, 131
- Mathie, R. A., F. W. Menk, I. R. Mann, and D. Orr (1999), Discrete Field Line Resonances and the Alfvén Continuum in the Outer Magnetosphere, *Geophys. Res. Lett.*, *26*, 659–662, doi:10.1029/1999GL900104. 48, 155, 156
- McPherron, R. L. (1991), Physical processes producing magnetospheric substorms and magnetic storms., in *Geomagnetism*, edited by J. A. Jacobs, pp. 593–739. 33
- McPherron, R. L. (1995), Magnetospheric dynamics, in *Introduction to Space Physics*, edited by M. G. Kivelson and C. T. Russell, pp. 400–458, Cambridge University Press. 33, 36
- McPherron, R. L., C. T. Russell, and M. P. Aubry (1973), Satellite studies of magnetospheric substorms on August 15, 1968: 9. Phenomenological model for substorms, *J. Geophys. Res.*, *78*, 3131, doi:10.1029/JA078i016p03131. 33
- McPherron, R. L., T. P. O’Brien, and S. Thompson (2005), Solar Wind Drivers for Steady Magnetospheric Convection, in *Multiscale Coupling of Sun-Earth Processes*, edited by A. T. Y. Liu, Y. Kamide, and G. Consolini, p. 113. 33
- McPherron, R. L., J. M. Weygand, and T.-S. Hsu (2008), Response of the Earth’s magnetosphere to changes in the solar wind, *Journal of Atmospheric and Solar-Terrestrial Physics*, *70*, 303–315, doi:10.1016/j.jastp.2007.08.040. 33, 34
- Mead, G. D. (1964), Deformation of the geomagnetic field by the solar wind, *Journal of Geophysical Research*, *69*(7), 1181–1195, doi:10.1029/JZ069i007p01181. 98
- Meerson, B. I., and P. V. Sasorov (1979), Nonlinear bounce resonant interaction between alfvén waves and geomagnetically trapped particles, *Planetary and Space Science*, *27*(4), 503 – 509, doi:http://dx.doi.org/10.1016/0032-0633(79)90127-2. 43
- Menk, F., Z. Kale, M. Sciffer, P. Robinson, C. Waters, R. Grew, M. Clilverd, and I. Mann (2014), Remote sensing the plasmasphere, plasmopause, plumes and other features using ground-based magnetometers, *Journal of Space Weather and Space Climate*, *4*(27), A34, doi:10.1051/swsc/2014030. 137

- Menk, F. W., D. Orr, M. A. Clilverd, A. J. Smith, C. L. Waters, D. K. Millng, and B. J. Fraser (1999), Monitoring spatial and temporal variations in the dayside plasmasphere using geomagnetic field line resonances, *J. Geophys. Res.*, *104*, 19,955–19,970, doi:10.1029/1999JA900205. 46, 47, 118, 136, 137, 138, 166
- Menk, F. W., I. R. Mann, A. J. Smith, C. L. Waters, M. A. Clilverd, and D. K. Milling (2004), Monitoring the plasmopause using geomagnetic field line resonances, *J. Geophys. Res.*, *109*, A04216, doi:10.1029/2003JA010097. 166
- Meredith, N. P., R. M. Thorne, R. B. Horne, D. Summers, B. J. Fraser, and R. R. Anderson (2003), Statistical analysis of relativistic electron energies for cyclotron resonance with EMIC waves observed on CRRES, *Journal of Geophysical Research (Space Physics)*, *108*, 1250, doi:10.1029/2002JA009700. 1
- Milan, S. E., G. Provan, and B. Hubert (2007), Magnetic flux transport in the Dungey cycle: A survey of dayside and nightside reconnection rates, *Journal of Geophysical Research (Space Physics)*, *112*, A01209, doi:10.1029/2006JA011642. 35
- Milan, S. E., J. Hutchinson, P. D. Boakes, and B. Hubert (2009), Influences on the radius of the auroral oval, *Annales Geophysicae*, *27*, 2913–2924, doi:10.5194/angeo-27-2913-2009. 126
- Millan, R. M., and R. M. Thorne (2007), Review of radiation belt relativistic electron losses, *Journal of Atmospheric and Solar-Terrestrial Physics*, *69*, 362–377, doi:10.1016/j.jastp.2006.06.019. 127
- Min, K., J. Bortnik, R. E. Denton, K. Takahashi, J. Lee, and H. J. Singer (2013), Quiet time equatorial mass density distribution derived from AMPTE/CCE and GOES using the magnetoseismology technique, *Journal of Geophysical Research (Space Physics)*, *118*, 6090–6105, doi:10.1002/jgra.50563. 105, 135
- Moldwin, M. B., M. F. Thomsen, S. J. Bame, D. J. McComas, and K. R. Moore (1994), An examination of the structure and dynamics of the outer plasmasphere using multiple geosynchronous satellites, *J. Geophys. Res.*, *99*, 11,475–11,482, doi:10.1029/93JA03526. 128

- Moore, T. E., and G. V. Khazanov (2010), Mechanisms of ionospheric mass escape, *Journal of Geophysical Research (Space Physics)*, *115*, A00J13, doi:10.1029/2009JA014905. 27
- Moore, T. E., M. O. Chandler, C. J. Pollock, D. L. Reasoner, R. L. Arnoldy, B. Austin, P. M. Kintner, and J. Bonnell (1996), Plasma heating and flow in an auroral arc, *J. Geophys. Res.*, *101*, 5279–5298, doi:10.1029/95JA03154. 27
- Moore, T. E., et al. (1999), Polar/TIDE results on polar ion outflows, *Washington DC American Geophysical Union Geophysical Monograph Series*, *109*, 87–101, doi:10.1029/GM109p0087. 28, 31
- Mouikis, C. G., L. M. Kistler, Y. H. Liu, B. Klecker, A. Korth, and I. Dandouras (2010), H⁺ and O⁺ content of the plasma sheet at 15–19 Re as a function of geomagnetic and solar activity, *J. Geophys. Res.*, *115*, A00J16, doi:10.1029/2010JA015978. 99, 130, 131, 141
- Mouikis, C. G., L. M. Kistler, G. Wang, and Y. Liu (2014), Background subtraction for the Cluster/CODIF plasma ion mass spectrometer, *Geoscientific Instrumentation, Methods and Data Systems*, *3*, 41–48, doi:10.5194/gi-3-41-2014. 63
- Nagai, T., J. H. Waite, Jr., J. L. Green, C. R. Chappell, R. C. Olsen, and R. H. Comfort (1984), First measurements of supersonic polar wind in the polar magnetosphere, *Geophys. Res. Lett.*, *11*, 669–672, doi:10.1029/GL011i007p00669. 27
- Nagata, D., S. Machida, S. Ohtani, Y. Saito, and T. Mukai (2007), Solar wind control of plasma number density in the near-Earth plasma sheet, *Journal of Geophysical Research (Space Physics)*, *112*, A09204, doi:10.1029/2007JA012284. 141
- Nagata, D., S. Machida, S. Ohtani, Y. Saito, and T. Mukai (2008), Solar wind control of plasma number density in the near-Earth plasma sheet: three-dimensional structure, *Annales Geophysicae*, *26*, 4031–4049, doi:10.5194/angeo-26-4031-2008. 141
- Nakagawa, T., T. Ishii, K. Tsuruda, H. Hayakawa, and T. Mukai (2000), Net current density of photoelectrons emitted from the surface of the GEOTAIL spacecraft, *Earth, Planets, and Space*, *52*, 283–292. 67

- Nishida, A. (1966), Formation of plasmopause, or magnetospheric plasma knee, by the combined action of magnetospheric convection and plasma escape from the tail, *J. Geophys. Res.*, *71*, 5669–5679, doi:10.1029/JZ071i023p05669. 128
- Nosé, M., A. Ieda, and S. P. Christon (2009), Geotail observations of plasma sheet ion composition over 16 years: On variations of average plasma ion mass and O⁺ triggering substorm model, *Journal of Geophysical Research (Space Physics)*, *114*, A07223, doi:10.1029/2009JA014203. 131, 141
- Nosé, M., K. Takahashi, R. R. Anderson, and H. J. Singer (2011), Oxygen torus in the deep inner magnetosphere and its contribution to recurrent process of O⁺-rich ring current formation, *J. Geophys. Res.*, *116*(A15), A10224, doi:10.1029/2011JA016651. 101, 130, 131, 132
- Nosé, M., et al. (2015), Formation of the oxygen torus in the inner magnetosphere: Van Allen Probes observations, *Journal of Geophysical Research (Space Physics)*, *120*, 1182–1196, doi:10.1002/2014JA020593. 101, 130
- Obayashi, T., and J. A. Jacobs (1958), Geomagnetic Pulsations and the Earth's Outer Atmosphere, *Geophysical Journal*, *1*, 53–63, doi:10.1111/j.1365-246X.1958.tb00034.x. 48, 155
- Ober, D. M., J. L. Horwitz, M. F. Thomsen, R. C. Elphic, D. J. McComas, R. D. Belian, and M. B. Moldwin (1997), Premidnight plasmaspheric “plumes”, *J. Geophys. Res.*, *102*, 11,325–11,334, doi:10.1029/97JA00562. 128, 132
- Obertz, P., and O. M. Raspopov (1968), Study of the Spatial Characteristics of Type Pc5 Geomagnetic Pulsations, *Geomagnetism and Aeronomy*, *8*, 424. 160
- O'Brien, T. P., and M. B. Moldwin (2003), Empirical plasmopause models from magnetic indices, *Geophys. Res. Lett.*, *30*, 1152, doi:10.1029/2002GL016007. 126, 128, 141
- O'Brien, T. P., K. R. Lorentzen, I. R. Mann, N. P. Meredith, J. B. Blake, J. F. Fennell, M. D. Looper, D. K. Milling, and R. R. Anderson (2003), Energization of relativistic electrons in the presence of ULF power and MeV microbursts: Evidence for dual ULF and VLF acceleration, *Journal of Geophysical Research (Space Physics)*, *108*, 1329, doi:10.1029/2002JA009784. 1

- Ohtani, S., M. Nosé, S. P. Christon, and A. T. Y. Lui (2011), Energetic O⁺ and H⁺ ions in the plasma sheet: Implications for the transport of ionospheric ions, *J. Geophys. Res.*, *116*(A15), A10211, doi:10.1029/2011JA016532. 99, 131
- Øieroset, M., J. Raeder, T. D. Phan, S. Wing, J. P. McFadden, W. Li, M. Fujimoto, H. Rème, and A. Balogh (2005), Global cooling and densification of the plasma sheet during an extended period of purely northward IMF on October 22-24, 2003, *Geophys. Res. Lett.*, *32*, L12S07, doi:10.1029/2004GL021523. 141
- Olsen, R. C. (1992), The density minimum at the earth's magnetic equator, *J. Geophys. Res.*, *97*, 1135–1150, doi:10.1029/91JA02719. 97
- Olsen, R. C., S. D. Shawhan, D. L. Gallagher, C. R. Chappell, and J. L. Green (1987), Plasma observations at the earth's magnetic equator, *J. Geophys. Res.*, *92*, 2385–2407, doi:10.1029/JA092iA03p02385. 97
- Orr, D., and J. A. D. Matthew (1971), The variation of geomagnetic micropulsation periods with latitude and the plasmopause, *Planet. Space Sci.*, *19*, 897–905, doi:10.1016/0032-0633(71)90141-3. 48, 155
- Ozhogin, P., J. Tu, P. Song, and B. W. Reinisch (2012), Field-aligned distribution of the plasmaspheric electron density: An empirical model derived from the IMAGE RPI measurements, *Journal of Geophysical Research (Space Physics)*, *117*, A06225, doi:10.1029/2011JA017330. 93, 126
- Öztürk, M. K., and R. A. Wolf (2007), Bifurcation of drift shells near the dayside magnetopause, *Journal of Geophysical Research (Space Physics)*, *112*, A07207, doi:10.1029/2006JA012102. 98
- Parker, E. N. (1958), Dynamics of the Interplanetary Gas and Magnetic Fields., *Astrophysical Journal*, *128*, 664, doi:10.1086/146579. 19
- Patra, S., and E. Spencer (2015), The effect of changing solar wind conditions on the inner magnetosphere and ring current: A model data comparison, *Journal of Geophysical Research (Space Physics)*, *120*, 6528–6540, doi:10.1002/2015JA021299. 38

- Pedersen, A. (1995), Solar wind and magnetosphere plasma diagnostics by spacecraft electrostatic potential measurements, *Annales Geophysicae*, *13*, 118–129, doi:10.1007/s00585-995-0118-8. 67
- Pedersen, A., et al. (2001), Four-point high time resolution information on electron densities by the electric field experiments (EFW) on Cluster, *Annales Geophysicae*, *19*, 1483–1489, doi:10.5194/angeo-19-1483-2001. 67
- Pedersen, A., et al. (2008), Electron density estimations derived from spacecraft potential measurements on Cluster in tenuous plasma regions, *J. Geophys. Res.*, *113*, A07S33, doi:10.1029/2007JA012636. 55, 67
- Perraut, S., H. de Feraudy, A. Roux, P. M. E. Décréau, and J. Paris (1990), Density measurements in key regions of the earth’s magnetosphere - Cusp and auroral region, *J. Geophys. Res.*, *95*, 5997–6014, doi:10.1029/JA095iA05p05997. 54
- Peterson, W. K., L. Andersson, B. C. Callahan, H. L. Collin, J. D. Scudder, and A. W. Yau (2008), Solar-minimum quiet time ion energization and outflow in dynamic boundary related coordinates, *Journal of Geophysical Research (Space Physics)*, *113*, A07222, doi:10.1029/2008JA013059. 98, 100, 116, 130, 134
- Plaschke, F., K.-H. Glassmeier, O. D. Constantinescu, I. R. Mann, D. K. Milling, U. Motschmann, and I. J. Rae (2008), Statistical analysis of ground based magnetic field measurements with the field line resonance detector, *Annales Geophysicae*, *26*, 3477–3489, doi:10.5194/angeo-26-3477-2008. 48, 155, 156
- Poulter, E. M., W. Allan, J. G. Keys, and E. Nielsen (1984), Plasmatrough ion mass densities determined from ULF pulsation eigenperiods, *Planet. Space Sci.*, *32*, 1069–1078, doi:10.1016/0032-0633(84)90132-6. viii, 48, 49, 155, 156
- Press, W. (1992), *Numerical Recipes in C: The Art of Scientific Computing*, no. bk. 4 in *Numerical recipes in C : the art of scientific computing* / William H. Press, Cambridge University Press. 163
- Reeves, G. D., K. L. McAdams, R. H. W. Friedel, and T. P. O’Brien (2003), Acceleration and loss of relativistic electrons during geomagnetic storms, *Geophysical Research Letters*, *30*(10), doi:10.1029/2002GL016513. 127

- Reinisch, B. W., X. Huang, P. Song, J. L. Green, S. F. Fung, V. M. Vasyliunas, D. L. Gallagher, and B. R. Sandel (2004), Plasmaspheric mass loss and refilling as a result of a magnetic storm, *Journal of Geophysical Research (Space Physics)*, *109*, A01202, doi:10.1029/2003JA009948. 126
- Rème, H., et al. (1997), The Cluster Ion Spectrometry (CIS) Experiment, *Space Sci. Rev.*, *79*, 303–350, doi:10.1023/A:1004929816409. 55, 56, 61, 70
- Rème, H., et al. (2001), First multispacecraft ion measurements in and near the Earth's magnetosphere with the identical Cluster ion spectrometry (CIS) experiment, *Annales Geophysicae*, *19*, 1303–1354, doi:10.5194/angeo-19-1303-2001. 55
- Rishbeth, H. (1988), Basic physics of the ionosphere: a tutorial review, *Electronic and Radio Engineers, Journal of the Institution of*, *58*(6), S207–S223, doi:10.1049/jiere.1988.0060. 16
- Roberts, W. T., Jr., J. L. Horwitz, R. H. Comfort, C. R. Chappell, J. H. Waite, Jr., and J. L. Green (1987), Heavy ion density enhancements in the outer plasmasphere, *J. Geophys. Res.*, *92*, 13,499–13,512, doi:10.1029/JA092iA12p13499. 101, 130, 131
- Russell, C. T., and R. L. McPherron (1973), The Magnetotail and Substorms, *Space Sci. Rev.*, *15*, 205–266, doi:10.1007/BF00169321. 33
- Samson, J. C., and G. Rostoker (1972), Latitude-dependent characteristics of high-latitude Pc 4 and Pc 5 micropulsations, *J. Geophys. Res.*, *77*, 6133–6144, doi:10.1029/JA077i031p06133. vii, 48, 49, 155
- Samson, J. C., J. A. Jacobs, and G. Rostoker (1971), Latitude-dependent characteristics of long-period geomagnetic micropulsations, *J. Geophys. Res.*, *76*, 3675–3683, doi:10.1029/JA076i016p03675. 48, 155
- Sandel, B. R., R. A. King, W. T. Forrester, D. L. Gallagher, A. L. Broadfoot, and C. C. Curtis (2001), Initial results from the IMAGE Extreme Ultraviolet Imager, *Geophys. Res. Lett.*, *28*, 1439–1442, doi:10.1029/2001GL012885. 128, 132
- Skopke, N. (1966), A general relation between the energy of trapped particles and the disturbance field near the Earth, *J. Geophys. Res.*, *71*, 3125–3130, doi:10.1029/JZ071i013p03125. 36, 108

- Scudder, J. D., X. Cao, and F. S. Mozer (2000), Photoemission current-spacecraft voltage relation: Key to routine, quantitative low-energy plasma measurements, *J. Geophys. Res.*, *105*, 21,281, doi:10.1029/1999JA900423. 67
- Seki, K., et al. (2003), Cold ions in the hot plasma sheet of Earth's magnetotail, *Nature*, *422*, 589–592. 73
- Sergeev, V. A., R. J. Pellinen, and T. I. Pulkkinen (1996), Steady Magnetospheric Convection: A Review of Recent Results, *Space Sci. Rev.*, *75*, 551–604, doi:10.1007/BF00833344. 33
- Shabanskiy, V. P., and A. Y. Antonova (1969), Topology of the Drift Shells of Particles in the Magnetosphere, *Geomagnetism and Aeronomy*, *8*, 799. 98
- Sheeley, B. W., M. B. Moldwin, H. K. Rassoul, and R. R. Anderson (2001), An empirical plasmasphere and trough density model: CRRES observations, *J. Geophys. Res.*, *106*, 25,631–25,642, doi:10.1029/2000JA000286. 93, 126, 128
- Shelley, E. G., R. G. Johnson, and R. D. Sharp (1972), Satellite observations of energetic heavy ions during a geomagnetic storm, *J. Geophys. Res.*, *77*, 6104, doi:10.1029/JA077i031p06104. 98, 100, 116, 130, 134
- Shelley, E. G., W. K. Peterson, A. G. Ghielmetti, and J. Geiss (1982), The polar ionosphere as a source of energetic magnetospheric plasma, *Geophys. Res. Lett.*, *9*, 941–944, doi:10.1029/GL009i009p00941. 98, 100, 116, 130, 134
- Shprits, Y. Y., R. M. Thorne, R. Friedel, G. D. Reeves, J. Fennell, D. N. Baker, and S. G. Kanekal (2006), Outward radial diffusion driven by losses at magnetopause, *Journal of Geophysical Research: Space Physics (19782012)*, *111*(A11), doi:10.1029/2006JA011657. 127
- Singer, H. J., D. J. Southwood, R. J. Walker, and M. G. Kivelson (1981), Alfvén wave resonances in a realistic magnetospheric magnetic field geometry, *J. Geophys. Res.*, *86*, 4589–4596, doi:10.1029/JA086iA06p04589. 145
- Singer, S. F. (1957), A new model of magnetic storms and aurorae, *Transactions, American Geophysical Union*, *38*, 175–190, doi:10.1029/TR038i002p00175. 30

- Slapak, R., H. Nilsson, L. G. Westerberg, and A. Eriksson (2012), Observations of oxygen ions in the dayside magnetosheath associated with southward IMF, *Journal of Geophysical Research (Space Physics)*, *117*, A07218, doi:10.1029/2012JA017754. 31
- Southwood, D. J. (1973), The behaviour of ULF waves and particles in the magnetosphere, *Planetary and Space Science*, *21*(1), 53 – 65, doi:http://dx.doi.org/10.1016/0032-0633(73)90019-6. 43
- Southwood, D. J. (1974), Some features of field line resonances in the magnetosphere, *Planet. Space Sci.*, *22*, 483–491, doi:10.1016/0032-0633(74)90078-6. 43
- Southwood, D. J., and W. J. Hughes (1983), Theory of hydromagnetic waves in the magnetosphere, *Space Sci. Rev.*, *35*, 301–366, doi:10.1007/BF00169231. 39
- Southwood, D. J., and M. G. Kivelson (1982), Charged particle behavior in low-frequency geomagnetic pulsations. II - Graphical approach, *J. Geophys. Res.*, *87*, 1707–1710, doi:10.1029/JA087iA03p01707. 43
- Southwood, D. J., J. W. Dungey, and R. J. Etherington (1969), Bounce resonant interaction between pulsations and trapped particles, *Planetary and Space Science*, *17*(3), 349 – 361, doi:http://dx.doi.org/10.1016/0032-0633(69)90068-3. 43
- Stewart, B. (1861), On the Great Magnetic Disturbance Which Extended from August 28 to September 7, 1859, as Recorded by Photography at the Kew Observatory, *Royal Society of London Philosophical Transactions Series I*, *151*, 423–430. 40
- Stokholm, M., H. Balsiger, J. Geiss, H. Rosenbauer, and D. T. Young (1989), Variations of the magnetospheric ion number densities near geostationary orbit with solar activity, *Annales Geophysicae*, *7*, 69–75. 101, 132
- Stone, R. G., et al. (1992a), The Unified Radio and Plasma wave investigation, *Astron. Astrophys. Suppl. Ser.*, *92*, 291–316. 54
- Stone, R. G., et al. (1992b), ULYSSES radio and plasma wave observations in the Jupiter environment, *Science*, *257*, 1524–1531, doi:10.1126/science.257.5076.1524. 54
- Su, Y.-J., M. F. Thomsen, J. E. Borovsky, and D. J. Lawrence (2001), A comprehensive survey of plasmasphere refilling at geosynchronous orbit, *J. Geophys. Res.*, *106*, 25,615–25,630, doi:10.1029/2000JA000441. 125, 126, 127, 128, 141

- Sugiura, M., and T. Kamei (1991), Equatorial dst index 1957-1986, in *IAGA Bull.*, vol. 40, edited by A. Berthelier and M. Menvielle, ISGI Publ. Off., Saint. Maur-des-Fosses, France. 36
- Sugiura, M., and D. J. Poros (1964), Hourly values of equatorial Dst for the IGY, *Ann. Int. Geophys. Year*, 35, 9–45. 36
- Summers, D., B. Ni, and N. P. Meredith (2007), Timescales for radiation belt electron acceleration and loss due to resonant waveparticle interactions: 2. Evaluation for VLF chorus, ELF hiss, and electromagnetic ion cyclotron waves, *Journal of Geophysical Research: Space Physics (19782012)*, 112(A4), doi:10.1029/2006JA011993. 127
- Svenes, K. R., B. Lybekk, A. Pedersen, and S. Haaland (2008), Cluster observations of near-Earth magnetospheric lobe plasma densities a statistical study, *Ann. Geophys.*, 26, 2845–2852, doi:10.5194/angeo-26-2845-2008. 55
- Tabachnick, B. G., and L. S. Fidell (2006), *Using Multivariate Statistics (5th Edition)*, Allyn & Bacon, Inc., Needham Heights, MA, USA. 79, 108
- Takahashi, K., and R. E. Denton (2007), Magnetospheric seismology using multiharmonic toroidal waves observed at geosynchronous orbit, *J. Geophys. Res.*, 112, A05204, doi:10.1029/2006JA011709. 44, 45, 46, 47, 102, 104, 105, 135, 138
- Takahashi, K., and R. L. McPherron (1984), Standing hydromagnetic oscillations in the magnetosphere, *Planet. Space Sci.*, 32, 1343–1359. 48, 156
- Takahashi, K., R. L. McPherron, and W. J. Hughes (1984), Multispacecraft observations of the harmonic structure of Pc 3-4 magnetic pulsations, *J. Geophys. Res.*, 89, 6758–6774, doi:10.1029/JA089iA08p06758. 48, 156
- Takahashi, K., R. E. Denton, and D. Gallagher (2002), Toroidal wave frequency at L = 6–10: Active Magnetospheric Particle Tracer Explorers/CCE observations and comparison with theoretical model, *Journal of Geophysical Research (Space Physics)*, 107, 1020, doi:10.1029/2001JA000197. viii, 46, 47, 48, 50, 51, 118, 135, 138, 155, 160
- Takahashi, K., R. E. Denton, R. R. Anderson, and W. J. Hughes (2004), Frequencies of standing Alfvén wave harmonics and their implication for plasma mass distribution along geomagnetic field lines: Statistical analysis of CRRES data, *J. Geophys. Res.*, 109,

- A08202, doi:10.1029/2003JA010345. 44, 45, 46, 47, 48, 87, 90, 98, 102, 104, 105, 130, 135, 138, 155
- Takahashi, K., R. E. Denton, R. R. Anderson, and W. J. Hughes (2006), Mass density inferred from toroidal wave frequencies and its comparison to electron density, *J. Geophys. Res.*, *111*, A01201, doi:10.1029/2005JA011286. 46, 47, 118, 131, 135, 138
- Takahashi, K., R. E. Denton, and H. J. Singer (2010), Solar cycle variation of geosynchronous plasma mass density derived from the frequency of standing Alfvén waves, *Journal of Geophysical Research (Space Physics)*, *115*, A07207, doi:10.1029/2009JA015243. 46, 47, 118, 135, 138
- Takahashi, K., R. E. Denton, M. Hirahara, K. Min, S.-I. Ohtani, and E. Sanchez (2014), Solar cycle variation of plasma mass density in the outer magnetosphere: Magnetoseismic analysis of toroidal standing Alfvén waves detected by Geotail, *Journal of Geophysical Research (Space Physics)*, *119*, 8338–8356, doi:10.1002/2014JA020274. 44, 45, 46, 47, 105, 118, 138
- Takahashi, K., M. D. Hartinger, V. Angelopoulos, and K.-H. Glassmeier (2015), A statistical study of fundamental toroidal mode standing Alfvén waves using THEMIS ion bulk velocity data, *Journal of Geophysical Research (Space Physics)*, *120*, 6474–6495, doi:10.1002/2015JA021207. 48, 155, 156
- Takahashi, S., T. Iyemori, and M. Takeda (1990), A simulation of the storm-time ring current, *Planet. Space Sci.*, *38*, 1133–1141, doi:10.1016/0032-0633(90)90021-H. 38
- Tamao, T. (1978), Modulation of energetic particle fluxes due to long-period geomagnetic oscillations, *Planetary and Space Science*, *26*(12), 1149 – 1159, doi:http://dx.doi.org/10.1016/0032-0633(78)90055-7. 43
- Terasawa, T., et al. (1997), Solar wind control of density and temperature in the near-Earth plasma sheet: WIND/GEOTAIL collaboration, *Geophys. Res. Lett.*, *24*, 935–938, doi:10.1029/96GL04018. 141
- Thaller, S. A., et al. (2015), Van Allen Probes investigation of the large-scale duskward electric field and its role in ring current formation and plasmasphere erosion in the 1 June 2013 storm, *Journal of Geophysical Research (Space Physics)*, *120*, 4531–4543, doi:10.1002/2014JA020875. 126, 128

- Thomsen, M. F. (2004), Why Kp is such a good measure of magnetospheric convection, *Space Weather*, *2*, S11004, doi:10.1029/2004SW000089. 119
- Thomsen, M. F., J. E. Borovsky, R. M. Skoug, and C. W. Smith (2003), Delivery of cold, dense plasma sheet material into the near-Earth region, *Journal of Geophysical Research (Space Physics)*, *108*, 1151, doi:10.1029/2002JA009544. 141
- Thorne, R. M., R. B. Horne, S. Glauert, N. P. Meredith, Y. Y. Shprits, D. Summers, and R. R. Anderson (2013), *The Influence of Wave-Particle Interactions on Relativistic Electron Dynamics During Storms*, pp. 101–112, American Geophysical Union, doi:10.1029/159GM07. 127
- Treumann, R., and W. Baumjohann (1997), *Advanced Space Plasma Physics*, Imperial College Press. 32
- Trotignon, J. G., J. Etcheto, and J. P. Thouvenin (1986), Automatic determination of the electron density measured by the relaxation sounder on board ISEE 1, *J. Geophys. Res.*, *91*, 4302–4320, doi:10.1029/JA091iA04p04302. 54
- Trotignon, J. G., et al. (2001), How to determine the thermal electron density and the magnetic field strength from the Cluster/Whisper observations around the Earth, *Ann. Geophys.*, *19*, 1711–1720, doi:10.5194/angeo-19-1711-2001. 54
- Trotignon, J. G., J. L. Rauch, P. M. E. Décr e, P. Canu, and J. Lemaire (2003), Active and passive plasma wave investigations in the earth’s environment: The Cluster/WHISPER experiment, *Adv. Space Res.*, *31*, 1449–1454, doi:10.1016/S0273-1177(02)00959-6. 54
- Tsyganenko, N. A. (1996), Effects of the solar wind conditions in the global magnetospheric configurations as deduced from data-based field models (Invited), in *International Conference on Substorms, ESA Special Publication*, vol. 389, edited by E. J. Rolfe and B. Kaldeich, p. 181. 60
- Turner, D. L., Y. Shprits, M. Hartinger, and V. Angelopoulos (2012), Explaining sudden losses of outer radiation belt electrons during geomagnetic storms, *Nature Physics*, *8*, 208–212, doi:10.1038/nphys2185. 127

- Van Allen, J. A., C. E. McIlwain, and G. H. Ludwig (1959), Radiation observations with satellite 1958 , *Journal of Geophysical Research*, *64*(3), 271–286, doi:10.1029/JZ064i003p00271. 30
- Wahlund, J. E., H. J. Opgenoorth, I. Hggstrm, K. J. Winser, and G. O. L. Jones (1992), EISCAT observations of topside ionospheric ion outflows during auroral activity: Revisited, *Journal of Geophysical Research: Space Physics*, *97*(A3), 3019–3037, doi:10.1029/91JA02438. 27
- Walsh, B. M., D. G. Sibeck, Y. Nishimura, and V. Angelopoulos (2013), Statistical analysis of the plasmaspheric plume at the magnetopause, *Journal of Geophysical Research (Space Physics)*, *118*, 4844–4851, doi:10.1002/jgra.50458. 128, 132
- Wang, C.-P., L. R. Lyons, T. Nagai, J. M. Weygand, and A. T. Y. Lui (2010), Evolution of plasma sheet particle content under different interplanetary magnetic field conditions, *Journal of Geophysical Research (Space Physics)*, *115*, A06210, doi:10.1029/2009JA015028. 141
- Wanliss, J. A., and K. M. Showalter (2006), High-resolution global storm index: Dst versus SYM-H, *Journal of Geophysical Research (Space Physics)*, *111*, A02202, doi:10.1029/2005JA011034. 36
- Warner, M. R., and D. Orr (1979), Time of flight calculations for high latitude geomagnetic pulsations, *Planet. Space Sci.*, *27*, 679–689, doi:10.1016/0032-0633(79)90165-X. 143, 144, 145, 160
- Waters, C. L. (2000), ULF Resonance Structure in the Magnetosphere, *Advances in Space Research*, *25*, 1541–1558, doi:10.1016/S0273-1177(99)00667-5. 39
- Waters, C. L., F. W. Menk, and B. J. Fraser (1991), The resonance structure of low latitude Pc3 geomagnetic pulsations, *Geophys. Res. Lett.*, *18*, 2293–2296, doi:10.1029/91GL02550. xvii, 161, 162, 163
- Waters, C. L., J. C. Samson, and E. F. Donovan (1995), The temporal variation of the frequency of high latitude field line resonances, *J. Geophys. Res.*, *100*, 7987–7996, doi:10.1029/94JA02712. 145, 162, 166

- Wild, J. A., T. K. Yeoman, and C. L. Waters (2005), Revised time-of-flight calculations for high-latitude geomagnetic pulsations using a realistic magnetospheric magnetic field model, *J. Geophys. Res.*, *110*(A9), A11206, doi:10.1029/2004JA010964. 144, 145, 146, 155, 156, 159, 160, 173
- Wilson, G. R. (1994), Kinetic modeling of O⁺ upflows resulting from $E \times B$ convection heating in the high-latitude F region ionosphere, *Journal of Geophysical Research: Space Physics*, *99*(A9), 17,453–17,466, doi:10.1029/94JA01214. 27
- Wing, S., D. G. Sibeck, M. Wiltberger, and H. Singer (2002), Geosynchronous magnetic field temporal response to solar wind and IMF variations, *Journal of Geophysical Research (Space Physics)*, *107*, 1222, doi:10.1029/2001JA009156. 141
- Wing, S., J. R. Johnson, P. T. Newell, and C.-I. Meng (2005), Dawn-dusk asymmetries, ion spectra, and sources in the northward interplanetary magnetic field plasma sheet, *Journal of Geophysical Research (Space Physics)*, *110*, A08205, doi:10.1029/2005JA011086. 141
- Wing, S., J. R. Johnson, and M. Fujimoto (2006), Timescale for the formation of the cold-dense plasma sheet: A case study, *Geophys. Res. Lett.*, *33*, L23106, doi:10.1029/2006GL027110. 141
- Winglee, R. M. (2000), Mapping of ionospheric outflows into the magnetosphere for varying IMF conditions, *Journal of Atmospheric and Solar-Terrestrial Physics*, *62*, 527–540, doi:10.1016/S1364-6826(00)00015-8. 31
- Wolf, R. A. (1995), Magnetospheric configuration, in *Introduction to Space Physics*, edited by M. G. Kivelson and C. T. Russell, pp. 288–329, Cambridge University Press. vii, 26, 28
- Yau, A. W., and M. Andre (1997), Sources of Ion Outflow in the High Latitude Ionosphere, *Space Sci. Rev.*, *80*, 1–25, doi:10.1023/A:1004947203046. 27, 28, 31, 98, 99, 100, 116, 130, 134
- Yau, A. W., L. Lenchyshyn, E. G. Shelley, and W. K. Peterson (1985), Energetic auroral and polar ion outflow at DE 1 altitudes Magnitude, composition, magnetic activity dependence, and long-term variations, *J. Geophys. Res.*, *90*, 8417–8432, doi:10.1029/JA090iA09p08417. 131

- Yau, A. W., A. Howarth, W. K. Peterson, and T. Abe (2012), Transport of thermal-energy ionospheric oxygen (O^+) ions between the ionosphere and the plasma sheet and ring current at quiet times preceding magnetic storms, *Journal of Geophysical Research (Space Physics)*, *117*, A07215, doi:10.1029/2012JA017803. 131
- Yermolaev, Y. I., I. G. Lodkina, N. S. Nikolaeva, and M. Y. Yermolaev (2010), Statistical study of interplanetary condition effect on geomagnetic storms, *Cosmic Research*, *48*, 485–500, doi:10.1134/S0010952510060018. 126
- Young, D. T., H. Balsiger, and J. Geiss (1982), Correlations of magnetospheric ion composition with geomagnetic and solar activity, *J. Geophys. Res.*, *87*(A11), 9077–9096, doi:10.1029/JA087iA11p09077. 31, 101, 125, 126, 127, 129, 131, 132, 141
- Yumoto, K., T. Saito, and T. Sakurai (1983), Local time asymmetry in the characteristics of Pc5 magnetic pulsations, *Planet. Space Sci.*, *31*, 459–471, doi:10.1016/0032-0633(83)90158-7. 48, 155, 156